SNOWMELT AND SOIL THAW ENERGY IN SUB-ALPINE TUNDRA, WOLF CREEK, YUKON TERRITORY, CANADA

by

Taskin Shirazi
B.Sc. (Honours), University of Toronto, 2000

THESIS SUBMITTED IN PARTIAL FULFILLMENT OF THE REQUIREMENTS FOR THE DEGREE OF

MASTER OF SCIENCE

In the
Department
of
Geography

SIMON FRASER UNIVERSITY

Summer 2006

APPROVAL

Name: Taskin Shirazi

Degree: Master of Science

Title of Thesis: Snowmelt and Soil Thaw Energy in Sub-Alpine Tundra, Wolf Creek, Yukon Territory, Canada

Examining Committee:

Chair: N.K. Blomley, Professor

Dr. D.M. Allen
Senior Supervisor
Associate Professor and Department Chair,
Department of Earth Sciences

Dr. J.W. Pomeroy
Committee Member
Canada Research Chair in Water Science and Climate Change, Department of Geography
University of Saskatchewan

Dr. M.G. Schmidt
Committee Member
Associate Professor, Department of Geography

Dr. R.D. Moore
External Examiner
Associate Professor and Chair of Forest Hydrology,
Departments of Geography and Forest Resource Management
University of British Columbia

Date Defended/Approved: July 21, 2006

ABSTRACT

To accurately represent subsurface flow in a hydrologic model of permafrost terrain during spring thaw, an understanding of soil thaw and soil thaw rates is required. Research was conducted on an organic-covered hillslope in Granger Basin, Yukon Territory, to quantify relationships between net radiation, snowmelt and soil thaw energy. The infiltration and freezing of meltwater into the soil may contribute to pre-thaw warming. When this energy (1.82 $MJ \cdot m^{-2} \cdot d^{-1}$) is taken into account, the daily mean contribution to soil thaw from net radiation is approximately 9%. Measured and estimated soil thaw depths compared well ($R^2 = 0.75$) when energy was distributed across the hillslope. This research contributes to the understanding of active layer development, sheds insight into the role of infiltrating and freezing meltwater on soil thaw, and provides an approach for the estimation of soil thaw based on a direct link between surface net radiation and the subsurface energy regime.

Keywords: **soil thaw energy; sub-arctic Canada; net radiation; frozen organic soils; sub-alpine tundra**

This thesis and all the hard work and effort that went into its completion is dedicated to my family. Thank you for always supporting me in everything I do.

ACKNOWLEDGEMENTS

There are many people that have assisted me in various capacities, without which, the completion of this thesis would not have been possible. Research (particularly in the North) is rarely accomplished alone, and this thesis was truly a co-operative endeavour. I would like to thank and acknowledge the following people.

First and foremost, I would like to express my deepest thanks to my senior supervisor, Dr. Diana Allen. Without your invaluable support, advice, guidance, encouragement and faith in my abilities, this project would not have been seen to completion. For that, I am forever grateful.

I would also like to thank Dr. John Pomeroy for his insightful comments and suggestions throughout my graduate program. Your contributions have helped to create a stronger piece of work and I appreciate the time and effort you have invested in reviewing my thesis. Thank you to Dr. Margaret Schmidt for support, advice and valuable editorial comments. Also, thank you to Dr. Kevin Shook for your helpful contributions and ideas earlier on in this project. A big thank you also goes to Dr. Dan Moore for taking the time to serve as the External Examiner and for your encouragement and valuable comments. Thank you also to NSTP, NSERC, CFCAS and SFU Geography for funding this research.

Fieldwork and data collection in the North is always an adventure and my field season would not have been the same without valuable field assistance and advice from Dan Bewley, Steve McCartney, Dr. Jean-Emmanuel Sicart, Chris DeBeer, Dr. Richard Essery, Dr. Gerald Flerchinger, Dr. Tim Link, Dr. Sean Carey, Dr. Raoul Granger, Dr. Doug Clark and Jonathan Lee. Thank you all for an interesting and entertaining stay on the north-facing slope. An extra thank you goes to Dan Bewley for his extremely helpful advice and suggestions long after field work was completed, for his expertise on snow and shrubs and most of all, his patience and speedy responses to any and all of my inquiries!

Thank you to all the people at NHRI who have assisted me in data acquisition, preparation or analysis. Tom Brown for providing the slope-corrected solar radiation data and for assistance with CHRM, Tom Carter for assistance in the creation of my patch transect map, Newell Hedstrom for logistical assistance during the field study, Brenda Toth for acquiring meteorological data, and Dwayne Keir for all the maps, photos and data. Thanks also go to Ric Janowicz and Glen Ford of the Department of Indian and Northern Affairs for kindly providing logistical assistance in the field.

I would also like to acknowledge and sincerely thank Dr. Owen Hertzman and Scott Weston for their priceless intellectual support, advice and encouragement. Thank you for always listening to my endless questions about radiation, snow and soil thaw. I truly appreciate having you both around to bounce my ideas and thoughts off of.

I would also like to thank and acknowledge the amazing staff and support people of the Geography Department: Marcia, Hilary, Dianne, Ravinder, Kathy, B-Jae, Jasper and John, for all their support and assistance.

Thank you to all the professors and instructors I've had the opportunity to TA for. Thank you to Dr. Ian Hutchinson, Mungandi Nasitwitwi, Dr. Mike Roberts, Dr. Owen Hertzman and Dr. Mark Johnson – it was a pleasure and an excellent learning experience.

A special thanks to Dr. Sharon Brewer of Thomspon Rivers University (Kamloops) and to Dr. Jonathan Driver for their valuable advice, assistance and support.

A massive shout-out and thank you to all my friends and colleagues that have made my time here at SFU truly enjoyable, memorable and at times, bearable. Thank you to Rosemary Hanna, Lydia Lee, Vikki Blouin, Damian Collins, Jenny Romero, Don Reid, Gift Dumedah, James Morley, Craig Emmerton, Jolie Gareis, Kenji Kitamura, Natalie Helmstetter, Arthur Aginam, Stephanie Campbell, Eric Evangelista, Mashaal Memon, Vipul Mehra, Michael Letourneau, Mayu Ishida and Andrew Clements. Beyond SFU, a thank you also goes to Andrea Lam, Katrina Tiongson and Vicky Tongco for all their encouragement, advice, editorial and moral support. I am truly grateful to you all for providing friendship, support, good times and good food!

I would especially like to acknowledge my Hydrology labmates – Kimberly Blais, Neil Goeller and Nicole Wright. Thanks for all the intellectual and moral support, crazy antics, and camaraderie that made the "dungeon" a place where we could "focus on the science" and still have a lot of fun! An extra "props" to Kim, I truly appreciate your enduring friendship and support. Our experience reminds me of Mark Twain's admonition "to never let school interfere with our education".

To my "peeps", Cathy Febria, Tanya Turk and James McLean – you have been an awesome and invaluable source of strength, support, friendship and encouragement. I am truly indebted to you for helping me get through the "tough times" and for always believing in me.

And most importantly, I would like to sincerely thank and acknowledge my family, Mom, Dad, Mahnaaz, Ruhee, Asad and Gudoo for their endless and immeasurable love, support, patience, guidance, advice, encouragement, and prayers. I am blessed to have such unconditional support and love to draw strength and security from. You have dealt admirably with me during the rough times and I am grateful for your support. I know that I can always count on you for anything. My *salaams* and *duas* are always with you.

Thank you.

TABLE OF CONTENTS

LIST OF FIGURES

LIST OF TABLES

LIST OF SYMBOLS AND UNITS

Symbol	Quantity	Units
B	thermal quality or fraction of ice in a unit mass of wet snow	dimensionless
c_{soil}	specific heat capacity of the soil	$J \cdot m^{-3} \cdot K^{-1}$
C	coefficient used in the parametric equation of Zhao and Gray (1999) for infiltration into frozen soils	dimensionless
C_w	volumetric heat capacity of water	$J \cdot K^{-1} \cdot m^{-3}$
dF/dt	rate of infiltrating water	$m \cdot s^{-1}$
D_h	diffuse radiation on a horizontal surface	$W \cdot m^{-2}$; $MJ \cdot m^{-2} \cdot d^{-1}$
dh/dt	rate of soil thaw	$m \cdot s^{-1}$; $cm \cdot d^{-1}$
D_s	diffuse radiation on a sloping surface	$W \cdot m^{-2}$; $MJ \cdot m^{-2} \cdot d^{-1}$
d_{snow}	depth of snow	m; cm
dT/dt	daily temperature change of the active layer	$K \cdot d^{-1}$
dT/dz	temperature gradient at the bottom of the active layer	$K \cdot m^{-1}$
dU/dt	rate of change of internal (stored) energy	$W \cdot m^{-2}$; $MJ \cdot m^{-2} \cdot d^{-1}$
e	vapour pressure	millibar
f_{ice}	fractional ice content in the soil	dimensionless
g	constant dependent on the spacing and geometry of a capacitor	dimensionless
h_f	latent heat of fusion of ice	$J \cdot kg^{-1}$
INF	frozen soil infiltration over the melt period	mm
I_r	intensity of extraterrestrial radiation	$W \cdot m^{-2}$; $MJ \cdot m^{-2} \cdot d^{-1}$
I_s	intensity of direct short-wave radiation falling on the surface	$W \cdot m^{-2}$; $MJ \cdot m^{-2} \cdot d^{-1}$

Symbol	Quantity	Units
K	thermal conductivity of the soil	$W \cdot m^{-1} \cdot K^{-1}$
K^*	net shortwave radiation	$W \cdot m^{-2}$; $MJ \cdot m^{-2} \cdot d^{-1}$
$K\uparrow$	outgoing shortwave radiation	$W \cdot m^{-2}$; $MJ \cdot m^{-2} \cdot d^{-1}$
$K\downarrow$	incoming shortwave radiation	$W \cdot m^{-2}$; $MJ \cdot m^{-2} \cdot d^{-1}$
L^*	net longwave radiation	$W \cdot m^{-2}$; $MJ \cdot m^{-2} \cdot d^{-1}$
$L\uparrow$	outgoing longwave radiation	$W \cdot m^{-2}$; $MJ \cdot m^{-2} \cdot d^{-1}$
$L\downarrow$	incoming longwave radiation	$W \cdot m^{-2}$; $MJ \cdot m^{-2} \cdot d^{-1}$
m	optical air mass	dimensionless
M	daily mean melt rate	$mm \cdot d^{-1}$
m_{dry}	weight obtained after drying the soil sample to a constant weight	g
M_{point}	daily melt rate at a point	$mm \cdot d^{-1}$
m_{wet}	weight of soil sample at the time of sampling	g
p	time period of HydroSense probe output	millisecond
Q^*	net all-wave radiation	$W \cdot m^{-2}$; $MJ \cdot m^{-2} \cdot d^{-1}$
Q_a	energy advected from external sources	$W \cdot m^{-2}$; $MJ \cdot m^{-2} \cdot d^{-1}$
Q_e	latent heat flux	$W \cdot m^{-2}$; $MJ \cdot m^{-2} \cdot d^{-1}$
Q_{freeze}	latent heat released due to the freezing of meltwater that has infiltrated into the soil	$W \cdot m^{-2}$; $MJ \cdot m^{-2} \cdot d^{-1}$
Q_g	heat flux into the soil	$W \cdot m^{-2}$; $MJ \cdot m^{-2} \cdot d^{-1}$
Q_h	sensible heat flux	$W \cdot m^{-2}$; $MJ \cdot m^{-2} \cdot d^{-1}$
Q_i	latent heat used to melt ground ice (i.e. soil thaw energy)	$W \cdot m^{-2}$; $MJ \cdot m^{-2} \cdot d^{-1}$
Q_{INF}	convective heat transfer by infiltrating water	$W \cdot m^{-2}$; $MJ \cdot m^{-2} \cdot d^{-1}$
Q_m	snowmelt energy	$W \cdot m^{-2}$; $MJ \cdot m^{-2} \cdot d^{-1}$
Q_p	heat flux conducted out of the active layer and into permafrost	$W \cdot m^{-2}$; $MJ \cdot m^{-2} \cdot d^{-1}$

Symbol	Quantity	Units
Q_s	sensible heat flux that warms the active layer	$W \cdot m^{-2}$; $MJ \cdot m^{-2} \cdot d^{-1}$
RH	relative humidity	%
S	unit co-ordinate vector expressing the position of the sun	dimensionless
S_0	surface saturation moisture content at the soil surface	$mm^3 \cdot mm^{-3}$
S_I	average soil saturation (water and ice) of the top 0.4 m soil layer at the start of infiltration	$mm^3 \cdot mm^{-3}$
SWE	snow water equivalent	mm
t_0	infiltration opportunity time	hours
T_{air}	air temperature	Kelvin
T_I	average soil temperature for the 0.4 m soil layer at the start of infiltration	Kelvin
T_{sfc}	surface temperature	Kelvin
v_{water}	volume of water	m^3
X	unit co-ordinate vector normal to surface and pointing away from ground	dimensionless
z	active layer thickness	m
α	albedo	dimensionless
β	angle between HydroSense probe rods and the ground surface	degrees
ΔT	difference in temperature between rainwater or snowmelt water and the soil	Kelvin
ε	emissivity of the surface	dimensionless
θ_g	gravimetric water content	dimensionless
θ_v	volumetric water content	dimensionless
κ	dielectric constant	dimensionless
Λ	angle between X and S	degrees; radians
ρ_{ice}	density of ice	$kg \cdot m^{-3}$

Symbol	Quantity	Units
ρ_{snow}	density of snow	kg·m^{-3}
ρ_{soil}	dry bulk density of the soil	kg·m^{-3}
ρ_{water}	density of water	kg·m^{-3}
ς	capacitance	farad
σ	Stefan-Boltzmann constant	W·m^{-2}·K^{-4}
τ_{atm}	daily atmospheric transmissivity	dimensionless
τ_z	mean zenith path transmissivity of the atmosphere	dimensionless
Φ	elevation angle of the surface	degrees

GLOSSARY

Active Layer the layer of ground above permafrost which thaws in summer and freezes again in winter.

CHRM Cold Regions Hydrological Model, uses modular modelling to develop, support and apply dynamic model routines for specific hydrological purposes. The integrated system of software provides the framework to develop and evaluate physically-based algorithms and effectively integrate selected algorithms into an operational model. Existing algorithms can be modified or new algorithms can be developed and added as modules to the module library. Modules from the library are coupled to create a physically-based model suitable for the specific application.

Cryofront the 0˚C boundary which is used to determine the transition from frozen to unfrozen soil in the thermo-calorimetric calculation of the soil heat flux, also referred to as the 0˚C isotherm.

Depth Hoar large flat ice crystals of low strength (weak mechanical structure) that form in the lowest layers of a cold shallow snowpack due to the diffusion of vapour from the relatively warmer soil below.

DOY Day Of Year, where DOY 1 corresponds to January 1st and DOY 365 corresponds to December 31st (refer to Appendix A).

Frost Table represents the upper surface of the seasonally frozen and saturated layer of soil. The frost table acts as a relatively impermeable boundary over which subsurface flow occurs.

Melt Energy (Q_m) the energy consumed in melting snow over a unit area per unit time (in $W \cdot m^{-2}$ or $MJ \cdot m^{-2} \cdot d^{-1}$).

Organic Soil soils of the Organic order are classified as containing >17% organic carbon or >30% organic matter by weight. Soils occurring in the sub-arctic regions of Canada are classified in the Organic Cryosol Great Group and are defined as having organic matter to a depth of 1 m below the surface. Organic soils consist mainly of mosses (such as *Sphagnum* moss), sedges, or other hydrophytic vegetation.

Permafrost a layer of ground below the surface in which the temperature of the material has remained below 0°C continuously for more than two years.

Saturated Layer depth through which subsurface flow occurs. The upper boundary of the saturated layer is the water table and the lower boundary is the frost table.

Snow-free Patch an area of bare ground that has been exposed due to snow ablation but that is still surrounded by snow on all sides, also referred to as a 'patch' in this study.

Soil Heat Flux (Q_g) the amount of energy transported through a unit area of soil per unit time (in $W \cdot m^{-2}$ or $MJ \cdot m^{-2} \cdot d^{-1}$).

Soil Moisture in this study, soil moisture refers to the calibrated liquid water content of the soil measured using a Campbell Scientific HydroSense Water Content Reflectometer.

Soil Pit a hole dug into the ground that is stratified into depth layers, instrumented with temperature and moisture sensors and then backfilled with soil. Moisture and temperature measurements recorded at the soil pit, along with information on the thermal properties of the soil, are used to calculate the soil heat flux into the soil profile using the thermocalorimetric method.

Soil Pre-warming in this study, the term soil pre-warming refers to the freezing of infiltrated meltwater and the subsequent release of latent energy that raises the temperature of the soil close to 0 °C.

Soil Thaw in this study, soil thaw is the depth to the frost table measured using a graduated steel rod, assuming that the soil above the frost table is unfrozen and unsaturated and the soil below is frozen and saturated.

Soil Thaw Energy (Q_i) the energy consumed in melting ground ice in the active layer over a unit area per unit time (in $W \cdot m^{-2}$ or $MJ \cdot m^{-2} \cdot d^{-1}$).

SWE Snow Water Equivalent, the depth of water (in cm or mm) that would result from the complete melting of a snowcover, calculated from snow depth (d) and density (ρ), where: $SWE = 0.01 \cdot d_{snow} \cdot \rho_{snow}$.

Water Table the surface along which water pressure equals air pressure. The water table separates the vadose and phreatic zones.

CHAPTER 1: INTRODUCTION

1.1 Background

The formation, accumulation and subsequent melting of a snowpack are important occurrences in cold landscapes. The snowcover exerts a considerable influence on the surface energy balance, as variations in snowcover change the surface albedo (Boike et al., 2003) and, therefore, influence the thermal regime of the active layer and permafrost (Ling and Zhang, 2003).

The heterogeneous nature of the depth and density of the snowcover and the energy available for melt causes the snowcover to become discontinuous as it melts. Snow water equivalent (SWE) varies spatially, and consequently, so does the duration of the snowcover during the melt period. The energy available for snowmelt also varies spatially as a result of local variations in energy exchange that are related to slope, aspect, aerodynamic roughness of the surface and other factors (Marsh, 1990). Once the snow has melted, the resulting soil thaw pattern controls the drainage pattern due to the depth dependency of hydraulic conductivity (Quinton et al., 2000).

Quinton et al. (2004) highlight the need for field investigations aimed at improving the understanding of the distribution of energy used to melt snow and thaw the snow-free ground during ablation. As well, given the large spatial variability of soil thaw depth, point measurements are of limited use in estimating subsurface drainage rates (Quinton et al., 2004). Therefore, to better predict subsurface flow rates, it is critical to develop a technique that uses point measurements of thaw depth to represent thaw depth at the larger hillslope scale.

1.2 Snow Distribution

Snow is a key component of the hydrologic cycle in cold and high latitude environments (Woo, 1998; Kane et al., 1991; Woo et al., 1983; Dingman, 1973). Snow can account for up to 80% of the annual precipitation, and blankets most of the arctic and sub-arctic landscape for at least half the year (Marsh, 1990). Water in the snowpack is released from storage during the brief spring melt period when air temperatures rise above 0°C. As a result, snowmelt is the principal source of soil moisture, surface-water supply, groundwater recharge and, in some areas, flooding (Dingman, 2002). According to Woo (1998), the areal distribution of snow is important for a number of reasons, particularly for its influence on the ground thermal regime. To a large extent, the ground thermal regime is controlled by the snowcover's physical properties, thickness, establishment and duration (Boike et al., 2003). Roth and Boike (2001) found that a thicker layer of snow greatly reduced the heat exchange of the permafrost soil with the atmosphere largely due to the low thermal conductivity of snow.

The spatial distribution of snow at the end of winter determines the spatial distribution of water available to recharge soil moisture and to generate runoff (Woo, 1998). The end-of-winter snow distribution is, therefore, especially important in arctic and sub-arctic environments where snowmelt is spatially variable, and its melt and runoff represent the major hydrological event of the year (Woo, 1998; Pomeroy and Gray, 1995). The distribution of snow also affects the development of the drainage network, thereby influencing the lag time between snowmelt and the initiation of streamflow (Woo, 1998; Roulet and Woo, 1986).

1.2.1 Effect of Elevation, Slope and Aspect on Snow Water Equivalent

The depth of a seasonal snowcover usually increases with increasing elevation due to the associated increase in the number of snowfall events and decrease in evaporation and melt (Pomeroy and Gray, 1995). In mountainous terrain, seasonal SWE and elevation are often strongly correlated (US Army Corps of Engineers, 1956). However, even along specific transects, the rate of increase in SWE with elevation can vary significantly from year to year (Meiman, 1970 as cited in: Pomeroy and Gray, 1995).

Slope, aspect, vegetation, wind, temperature and characteristics of parent weather systems also influence the distribution of SWE (Pomeroy and Gray, 1995; Shook, 1993). For example, frequent winds of high speed and long duration at higher elevations can cause additional snow redistribution and sublimation (Pomeroy and Gray, 1995).

Aspect influences snow distribution patterns due to its influence on the surface energy exchange processes. For example, snow melts earliest on slopes that receive large amounts of solar radiation and/or slopes exposed to the movement of warm winds (Pomeroy and Gray, 1995). Male and Gray (1981) and Dunne and Leopold (1978) noted that it is commonly observed that snow on a south-facing slope melts faster than snow on a north-facing slope, the reason being that the orientation of the slope affects the amount of direct beam shortwave radiation that the area receives.

1.2.2 Snow Accumulation in Open Environments

In many arctic and sub-arctic environments, snow on the ground undergoes frequent redistribution by wind (Woo et al., 2000; Woo, 1998). In these windswept regions, snowcover growth is governed by wind drift events and is characterized by patterns of deposition and erosion (Figure 1-1) (Marsh, 1990). Killingtveit and Sand (1991) examined variations in the mean depth and coefficient of variation of SWE as a function of elevation for snowpacks in Norwegian mountains. Their results suggest that wind redistribution of snow is significant at high elevations. In many open environments, erosion of the snowcover by wind more than compensates for the increase in precipitation received at higher elevations (Pomeroy and Gray, 1995).

The erosion and deposition of snow is largely controlled by the roughness of the surface (Shook, 1993). Shook (1993) observed that the spatial variability of surface roughness occurs at many scales, and suggested that this produces a variation in SWE at several spatial scales as well. In open terrain, meso-scale (~ 100-10 000 m) and micro-scale (~ 10-100 m) differences in vegetation and topography can create wide variations in snow accumulation patterns due to the effects of surface roughness on airflow patterns and snow transport (Pomeroy and Gray, 1995). For example, in the Coast Mountains of the southern Yukon Territory, SWE was found to decrease with increasing elevation, a trend opposite to the association found between these variables in most mountainous environments (Pomeroy et al., 1999; Pomeroy and Gray, 1995). According to Pomeroy and Gray (1995), accumulation, in this case, was more influenced by vegetation and exposure to the wind than by elevation.

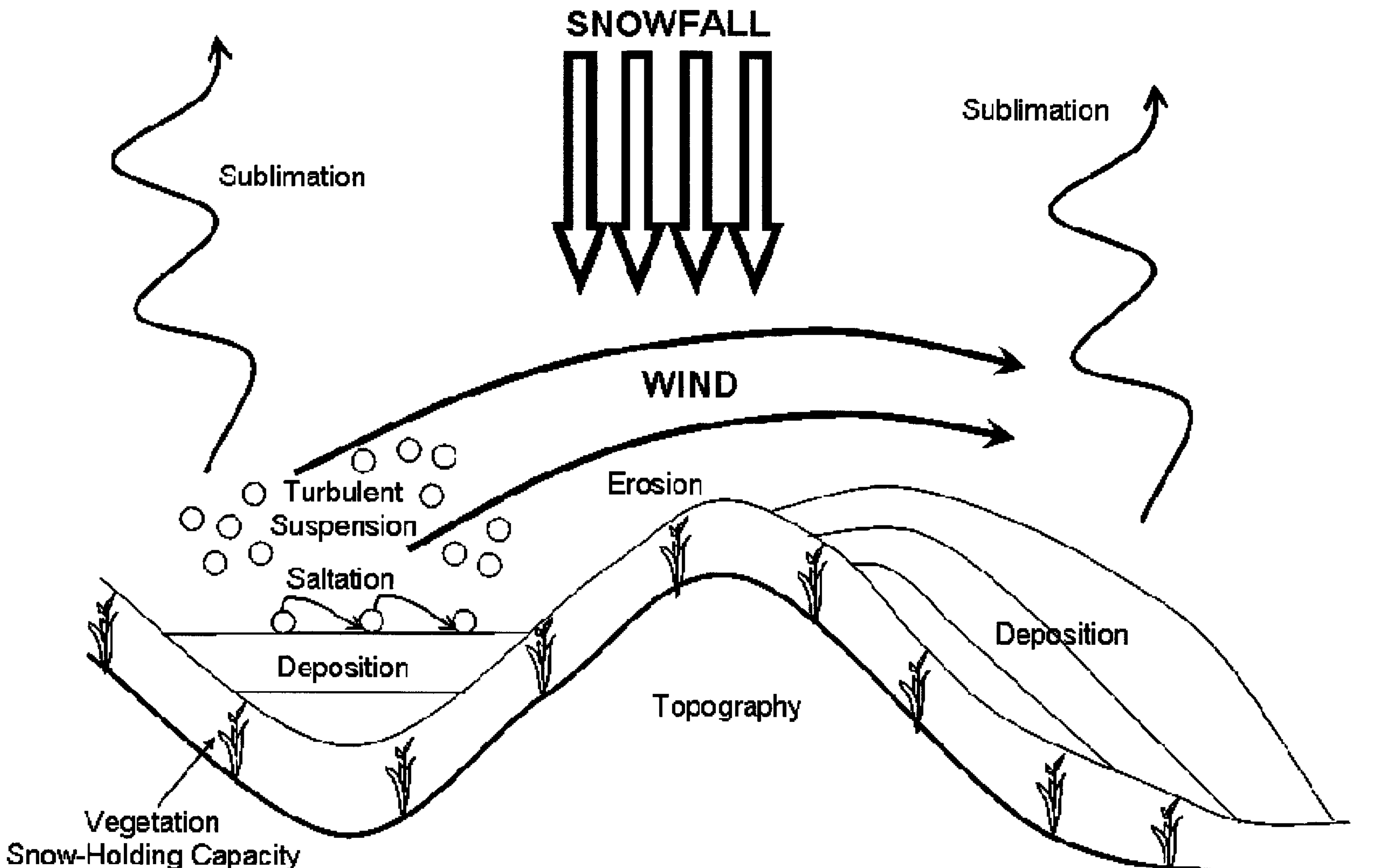

Adapted from Liston and Sturm (1998), by permission

Figure 1-1: Key processes of snow transport and deposition in open and topographically variable terrain.

1.2.3 Snowcover Measurement

There are a variety of instruments and methodologies for collecting snow survey data (snow depth, density, and water equivalent). Snow water equivalent (SWE) is defined as the equivalent depth of water of a snowcover, and is calculated by:

$$SWE = 0.01 \cdot d_{snow} \cdot \rho_{snow} \tag{1-1}$$

where, SWE is snow water equivalent (mm), d_{snow} is snow depth (cm), and ρ_{snow} is the snow density (kg·m^{-3}) (Pomeroy and Gray, 1995).

Several point and areal methods used in North America for measuring these snow parameters are summarized in Pomeroy and Gray (1995). Techniques for making point measurements of SWE include snow rulers, snow gauges, snow pits, snow pillows and radar. Traditionally, point observations have been extrapolated to large areas to generate snow distribution maps, which according to Woo (1998), have been of questionable accuracy (Woo, 1998). Areal measurements are mainly derived from snow surveys or remote sensing (Pomeroy and Gray, 1995). Aerial photography, both vertical and oblique, allows the snowcover extent to be mapped in rugged terrain where parts of the basin are swept clear of snow (Kirnbauer et al., 1991).

1.3 Snowmelt Processes

Snowmelt is an important process that exerts a strong influence on the hydrology of cold environments and in particular, permafrost areas (Woo, 1998; Church, 1974). Snowmelt can be divided into warming, ripening and output phases (Dingman, 2002). During the warming phase, the temperature of the snowpack is raised to isothermal conditions at the melting point. Any additional energy input produces surface melt. Water is retained in the snowpack up to the point where the liquid holding capacity is exceeded; this is known as the ripening phase. This initiates the output phase, where water flows out of the snowpack, and the energy input is proportional to the meltwater produced (Dingman, 2002).

The energy balance approach has often been used to study snowmelt in permafrost areas (Boike et al., 2003; Woo et al., 1983; Woo et al., 1981; Price and Dunne, 1976; Outcalt et al., 1975; Weller and Holmgren, 1974). Empirical methods, such as the temperature index method, have also been attempted (James and Vieira-Ribeiro, 1975; Woo, 1976). Empirical methods are used to obtain indices for a single site and for particular years and, therefore, do not have general validity (Woo, 1986).

Because snowmelt is essentially a phase change process, the energy balance equation provides a physical framework for snowmelt calculations. This framework involves the application of the law of conservation of energy to a control volume of snow (Figure 1-2), where the lower boundary is the snow-frozen-ground interface and the upper boundary is the snow-atmosphere interface (Male and Gray, 1981). By using a control volume, it is possible to express the fluxes of energy penetrating the snow surface and retained by the volume as internal energy changes (Shook, 1993):

$$Q_m = Q^* - Q_h - Q_e - Q_g - Q_a - \frac{dU}{dt} \tag{1-2}$$

where, Q_m is the energy available for snowmelt, Q^* is the net all-wave radiation, Q_h and Q_e are the turbulent fluxes of sensible and latent energy, respectively, Q_g is the soil heat flux (which is small when the ground is snow-covered), Q_a is the energy advected from external sources, such as heat added by falling rain in the vertical direction or horizontal advection of heat from patches of soil and dU/dt is the rate of change of internal (stored) energy in the volume per unit surface area per unit time. Generally, Q_a is considered to be the local horizontal advection from areas of surrounding bare ground and/or patches

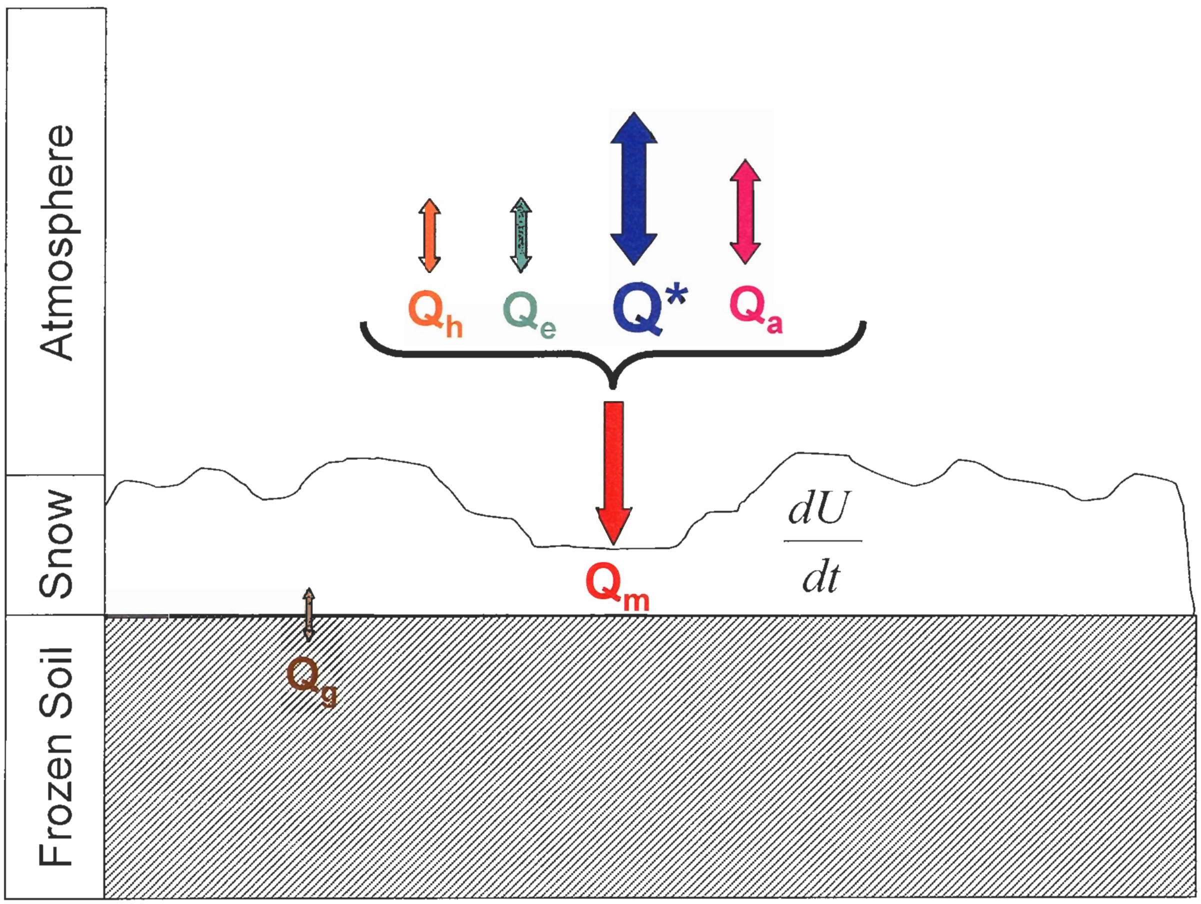

Figure 1-2: **Generalized energy balance over a melting snow surface where Q^* is net all-wave radiation, Q_a is energy from advection, Q_h is sensible heat, Q_e is latent heat, Q_m is the energy used for snow melt, Q_g is the soil heat flux and dU/dt is the change in internal energy of the snowpack. The size of the arrows represents the relative magnitudes of the fluxes. Fluxes are positive in the direction of the snow surface, but in reality can actually occur in both directions (i.e. towards and away from the surface).**

of bare soil surrounding the melting snowcover, but in practice however, it is quite difficult to actually distinguish between the horizontal components of Q_h, Q_e and Q_a. All terms have units of W·m^{-2}

In Equation 1-2, the fluxes of energy directed towards the volume are taken as positive. The melt rate (i.e. the rate of liquid water generation), M (mm·d^{-1}), is calculated from Q_m using the following expression:

$$M = \frac{Q_m}{\rho_w \cdot B \cdot h_f} \tag{1-3}$$

where ρ_w is the density of water (1000 kg·m^{-3}), B is the thermal quality or fraction of ice in a unit mass of wet snow, B usually ranges from 0.95 to 0.97 (Shook, 1993), and h_f is the latent heat of fusion of ice (3.335 x 10^5 J·kg^{-1}).

Daily melt, M (mm·d^{-1}) can be estimated as:

$$M = 0.270 \cdot Q_m \tag{1-4}$$

where Q_m, the mean daily melt flux, is in units of W·m^{-2} (Shook, 1993).

According to Male and Granger (1981), the radiation exchange (Q*) is considered the most important flux during the day, followed by the turbulent exchange processes (Q_h and Q_e). Generally, both rain-on-snow fluxes (Q_a) and the soil heat flux (Q_g) represent a small fraction of the daily energy budget, although the soil heat flux can have a strong cumulative influence during the winter (Male and Granger, 1981). Shook (1995, pg 6) stated that when "averaged over a snow season, the relative importance of radiation and turbulent energy sources for snowmelt depends on the size and patchiness of the snow field". Shook (1995) also noted that the turbulent fluxes largely control the melt of small snow patches throughout the season (or until they disappear), whereas larger snowpacks are controlled by radiation melt early in the season and turbulent melt later on as they decrease in area.

Snowcovers in open, windswept environments typically have highly variable snow depths, which quickly become patchy during melt (Woo et al., 2000). Often, there are large differences between the albedo, surface roughness and surface temperature of snow and snow-free patches (Woo et al., 2000). Local advection of sensible heat from the snow-free patches to snow can significantly increase melt rates (Granger et al., 2002; Shook and Gray, 1997; Shook, 1995). As the melt season progresses, an initially continuous snowcover of variable SWE evolves into a discontinuous snowcover, containing snow-free patches that expand and coalesce with time until the snowcover is completely ablated.

1.4 Ground Thermal Regime

The active layer is defined as "the layer of ground above permafrost which thaws in summer and freezes again in winter" to a temperature of 0°C or lower (Muller, 1947). In the case of spring and summer thaw, French (1996) suggested that it is useful to distinguish between the cryofront (the 0°C boundary) and the thawing front (the boundary between the seasonally-frozen and seasonally-thawed soil).

The thickness of the active layer can vary from year to year, depending on variations in ambient air temperature, degree and orientation of the slope, vegetation, drainage, snowcover, soil and/or rock type, and water content (French, 1996). Understanding and being able to predict the thickness of this seasonally-thawed zone and its duration are important, because almost all hydrological, chemical, biological, pedologic, and geomorphic processes occur in this layer (Putkonen, 1998).

1.4.1 Soil Heat Flux

Sauer (2002) defined the soil heat flux, Q_g as "the amount of energy transported through a unit area of soil per unit time ($W{\cdot}m^{-2}$ or $MJ{\cdot}m^{-2}{\cdot}d^{-1}$)". It is the portion of net radiation (Q*) that is transferred to the ground for thawing and heating of the soil. Q_i is the fraction of Q_g that is used to melt the ice in the active layer, and hence lower the frost table (Woo and Xia, 1996). Q_s is the fraction of Q_g that is used to warm the active layer, and Q_p is the fraction of Q_g that represents the heat conducted out of the active layer and into the permafrost below (Woo and Xia, 1996).

In temperate latitudes, Q_g is a minor component of the surface energy balance and typically comprises approximately 10% of Q* (Halliwell and Rouse, 1987). However, in organic-covered permafrost terrains, Q_g can be much larger (as much as 20% of Q*), due to the relatively large amount of energy (latent heat) required for the phase change of ice to water in highly porous organic material. Brown and Grave (1979) stated that the phase change of water is the most important factor in cryogenic processes, because it represents a major energy sink or source and can change the magnitude of the soil heat flux appreciably (Halliwell and Rouse, 1987). This is due to the large quantity of energy (latent heat) required for the phase change of ice to water, water to vapour, and vice versa (Hinzman et al., 1991). Therefore, in permafrost terrains, Q_i is generally the largest component of Q_g, typically comprising approximately 60-85% of the total soil heat flux (Boike et al., 2003; Carey and Woo, 2000; Carey and Woo, 1998; Woo, 1998; Halliwell and Rouse, 1987; Rouse, 1984).

1.4.2 Soil Thaw and Active Layer Development

In snow-covered terrain, active layer thaw usually begins after the removal of the 0°C upper boundary condition that is imposed on the ground surface due to the presence of a melting snowcover (Woo and Xia, 1996). Heat input to the active layer is supplied by the energy flux at the surface, Q_g; this flux is used mainly to thaw ground ice, warm the active layer and warm the permafrost (Woo and Xia, 1996). During active layer thaw, the one-dimensional energy balance for the active layer (Figure 1-3) is:

$$Q_g = Q_i + Q_s + Q_p \tag{1-5}$$

where, Q_g is the heat flux into the ground, Q_i is the latent heat used to melt the ground ice, Q_p is the heat conducted out of the active layer and into the permafrost, and Q_s is the sensible heat that warms the active layer. All terms have units of W·m^{-2}.

The primary method of heat transfer in frozen soils is conduction (Nixon, 1975). The first law of heat conduction, known as Fourier's law, states that the flux of heat in a homogeneous body is in the direction of, and is proportional to, the temperature gradient (Hillel, 1982). Therefore, the downward conduction of heat out of the active layer and into the permafrost is calculated by:

$$Q_p = -K \cdot \frac{dT}{dz} \tag{1-6}$$

where K is the thermal conductivity of the soil (W·m^{-1}·K^{-1}), and dT/dz is the temperature gradient (K·m^{-1}) at the bottom of the active layer.

Non-conductive (i.e., advective) heat transfer processes, however, can also have a significant influence on the ground thermal regime as well (Kane et al., 2001). For example, infiltration of water into frozen soils results in refreezing and the release of latent heat, which in turn causes soil temperature to rise rapidly to 0°C (Kane et al., 2001). However, due in part to the difficulties in quantifying the importance of non-conductive heat transfer processes, most studies have assumed that heat transfer in frozen soils is dominated by conduction. Although Kane et al. (2001) suggested that this is a valid assumption in most cases, Zhao et al. (1997) state the effect of convective heat transfer (due to the infiltration and freezing of meltwater) cannot be ignored and that the latent heat released can contribute up to 27% of the energy needed to raise the soil temperature. Therefore, if advective processes related to infiltrating water are taken into account, the total heat flux into the ground can be defined as:

$$Q_g = Q_i + Q_s + Q_p + Q_{INF} \tag{1-7}$$

The convection of heat by infiltrating water, Q_{INF}, is defined as:

$$Q_{INF} = C_w \cdot \Delta T \cdot \frac{dF}{dt} \tag{1-8}$$

where C_w is the volumetric heat capacity of water (4.19×10^6 J·K^{-1}·m^{-3}), ΔT is the difference in temperature between rainwater or snowmelt water and the soil (Kelvin), and dF/dt is the rate of infiltrating water (m·s^{-1}).

If the fractional ice content in the soil (f_{ice}) and the rate of ground thaw (dh/dt) in m·s^{-1} are known, Q_i can be computed using:

$$Q_i = \rho_{ice} \cdot h_f \cdot f_{ice} \cdot \frac{dh}{dt} \tag{1-9}$$

where ρ_{ice} is the density of ice (917 kg·m^{-3}) and h_f is the latent heat of fusion of ice (3.335×10^5 J·kg^{-1}).

The heat flux that warms the active layer is simply defined by:

$$Q_s = c_{soil} \cdot \frac{dT}{dt} \cdot z \tag{1-10}$$

where c_{soil} is the specific heat capacity of the soil (J·m^{-3}·K^{-1}), dT/dt is the daily temperature change of the active layer (K·d^{-1}) and z is the active layer thickness (m). In reality, c_{soil} varies with depth and thus, the flux can be depth-integrated.

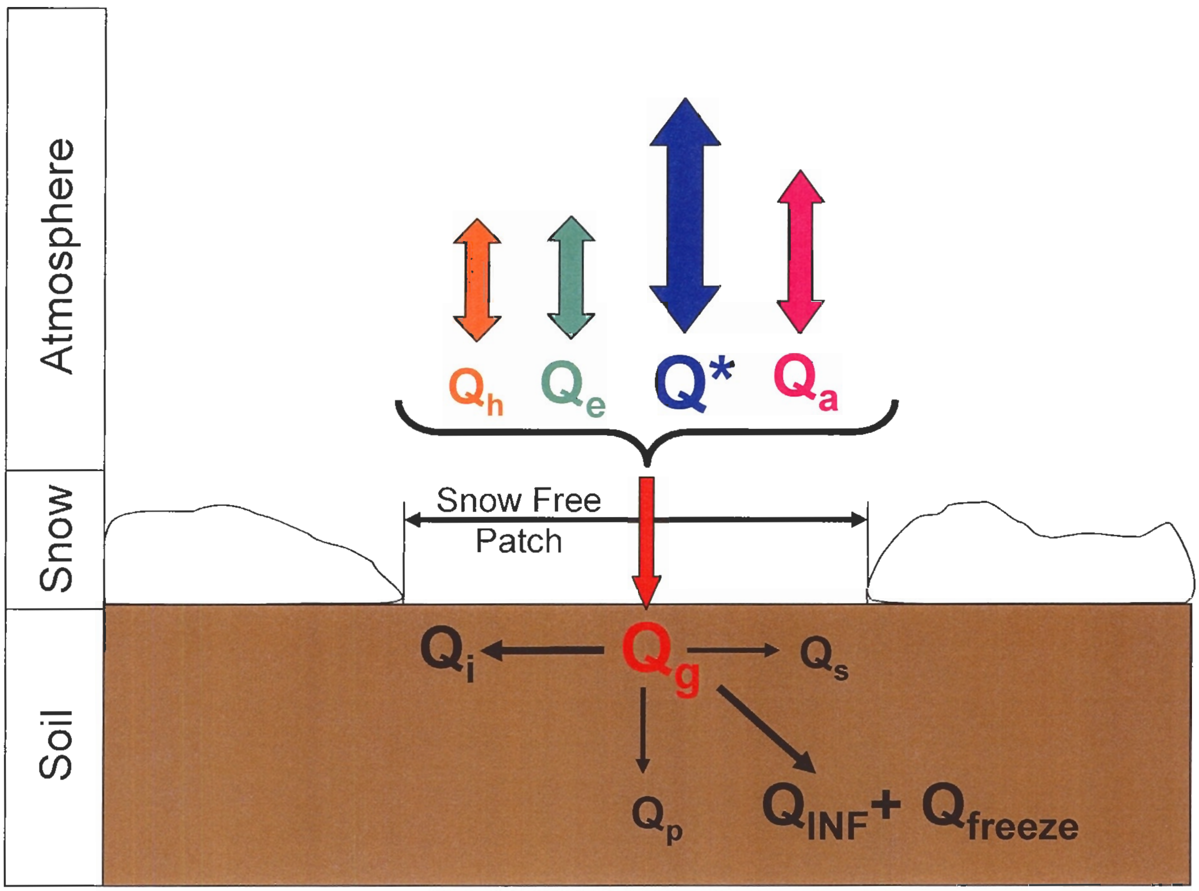

Figure 1-3: Generalized energy balance at the soil surface where Q^* is net radiation, Q_a is energy from advection, Q_s is sensible heat, Q_e is latent heat, Q_g is the soil heat flux. Q_g can further be partitioned into its four main components: Q_i, the energy used to melt ice in the soil, Q_s, the energy used to warm the thawed soil, Q_p, the energy used to warm the permafrost, and Q_{INF}, the energy advected from infiltrating water. Of these three terms, Q_i is generally the largest component of Q_g. The size of the arrows represents the relative magnitude of the fluxes. Fluxes are positive in the direction of the snow surface, but in reality can actually occur in both directions (i.e. towards and away from the surface).

Therefore, Q_i as a function of the full energy balance would be defined as:

$$Q_i = Q^* - Q_s - Q_p - Q_{INF} - Q_{freeze} - Q_h - Q_e \qquad (1\text{-}11)$$

The relative magnitude of the four terms that comprise Q_g can vary considerably across time and space, even among soils that are of a similar type (Carey and Woo, 1998). However, many studies have demonstrated that latent heat consumption (Q_i) is a significant component of the active layer heat balance for permafrost soils (Boike et al., 2003; Carey and Woo, 2000; Woo and Xia, 1996; Roulet and Woo, 1986; Rouse, 1982).

In summary, snowmelt and soil thaw can be regarded as similar processes where Q_m represents the amount of energy required to melt snow, and Q_i represents the amount of energy used to melt the ice in the active layer.

1.4.3 Soil Thermal Properties and Soil Moisture

Thermal conductivity (K), heat capacity (c) and thermal diffusivity, which is the ratio of these (K/c), are collectively known as the soil's thermal properties. Thermal conductivity controls the rate at which heat is transferred through the soil. Heat capacity reflects the capacity of the soil to store heat and is defined as the amount of heat required to change the temperature of the soil. The bulk thermal conductivity of the soil and its heat capacity are controlled by the fractional composition of its various constituents (Table 1-1). In the case of thermal conductivity, Woo and Xia (1996) found that $K_{mineral} > K_{ice} > K_{water} > K_{organic} > K_{air}$. Similarly, for heat capacity, $c_{water} > c_{ice} > c_{soil} > c_{air}$ (as reported by Quinton et al., 2001). As a result, the thermal properties of organic soils are strongly linked to the state of soil moisture, because the bulk soil volume of organic soils is largely water, when saturated. For example, due to their high storage potential, peat soils can exhibit a wide range of heat capacities depending on their water contents, ranging anywhere from 0.58 $MJ \cdot m^{-3} \cdot K^{-1}$ to 4.02 $MJ \cdot m^{-3} \cdot K^{-1}$ for dry and saturated water contents respectively (Turcotte, 2002). The transition of ice to water during thaw results in large changes to the soil's thermal properties and, thereby results in a strong coupling between moisture and thermal regimes of the active layer.

Woo and Xia (1996) demonstrated that for saturated soils, thawing causes a sudden change in the soil's thermal properties. As the soil thaws and water replaces ice, the increase in soil water content will result in an increase in soil heat capacity and a decrease in thermal conductivity. Subsequently, as the soil drains and dries, the heat capacity and thermal conductivity both decrease as air replaces the water. For example, the thermal conductivity of a saturated organic soil decreases by 50% upon thawing (Hinzman et al., 1991). As a result, the presence of moisture has a profound effect on the thermal and hydrological dynamics of the active layer (Hinzman et al., 1991).

1.4.4 Thaw Depth and Implications for Hillslope Drainage

Organic soils exert a strong influence on the hydrologic response of sub-arctic and arctic landscapes (Slaughter and Kane, 1979). Continuous organic terrain surfaces (such as the tundra, taiga and high-boreal regions) underlain by permafrost or seasonal frost occur widely in high latitude regions (Bliss and Matveyeva, 1992). In these areas, the organic soil is approximately 0.2 - 0.5 m thick and consists of a layer of living and lightly decomposed vegetation, overlying a more decomposed layer (Slaughter and Kane, 1979). Runoff processes in organic-covered permafrost terrains are distinct from those of other permafrost terrains in that the dominant runoff mechanism is subsurface flow through the seasonally-thawed organic layer (Quinton and Marsh, 1999) as illustrated in Figure 1-4.

Many organic-covered areas in cold regions experience little or no surface flow due to the large porosity of the organic soil (Quinton and Gray, 2001), which ranges from

0.7 - 0.95 (Hinzman et al., 1991). The high potential infiltration rates of these organic soils generally surpass the rates of input from snowmelt or precipitation (Dingman, 1973). As a result, meltwater can percolate through the unsaturated, highly porous organic soil and move rapidly downslope as subsurface flow over the relatively impermeable frost table.

Table 1-1: **Selected hydraulic and thermal properties of Granger Basin soils and their various constituents. Reproduced and adapted from Quinton et al. (2001). Note that heat capacities are of the soil phase.**

	Depth (m)	Porosity (%)	Density ($kg \cdot m^{-3}$)	Specific Heat ($J \cdot kg^{-1} \cdot K^{-1}$)	Volumetric Heat Capacity ($J \cdot m^{-3} \cdot K^{-1}$)	Thermal Conductivity ($W \cdot m^{-1} \cdot K^{-1}$)	Thermal Diffusivity ($m^2 \cdot s^{-1}$)
Organic Soil	0.05	94	6.83×10^{1}	1.92×10^{3}	1.31×10^{5}	2.1×10^{-1}	1.6×10^{-6}
Organic Soil	0.10	92	8.05×10^{1}	1.92×10^{3}	1.55×10^{5}	2.1×10^{-1}	1.4×10^{-6}
Organic Soil	0.20	85	1.41×10^{2}	1.92×10^{3}	2.71×10^{5}	2.1×10^{-1}	7.8×10^{-7}
Organic Soil	0.30	75	2.90×10^{2}	1.92×10^{3}	5.56×10^{5}	2.1×10^{-1}	3.8×10^{-7}
Mineral Soil	0.40	49	1.10×10^{3}	8.90×10^{2}	9.83×10^{5}	2.5	2.5×10^{-6}
Ice	-----	-----	9.20×10^{3}	2.12×10^{3}	1.95×10^{6}	2.2	1.1×10^{-6}
Water	-----	-----	1.00×10^{3}	4.12×10^{3}	4.19×10^{6}	5.7×10^{-1}	1.4×10^{-7}
Air	-----	-----	1.20	1.01×10^{3}	1.21×10^{3}	2.5×10^{-2}	2.1×10^{-5}

Quinton and Gray (2001) determined that in order to estimate subsurface flow from organic-covered hillslopes underlain by permafrost, it is necessary to know the thickness and elevation of the saturated layer, whose lower boundary is delineated by the frost table and whose upper boundary is the water table (Figure 1-4). Quinton et al. (2000) observed that the saturated hydraulic conductivity of organic material decreases exponentially with depth, largely due to the compaction of pore spaces. Therefore, it is reasonable to expect that spatial variations in thaw depth would lead to spatial variations in saturated layer elevation, which would in turn result in spatial variations in subsurface hillslope flow rates (Figure 1-5). The rate of hillslope flow will also change with time as snowmelt progresses and the thawed layer thickens. In this way, the surface energy balance influences subsurface flow through the active layer. Therefore, in order to accurately represent subsurface flow during spring thaw in hydrologic models, an understanding of soil thaw and soil thaw rates is required.

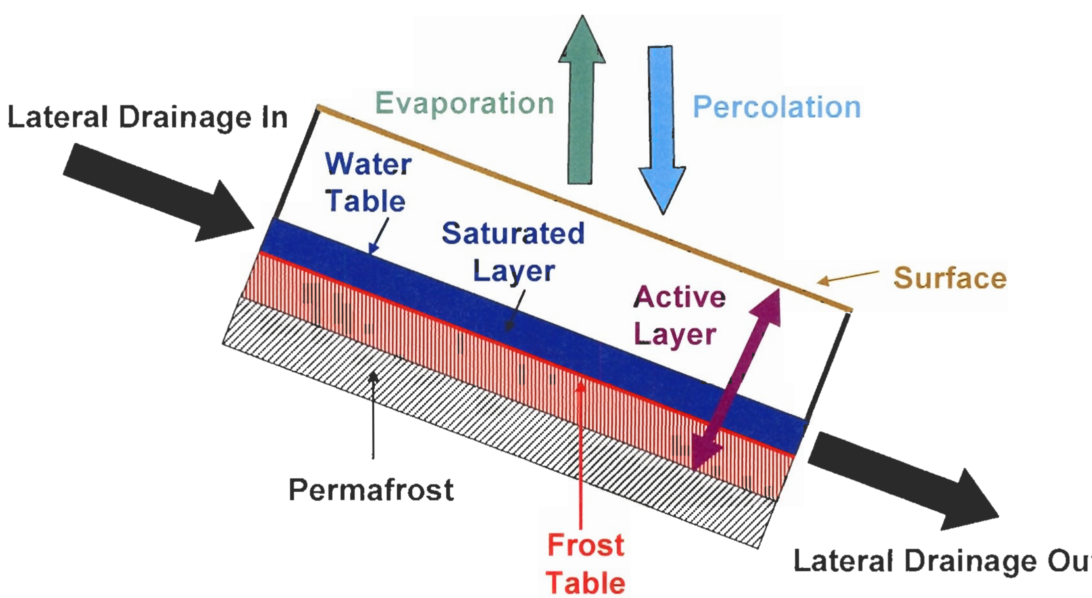

Figure 1-4: Schematic of water fluxes through a typical permafrost slope. The frost table acts as a relatively impermeable boundary over which water can flow laterally downslope. Liquid soil moisture content is determined by the relative magnitudes of percolation and by lateral drainage from upslope minus evaporation and lateral drainage downslope.

Complicating the estimation of thaw depth is the variability in the thermal properties of the organic soils, as discussed previously. On a permafrost slope, soil moisture content is determined by the relative magnitudes of snowmelt input (through vertical percolation) and lateral drainage from upslope (Figure 1-4). The quantity of moisture in the soil profile affects the depth and rate of freezing and thawing (Hinzman et al., 1991), due to the large differences in K and c of the water, ice, air, mineral and organic soil constituents (Nixon and McRoberts, 1973). Soils that experience moisture fluctuations have thermal properties that are also sensitive to drying and wetting events (Woo and Xia, 1996). Therefore, the moisture dynamics of the active layer strongly influence its thermal regime.

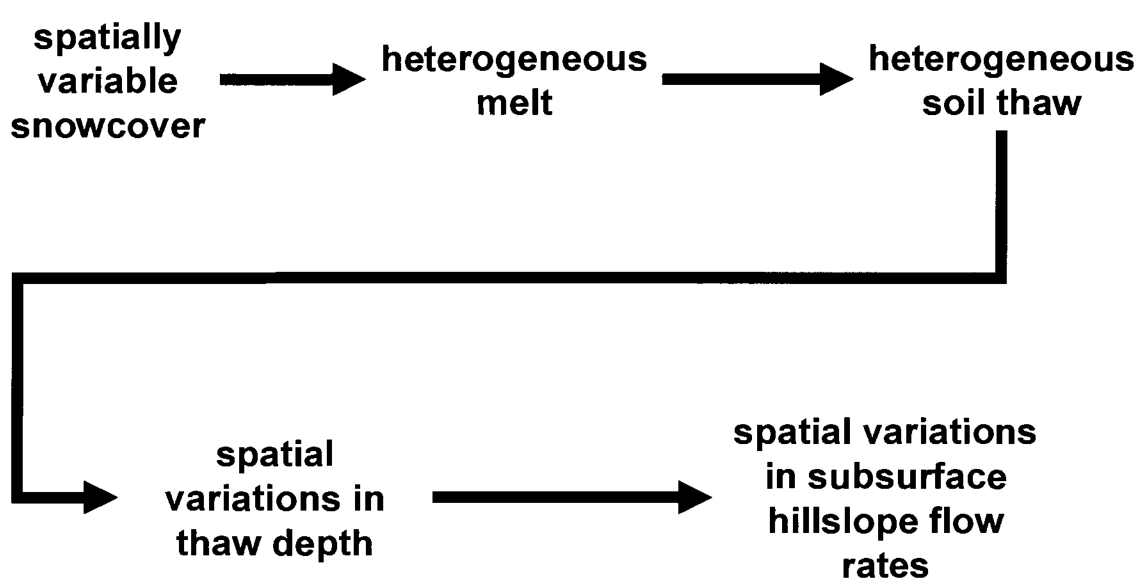

Figure 1-5: Summary flowchart of the various processes that result in variations in subsurface flow rates.

1.5 Purpose and Objectives

The overall purpose of this study was to determine the relation between net radiation and the energy used to melt snow and thaw the snow-free ground during the snowmelt season, and use these relations to predict soil thaw at the hillslope scale. This will lead to a better understanding of active layer development, possibly shed insight into the role of lateral drainage pathways from organic-covered hillslopes, and provide an approach for the estimation of soil thaw based on a direct link between surface fluxes and the subsurface energy regime.

The study site is located within Granger Basin, which is part of the larger Wolf Creek Research Basin, situated in the southwestern corner of the Yukon Territory, Canada, approximately 15 km south of Whitehorse, Yukon. This site is ideal for such research, because the basin is representative of several northern sub-arctic and sub-alpine biomes and terrains and contains organic-covered tundra hillslopes on which subsurface flow is the dominant run-off mechanism. This area has been the site for much interdisciplinary scientific research since 1992 (Pomeroy and Granger, 1995).

The objectives of the study are three-fold:

1) To determine the percentage of Q^* that contributes to snowmelt (Q_m) from a physically based perspective

2) To determine the percentage of Q^* that contributes to soil thaw (Q_i) and from a physically based perspective

3) To estimate the energy used to thaw the soil over the hillslope in order to comment on slope-scale active layer development, by considering the relationship between soil moisture and soil thaw rate.

1.6 Scope of Work

In order to meet the objectives of this study, the following scope of work was undertaken:

1) Field data, including meteorological, snowmelt and soil thaw data were collected at the Granger Basin site. Daily slope photographs were taken to document the areal ablation of the snowcover; snow surveys were conducted to obtain SWE and to calculate melt energy, soil thaw depth data was collected to obtain thaw rates and to calculate soil thaw energy, soil moisture data was collected to understand the relationship between soil moisture and soil thaw rate.

2) The amount of net radiation, Q^* over snow and snow-free surfaces on the hillslope was computed, and incoming shortwave radiation from the valley bottom for the north-facing slope was corrected. An attempt was made to model net radiation in order to extend the time series.

3) The change in SWE was converted into a melt rate, which was used to calculate melt energy (Q_m). Melt energy was then compared with net radiation to determine the average percent contribution of Q^* to Q_m.

4) The change in soil thaw depth was converted into a thaw rate, which was used to calculate soil thaw energy (Q_i). Soil thaw energy was then compared with net radiation to determine the average percent contribution of Q^* to Q_i.

5) Using the Q^*-Q_i relationship, and accounting for the energy released due to the infiltration and freezing of meltwater into the soil, soil thaw depth

was estimated over the hillslope at 4 representative days during the study period.

1.7 Thesis Organization

This thesis is organized into eight chapters. The first three are the introductory, study site and methodology chapters, respectively. Chapter 4 presents the results of the radiation analyses. Chapter 5 determines the mean contribution of net radiation to snowmelt energy. Chapter 6 comprises a similar analysis, but with net radiation and soil thaw energy and also attempts to estimate the contribution of energy released due to the infiltration and freezing of meltwater into the soil. Chapter 7 uses the results obtained in Chapter 6 to estimate soil thaw depth over the hillslope. Finally, Chapter 8 provides some conclusions as well as highlights some recommendations for future research.

CHAPTER 2: STUDY SITE

2.1 Study Site Description

Field research was conducted between April 23 and June 15, 2003 (DOY 113-166) in Granger Basin, Yukon (60°32'N, 135°18'W) (Figure 2-1). Granger Basin is a headwater sub-catchment located within the Wolf Creek Research Basin, approximately 15 km south of Whitehorse, Yukon Territory, Canada. A brief description of the study site is given below; for a comprehensive overview of the physiography, geology and soils of the Wolf Creek Basin refer to Janowicz (1999).

2.1.1 Regional Physiography and Climate

The Wolf Creek Research Basin is a complex sub-arctic, sub-alpine catchment that occupies an area of 195 km^2 in the southern Yukon headwater region of the Yukon River (Janowicz, 1999). The basin lies within the zone of discontinuous permafrost and is situated within the Boreal-Cordillera Ecozone. It has a sub-arctic continental climate, which is characterized by a large variation in temperature, low relative humidity and relatively low precipitation (Janowicz, 1999). Mean annual temperature over the period of 1971-2000 was –3 °C, with average temperatures of 5 °C to 15 °C in summer and –10 °C to –20 °C in winter (Meteorological Service of Canada, 2005). Mean annual precipitation ranges from 300-400 mm, with approximately half of that falling as snow, although the Whitehorse airport (with an elevation of 703 metres above sea level) generally underestimates basin precipitation by 25-35% (Janowicz, 1999).

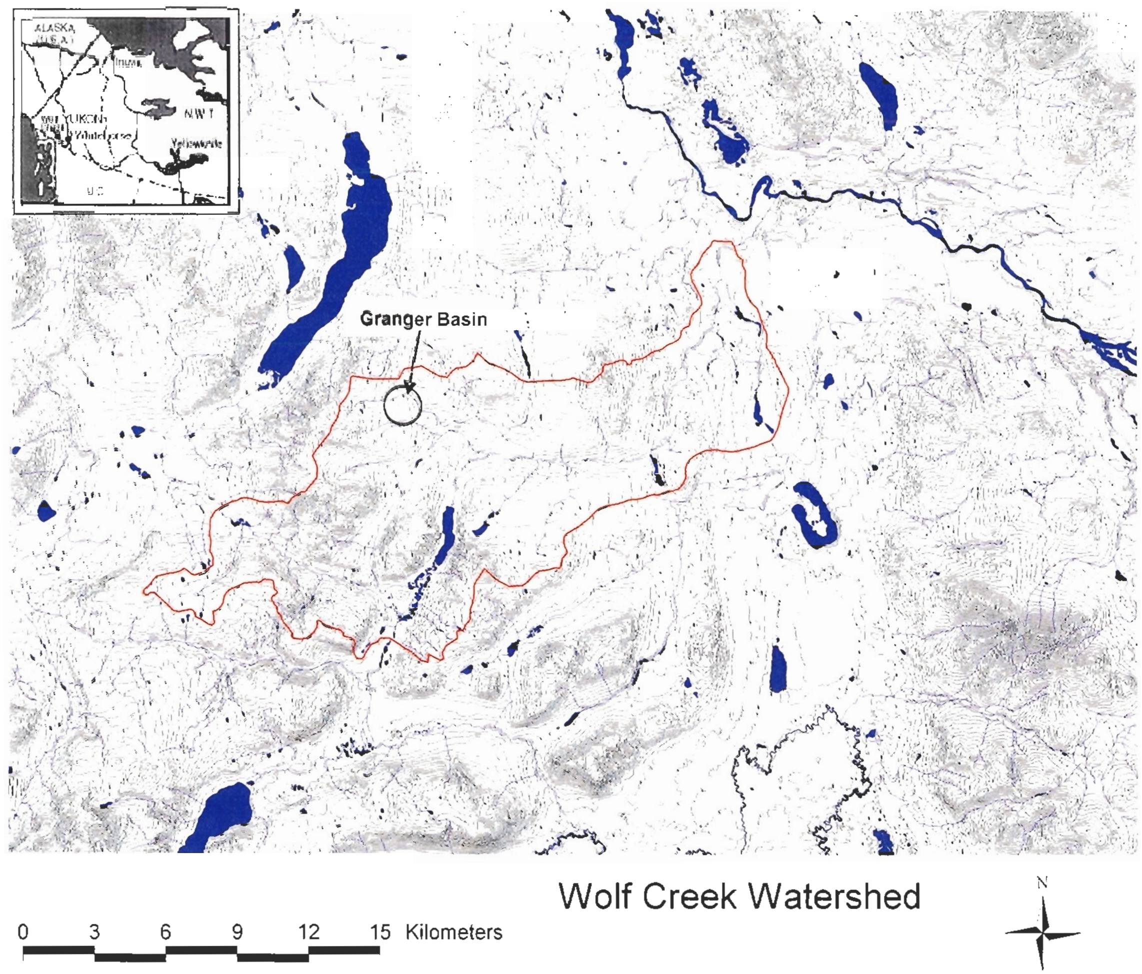

Adapted from Goeller (2005), by permission

Figure 2-1: Location of Granger sub-basin within the Wolf Creek Watershed, Yukon Territory, Canada.

The basin has a general northeasterly aspect, and elevations range from 800 to 2250 m with the median elevation at 1325 m. The elevation of the sub-alpine ecosystem ranges from approximately 1100-1500 m (Janowicz et al., 2004).

2.1.2 Geology

The geology of the Granger Basin area is comprised of limestone, sandstone, siltstone and conglomerate (Carey and Quinton, 2005). The basin is blanketed with glacial till, ranging from a thin layer to several metres in thickness (Janowicz, 1999). The deposits are of glacial, glaciofluvial and glaciolacustrine origin (Janowicz, 1999). Upper elevations have shallow deposits of colluvial material and frequent bedrock outcrops (Janowicz, 1999).

2.1.3 Soils

Soils within the sub-alpine areas are primarily Orthic Eutric Brunisols, with textures ranging from sandy loam to gravelly sandy loam. The parent material consists largely of moderately stony morainal deposits. The basin is also underlain by a volcanic ash layer approximately 0.02 m thick and located approximately 0.1 m below the surface (Janowicz, 1999).

The thickness of the organic soil on the North-facing slope ranges from 0.05-0.1 m in the upper slope area to 0.2-0.25 m in the lower slope area. The upper layer of organic soil consists of living vegetation mixed with lightly decomposed peat, with the degree of decomposition increasing with depth (Quinton and Gray, 2001). Below this, there is also a considerable (~0.1-0.25 m) thickness of a mixed organic-mineral layer consisting of organic soil, decomposing vegetation, rocks and mineral soil. A 15-litre sample of mineral sediment was removed from below the organic layer near the soil pit and shipped to Soilcon Laboratories (Vancouver, British Columbia, Canada) for particle size analysis. For the < 2.00 mm diameter fraction, 58% was classified as sand (0.053-2.00 mm), 34% as silt (0.002-0.053 mm), and 8% as clay (< 0.002 mm). This textural description classifies the sediment as a sandy loam (Quinton et al., 2005). Approximately 31% (by weight) of the mineral sediment had a particle diameter > 2.0 mm. The largest measured size range was 37.5-75.0 mm (approximately 10% by weight); however, 18% of the sample weight was composed of sediment with a diameter greater than 75.0 mm.

2.1.4 Vegetation

The Wolf Creek Basin consists of three principle ecosystems: boreal forest (spruce, pine, aspen), sub-alpine taiga (shrub tundra) and alpine tundra with proportions of 22, 58 and 20%, respectively (Janowicz et al., 2004). Granger Basin lies within the sub-alpine zone. The sub-alpine zone forms a broad ecotone between the forested lowlands and unvegetated alpine regions of the basin (Janowicz et al., 2004). The sub-alpine zone is a gently rolling plateau with only localized areas that contain extreme topographic relief. It is at these locations that transitions between sub-alpine and alpine vegetation communities occur. The upper sub-alpine zone is generally treeless, with willow (*Salix sp.*), dwarf birch (*Betula pumila*) and Labrador tea (*Ledum sp.*) dominating the vegetation composition. Shrub height is strongly controlled by microtopography (ridges, hollows and level ground), thus creating fine-scale vegetation patterns (Janowicz et al., 2004).

2.1.5 Basin Hydrology

Basin streamflow characteristics and responses are typical of a mountainous sub-arctic regime (Janowicz, 1999). Peak flows occur in late May or early June due to snowmelt, with low flows occurring around March. The basin is prone to intense summer rainstorm events that can produce secondary peaks in the stream hydrograph (Janowicz, 1999).

2.1.6 Granger Sub-Catchment

Granger Basin (Figure 2-2) is located at the transition zone of the treeline (~1300 m) and, therefore, vegetation consists primarily of sub-alpine shrub tundra and alpine tundra with a few scattered clusters of stunted spruce trees. Most of the basin is covered by an organic layer up to 0.4 m thick, which consists of peat, lichens, mosses, sedges and grasses. The organic layer is underlain by mineral soil. Permafrost is found under most of the north-facing slopes, while seasonal frost is predominantly found on the south-facing slopes.

The basin drains an area of approximately 8 km^2, and ranges in elevation from 1310 m to 2250 m (Carey and Quinton, 2005). The basin is drained by Granger Creek, which flows into Wolf Creek and, subsequently, the Yukon River. At lower elevations, the main Wolf Creek valley runs west to east, resulting in a prevalence of north and south-facing slopes (Carey and Quinton, 2005).

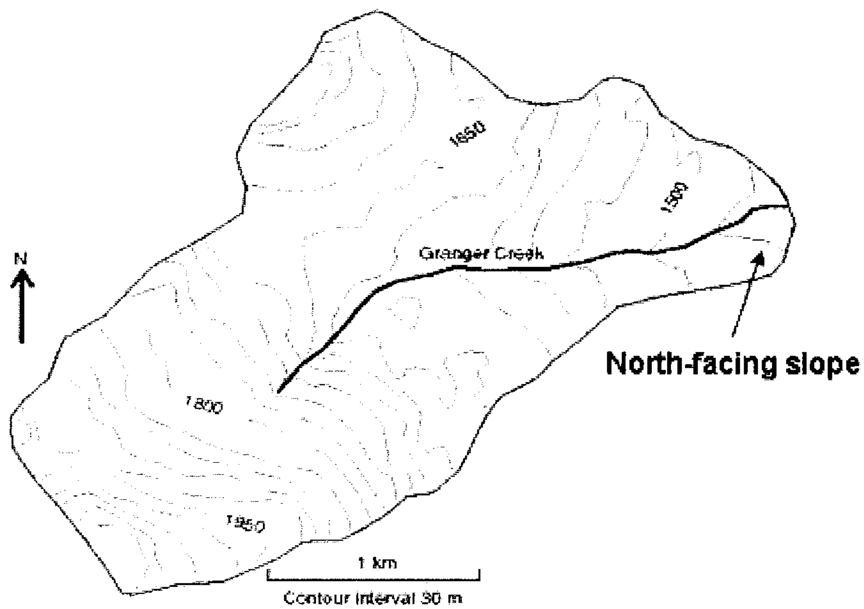

Adapted from Carey and Quinton (2005), by permission

Figure 2-2: Topographic map of Granger Basin.

2.1.7 The North-Facing Slope

Data for this study were collected from a north-facing slope and the valley bottom near the outlet where Granger Creek joins Wolf Creek. The north-facing slope averages 17.5° (Pomeroy et al., 2003), and consists of undulating terrain with numerous hummocks and depressions. The slope is also underlain by permafrost and has an average active layer depth of 0.4 m in late summer (Quinton and Gray, 2001).

In late winter of each year, a substantial snowdrift forms near the top of the north-facing slope. Depending on the amount of snowfall and dominant wind direction, the SWE can be highly variable from year to year. Pre-melt snowcover varies throughout the basin mainly due to redistribution by wind as influenced by vegetation and topography. Snow tends to accumulate close to the crest of the north-facing slope (in the form of a drift), near the valley bottom and stream channel, and in topographic hollows.

CHAPTER 3: METHODOLOGY

3.1 Field Methods

Field measurements were initiated on April 23, 2003 (DOY 113) and continued until June 15, 2003 (DOY 166). These included daily photographs, meteorological measurements, measurements of snow depth and snow density, soil thaw depth and soil moisture. Snow and soil measurements were repeated daily or every other day during the beginning of the monitoring period. Thaw depth and soil moisture measurements were reduced to every 3-5 days near the end of the study because most of the snow had melted and the ground had thawed appreciably.

3.1.1 Digital Photographs

Daily photographs were taken using an Olympus Camedia (C-3000 Zoom) digital camera to document the depletion of the continuous snowcover on the north-facing slope. The digital images had a resolution of 2048 x 1536 pixels. Photographs were taken each morning (usually between 9-10 am local time) at a fixed point near the meteorological tower, approximately half-way up the north-facing slope. A tripod was fixed at this location so that photographs were taken from the same point every day.

3.1.2 Micrometeorological Measurements

Meteorological data used for this study were obtained from two meteorological stations. One was located approximately half-way up the north-facing slope (~150 m upslope of the stream channel) (Figure 3-1), and the other within the valley bottom (Figure 3-2). Data recorded at the hillslope meteorological station included net radiation, relative humidity, air and surface temperature, and snow depth. Data recorded at the valley bottom station included incoming shortwave radiation (K↓). Instruments were mounted approximately 1.5-1.6 m above the top of the vegetation and oriented such that fluxes were measured normal to the slope (Figure 3-1). Data were recorded by Campbell Scientific 10X and 23X dataloggers powered by solar panels (Pomeroy et al., 2003).

Net Radiation (Q*)

Net radiation (in $W \cdot m^{-2}$) was measured using a Radiation Energy Balance Systems Q7 aspirated radiometer. Values were recorded every minute by a Campbell Scientific CR10X datalogger and averaged every half hour. Based on the height of the instrument and a 90% view factor, the area contributing to the total view of the radiometer is approximately 64 m^2 (Berard, personal communication, March 8, 2006).

Relative Humidity, Air Temperature and Surface Temperature

Relative humidity and air temperature were measured using a Vaisala HMP35CF hygrothermometers in Gill Instruments radiation shields. Surface temperature was measured with Everest Interscience infrared thermometers with measured ellipses of approximately 2 m x 3 m.

Snow Depth

Snow depth at the meteorological tower was measured using a Campbell Scientific SR50 ultrasonic sounder. The SR50 has a 22° viewing angle and an error of 0.4% or 0.01 m.

Photo: copyright D.Bewley, reprinted by permission.

Figure 3-1: Meteorological tower located approximately half-way up the north-facing slope, Granger Basin. A number of meteorological measurements were made here, including net all-wave radiation, surface temperature, air temperature, relative humidity and snow depth.

Photo: copyright D.Bewley, reprinted by permission.

Figure 3-2: Meteorological station located on valley bottom, Granger Basin. Incoming shortwave radiation was measured at this station. Geometric corrections were applied to this data for the north-facing slope.

Incoming Shortwave Radiation

Shortwave radiation (in W·m^{-2}) was measured only at the valley bottom meteorological tower (Figure 3-2) using two Kipp & Zonen CM5 Solarimeters. Values were recorded every minute by a Campbell Scientific CR10X datalogger, and averaged every half hour. One solarimeter was mounted facing-up, 2.89 m above the vegetation to measure incoming shortwave radiation from the sun. The other was mounted facing-down, 2.80 m above the vegetation to measure reflected shortwave radiation from the ground/shrubs. Both solarimeters were oriented such that fluxes were measured normal to the slope.

3.1.3 Snow Surveys

During pre-melt and melt, snow depth and density were measured daily along two parallel snow survey transects (Figure 3-3). When only the late-lying snowdrift remained, measurement frequency was reduced to one measurement every 2 or 3 days. Snow depth was measured every 5 m using a snow depth rod. Snow density was measured every 20 m using an ESC (Eastern Snow Conference) snow tube. The two transects, (A and F) were approximately 100 m apart and extended from the crest of the north-facing slope to the stream channel, approximately 200 m downslope.

Due to the redistributed, deeper nature of the late-lying snowdrift on the hillslope, the drift could have different properties (i.e. depth and density and hence SWE) and potentially different melt rates when compared to the non-drift section of the hillslope. In order to obtain an estimate of SWE for the hillslope, the snowcover was separated into "drift" and "non-drift" regions. Because the drift depth often exceeded the length of the ESC tube, a snow pit was excavated in the drift to a depth of 2.2 m along Transect F. A large solar blanket was placed over the snow pit to minimize melting in between sampling periods (McCartney, 2006). Snow density was determined gravimetrically at 0.2 m intervals throughout the snow pit using 143 cm^3 (0.143 L) tins. Before each sampling, the old pit face was sheared off to expose the un-weathered snow (McCartney, 2006). The density of the drift was determined by taking the average of the densities for each snow layer in the snow pit. According to Pomeroy and Gray (1995), this technique is quite accurate and straightforward, the only disadvantage being that it is labour-intensive and destroys the snowpack. SWE for the entire drift was then calculated using the average drift depth of Transect A and F and density values obtained from the snow pit.

The gravimetric technique is the most commonly used SWE measurement method (Pomeroy and Gray, 1995). In this study, although both drift and non-drift densities are determined gravimetrically, drift densities are probably more accurate than non-drift densities. Drift densities provide a vertically integrated average of density measurements whereas non-drift densities were determined using a snow tube (with a cutter fitted to the end) to obtain a vertical core of snow. However, it is difficult to obtain a full core of snow, due to the following potential sources of measurement error: spillage, the presence of woody vegetation underneath the snowpack, or the occurrence of a layer of depth hoar at the snowpack base (Pomeroy and Gray, 1995).

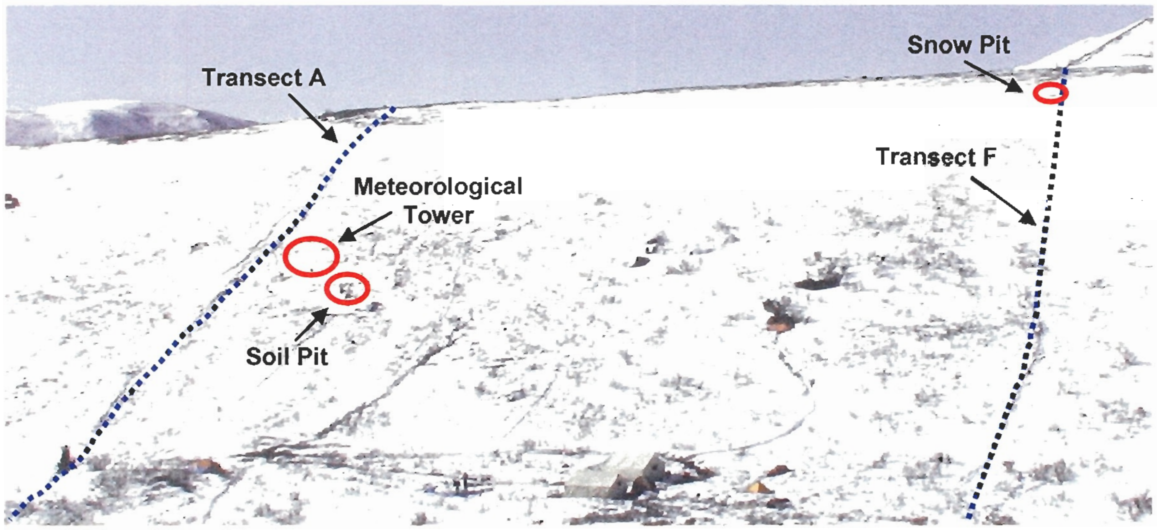

Figure 3-3: Photo of north-facing slope taken on DOY 114 (April 24) showing the location of the two snow survey transects (A and F), the snow pit, soil pit and meteorological tower that were used in this study. Transects A and F are approximately 100 m apart.

3.1.4 Snow-Free Patch Selection

Patches of bare ground surrounded by snow were chosen for monitoring soil thaw depth and soil moisture. The primary factor in selecting snow-free patches for measurement was the time at which an area became snow-free. Smaller snow-free patches were preferable, as they provided a continuous record of growth from the onset of snowcover removal. Other selection criteria included accessibility (minimum amount of disturbance), location (isolated rather than clustered) and representative patches from different slope areas (upper slope, mid-slope and lower slope). Figure 3-4 and Figure 3-5 show the location of the patches on the north-facing slope.

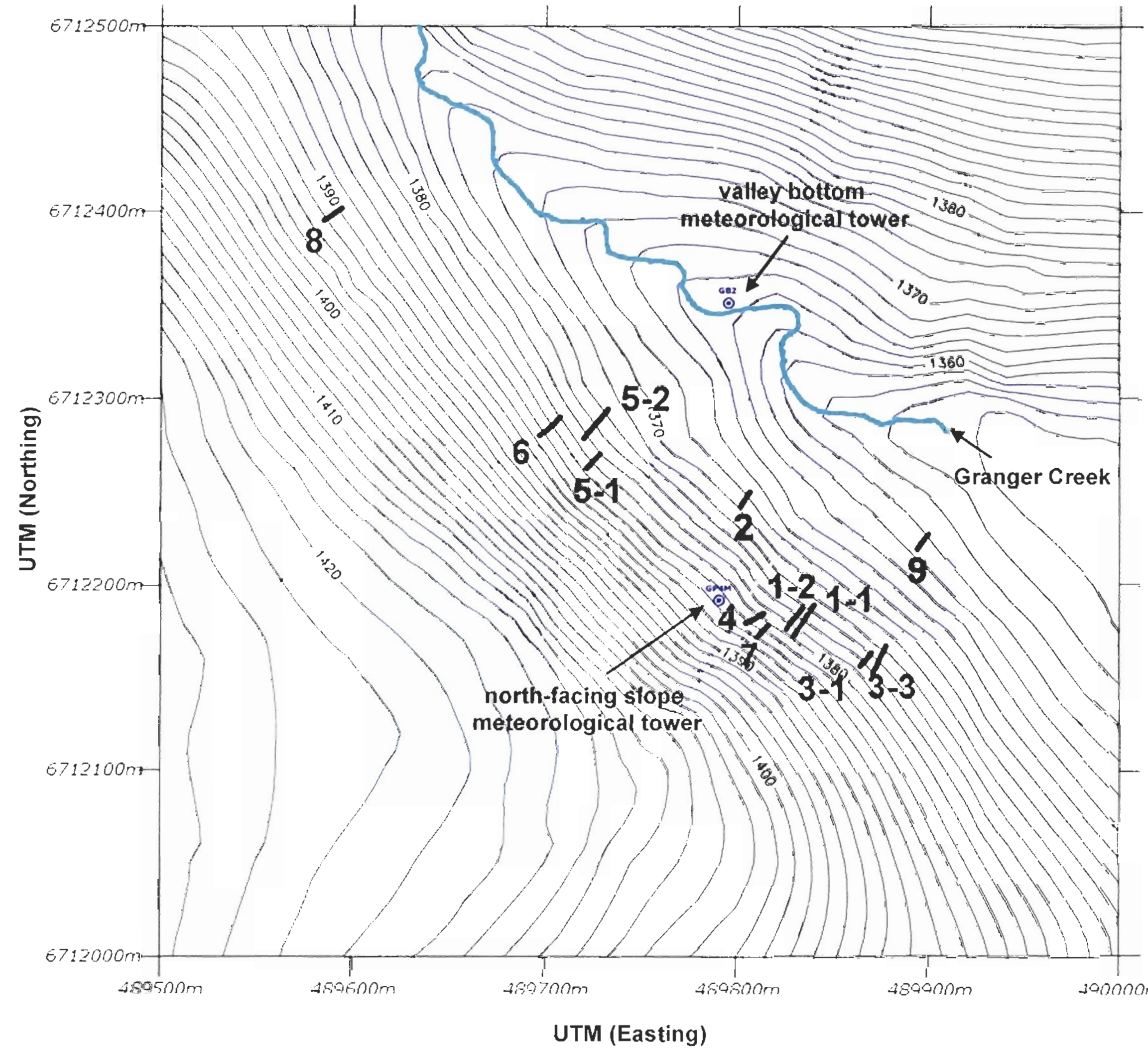

(Source: Granger Basin Topographic Map - Tom Carter, National Water Research Institute, unpublished)

Figure 3-4: **Map of the north-facing slope (contour interval = 2 m). The dark lines represent the transects that were set up in each of the snow-free patches. The blue line is Granger Creek. The two small circles represent the location of the two meteorological towers (north-facing slope and valley bottom) from which data were used for this study. The x and y-axes are UTM distances. Approximately 1 cm on this map represents 38.5 m.**

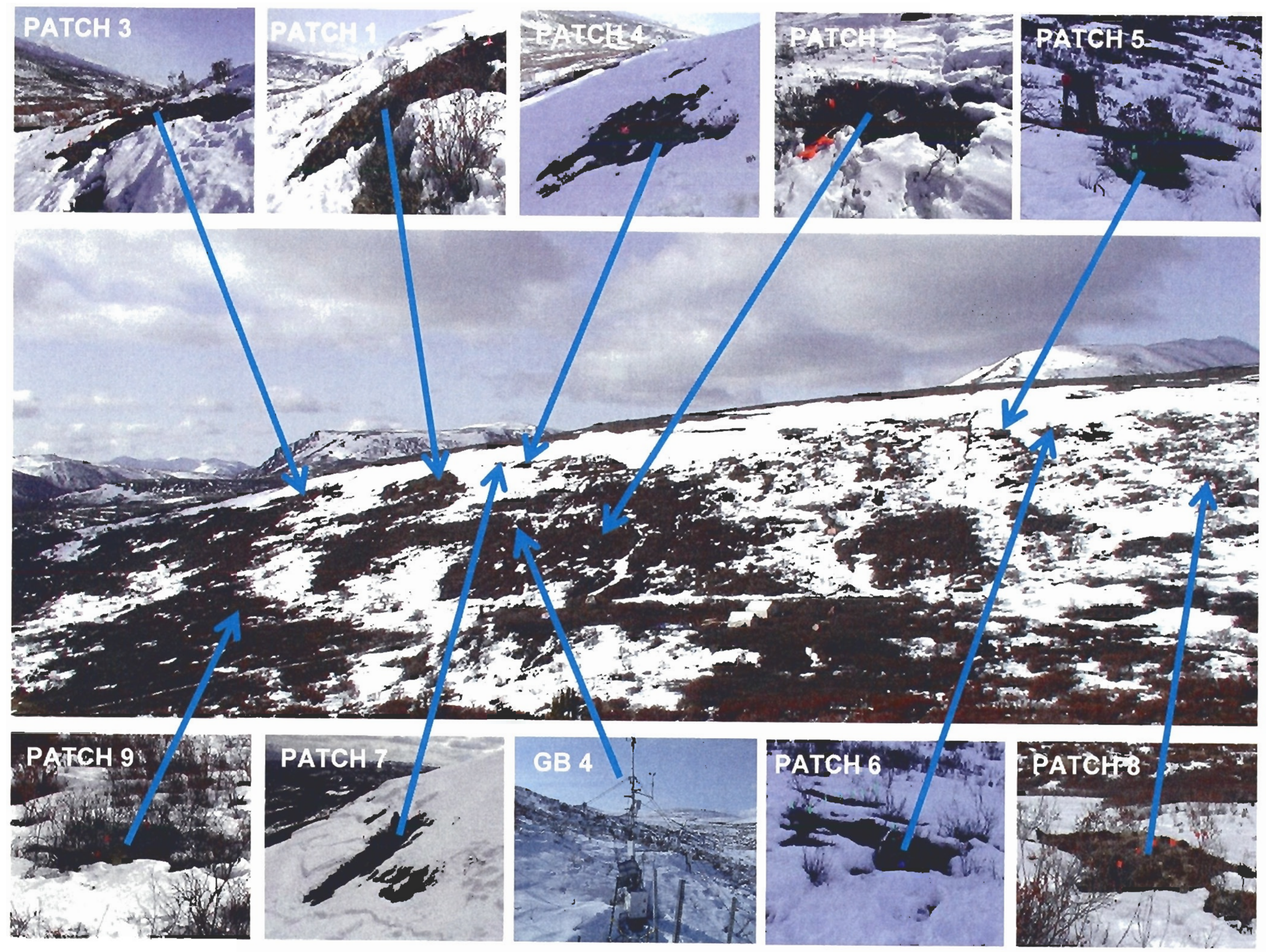

Figure 3-5: Photo of study slope taken on May 8 (DOY 128) and the nine patches that were monitored for frost table and soil moisture. The location of the hillslope meteorological tower (GB4) is also shown for reference.

3.1.5 Soil Thaw Depth

Soil thaw depth was determined by inserting a length of rebar into the ground at each point along each transect until resistance was met. A marker was inserted into the ground at each measurement point to ensure that thaw depth was measured at the same point each day. For the purpose of this study, it was assumed that thaw depth is a measure of the depth to the top of the frozen saturated layer, which is essentially impermeable to water. Also, during the soil thaw period, the elevation of this relatively impermeable surface (i.e., the frost table) is typically within 0.02 m of the elevation of the 0°C isotherm, with most of the difference occurring within the first few days of thaw (Carey and Woo, 1998). The top of the frozen saturated layer, therefore, is the bottom of the saturated layer through which water can flow laterally downslope. Due to the rocky nature of the material underneath the organic layer and the presence of shrubs, the rebar was often impeded by rocks instead of ice. However, these points could be identified and removed from the data set, because on a plot of soil thaw over time, thaw appeared to stop once the rock was encountered.

A downhill transect was oriented normal to the hillslope in each of the nine snow-free patches. In an attempt to capture the small-scale spatial variability of thaw depth, measurements were made at 0.5 m intervals along each transect. As each snow-free patch expanded, monitoring points were added to upslope and downslope ends of the transect at 0.5 m intervals. Once a snow-free patch coalesced with other patches, or the snow around it was completely ablated, no additional points were added to the transect.

In certain patches, multiple transects were established to conform to the actual downslope (or upslope) growth of the patch with time. For example, additional transects were set up in Patches 3 and 5, either because they grew laterally (across the slope) much faster than they did downslope, or because the original monitoring transect did not accurately reflect the downslope growth of the snow-free patch. Transects 1, 3, 4, 5, 6, 7 and 8 were located on the upper portions of the north-facing slope. Transect 2 was near the hillslope meteorological tower and soil pit, approximately mid-way up the north-facing slope. Transect 9 was the only transect located on the lower portion of the slope (Figure 3-6). Table 3-1 and Table 3-2 summarize patch vegetation and soil characteristics.

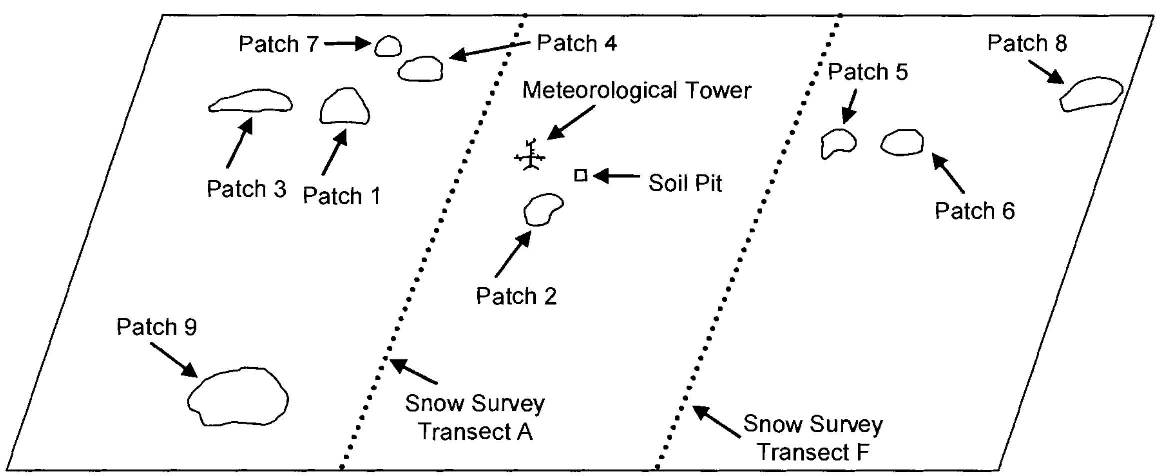

Figure 3-6: Schematic of the north-facing slope and relative location of patches, meteorological tower, soil pit and snow survey transects for reference and comparison. Transects were set-up in approximately the centre of each patch. Two transects were set up in Patch 3 (T1 and T3) and Patch 5 (T1 and T2). Note that schematic is not to scale.

Table 3-1: General soil profiles found in snow-free patches

Patch/Transect Number	Relative Location on North-facing Slope	Average Depth (cm)	Material Description
1, 3 (T1), 3 (T3)*, 4, 5 (T1)*, 6, 7, 8	Upper Slope	0 – 10 10 – 25 > 25	- organic - organic/mineral transition material - mineral with increasing amounts of rocks and gravelly material
2, 5 (T2)*	Mid-Slope	0 – 10 10 – 25 > 25	- organic - organic/mineral transition material - mineral with gravelly material (but not as rocky as upper slope)
9	Lower Slope	0 – 25 25 – 35 > 35	- organic - ash layer (fine greyish material) - organic/mineral transition material

*Multiple transects were established in Patches 3 and 5. Three transects were set up in Patch 3; however, only T1 and T3 were used in this study. T2 was a small transect that did not conform to the upslope or downslope growth of the patch and was therefore, abandoned.

Table 3-2: Common vegetation types found in snow-free patches

Relative Location on North-Facing Slope	Predominant Vegetation and Ground Cover	Latin Name
Upper Slope	Lichens Mosses in small hollows and depressions Graminoids Heather Some small shrubs (<1m in height)	*Cladina mitas* *Cladina rangiferina* *Cladonia chlorophaea* *Campylium stellatum* *Cassiope sp.* *Betula pumila var. glandulifera*
Mid-Slope	Lichens Mosses Shrubs (1-2 m in height) Labrador tea	*Cladina mitas* *Cladina rangiferina* *Cladonia chlorophaea* *Campylium stellatum* *Willow – Salix sp.* *Birch - Betula pumila var. glandulifera* *Alder – Alnus sp.* *Ledum sp.*
Lower Slope	Mosses Shrubs (1-2 m in height) Graminoids Labrador tea	*Campylium stellatum* *Willow – Salix sp.* *Birch - Betula pumila var. glandulifera* *Alder – Alnus sp.* *Ledum sp.*

3.1.6 Near Surface Soil Moisture

An alternative to using the accurate yet expensive technique of time domain reflectometry (TDR) to measure near surface soil moisture, is the use of soil capacitance (the ability of a material to store electrical charge), to determine the soil dielectric constant (Paltineanu and Starr, 1997; Evett and Steiner, 1995; Dean et al., 1987). The dielectric constant of a material is "a measure of the tendency of its molecules to orient themselves in an electrostatic force field" (Hillel, 1998, p139). Due to the polar nature of water molecules, the dielectric constant of water (κ_{water} = 80) is relatively high compared to the dielectric constant of soil solids (κ_{soil} = 3-5), air (κ_{air} = 1) or even ice (κ_{ice} = 3). As a result, it is possible to relate water content to the measured dielectric constant.

The approach is based on the principle that when a capacitor is subjected to an oscillating current, the resultant oscillation frequency is related to the capacitance of the circuit (Seyfried and Murdock, 2001). As the oscillation frequency decreases, the capacitance increases, but the exact relationship is specific to the circuitry of the instrument (Seyfried and Murdock, 2001). In general, the relationship between the capacitance, ς and the dielectric constant, κ is:

$$\varsigma = g \cdot \kappa \tag{3-1}$$

where g is a constant dependent on the spacing and geometry of the capacitor and both ς and g are measured in farads (Dean et al., 1987 in: Seyfried and Murdock, 2001). Thus, κ decreases with increasing oscillation frequency. Due to the uncertainty in the value of g, and in the complex relationship between Volumetric Water Content (VWC) and κ, empirical calibrations are employed to relate VWC to frequency (Whalley et al., 1992 as cited in: Seyfried and Murdock, 2001).

Near surface soil moisture (0-0.05 m) was measured using a HydroSense Soil Water Content Measurement System (Campbell Scientific Inc, 2001). The unit consists of a HydroSense Display Unit and a CS620 Water Content Reflectometer. The Water Content Measurement Mode displays the measurement result as percentage volumetric water content and the period of the probe output in milliseconds. The HydroSense System uses the soil physical property dielectric constant (κ) to estimate the volumetric water content (VWC).

The HydroSense's Water Content Reflectometer (CS620) generates enough high frequency electromagnetic energy to polarize water molecules to the extent required to measure the dielectric constant (Campbell Scientific Inc, 2001). When the instrument is inserted into the ground, the waveguide and soil act as a capacitor. Soil between and along the length of the rods affects the capacitance but the instruments are most sensitive to conditions immediately adjacent to the rods. The HydroSense uses a waveguide technique similar to TDR, which is in direct contact with the soil and senses an integrated average along and between the waveguides (Seyfried and Murdock, 2001). The probe rods act as a waveguide and the applied signal travels to the end of the rods and then reverses the direction of travel. The travel time of the electromagnetic energy along a waveguide is dependent on the dielectric constant. Changes in the overall κ of the bulk soil volume, which are primarily due to changes in VWC, are recorded as changes in the oscillation frequency (Seyfried and Murdock, 2001). Electronics in the probe head both generate the applied signal and sense the return. The measurement reflects the average water content over the length of the rods. The high frequency signals are transformed to a square wave output with a frequency proportional to the water content (Campbell Scientific Inc, 2001).

The HydroSense is very sensitive to changes in the dielectric constant and the probe has a stated water content measurement resolution better than 0.1% (Campbell Scientific Inc, 2001). However, Pomeroy (personal communication, September 12, 2005) indicated that HydroSense measurements are typically quite poor in organic soils or frozen terrain, even when calibrated (see Section 3.2.7). Nevertheless, these measurements are used for the lack of a better-suited measurement technique for VWC.

Soil moisture was recorded concurrently and at the same points where the depth of soil thaw was measured. The 0.2 m rods were inserted into the ground at an angle of 15° into the soil surface. The water content was averaged over the length of the 0.2 m probe rods for the upper surface 0.05 m of the soil (cos β =5/20, where β is the angle between the probe rods and the ground surface). The total volume of the HydroSense measurement extends outward radially from the rod surface about 0.03 m, and is approximately 0.0011 m^3 for the 0.2 m probe rods (Campbell Scientific Inc, 2001). Soil samples were collected in 68.7 cm^3 (0.0687 L) aluminium tins to calibrate the HydroSense readings. Soil samples were collected along each transect throughout the monitoring period in order to capture spatial and temporal variability in soil moisture as best possible, given the limitations of the instrumentation. The samples were weighed in the field to determine the wet weight. Upon return to Simon Fraser University, the samples were dried in an oven at 110°C for 24 hours and re-weighed to determine the dry weight, which was used to compute the gravimetric water content using the expression:

$$\theta_g = \frac{m_{wet} - m_{dry}}{m_{dry}} \tag{3-2}$$

where θ_g is the gravimetric water content, m_{wet} is the weight of the sample at the time of sampling, and m_{dry} is the weight obtained after drying the sample to a constant weight in an oven (Hillel, 1998). Volumetric water content was then calculated using the expression:

$$\theta_v = \frac{\theta_g \cdot \rho_{soil}}{\rho_{water}} \tag{3-3}$$

where θ_v is the volumetric water content, ρ_{soil} is the dry bulk density of the soil, and ρ_{water} is the density of water. This information was used to calibrate the HydroSense's electrodes as described in Section 3.2.7.

3.1.7 Soil Temperature and Moisture within the Soil Pit

Soil temperature and volumetric soil moisture data were recorded using Campbell Scientific 107B thermistors and Campbell Scientific CS615 Water Content Reflectometers respectively at a soil pit (Figure 3-7) located approximately 100 m upslope of the stream channel, near the north-facing slope meteorological tower. All sensors were connected to CR10X data loggers and measurements were taken every minute and averaged half-hourly. Data was obtained at 0.02 m, 0.05 m, 0.10 m, 0.20 m, 0.30m and 0.40 m below the surface of the soil pit.

The soil profile consisted of two organic layers: i) an upper layer composed of living and lightly decomposed fibric peat and ii) a lower layer composed of sylvic peat containing dark, woody material, and the remains of mosses, lichen and rootlets (Quinton et al., 2005). Soil samples were taken from the face of the soil pit at each depth adjacent to where the moisture and temperature sensors were inserted in order to determine porosity and bulk density of the organic material as prescribed by Boelter (1965). The volumetric soil moisture contents of these samples were determined and used to create a site-specific soil moisture calibration curve for the CS615 moisture sensors (Quinton et al., 2005). Data obtained from these sensors were adjusted according to their calibration (Goeller, 2005). Goeller (2005) analyzed the data from the soil pit data and determined the soil heat flux (Qg) for 2002 and 2003 using the thermocalorimetric method.

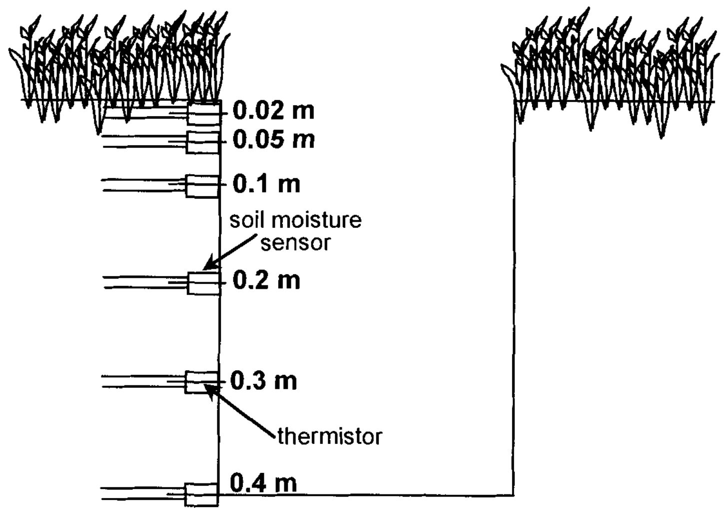

Figure 3-7: **Schematic of the soil pit installed in 2001 with temperature and moisture sensors. The soil pit was backfilled once the sensors were installed. Data from the soil pit were used by Goeller (2005) to calculate the soil heat flux using the thermo-calorimetric method.**

3.2 Analytical Methods

3.2.1 Image Analysis and Slope Correction of Digital Photographs

Digital images of the slope were imported into PhotoShop for some minor adjustments. Images were first cropped and stretched so that each image displayed exactly the same area of the hillslope. They were then exported as ".Tiff" files into the Sigma Scan Pro Image Analysis (version 5.0) software, and converted to greyscale, before being thresholded.

Snow covered area was calculated using a procedure similar to that used by Pomeroy et al., (2003) and Shook (1993). The fraction of snow-covered area was determined using the ratio of snow pixels to total slope pixels using SigmaScan. The threshold between snow and non-snow for each image was set subjectively, by visually comparing the histogram of pixel brightness to the snow covered area mask and to the image (Pomeroy et al., 2003). It is important to note that much of the lower portion of the north-facing slope is covered in shrubs. Thresholding the images allows a distinction between snow and non-snow areas. However, some of the areas thresholded as non-snow were shrubby areas that probably had some snow at the base of the shrubs, which could not be detected from the slope photo. Since the thresholding could not distinguish between bare ground and shrubs, the actual fraction of snow-covered areas is probably underestimated.

Images were corrected for slope using a simple vertical and horizontal scale. Known horizontal and vertical distances on the hillslope were delineated on each digital image, and the equivalent pixel lengths were measured using SigmaScan. For example, the distance between the two snow survey lines (Transects A and F) is approximately 100 m. The transect stakes could be seen in the photo and the distance between them was measured in pixels. Vertical and horizontal scales were determined based on the ratio of known distances on the slope and the number of pixels between these positions in order to determine the dimensions that each pixel in the image represented on the ground. Although each photo was taken from the same location, vertical and horizontal scales were calculated for each individual image used in the analysis. Based on the analysis of 15 digital images, the mean region on the hillslope that each pixel represents is 0.36 ± 0.03 m (vertically) x 0.17 ± 0.01 m (horizontally).

Ground measurements between specific points on the hillslope were made on DOY 157 (June 6). For example, the distance between the soil pit and the downslope edge of the snowdrift was measured on this day. Comparing these known distances to the distances calculated from the vertical and horizontal scale derived from this image of the slope taken on that day yielded a difference of approximately 5 m and a relative error of 8%. Considering the snow transect lengths were approximately 200 m and the north-facing slope is approximately 0.08 km^2, the slope correction provides reasonably accurate results.

3.2.2 Net All-Wave Radiation (Q*)

Half-hourly net radiation values (Q*) were converted into $MJ \cdot m^{-2} \cdot d^{-1}$ to compare with daily melt energy (Q_m) and soil thaw energy (Q_i).

3.2.3 Incoming Shortwave (K↓)

To correct for slope and aspect effects, geometric corrections were applied to incoming shortwave radiation at the valley bottom using the "global" module in the Cold Regions Hydrological Model (CHRM). The theoretical direct-beam component of shortwave radiation was developed from an expression proposed by Garnier and Ohmura (1970):

$$I_s = I_r \cdot \tau_z{}^m \cdot \cos(X \Lambda S) \tag{3-4}$$

where, I_s is the intensity of direct short-wave radiation falling on the surface (in $W \cdot m^{-2}$), I_r is the intensity of extraterrestrial radiation (in $W \cdot m^{-2}$), τ_z is the mean zenith path transmissivity of the atmosphere, m is the optical air mass, X is a unit co-ordinate vector normal to the surface and pointing away from the ground, and S is a unit co-ordinate vector expressing the position of the sun. A denotes the angle between X and S (Garnier and Ohmura, 1970).

The diffuse portion of sky radiation was also developed from Kondratyev (1965), as cited in: Garnier and Ohmura (1970):

$$D_s = D_h \cdot \cos^2(\phi / 2) \tag{3-5}$$

where, D_s is the diffuse radiation (in W·m^{-2}) on a surface of elevation angle Φ, and D_h is the same but recorded on a horizontal surface (in W·m^{-2}). This equation assumes a homogenous celestial atmosphere that radiates isotropically (Garnier and Ohmura, 1970).

CHRM separates the valley bottom incoming shortwave radiation into its direct and diffuse components, recalculates them as fluxes to the slope using geometrical corrections, and combines them to produce incoming shortwave to the slope (Pomeroy et al., 2003).

3.2.4 Energy Used for Snowmelt (Q_m)

The energy required for snowmelt, Q_m (in W·m^{-2}), is calculated from the loss of SWE over successive snow survey measurements. The snowcover was separated into drift and non-drift sections, based on an examination of the digital photographs of the slope, visual observations, and differences in depth and density measurements. For each point on Transects A and F, a melt rate, M_{point}, was determined by calculating the change in SWE for each time interval (i.e., from one snow survey to the next), where $SWE2 > 0$.

$$M_{point} = \frac{SWE1 - SWE2}{time2 - time1} \quad (3\text{-}6)$$

A mean melt rate (per unit area of snow), M, for the entire transect was then determined and Q_m was calculated using:

$$Q_m = \frac{M}{0.270} \quad (3\text{-}7)$$

where M is daily mean melt in mm·d^{-1} (Shook, 1993).

3.2.5 Soil Heat Flux (Q_g)

Thaw depth was estimated from the position of the 0°C isotherm, within the soil pit. Goeller (2005) used data obtained in 2003 to calculate Q_g based on the thermo-calorimetric method of Woo and Xia (1996) and Farouki (1981). Briefly, this method of calculating Q_g is based on determining the individual components of Q_g and summing them together using Equation 1-5 (where Q_i is the energy used to lower the frost table, Q_s is the energy used to warm the thawed soil and Q_p is the energy transferred to the permafrost). For a detailed explanation of how volumetric heat capacity and conductivity were calculated, refer to Goeller (2005). Q_g and Q_i from the soil pit were compared with Q_i calculated directly from thaw depth (dh/dt) measurements made at the snow-free patches.

3.2.6 Energy Used for Soil Thaw (Q_i)

The energy required for soil thaw (i.e., the latent heat consumed by melting ground ice) is calculated using the change in soil thaw depth between successive measurements. For each point on every thaw depth transect, a thaw rate, dh/dt was determined by calculating the change in soil thaw depth for each time interval (i.e., from one thaw depth measurement to the next). A mean thaw rate for the entire transect was then determined and Q_i was calculated using Equation 1-10. The fractional ice content, f_{ice}, was assumed to equal the porosity values determined from the soil pit samples (Goeller, 2005; Quinton et al., 2005).

3.2.7 Soil Moisture Calibrations

The HydroSense system applies a standard calibration to convert the probe response to volumetric water content. The calibration was derived from laboratory measurements in typical agronomic soils (Campbell Scientific Inc., 2001). The HydroSense is predominantly sensitive to the dielectric constant (and consequently VWC), but other soil physical properties can also affect the measurement. For example, very high organic matter content can attenuate the applied signal and affect the detection of the reflected signal in the probe's electronics. In these situations, the manufacturer (Campbell Scientific Inc.) recommends that if actual water content values are required, a calibration using curve fitting methods can be performed using an independent measurement of the water content (Campbell Scientific Inc., 2001). Since the HydroSense was used in highly organic and rocky soils, a separate site-specific calibration was required to obtain the corrected soil moisture values. The calibration coefficients are derived from a curve that is fit to known water content values and probe output periods.

Out of 28 soil samples that were collected during the monitoring period, twenty-six were used in the calibration. One sample was removed because it was entirely frozen when sampled (ice through the entire sample) and the other was an apparent outlier, probably due to sampling error (i.e. the sample contained rocks). When the samples were stratified spatially and/or temporally there were no consistent trends to the data. Thus, all the volumetric water contents of the samples (minus the outlier) were plotted against the probe output period, and a line was fitted through the data points as shown in Figure 3-8 (R^2 = 0.66, n = 26, σ = 0.15):

$$\theta_v = 1.1125 \cdot p - 0.7781 \qquad (3\text{-}8)$$

where θ_v is the volumetric soil moisture and p is the measured time period (in milliseconds). The calibration coefficients obtained from the regression were then applied to all HydroSense VWC measurements to obtain the calibrated VWC's.

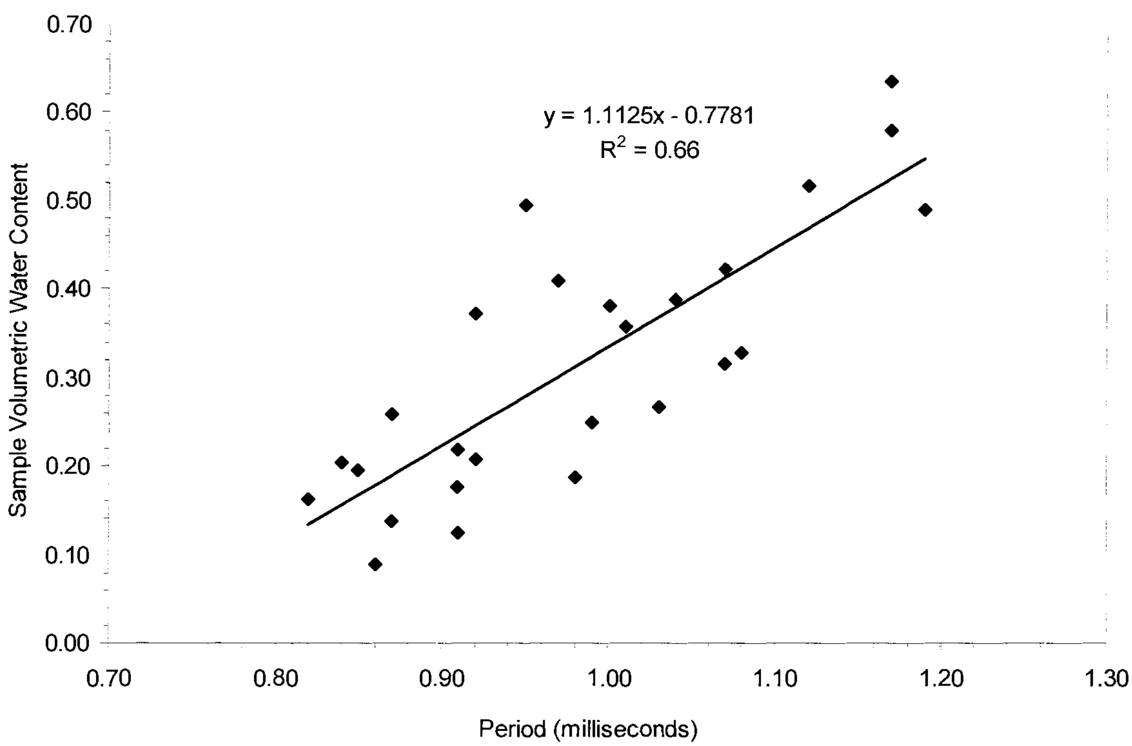

Figure 3-8: Regression between HydroSense probe output period and the volumetric water content of the sample obtained through the oven-drying method. The regression equation is given in Equation 3-8.

CHAPTER 4: RADIATION ANALYSIS

Net all-wave radiation is a critical component of the energy balance at the land surface, and accurate measurements of this parameter are needed in order to estimate the amount of energy available for snowmelt and soil thaw. In order to determine the amount of net radiation (Q^*) that is used for snowmelt (Q_m) and soil thaw (Q_i), a continuous measurement of Q^* over both these surfaces is required, over the entire study period. However, one of the major limitations of this study was that there was only one location on the north-facing slope where Q^* was measured (i.e., at the hillslope meteorological tower).

The snow-depth sensor located on the hillslope meteorological tower recorded snow-free conditions on DOY 128. This means that measurements of Q^* over a snow surface stopped (at the latest) on DOY 127 and that on DOY 128 and beyond, measurements of Q^* at the meteorological tower were made over the snow-free ground (Figure 4-1). However, approximately 36% of the slope was still snow covered at this time as shown in Figure 5-6 in the following chapter. The spatial and temporal variation of snowmelt at the hillslope scale did not correspond to the spatial and temporal variation of snowmelt underneath the net radiometer. This is problematic because it effectively means that at the hillslope scale, both Q_m (for the snow covered portions of the slope) and Q_i (for the snow-free portions of the slope) cannot be known together at any given time, as Q^* data only exists for one particular surface at any given time.

Therefore, the radiation dataset over which to partition Q^* to snowmelt energy is limited to DOY 113-127 (at the latest), which is a relatively short time (14 days) compared to the entire monitoring period (53 days). Similarly, the time over which Q^*

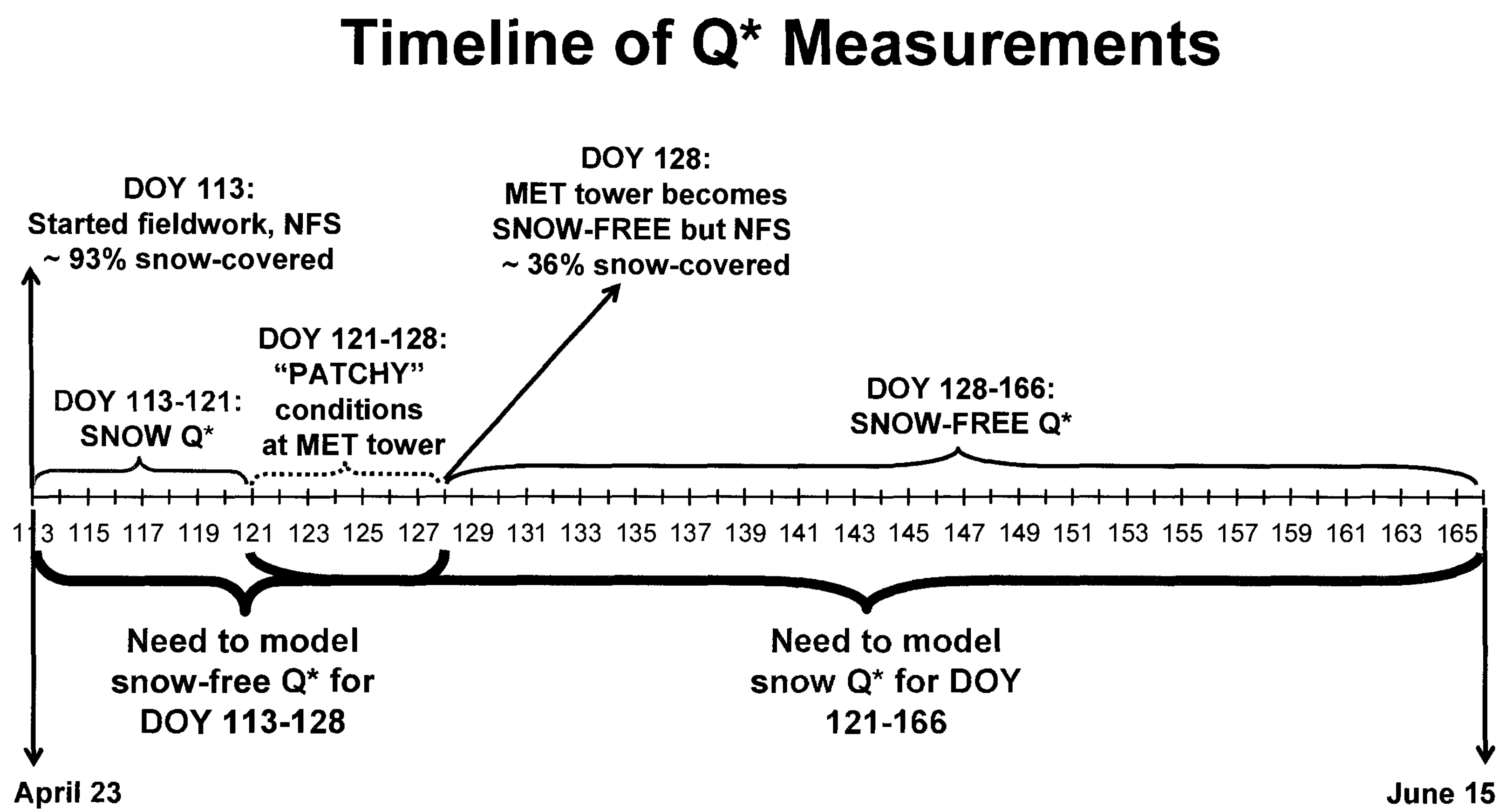

Figure 4-1: Timeline of Q* measurements made over a changing surface at hillslope meteorological tower

can be partitioned to soil thaw energy can only start from DOY 128 (i.e., there are 14 days for which measured snow-free Q^* is not available). Ideally, two separate measurements of Q^*, one over a snow surface and the other over a snow-free surface would have been made concurrently, so that at any given time on the hillslope, the amount of Q^* could be related to snowmelt energy or soil thaw energy (depending on how much of the hillslope was snow covered or snow-free). Thus, the dataset for energy balance calculations was considerably limited, particularly for the partitioning of Q^* to snowmelt energy.

In an attempt to extend the time series for both snow and snow-free net radiation data, a method was tested to model Q^* over snow and snow-free surfaces. The model results were then compared to the measured values. If successful, modelled Q^* values for the snow surface could be used as a surrogate for measured Q^* for the snow covered slope. These modelled Q^* values could then be compared with the measured Q_m values (i.e., the energy available for snowmelt) for the time period after which measured Q^* data are available for the snow-free surface only (DOY 128). In a similar fashion, these Q^* values can also be compared with the measured Q_i values (i.e., the energy available for soil thaw) for the time period before which measured Q^* data are available for the snow-surface only (at least DOY 127). This methodology would provide a more representative and accurate partitioning of Q^* to Q_m and of Q^* to Q_i over the entire monitoring period.

This chapter describes the methodology used to model Q^* (net all-wave radiation) for both snow and snow-free surfaces. Ultimately, it was determined that only the measured snow covered Q^* should be used (i.e., up until DOY 121). Beyond this day, Q^* was probably measured over a combination of snow and snow-free surfaces and could not be used to compare with Q_m. Therefore, the measured Q^* over a snow covered surface was limited to DOY 113-121. Thus, the net radiation data set limited the time period over which energy balance calculations could be made, particularly for the snow covered period. However, results from this chapter also suggest that it is possible to reasonably model Q* over the snow-free surface. Hence, modelled snow-free Q* values prior to DOY 128 could be used to extend this time series earlier (i.e., snow-free Q* from DOY 113-166, instead of just from DOY 128-166).

4.1 Net Radiation Over A Changing Mixture of Snow, Shrubs and Snow-free Ground

Technically, net all-wave radiation was not measured over a strictly uniform snow surface nor over a uniform snow-free ground surface; a significant portion of the north-facing slope was covered by shrubs. Approximately 58% of the Wolf Creek Basin (of which Granger is a part of) is dominated by shrub tundra (Janowicz, 1999). Therefore, the presence of shrubs plays an important role in the surface energy balance of the sub-arctic, particularly during snowmelt (this will be discussed in more detail in Chapter 5). Although numerous studies have demonstrated that forest canopies above a snow surface can significantly modify the surface energetics (Nakai et al., 1999; Harding and Pomeroy, 1996; Yamazaki and Kondo, 1992), there has been relatively little work done on the effect of the shorter shrub vegetation on snow processes (Lee and Mahrt, 2004). Sub-arctic shrub-tundra consists of discontinuous and continuous canopies of deciduous shrubs of dwarf alder (*Alnus sp.*), willow (*Salix sp.*) and/or birch (*Betula sp.*) that is approximately 0.3 m to 3 m in height (Jorgenson and Heiner, 2004 as cited in: Pomeroy et al., 2006).

The transmission of shortwave radiation through the shrub tundra canopy is a complex and important process because it affects the albedo above the surface, the transmittance of radiation to the snow surface, and ultimately the magnitude of energy fluxes to the snow surface (Pomeroy et al., 2006; Bewley et al., submitted). Consequently, the presence of shrubs may limit the amount of radiation reaching the snow surface. Pomeroy (personal communication, September 12, 2005) indicated that trying to match a calculated Q* for snow to a measured Q* over a changing mixture of shrubs, snow and bare patches is not possible. To investigate this, the modelled and measured Q* values were compared for the early winter when shrub exposure was smallest (see Appendix E). Unfortunately, the modelled and measured values did not compare favourably, and no indication of the effect of shrubs on the results could be determined. Thus, for the purposes of this study, an assumption was made that the presence of shrubs would not significantly affect the results for Q*.

4.2 Modelling Net Radiation

The net all-wave radiation flux (Q^*) is composed of the net shortwave (K^*) and net longwave fluxes (L^*):

$$Q^* = (K\downarrow - K\uparrow) + (L\downarrow - L\uparrow) = K^* + L^* \qquad (4\text{-}1)$$

where $K\downarrow$ is the incoming shortwave radiation, $K\uparrow$ is the outgoing shortwave radiation, $L\downarrow$ is the incoming longwave radiation and $L\uparrow$ is the outgoing longwave radiation (in $W \cdot m^{-2}$).

4.2.1 Shortwave Radiation

Incoming shortwave radiation ($K\downarrow$) was measured at the valley bottom and was corrected for slope using the Cold Regions Hydrological Model (CHRM) – refer to Section 3.2.3. Corrected daily incoming shortwave radiation to the north-facing slope is considerably less than that measured at the valley bottom (Figure 4-2). Over the monitoring period (40 cloudy days and 13 cloudless days), cumulative incoming shortwave fluxes to the north-facing slope were approximately 82% of those to the valley bottom. When the data were separated into cloudy and cloudless days, the cumulative incoming shortwave fluxes to the north-facing slope were 79% (over the 13 cloudless days) and 83% (over the 40 cloudy days), respectively to those of the valley bottom (Figure 4-3 and Figure 4-4). Pomeroy et al. (2003) calculated slope corrected shortwave fluxes for the same study site and found similar results, although on clear days the difference was slightly more pronounced than on relatively cloudy days.

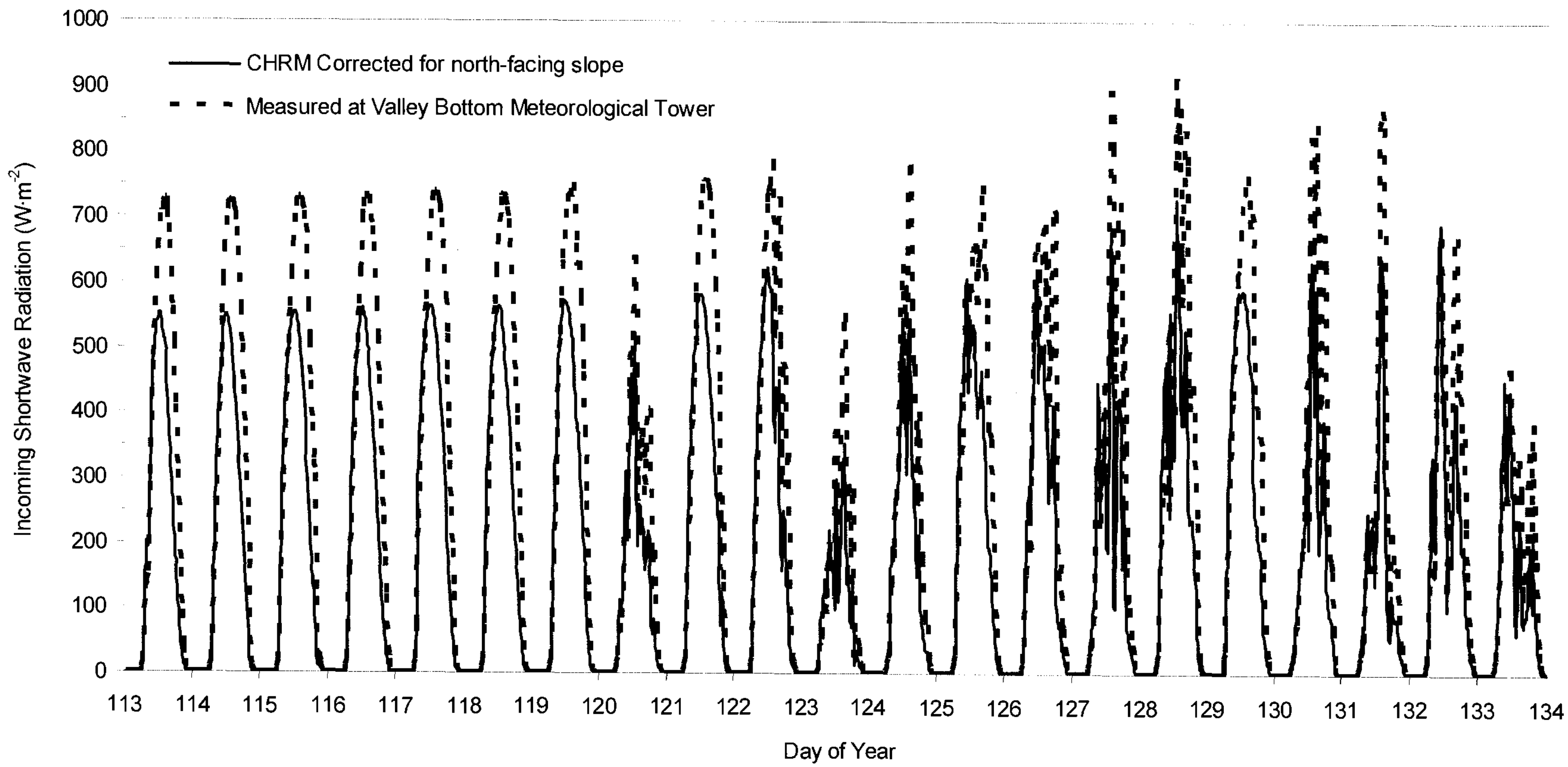

Figure 4-2: **Incoming shortwave radiation measured at valley bottom compared to slope-corrected incoming shortwave radiation using CHRM (Cold Regions Hydrologic Model) for the first 20 days of the study period, DOY 113-133 (April 23 – May 13, 2003).**

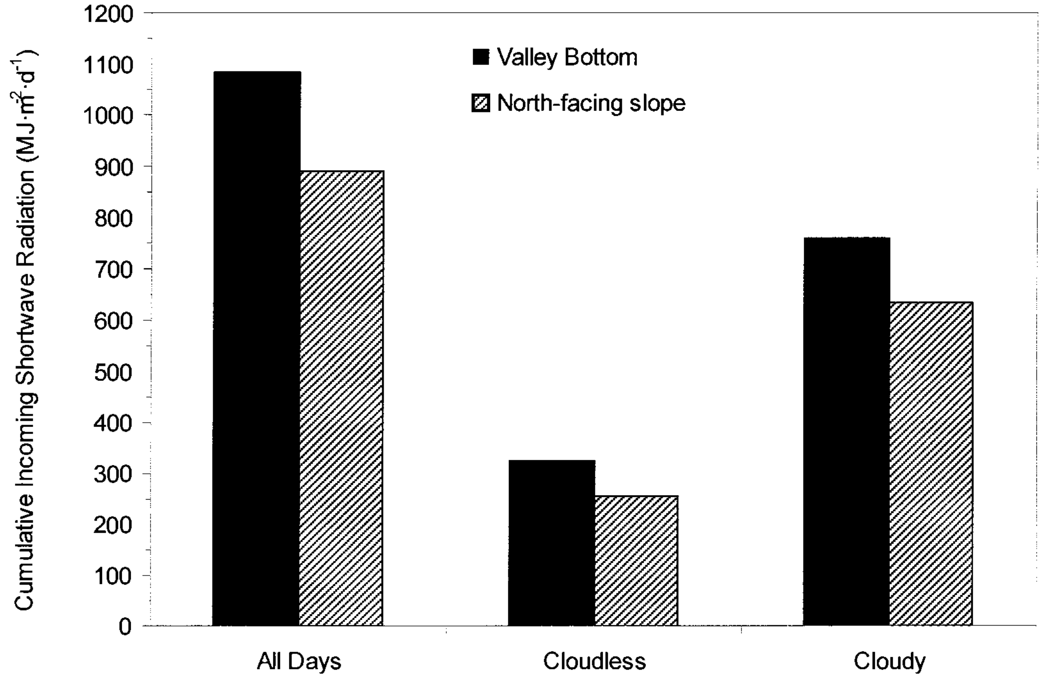

Figure 4-3: **Cumulative incoming shortwave radiation fluxes for the valley bottom compared to the north-facing slope for the entire study period (53 days) and separated into cloudless (13 days) and cloudy days (40 days).**

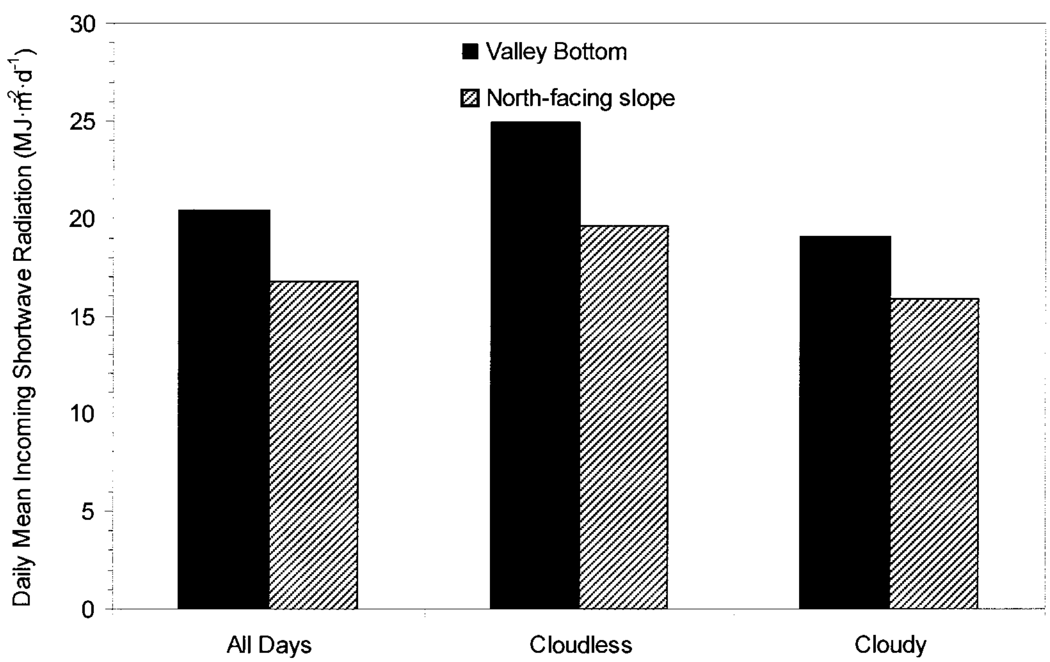

Figure 4-4: **Daily mean incoming shortwave radiation flux for the valley bottom compared to the north-facing slope for an average day over the entire study period and separated into mean values for a cloudless and cloudy day.**

There was no direct measure of the outgoing shortwave radiation (K↑), but as it is a function of surface albedo, the net shortwave flux (K*) can be determined using the following equation:

$$K^* = K \downarrow \cdot (1-\alpha) \tag{4-2}$$

where α is albedo. Albedo was measured at the valley bottom meteorological tower, but the downward looking pyranometer was above the canopy, and hence, was "looking at" a mixture of shrubs and snow (Bewley, personal communication, May 19, 2005). As a result, measured albedo values were quite low, generally ranging from 0.3-0.4. Instead of using these measured albedo values, a constant albedo of 0.8 was assumed for the snow surface (Oke, 1987) and a value of 0.15 was assumed for the snow-free surface (Bewley, personal communication, May 19, 2005). Values obtained from a linear interpolation between 0.8 and 0.15 were used for albedo during the "patchy" stage (DOY 116-128, April 26-May 8), due to the fact that during this time period, the area underneath the meteorological tower was neither that of a completely snow covered surface nor that of a completely snow-free surface.

The decision on where to start the interpolation was based on examining the graphs of measured Q* and modelled Q* (Figure 4-7) and determining which dates the values began to visually diverge most significantly as well as by examining the daily slope photographs. After DOY 115 (April 25), computed Q* is consistently lower than measured Q* values (likely due to the albedo directly underneath the radiometer being neither that of a complete snow cover nor of the bare ground). An alternative approach, which was tested, was to use a value of 0.8 for the entire period up to DOY 127 and then abruptly change the value to 0.15. However, the interpolated scheme produced results that were more reasonable.

Based on the linearly interpolated transitional albedo values (i.e., linearly interpolating albedo from that of a complete snowcover (α=0.8) to a snow-free surface (α=0.15)), the albedo is < 0.5 after DOY 121 (refer to Appendix C). Although Oke (1987) provides a range of snow albedo from 0.4-0.95, 0.5 was used as a conservative "cut-off" or threshold for what would be considered a "snow albedo". Sicart et al. (2004) state that "clean" snow generally has an albedo of > 0.5 and Lee and Mahrt (2004) classified a day as belonging to an "intercepted snow class" in their model when daily mean albedo was > 0.5. Based on this, it seems reasonable to assume a measured snow Q* at the hillslope meteorological tower up until DOY 121. Beyond that day, it is reasonable to expect that most of the area underneath the radiometer located at the meteorological tower was probably snow-free and that the Q* measured during that time (from DOY 121-127) would more closely approximate that of a snow-free surface rather than a snow covered surface.

4.2.2 Modelling Q* For A Snow-Free Surface Prior to DOY 128

Although the area underneath the net radiometer at the meteorological tower was at least partially snow covered until DOY 128, there were many patches on the hillslope that had already become snow-free, and hence began to thaw. In order to compare Q* with Q_i (the energy available to melt the ice in the ground and hence lower the frost table, i.e., thaw) for these patches, Q* over a snow-free surface prior to DOY 128 was required. Due to the low albedo of the snow-free surface (α = 0.15), incoming shortwave radiation is the dominant component of the daytime net radiation balance. The relatively low values of albedo and net longwave radiation of snow-free alpine tundra surfaces suggest that there is a well-defined linear relationship between Q* and $K\downarrow$ (Huo, 1991; Bailey et al., 1989) and, therefore, it is possible to estimate net radiation using incoming shortwave radiation. Kaminsky and Dubayah (1997) determined that a single linear regression relationship between net radiation and solar radiation could be applied to a large area with variable land cover types found in the boreal forest and northern prairie regions. Oliver (1992) found that it was possible to obtain reasonable estimates of daily net radiation totals from daily solar radiation values for both horizontal and sloping surfaces. To estimate Q* over the snow-free surface prior to DOY 128, a linear regression (Figure 4-5) between daily Q* and daily slope-corrected K↓ (from DOY 128-165) was determined and applied to daily slope-corrected K↓ values from DOY 113-127 (the days the hillslope meteorological tower was not completely snow-free) in order to obtain snow-free Q* values during this period.

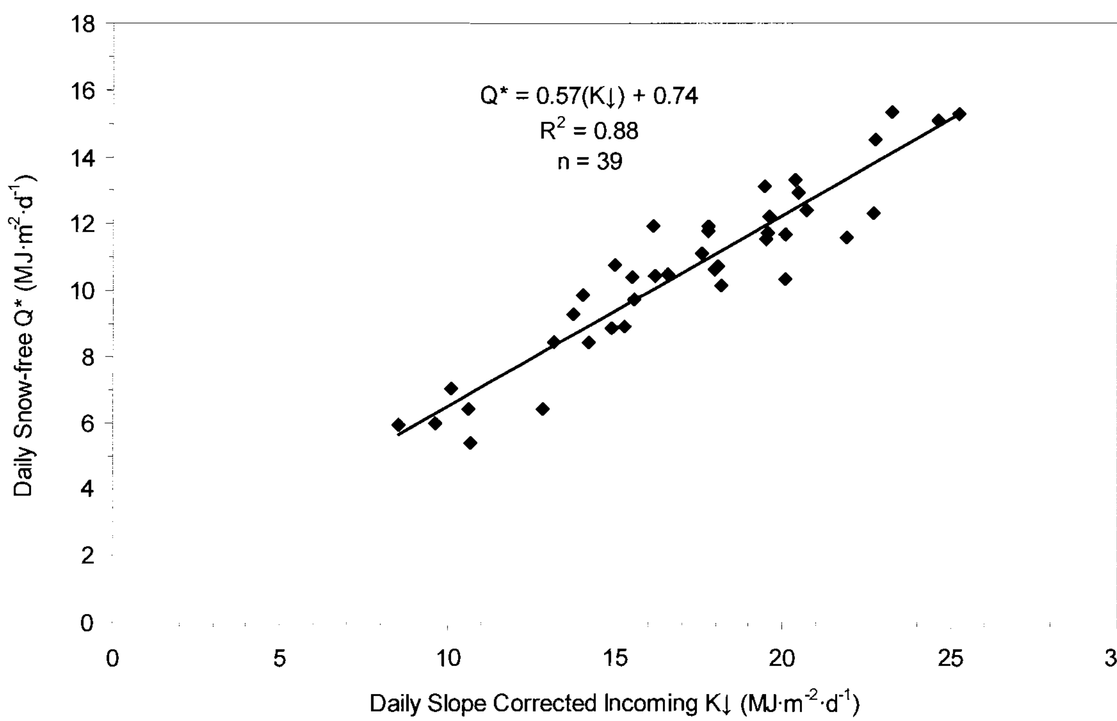

Figure 4-5: **Relationship between daily slope-corrected incoming shortwave radiation and daily net radiation over a snow-free surface (from DOY 128-166). The regression equation was used to estimate daily Q* over the snow-free surface prior to DOY 128.**

4.2.3 Modelling Q* Over A Snow Covered Surface After DOY 128

Unlike the snow-free surface, the relationship between Q* and K↓ is poorly defined for a snow-covered surface (Saunders, 1990). Figure 4-6 shows the poor relationship between daily slope corrected incoming shortwave radiation and daily snow-covered Q* (assumed to be from DOY 113-121) based on the analysis in Section 4.2.1. Even if the outlier is removed and a regression line fit through the data, the slope = 3.35, y-intercept = -57.52, and low number of data points (n = 8) which still suggest that the relationship remains poor

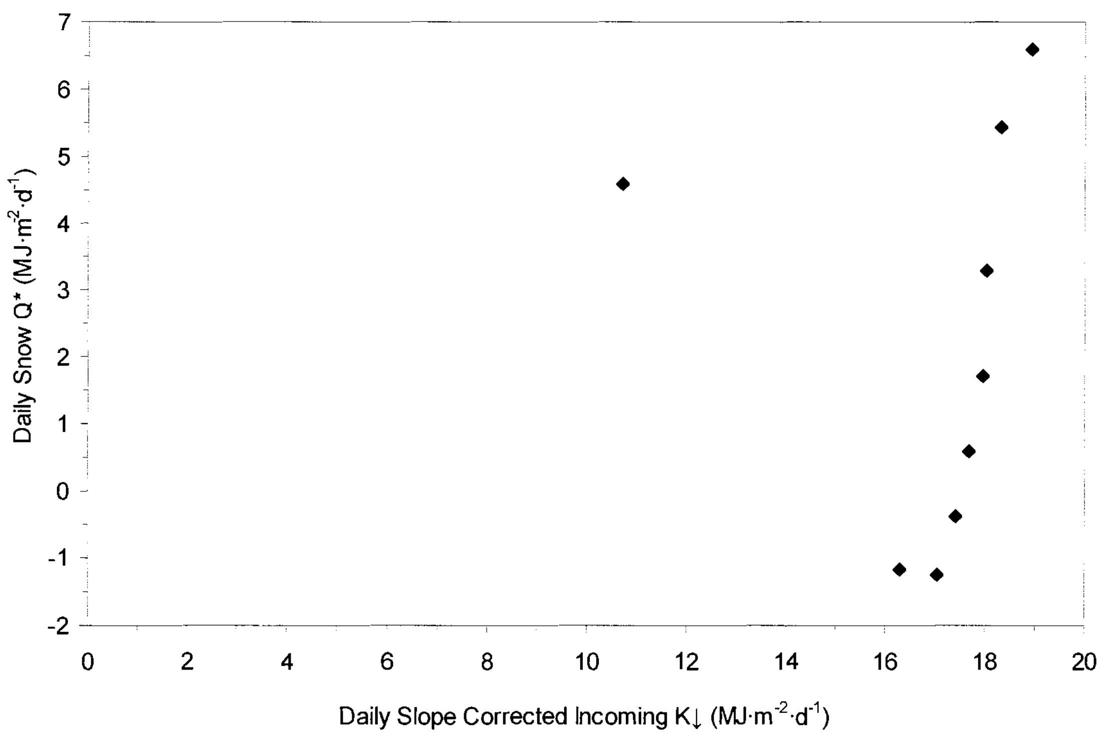

Figure 4-6: Relationship between daily slope-corrected incoming shortwave radiation and daily net radiation over a snow covered surface (from DOY 113-121).

Therefore, an alternative approach was necessary. Net all-wave radiation over the snow surface was modelled for half-hour intervals for the time period in which the net radiometer was assumed to be measuring Q* over a snow covered surface (DOY 113-

121), using the measurements of K↓ at the valley bottom (corrected for slope), and calculating K*, L↑ and L↓.

The outgoing longwave flux (L↑) was calculated using:

$$L\uparrow = \varepsilon \cdot \sigma \cdot T_{sfc}^{\ 4} \tag{4-3}$$

where ε is the emissivity of the surface, assumed to be 0.99 (Oke, 1987), σ is the Stefan-Boltzmann constant (5.67 x 10^{-8} W·m^{-2}·K^{-4}), and T_{sfc} is the surface temperature in Kelvin (K), obtained from the hillslope meteorological tower.

Sicart et al. (submitted) developed a simple parameterisation of atmospheric long-wave radiation suitable for energy studies in open, northern environments. The equation for longwave irradiance, $L\downarrow$ in open environments is defined by:

$$L\downarrow = 1.24 \cdot (e / T_{air})^{1/7} \cdot (1 + 0.44 \cdot RH - 0.18 \cdot \tau_{atm}) \cdot \sigma \cdot T_{air}^{\ 4} \tag{4-4}$$

where e is vapour pressure in millibars, T_{air} is air temperature in Kelvin, RH is relative humidity and τ_{atm} is daily atmospheric transmissivity between 0 and 1 (Sicart et al., submitted). Vapour pressure, air temperature and relative humidity data for this parameterisation are half-hourly averages and were obtained from the hillslope meteorological tower (GB4). Daily atmospheric transmissivity was calculated using:

$$\tau_{atm} = \frac{K\downarrow}{I_r} \tag{4-5}$$

where $K\downarrow$ is the incoming shortwave radiation on a flat surface and I_r is the intensity of extraterrestrial radiation (both in W·m^{-2}). The resulting values for L↓ were compared against L↓ that was determined by regressing L↓ values obtained from a meteorological tower located on the plateau above the hillslope and available measured L↓ at the valley bottom in May of 2003 (see Appendix D for a full explanation of how 'measured incoming longwave radiation' was derived). Although the parameterisation was developed at this site, it appears that the modelled and measured values of L↓ show a poor fit (R^2 = 0.28), even though Sicart et al. (submitted) report strong correlations (ranging from R^2 = 0.61 to 0.91) between measured and modelled incoming longwave radiation for 2002 and 2004 data. The reason for the lack of correlation for 2003 is unclear.

Figure 4-7 (time series) and Figure 4-8 (scatter plot) show the modelled and measured Q* over the first 15 days of the monitoring period, which corresponds to the days during which the snow-depth sensor (located on the hillslope meteorological tower) was measuring snow-depth at a point near to the net radiometer. Although the values appear to be in rough agreement, the modelled values tended to underestimate the measured values, most notably up to approximately DOY 125. The time series was also extended back to DOY 60 (March 1), in order to see if the fit would be improved when the parameters were better constrained (i.e., uniform snow cover, no shrubs exposed). For the most part, the fit is just as poor; however, there are distinct time periods where the fit is very poor (e.g., DOY 64 to 74 and DOY 89 to 96 – see Appendix E).

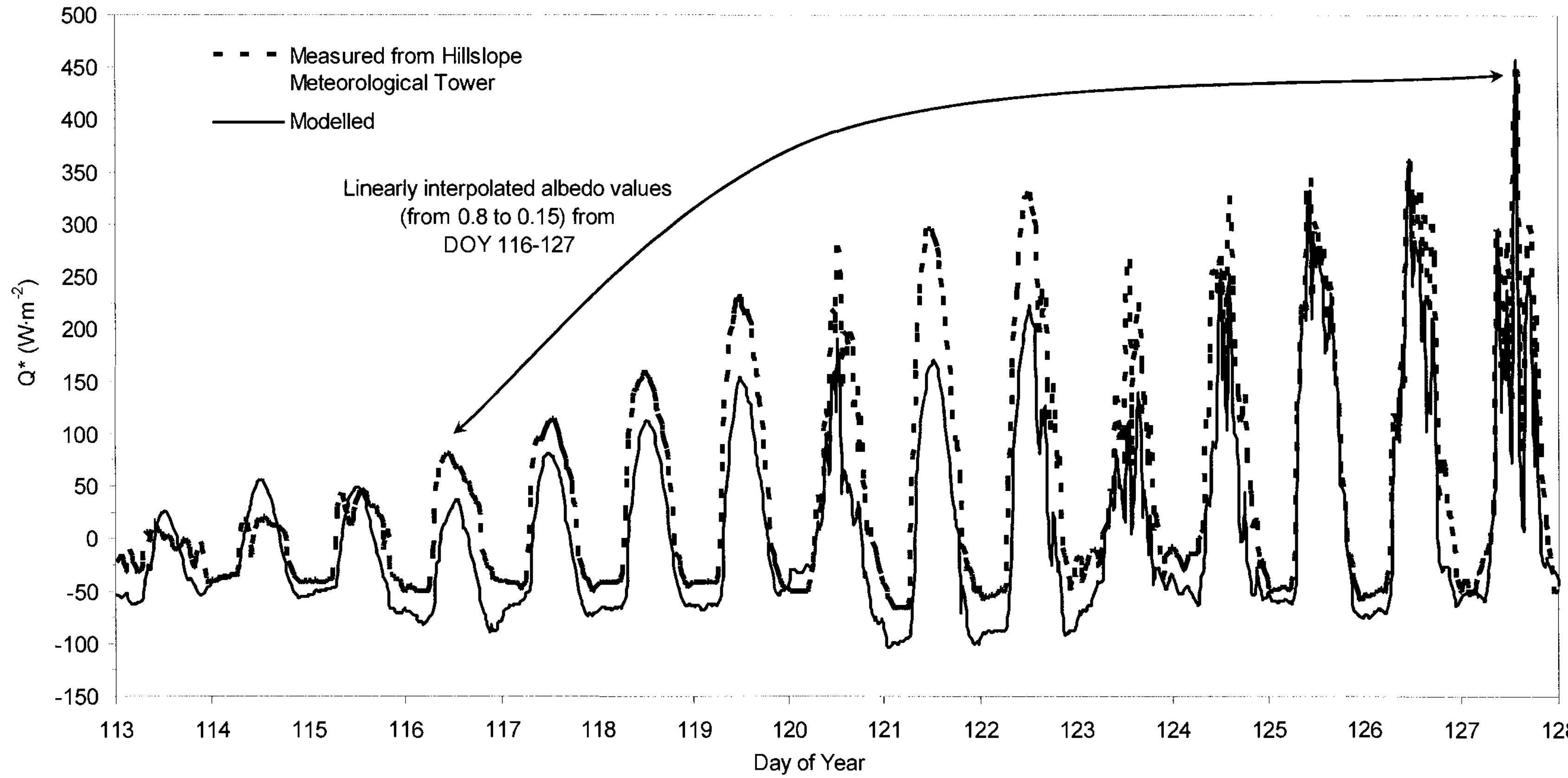

Figure 4-7: **Measured and modelled net radiation for the first 15 days of the monitoring period over which net radiation was measured over a snow covered surface, DOY 113-127 (April 23 – May 7, 2003).**

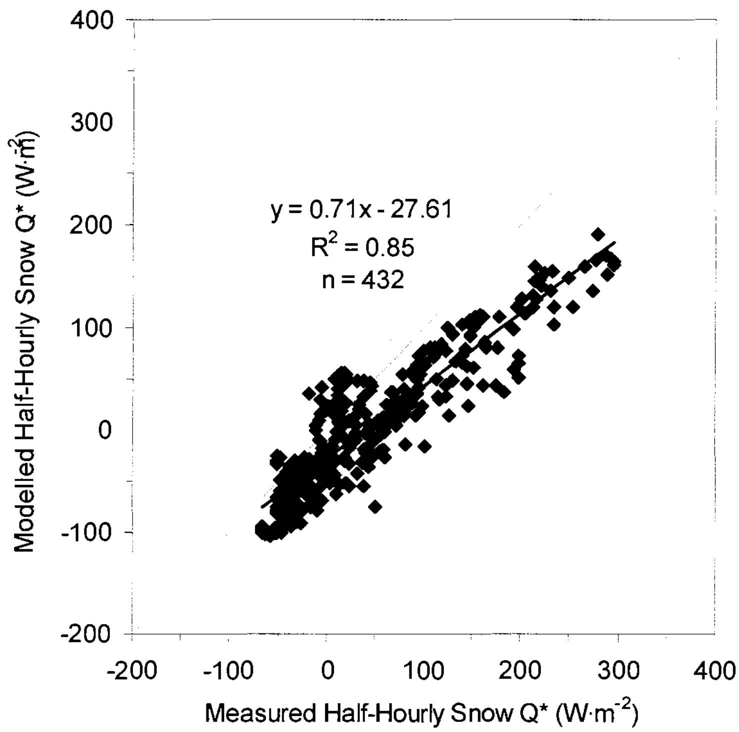

Figure 4-8: Comparison of half-hourly measured and modelled snow Q* from DOY 113-121 (April 23-May 1, 2003).

In an attempt to investigate the discrepancy between the modelled and measured values, the data were separated into daytime and nighttime values. At night,

$$Q^* = L^* \tag{4-6}$$

(i.e., there is no short-wave radiation), and the calculation of Q* is relatively straightforward. The results for daytime and nighttime values for snow covered conditions are shown in Figure 4-9. Daytime values show a relatively good correlation (R^2 = 0.80) although there is a negative bias (indicated by the slope = 0.68 and y-intercept = -24.13) between measured and modelled half-hourly Q* values. However, the lack of correlation for the nighttime values (R^2 = 0.18, slope=0.85 and y-intercept = -24.85) suggests a potential problem with the measured parameters and/or the

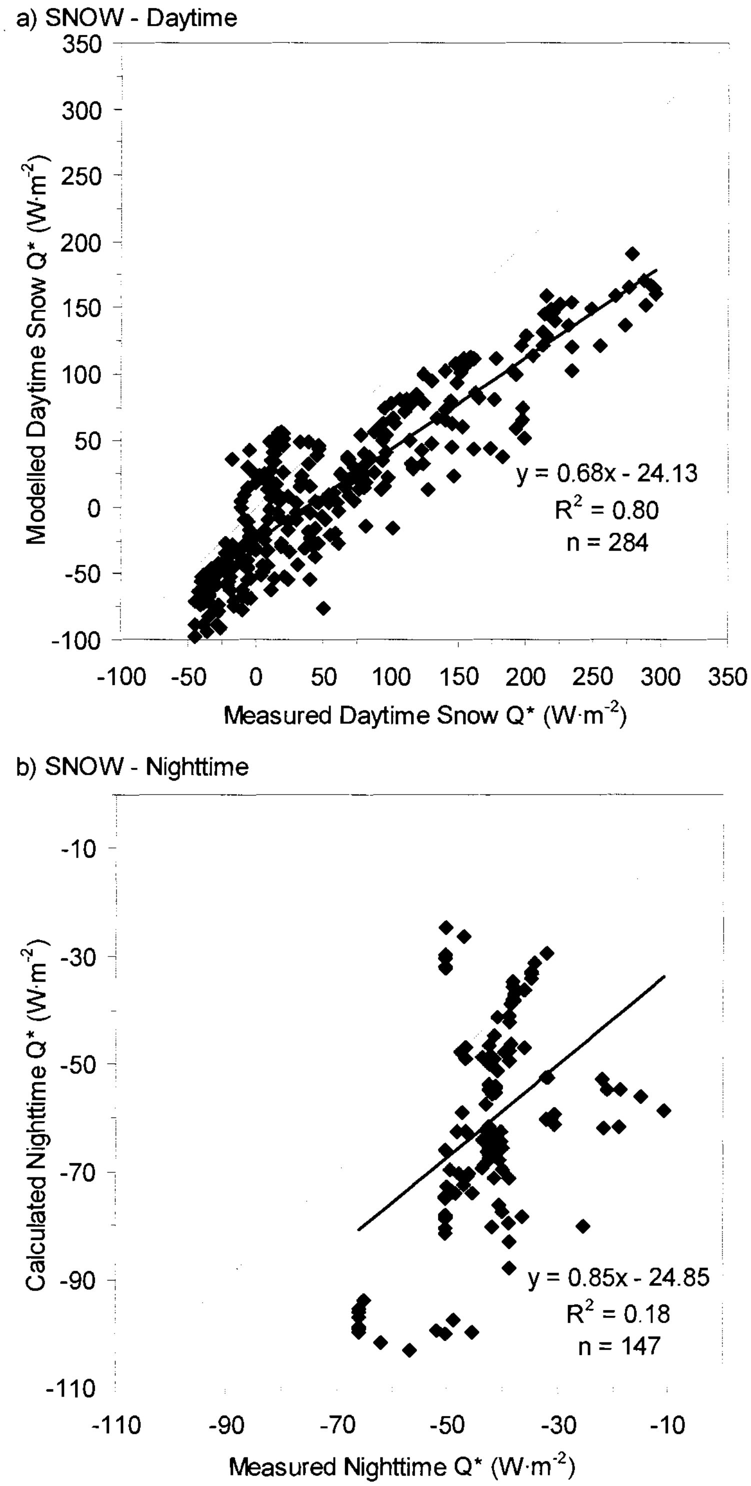

Figure 4-9: Comparison of half-hourly measured and modelled snow Q* separated into a) daytime b) nighttime values from DOY 113-121.

parameterization of L↓ used to compute the net longwave flux, thus limiting the use of the modelled values.

Although the half-hourly daytime values are significantly better than the nighttime results, the overall total daily modelled Q* values for the snow surface are generally quite poor. Ultimately, when the values of Q* are accumulated over the day, the relatively small half-hourly errors also begin to accumulate, such that daily total modelled Q* values are significantly lower than measured Q* (Figure 4-11 and Figure 4-11). As the modelled values were usually less than the measured values, the errors did not cancel (i.e., the errors were not random, but instead, rather systematic), and as a result, the total cumulative measured Q* over the 9 day period (from DOY 113-121) was 19 $MJ \cdot m^{-2}$ whereas the total cumulative modelled Q* was only -8 $MJ \cdot m^{-2}$.

One possible explanation for the poor snow surface results is the uncertainty in the value of albedo, although Shook (1993) suggested that the surface albedo of a melting snowcover does not change appreciably. Recall that a constant albedo value (of 0.8 was used up until DOY 115, after which a range of values derived from a linear interpolation from 0.8 to 0.15) were used for calculating K↑, which in turn was used to calculate Q*. It is widely known that snow albedo can vary diurnally (McGuffie and Henderson-Sellers, 1985; Dirmhirn and Eaton 1975; Hubley, 1955) as well as daily (Winther et al., 2002; Foster, 1989; Maykut and Church, 1973). Thus, it is possible that in using a fixed value and/or the linearly interpolated range of values for snow albedo, K* was poorly defined over the course of the day. Unfortunately, because the measured snow albedo values were artificially low (due to the presence of shrubs under the pyranometer), it was difficult to derive a more accurate value (or range of values) than the one used. Nevertheless, the linearly interpolated values did provide an estimate of the areal albedo underneath the net radiometer (recall that the net radiometer measures the net all-wave radiation over an area, not a point).

The second possible explanation for the poor snow surface results could be attributed to the problems associated with modelling longwave irradiance. Generally, the components of L* are more variable and difficult to measure, compared to the components of K* (which only requires incoming shortwave and albedo). For example, Oliphant et al. (2003) also found that they could simulate shortwave fluxes more accurately than longwave fluxes.

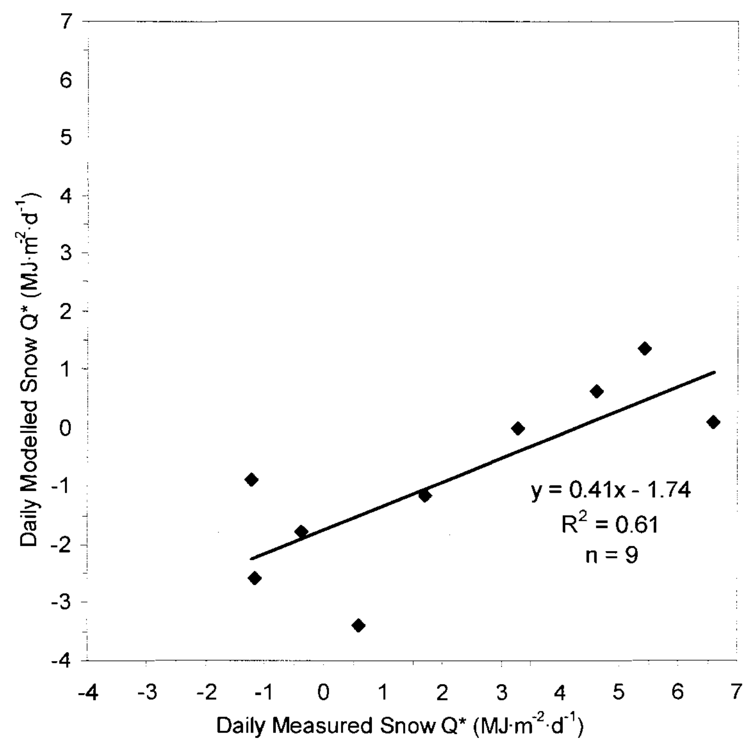

Figure 4-10: Comparison of daily measured and modelled Q* for the snow covered surface (DOY 113-121).

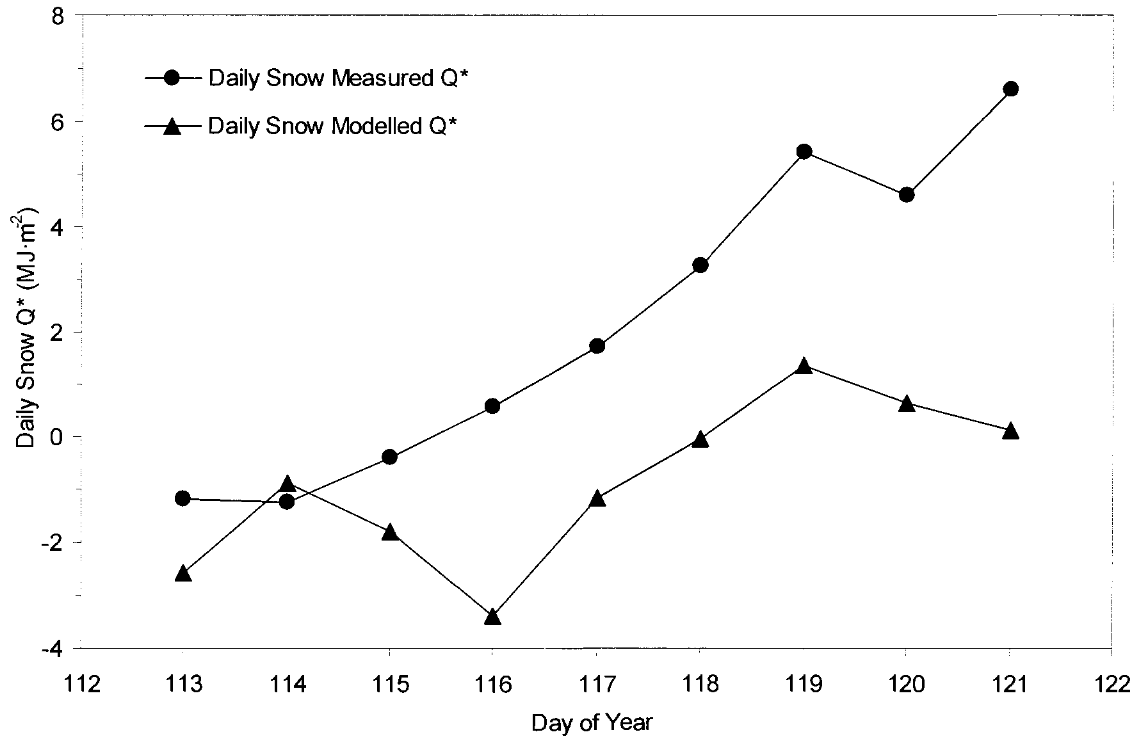

Figure 4-11: Total daily measured and modelled Q* for the snow covered period DOY 113-121 (April 23-May 1, 2003).

4.2.4 Final Values of Q*

It is believed that Q* measured with the net radiometer was probably quite accurate and reliable during the study period (i.e., from a snow surface, to a patchy surface composed of snow and snow-free areas, and finally to a completely snow-free surface). Nevertheless, the fact remains that a significant percentage of the hillslope remained snow covered long after the area beneath the meteorological station became snow-free. Attempts to relate measured and calculated Q* over the entire period proved unsuccessful, and it was not possible to extend the time beyond the snow-covered period as measured at the meteorological station on the hillslope. Therefore, Q* measurements for the snow surface could only be used from DOY 113 up until DOY 121. However, Q* over the snow-free surface prior to DOY 128 could be reasonably determined using the relationship between K↓ and Q* (Figure 4-5).

CHAPTER 5: SNOWMELT ENERGY

5.1 Introduction

The objective of this chapter is to examine the snowmelt energetics of the snowcover on the north-facing slope in order to define a relationship between net all-wave radiation and snowmelt energy. The mean percentage of net radiation used for snowmelt (Q_m) and a mean daily areal melt rate will also be calculated.

5.2 Snow Surveys and Snow Water Equivalent

In order to estimate SWE for each point along the two transects, a relationship between mean snow density and time was determined (Figure 5-1). This relationship was then used to calculate mean snow density on a given day during the study period. The predicted densities, along with snow depth at each transect point, were then used to calculate SWE using Equation 1-1 (Figure 5-2).

A weak correlation between measured snow depth and snow density is observed, particularly for the non-drift snowcover (Figure 5-1), as exhibited by the large degree of variability (recall the methodology used to obtain these densities from Section 3.1.3, where non-drift densities were determined using a snow tube and drift densities were obtained by digging a snow pit). Fluctuation in mean snow density during snowmelt was observed in this study as well as in other studies (Anderton et al., 2004; Pomeroy et al., 2003). These fluctuations have been related to dry and wet metamorphic processes, which tend to increase the density of a snowpack (Dingman, 2002). Also during snowmelt, the density of a snowpack can vary greatly due to the formation and drainage of meltwater (Dingman, 2002; Pomeroy and Gray, 1995).

However, the removal of snow through ablation generally compensates for this latter effect, such that the overall SWE decreases with time.

Maximum SWE for the drift was 277 mm, compared with 187 mm for the non-drift portion of the north-facing slope. As there was no new accumulated snowfall during the study period, the temporal fluctuations in SWE (particularly the small increases in SWE with time) are likely due to errors associated with the measurement of snow depth and/or measurement and calculation errors of snow density.

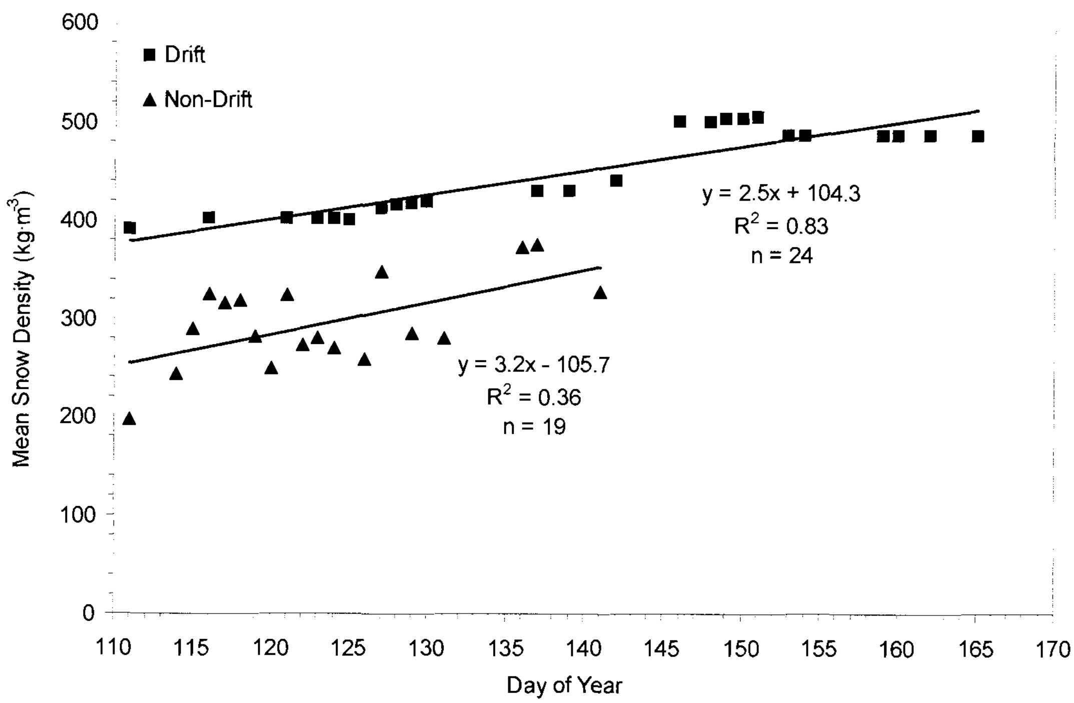

Figure 5-1: **Variations in mean snow density during snowmelt for both the non-drift and drift snowcover and their relationship with time. Mean drift densities are the daily depth-integrated averages from the snow pit. Mean non-drift densities are the daily averages of density measurements made using the ESC tube on the non-drift portion of Transect A and Transect F.**

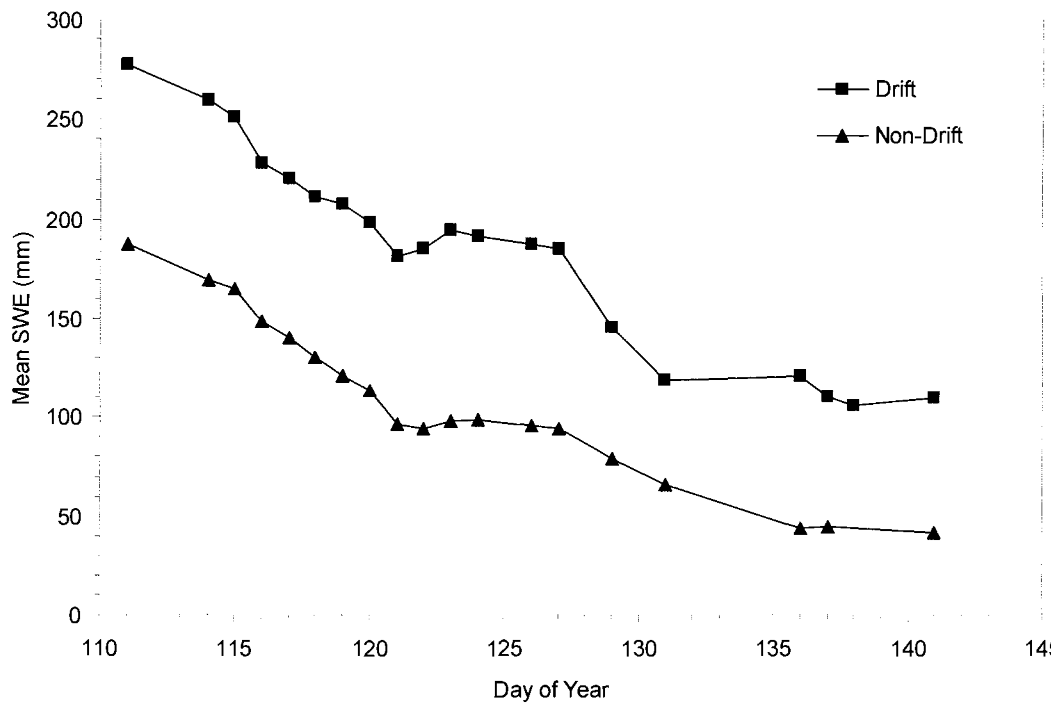

Figure 5-2: Change in the mean SWE (calculated using mean snow density determined from Figure 5-1) of the drift and non-drift portions of the north-facing slope with time.

5.3 General Snowcover Characteristics

In Granger Basin, prevailing winds from the north, which redistribute snow, coupled with an east-west valley orientation, create snowdrifts on north-facing slopes and high insolation on south-facing slopes (Pomeroy et al., 2003). The presence of a substantial snowdrift on the crest of the north-facing slope results in two distinct types of snowcover at the site – drift (on the upper 100 m of the slope) and non-drift (across the face of the slope).

SWE measurements effectively show the variation in snow depth along Transects A and F (Figure 5-3 and Figure 5-4, respectively). Transect A has a relatively deep area of snow accumulation near the bottom of the slope (right side of the plot), which persists after much of the SWE on the rest of the transect has ablated (as indicated by the SWE on DOY 141). In contrast, Transect F has a relatively thin accumulation area at the bottom of the slope. Overall though, the non-drift portion of the north-facing slope became snow-free earlier than the drift, as portions of the drift remained at the top of the slope well into the late spring.

5.4 Snowcover Depletion

As indicated in the previous chapter, the snow depth sensor at the hillslope meteorological station indicated completely snow-free conditions at the north-facing slope on DOY 128 (May 8). However, there remained a patchy snowcover over the majority of the slope, and a substantial snowdrift at the top of the slope for a much longer period. Parts of the snowdrift remained even until mid-June when the study period was completed.

Figure 5-5 shows air temperature, surface temperature and snow depth recorded at the hillslope meteorological station. The data indicate that snowmelt began on the north-facing slope on DOY 111 (April 21), with more than half of the snowcover ablating by DOY 121 (May 1). Two cold spells followed, in which average daily temperatures remained at or dropped below 0°C for a period of approximately 9 days (DOY 121-128) and 5 days (DOY 133-137), respectively. Consequently, the rate of snowmelt during those cold spells was not as significant.

Following the initiation of melt, the snow cover quickly became patchy with the snowcover declining from approximately 96% on DOY 112 to approximately 50% on DOY 120 (Figure 5-6). Figure 5-6 was constructed by estimating, through image analysis, the percentage of snowcover from a slope-corrected photographic time series. The north-facing slope was almost completely snow covered (96%) at the time of the first photograph on DOY 112 (April 22) and was entirely snow-free by DOY 159 (June 8) with the exception of a few patches of drift snow remaining (1% snow covered).

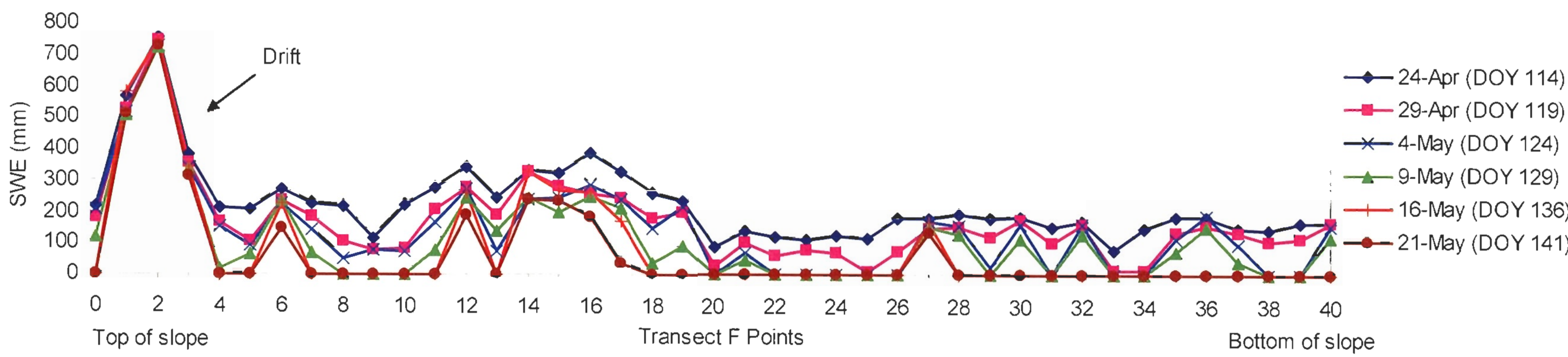

Figure 5-3: Snow water equivalent along Transect A from the top of the north-facing slope (left side of the graph) to the stream (right side of the graph). Transect points are spaced 5 m apart. The drift is the distinct area of much greater snow depth that occurs at the top of the slope. Along this transect, there is also a relatively deep area of snow accumulation near the bottom of the slope.

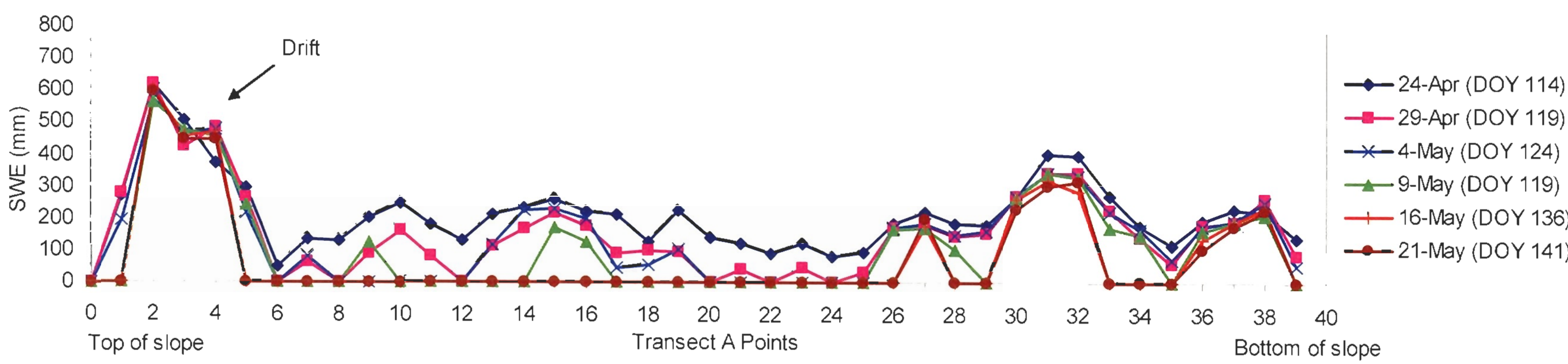

Figure 5-4: Snow water equivalent along Transect F from the top of the north-facing slope (left side of the graph) to the stream (right side of the graph). Transect points are spaced 5 m apart. The drift corresponds to the distinct area of much greater SWE.

5.5 Snowmelt Energy and Net Radiation

Because net radiation (Q*), is frequently the dominant flux in the energy exchange (Boike et al., 2003; Male and Granger, 1981; Gray et al., 1974), its association with melt energy (Q_m) was tested. Q* values were determined according to the methodology provided in Chapter 4. Melt energy values (in $W \cdot m^{-2}$) were calculated by converting the daily melt rate (i.e., loss of mean SWE in $mm \cdot d^{-1}$ from successive snow survey measurements) into an energy flux using Equation 3-5. As a preliminary comparison, mean daily Q_m and Q* values (in $W \cdot m^{-2}$) were compared for each of the drift and non-drift areas (Figure 5-7). No clear relationship was observed, likely due to the wide variability of the radiative or melt terms caused by daily changes in other components (such as latent or sensible heat) of the energy balance as well as atmospheric moisture and other conditions (Gray et al., 1974).

Total daily Q* was positive from DOY 116 onward, and previously (see Chapter 4), it was determined that DOY 121 was the last day on which Q* could be reasonably measured over a snow-surface. Consequently, the time over which Q* and Q_m could be compared was limited by Q*. Nevertheless, based on the limited time period (six days) a mean value for Q_m (for the drift and non-drift) and Q* was determined (Table 5-1).

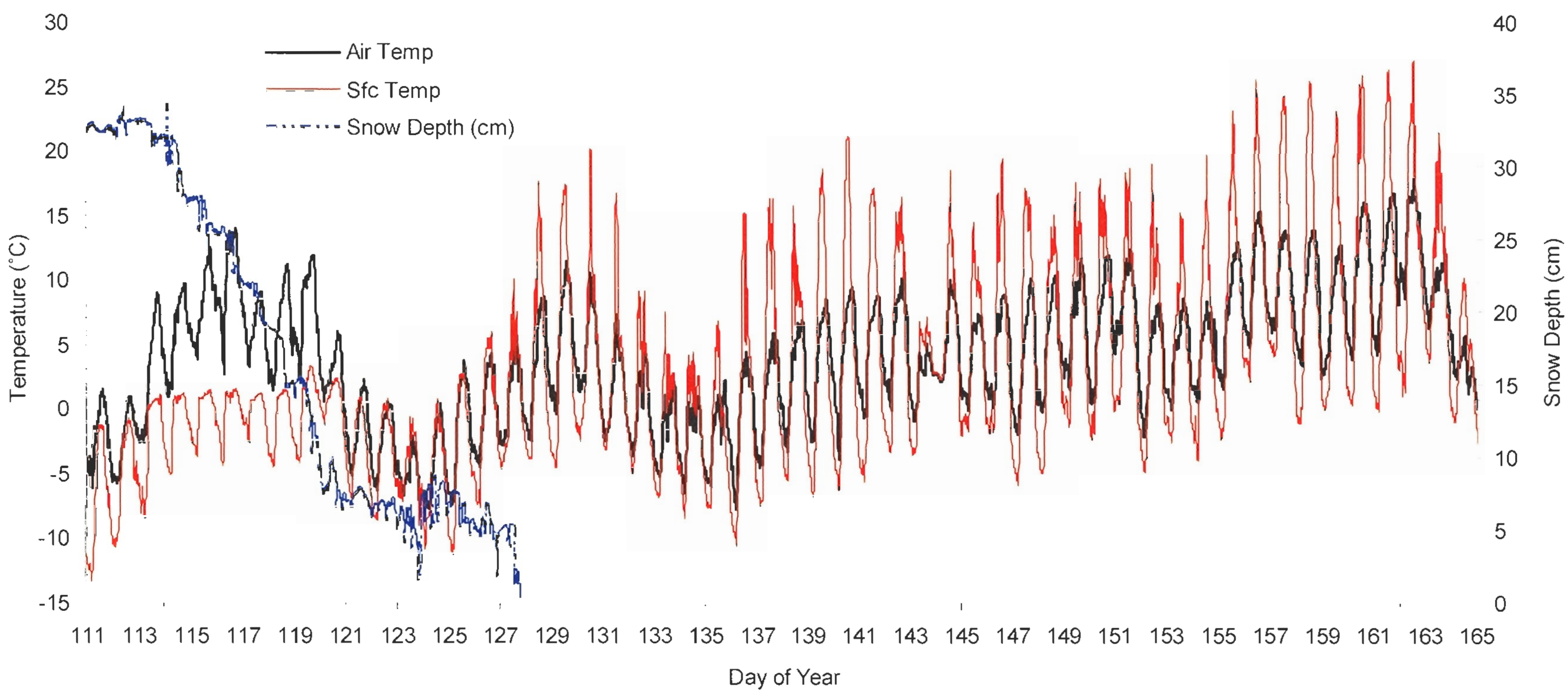

Figure 5-5: **Air temperature, surface temperature and snow depth at the north-facing slope meteorological tower for the monitoring period.**

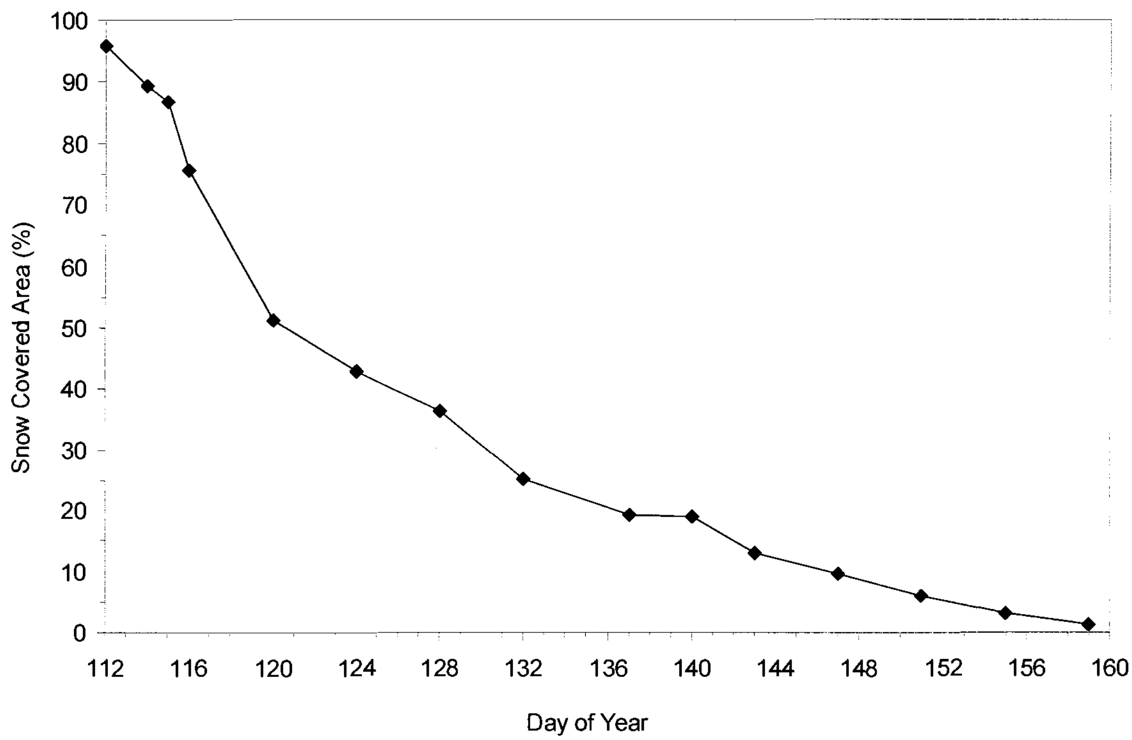

Figure 5-6: **Percent snowcover depletion curve for the entire north-facing slope (drift and non-drift) from slope corrected photographs and image analysis.**

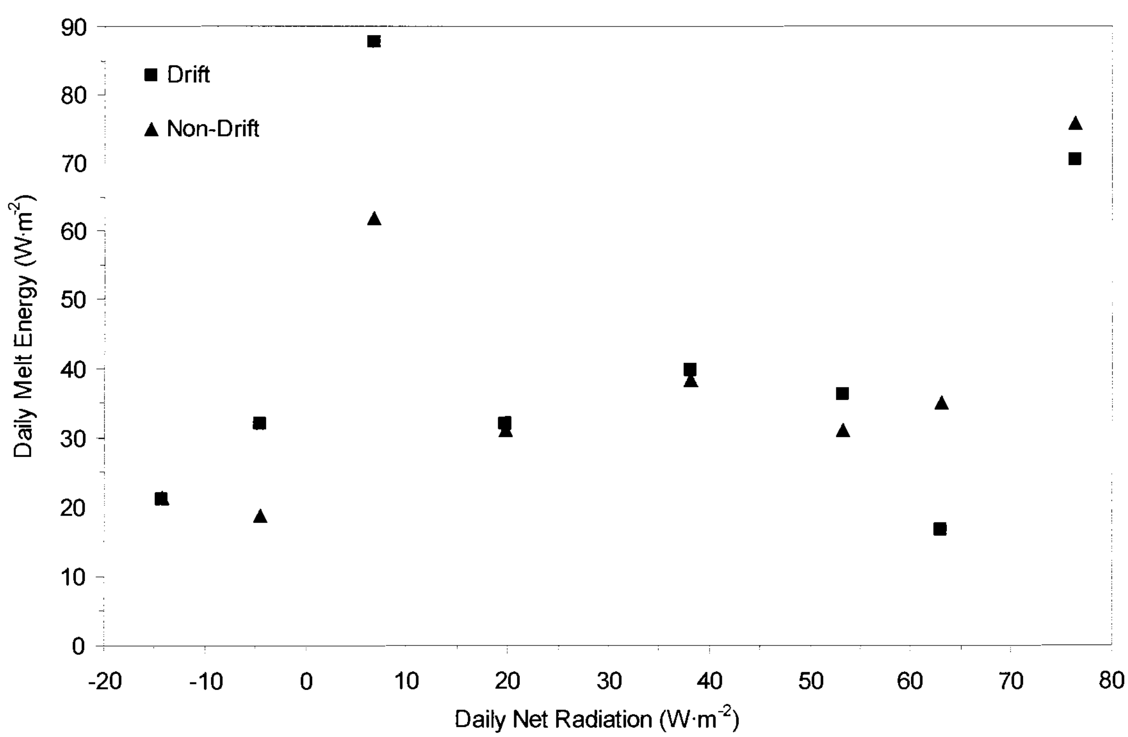

Figure 5-7: **Daily net radiation and daily melt energy for the drift and non-drift snowcovers from DOY 114-121 (April 24-May 1).**

Table 5-1: **Daily values of Q_m and Q* for the drift and non-drift portions of the north-facing slope. The mean and standard error is also computed.**

DRIFT		
DOY	Q_m ($MJ \cdot m^2 \cdot d^{-1}$)	Q* ($MJ \cdot m^2 \cdot d^{-1}$)
116	7.57	0.59
117	2.76	1.71
118	3.43	3.29
119	1.44	5.43
120	3.12	4.60
121	6.09	6.60
Mean	**4.07**	**3.70**
Standard Error	**0.94**	**0.93**
NON-DRIFT		
DOY	Q_m ($MJ \cdot m^2 \cdot d^{-1}$)	Q* ($MJ \cdot m^2 \cdot d^{-1}$)
116	5.36	0.59
117	2.68	1.71
118	3.30	3.29
119	3.03	5.43
120	2.69	4.60
121	6.55	6.60
Mean	**3.93**	**3.70**
Standard Error	**0.66**	**0.93**

Diez Monux (1991), as cited in Anderton et al. (2002), found that solar radiation tended to be the prevailing term in the energy balance of a melting snowpack, while the turbulent transfer of sensible heat played a secondary role. However, situations in which melt energy, Q_m exceeds Q*, indicate that in addition to Q*, there are other sources of energy for melt (e.g., the turbulent fluxes of sensible and latent heat). For example, Willis et al. (2002) presented a list of 17 studies conducted in continental alpine areas (over both snow and ice), in which they compared the contribution of various fluxes towards melt. They found, that on average, the net radiation flux contributes 77% to the melt energy. However, it is important to note that the contributions to melt from the net radiation flux for the various studies ranged widely: from 44% (Fohn, 1973 as cited in: Willis et al., 2002) to 100% (De la Casiniere, 1974 as cited in: Willis et al., 2002). In their own study of a supraglacial catchment, Willis et al. (2002) found that net shortwave radiation was the dominant energy component, and that over the whole measurement period, the radiation fluxes contributed 86% of the melt with the turbulent fluxes contributing the remaining 14%.

McKay and Thurtell (1978) determined that what controlled energy storage and the melt process at a site in Guelph, Ontario depended upon what they termed the "meteorological situation". Net radiation was the controlling component during periods when an air mass was well established over the region, while the sensible heat component became the dominant contributor to melt when warm air was advected into the region (McKay and Thurtell, 1978). Neumann and Marsh (1998) found that once the snowcover became patchy and discontinuous, sensible heat contributed approximately 54% of melt energy, while net radiation comprised 36% of melt energy and latent heat 10%. However, this partitioning was for one day (May 30) on an arctic tundra site and may not accurately reflect the average contribution of turbulent fluxes over a melt season.

For this study, it should be noted that, on average, Q^* contributes 91% and 94% to melt (Q_m), for the drift and non-drift areas, respectively. These values were based on a relatively short time period (six days) and that snow melt on the slope continued well into June. As a result, these percentages provide a relatively short "snapshot" of the amount of energy Q^* contributes to melt and, consequently, may not represent the actual contribution of Q^* to melt over the entire study period. Results from this study and those cited above suggest that the percentage of Q^* that contributes to melt energy is not static and that this value can change with time due to changing meteorological and surface conditions as well as change depending on the time period over which the fluxes are compared. For example, Figure 5-8 is a plot of mean daily Q* and mean daily Q_m for both the drift and non-drift snowcover. It is clear that from DOY 114 up to DOY 118, daily Q_m exceeds Q*. However, on DOY 118 and beyond, daily Q* exceeds daily Q_m. A possible explanation for this is that in early spring, there is low solar input and therefore the turbulent components can play a larger role in melt, whereas later in the spring and early summer, the net radiation flux tends to be the chief contributor to melt (Pomeroy, personal communication, September 12, 2005). However, as melt continues further into the spring and the snowcover becomes discontinuous, the turbulent fluxes can again assume greater importance due to local advection and sensible heat transfer from surrounding snow-free patches. Again, a longer period of comparison would have been ideal, and may have assisted in ascertaining a greater understanding of the contributions of the net radiation flux to melt over the study period.

This study site is also located in a shrub tundra environment. These shrubs begin to protrude from the snow surface as the snow melts. Pomeroy et al. (2003) suggested that the progressive exposure of shrubs during ablation exacerbated the effect of slope and aspect on surface energetics. Lundberg and Beringer (2005) state that the exposure of stems (with a much lower albedo than the surrounding snow), absorb more radiation, and thus increase melt around the stems. Recent studies (Bewley et al., submitted; Pomeroy et al., 2006; Lundberg and Beringer, 2005; Lee and Mahrt, 2004) have demonstrated the enhancement of melt rates in the presence of shrubs.

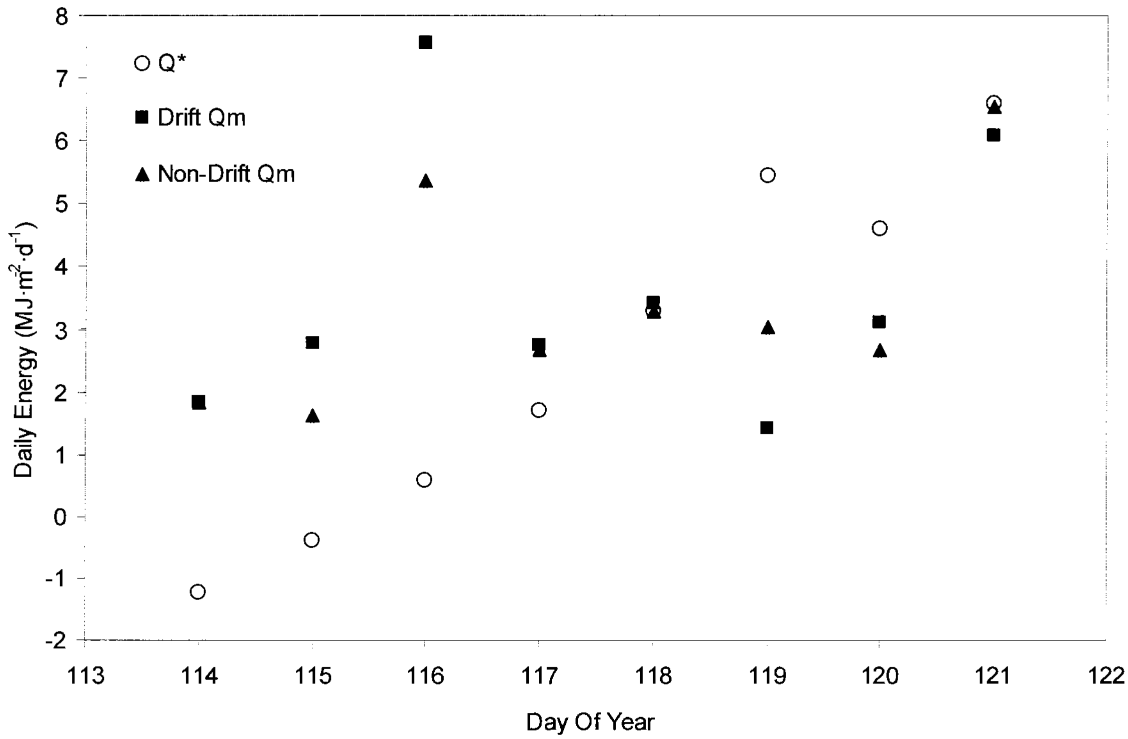

Figure 5-8: Daily values of net radiation, Q* and melt energy, Q_m for the drift and non-drift snowcovers.

Based on the studies cited above, the non-drift Q_m would be expected to be higher due to the presence of shrubs enhancing the melt rate. However, in this study, the mean Q_m for drift was 4.07 ± 0.94 $MJ \cdot m^{-2} \cdot d^{-1}$ and for the non-drift was 3.93 ± 0.66 $MJ \cdot m^{-2} \cdot d^{-1}$. Due to the relatively similar values of Q_m and the short time period available for comparison, it is therefore difficult in this study, to make a conclusive statement about the melt-enhancing effects of shrubs.

Q* was measured at one location on the north-facing slope, and this Q* was applied to snow-covered areas over the entire hillslope. However, once the meteorological tower became snow-free, there were no more measurements of Q* over the snow surface. This means that although there was a significant portion of the slope that was still snow covered and continued to ablate after this day (see percent snow covered area curve, Figure 5-6), Q_m values calculated after DOY 121 could not be related to Q* directly (after DOY 121, measurements of Q* were determined to be made over an increasingly snow-free surface, as discussed in Chapter 4).

Although it was only possible to compare Q* and Q_m for a short period of time, the measured melt rates were used to compute a mean daily areal melt for the entire north-facing slope for later into the melt period. To determine this, the daily mean melt rate (in $mm \cdot d^{-1}$) per unit area of snow for the entire slope was calculated using the daily mean of both drift and non-drift melt rates. Only those days for which both measured drift and non-drift measured values co-existed and were negative (i.e., melt) could be used. This value was then multiplied by the % snow-covered area of the slope (interpolated from the snow-covered area curve, Figure 5-6) to obtain the daily mean areal melt rate per unit area of snow for the entire slope in $mm \cdot d^{-1}$ (Table 5-2).

Table 5-2: Daily mean slope melt rate and mean areal melt rate.

DOY	*Daily Mean Slope Melt Rate (per unit area of snow) ($mm \cdot d^{-1}$)	Standard Error	Snow-Covered Area (%)	**Mean Areal Melt Rate (per unit area of snow) ($mm \cdot d^{-1}$)
116	20.20	3.45	77	15.66
117	8.49	0.13	74	6.26
118	10.53	0.20	70	7.36
119	6.98	2.48	66	4.62
120	9.07	0.67	63	5.69
121	19.75	0.71	59	11.72
126	2.45	0.12	44	1.07
129	19.12	5.10	36	6.83
131	17.62	4.80	31	5.44
141	1.97	1.95	13	0.25
Mean				**6.49**
Standard Deviation				**4.54**

*Mean slope melt rate was determined by taking the mean of the daily drift and non-drift melt rates
**Mean area melt rate was determined by multiplying the daily mean slope melt rate and the % snow-covered area

CHAPTER 6: SOIL THAW ENERGY

6.1 Introduction

At any point on the ground surface, local variations in the energy balance resulting from, for example, differences in terrain slope, aspect, soil properties, vegetation and incoming radiation can influence the rate of soil thaw (Pomeroy et al., 2003; Affleck and Shoop, 2001). Local variations in thaw depth can also be largely controlled by local variations in soil moisture and, therefore, thermal conductance (Quinton et al., 2004). Soil moisture itself is a function of the rate of thaw and the drainage of the soil. Thus, complex relationships exist between thaw depth and a number of variables. Leverington (1995) stated that very few areas have been thoroughly sampled with respect to frozen ground and that more datasets are required in order to ascertain the utility of correlative methods for thaw depth prediction. Leverington (1995) also suggested that correlations between surface characteristics, such as topography, vegetation and aspect, and depth to frozen ground cannot be assumed to be constant across different areas, even with relatively similar climatic conditions.

This chapter examines the spatial and temporal patterns of soil thaw during the snowmelt season at the study site, and attempts to relate these to soil moisture measurements. The chapter also examines the partitioning of Q_g into its three main components (Q_i, Q_s and Q_p), and determines the mean percentage of Q^* that is used for soil thaw (Q_i).

6.2 Spatial Variability of Soil Thaw Within A Patch

Many studies on active layer development (Turcotte, 2002; Gomersall and Hinkel, 2001; Carey and Woo, 1998; Woo and Xia, 1996; Leverington, 1995; Romanovsky and Osterkamp, 1995) indicate that differences in thaw depth can vary considerably even between sites that are relatively similar in terms of their general climatic conditions. Results from this study also support that observation, as thaw depth was found to be highly variable even within a single patch (Figure 6-1). The "noisy" nature of the graphs results from the small-scale spatial variability of soil thaw. Some of the individual measurement points show a decrease in thaw depth at certain times or an increase in thaw depth with time which then "levels off". This is likely due to many of the patches having a relatively thin organic layer (~0.05-0.15 m) and being underlain by rocky material and/or roots, which would sometimes impede the rebar and, therefore, may have resulted in erroneous recordings of depth to the frost table. Also, due to cold air temperatures in the beginning of May (Figure 5-5), most of the patches re-froze and, as a result, thaw depths measured during this time were almost always less than when they had first been measured (e.g., Patch 3 (T1) in which thaw depths on DOY 126/May 6 are less than those measured on DOY 117/April 27).

For most of the patches, however, thaw depth increased dramatically after the frost table had descended past the organic layer (Figure 6-1); in most of the patches the organic layer was relatively thin (ranging from 5-20 cm – see Table 3-1). Possible explanations for this rapid increase in thaw depth are differences in the thermal properties of the soils, ice content and energy supply. Mineral sediment, with its large proportion of gravel, pebbles and cobbles, has a higher thermal conductivity than the organic soil (Leverington, 1995). Thus, less energy is required to thaw the mineral sediment than the organic soil. The low porosity of the mineral soil will similarly result in there being less ice in these layers and, consequently, less energy is required for thaw. Finally, the increase in net radiation received at the surface later in the thaw period (due to longer daytime hours) would mean that more energy is available to thaw the soil. Thus, in terms of energy fluxes, even though the contribution of Q_i to Q_g decreases with time (discussed later), the increase in Q^* will concurrently increase the magnitude of Q_i (in terms of actual amount of energy, not as a percentage of Q^*).

It was expected that measurement points in the centre of each transect (i.e., those that have been snow-free for the longest time) would have greater thaw depths than those points that have most recently become snow-free. However, data presented in Figure 6-1 suggest that this was not always the case. In particular, Patch 5 (T1) and Patch 5 (T2) both exhibit preferential thaw on one side of their respective transects. In Patch 5 (T1), preferential thaw occurred on the downslope edge, whereas in Patch 5 (T2), preferential thaw occurred on the upslope edge. Again, there are a number of possible explanations for this, the most likely of which is the variability in SWE above the patch, resulting from the variability in the spatial distribution of SWE on the hillslope. As well, latent heat transfer from melting snow, microtopography, differences in soil characteristics that may facilitate heat transfer, and local variations in vegetation could also result in preferential thaw.

Figure 6-1: Individual thaw depth points within a patch through time. Measurements were made at 50 cm intervals and new points were added as upslope and downslope points along the transect line became snow-free. The first point in each transect starts at distance = 0. The first DOY series signifies the initial transect length. Negative distance values indicate points that were added upslope of the original transect's starting point.

See following pages

a) Patch 1 - Upper Slope

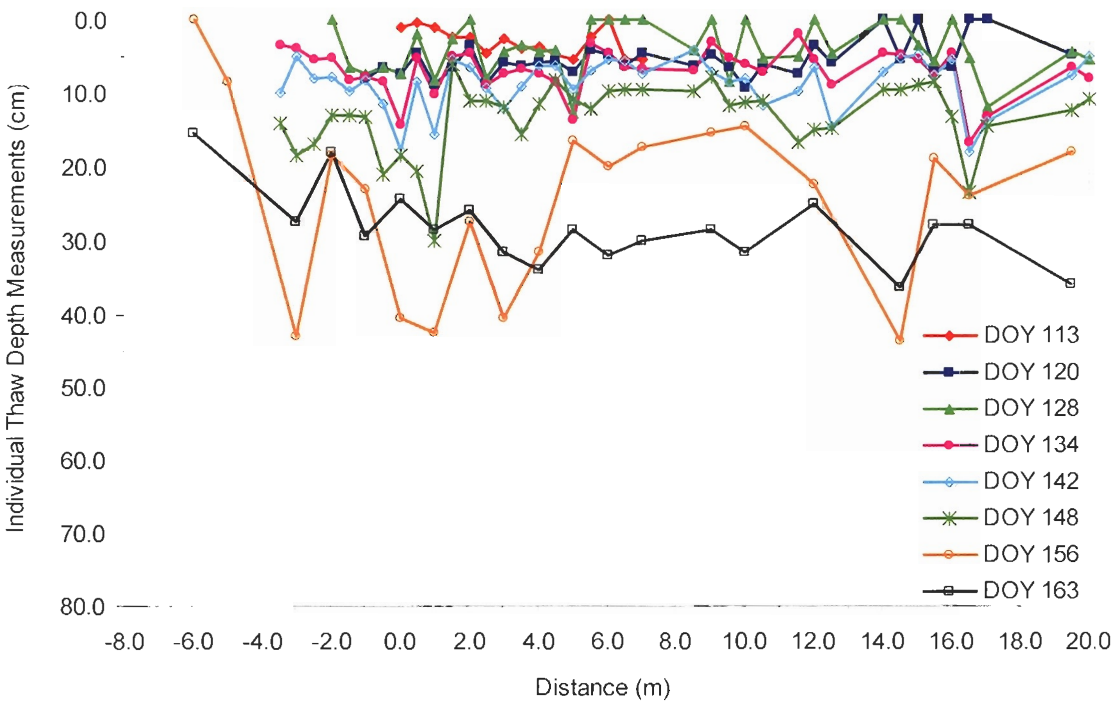

b) Patch 2 - Mid-Slope

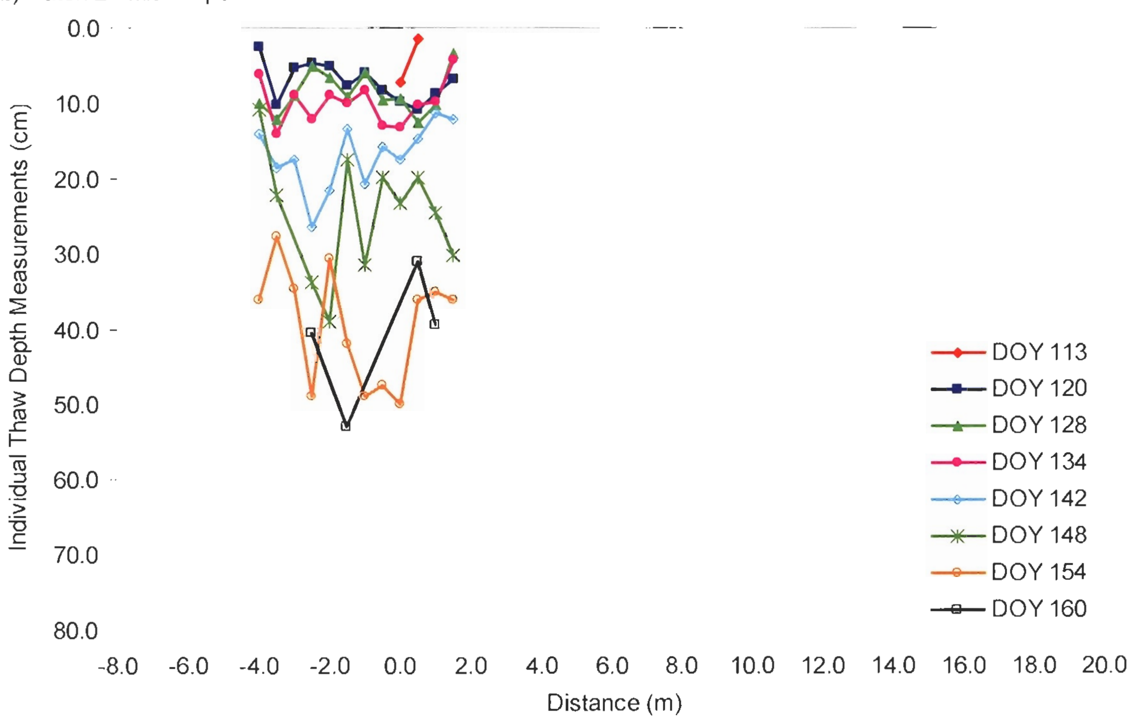

c) Patch 3 (T1) - Upper Slope

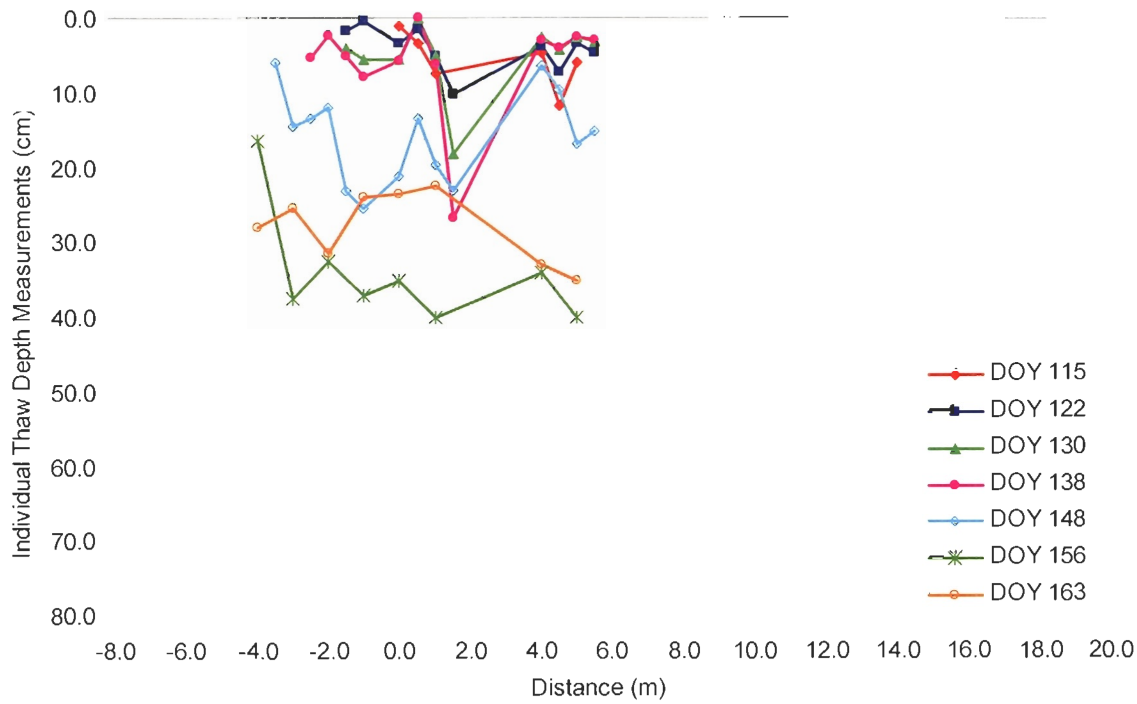

d) Patch 3 (T3) - Upper Slope

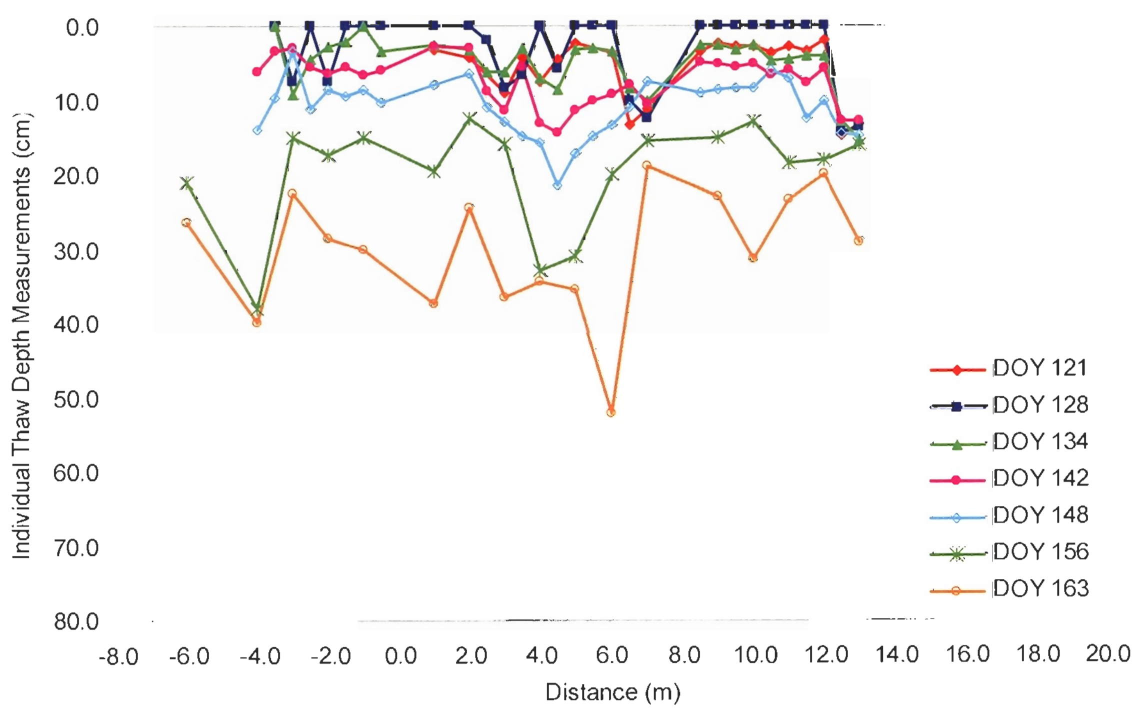

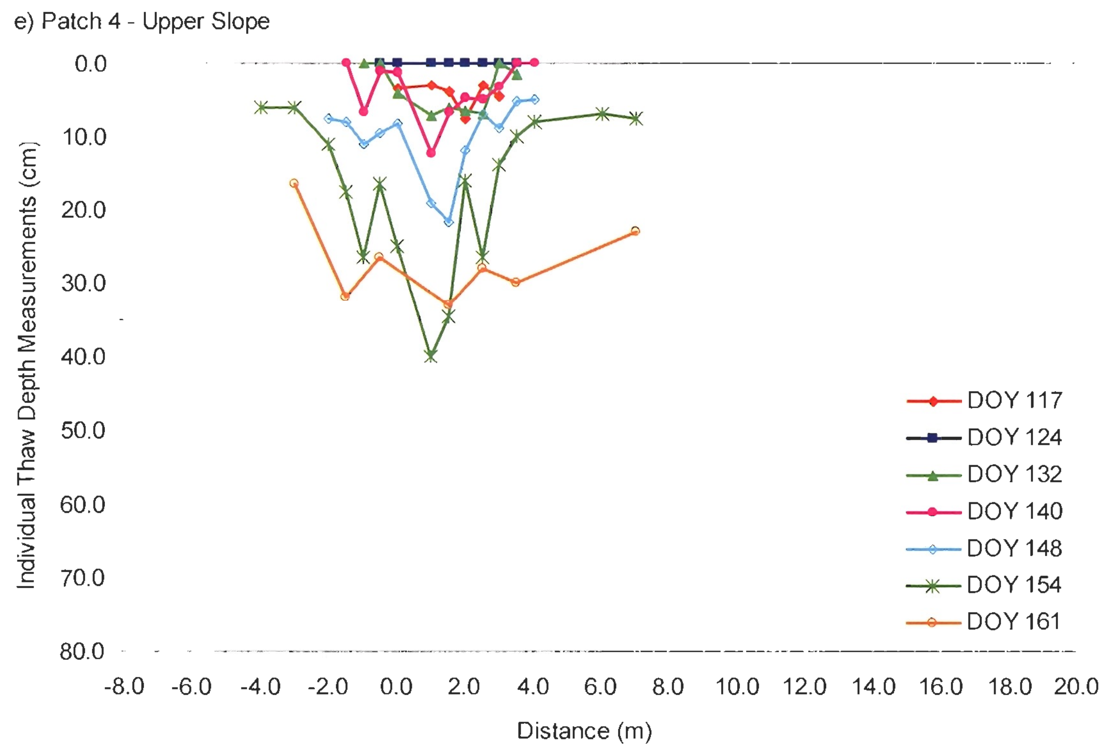
e) Patch 4 - Upper Slope
Individual Thaw Depth Measurements (cm)
0.0
10.0
20.0
30.0
40.0
50.0
60.0
70.0
80.0
-8.0 -6.0 -4.0 -2.0 0.0 2.0 4.0 6.0 8.0 10.0 12.0 14.0 16.0 18.0 20.0
Distance (m)
DOY 117
DOY 124
DOY 132
DOY 140
DOY 148
DOY 154
DOY 161

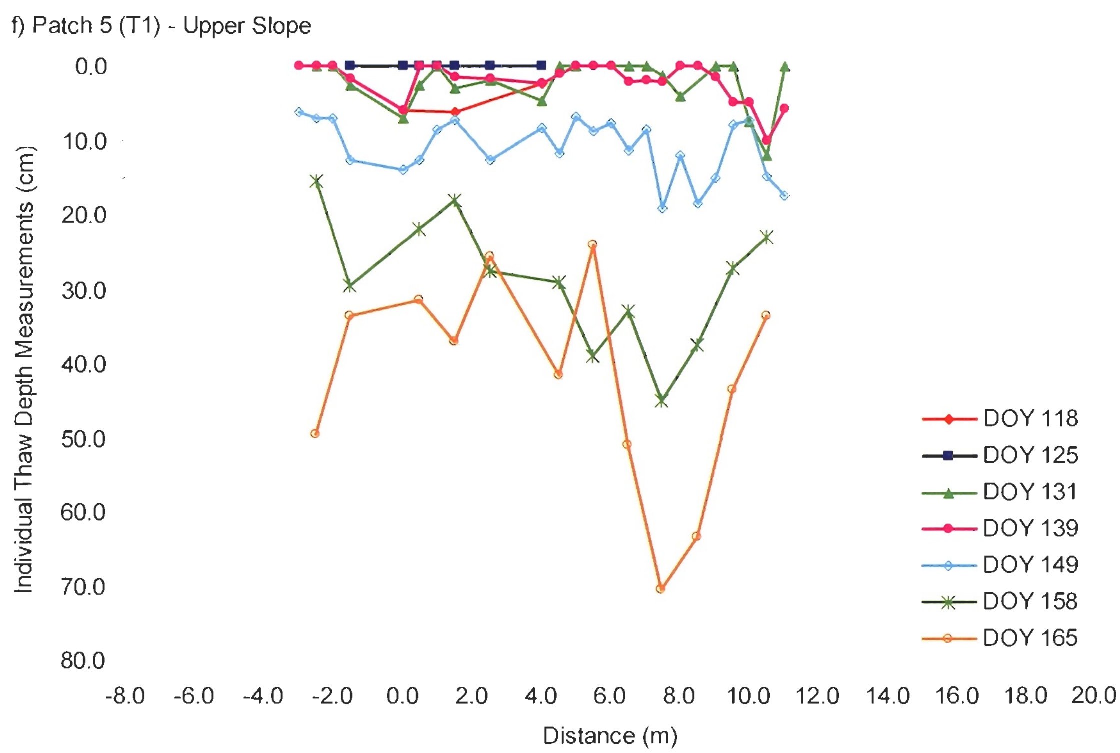
f) Patch 5 (T1) - Upper Slope
Individual Thaw Depth Measurements (cm)
0.0
10.0
20.0
30.0
40.0
50.0
60.0
70.0
80.0
-8.0 -6.0 -4.0 -2.0 0.0 2.0 4.0 6.0 8.0 10.0 12.0 14.0 16.0 18.0 20.0
Distance (m)
DOY 118
DOY 125
DOY 131
DOY 139
DOY 149
DOY 158
DOY 165

g) Patch 5 (T2) - Mid-Slope

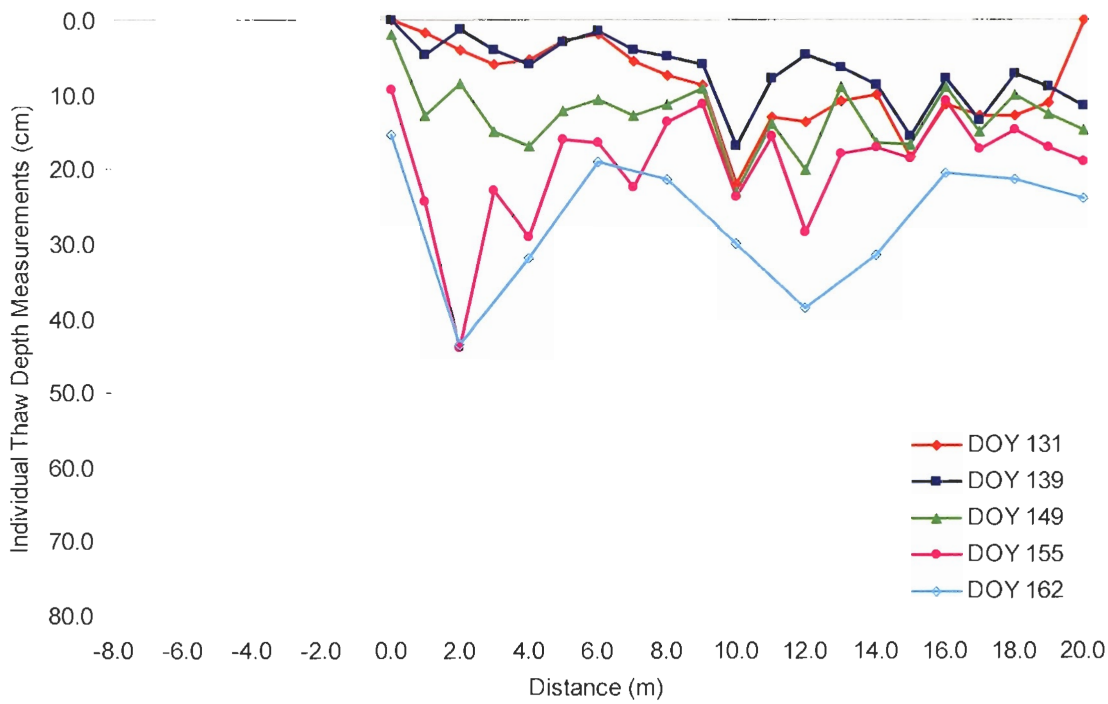

h) Patch 6 - Upper Slope

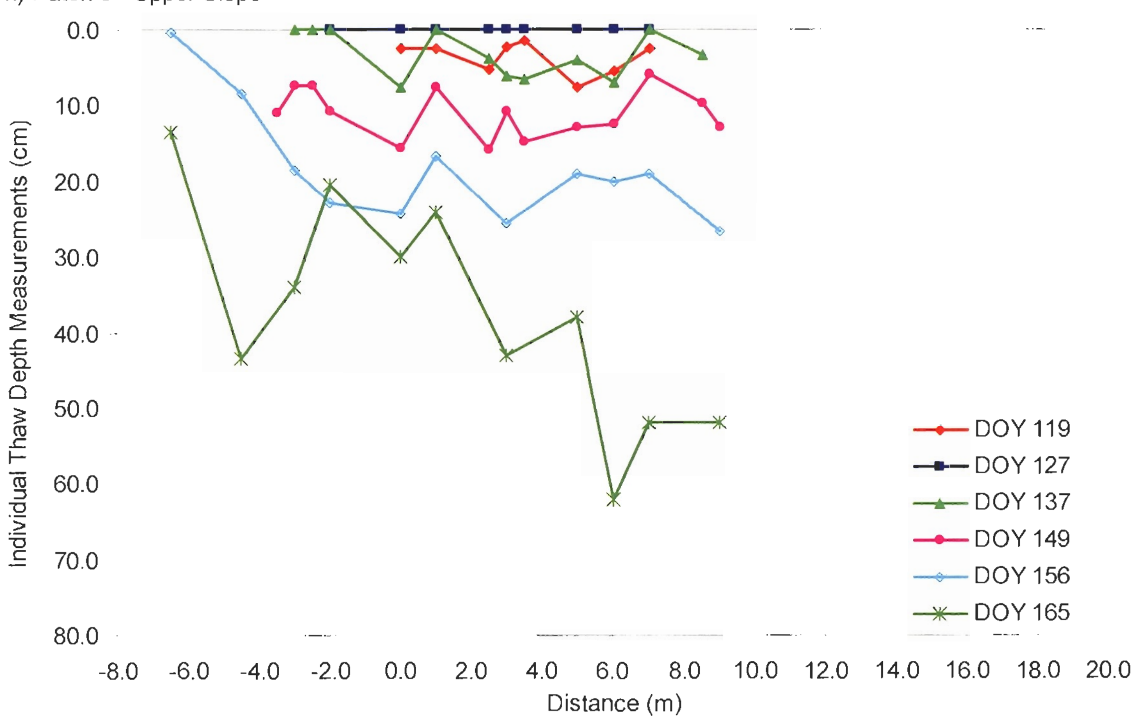

i) Patch 7 - Upper Slope

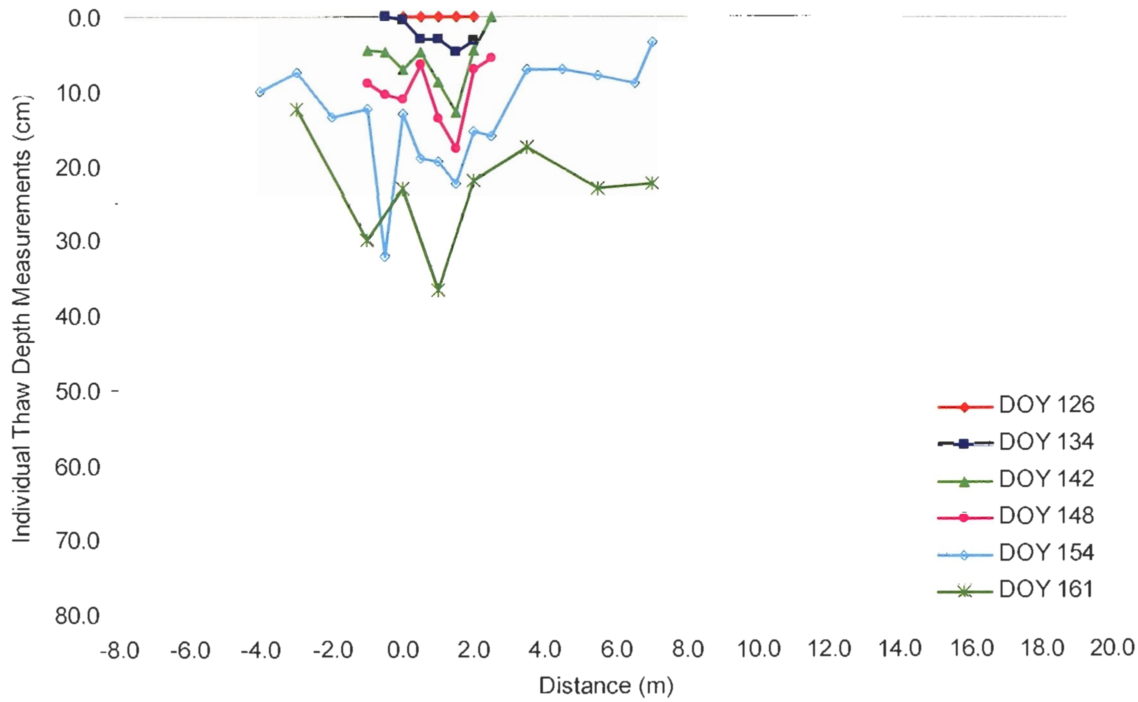

j) Patch 8 - Upper Slope

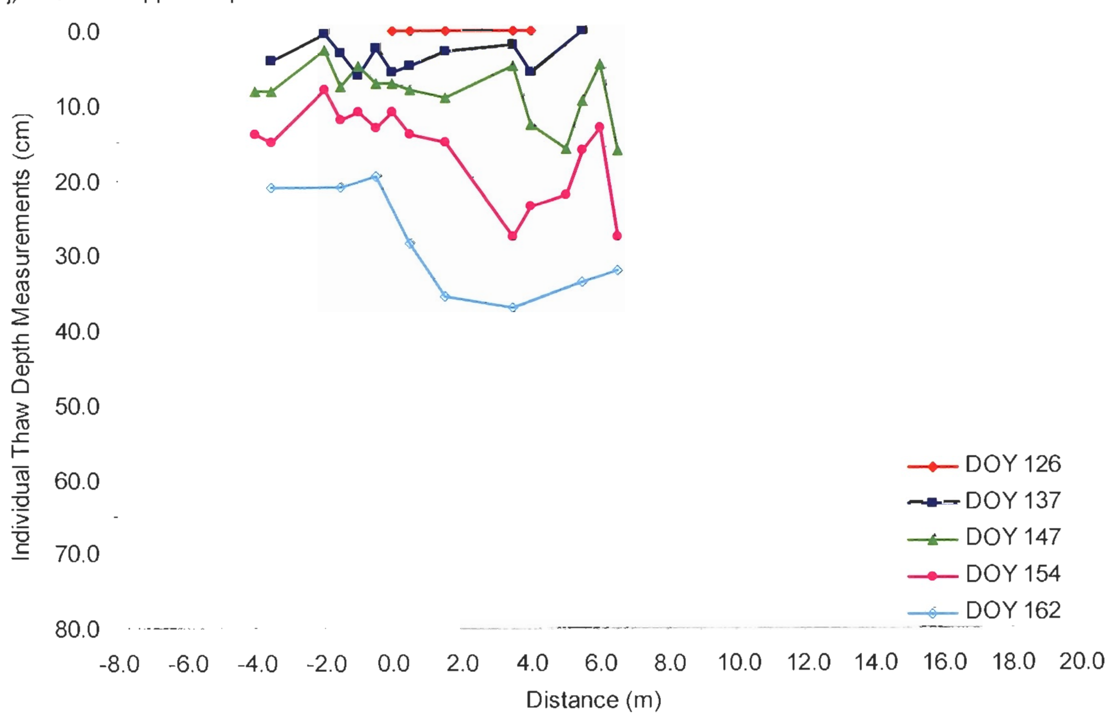

k) Patch 9 - Lower Slope

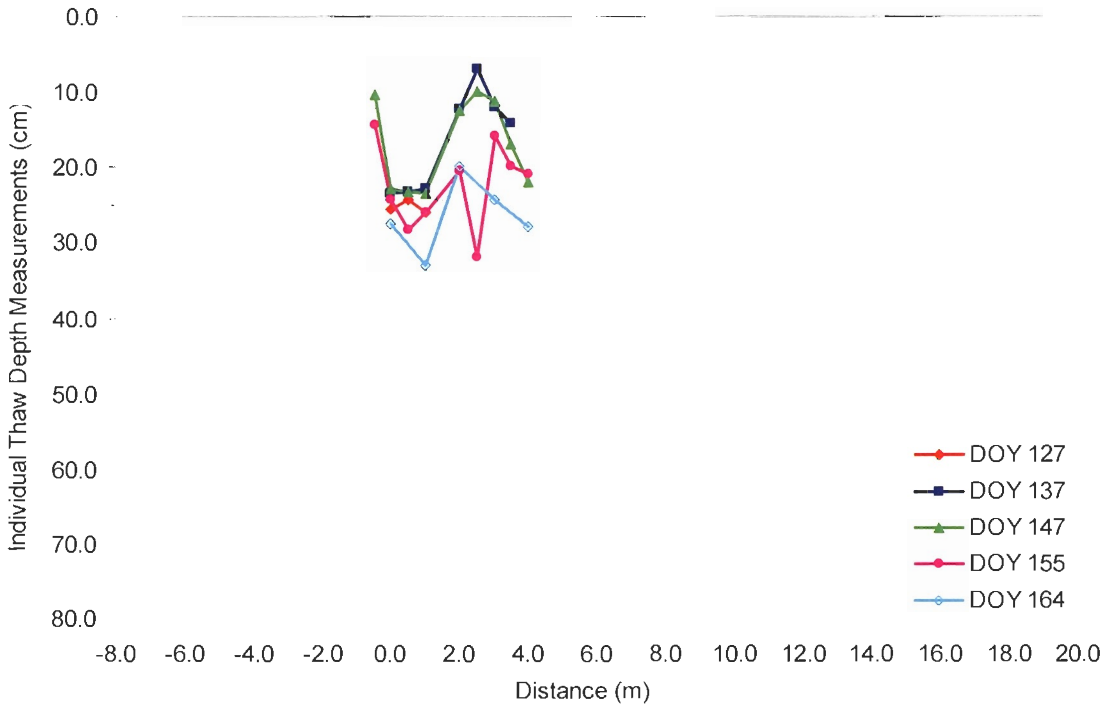

To characterize the spatial variability of thawing soil, two histograms were constructed for each patch over three one-day periods. One histogram shows soil thaw depth and the other, the logarithm of soil thaw depth (Figure 6-2). The bin size for the non-logged histograms was 2 cm (i.e. 0-2 cm, 2-4 cm, etc.) and the bin size for the logged histograms was 0.2 cm. Data for all patches combined are shown in Figure 6-3. The three periods roughly correspond to "early thaw" (corresponding to the beginning of the monitoring period at the end of April), "mid-thaw" (mid-May) and "late-thaw" (late May or early June). Because the study period ended in mid-June, the terms "early", "mid" and "late-thaw" refer to thaw during the snowmelt period, and not the final depths of the thawed layer. The histograms were constructed using points that were measured on the first day of monitoring, so that they would have the most continuous record of thaw. If there were too few points on the first day of measurement, then the next date that had more points was used. Histograms were also constructed using the same set of points, instead of incorporating new points as they became snow-free. Since the transect lengths varied, the number of points ranges from 4 to 30. In order to standardize the histograms, relative frequency (%) was used for the y-axis. Mean (average) thaw depth, standard deviation (std dev) and coefficient of variation (CV) were calculated for each histogram. The CV represents the dispersion in the dataset, and is the ratio of the standard deviation to the mean. A CV of greater than one indicates high variability in the data set (Affleck and Shoop, 2001).

Although there is no clear pattern for all patches, generally CV's tended to be quite low and decrease with the increasing mean depth of thaw (as does the standard deviation). Affleck and Shoop (2001) found similar results for the nine thaw depth data sets they analyzed. Log histograms appear to be more normally distributed compared to the standard histograms. All patches, with the exception of Patch 9 approximated a normal distribution at the beginning of the thaw period. For the non-logged plots, near the end of the thaw period, almost all patches displayed a flatter distribution with a larger range of thaw depths (reflected by the larger standard deviation). This is expected, because during the beginning of the snowmelt period, points will have just become snow-free and, therefore, thaw depths will be zero or very small. As thaw progresses, thaw depths will increase and there will be a greater range of thaw depths due to differences in soil properties, vegetation/terrain influences, etc. Patch 9 probably did not conform to this pattern because thaw depth monitoring at this site was initiated at least 7-8 days after the site had become snow-free (partly due to the problem of locating a lower slope snow-free area that was still surrounded by snow). This is why the initial thaw depth measurements along this transect were ~ 0.25 m. This patch had therefore already "thawed out" before it had begun to be monitored. In addition, the histogram for this site was constructed using only 7 points, so the small number of measurement points may not have provided an accurate representation of the thaw depth distribution at that patch. The same general pattern is observed for all patches combined (Figure 6-3).

Figure 6-2: Histograms of thaw depth and the log of thaw depth for each patch and for 3 different days that approximately corresponded to early thaw, mid thaw and late thaw during the study period.

See following pages

a) Patch 1 - Upper Slope

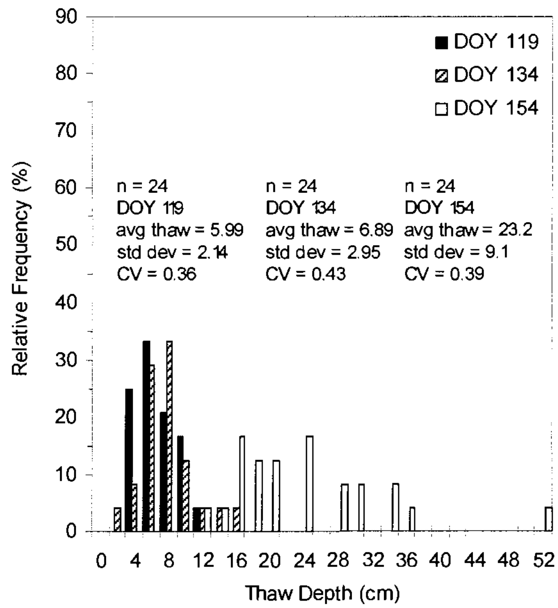

a) Patch 1 - Upper Slope

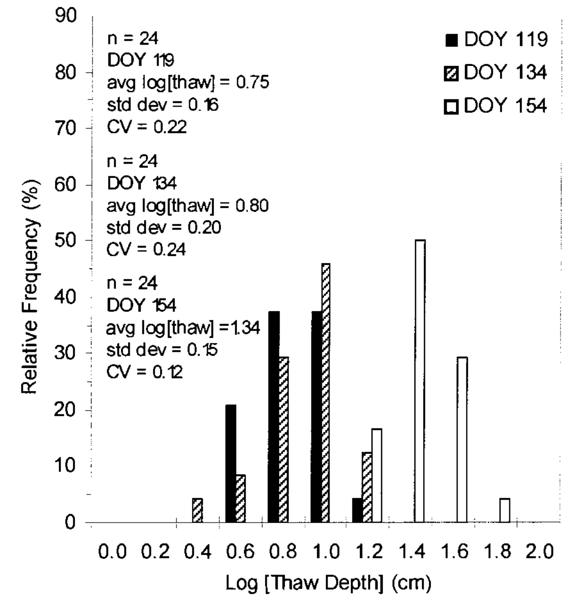

b) Patch 2 - Mid-Slope

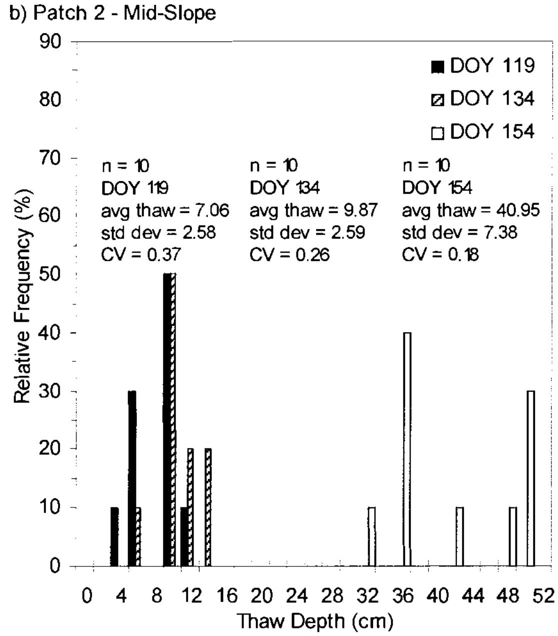

b) Patch 2 - Mid-Slope

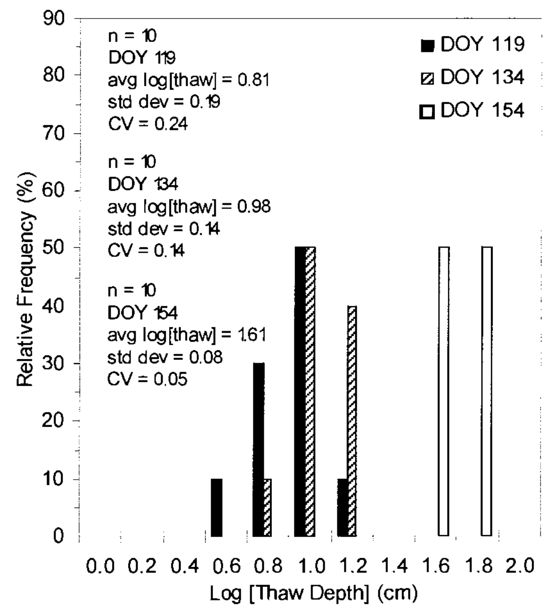

c) Patch 3 - Upper Slope

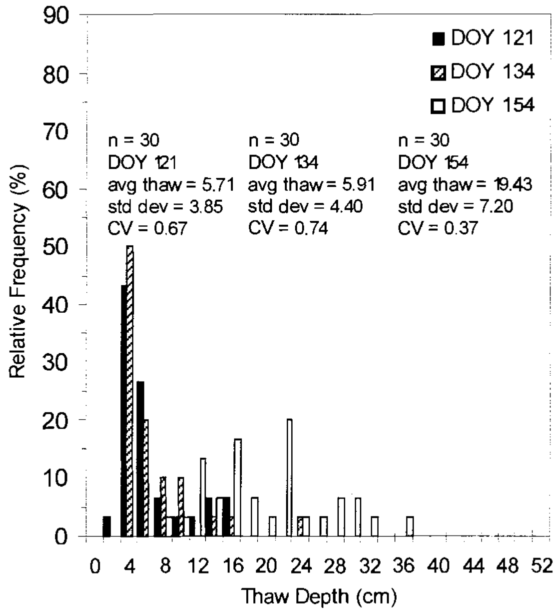

c) Patch 3 - Upper Slope

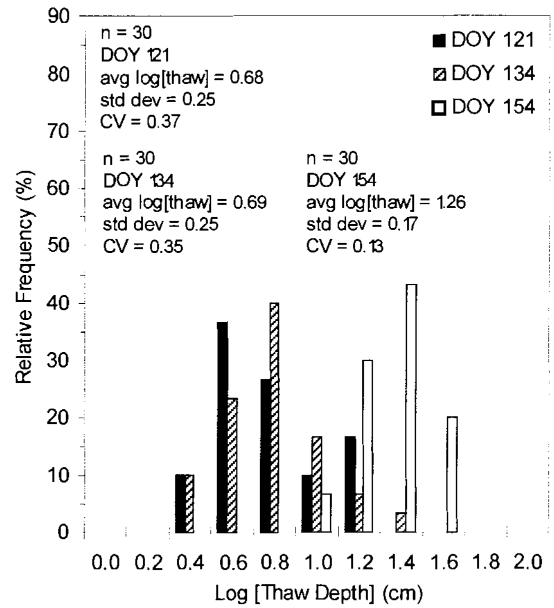

d) Patch 4 - Upper Slope

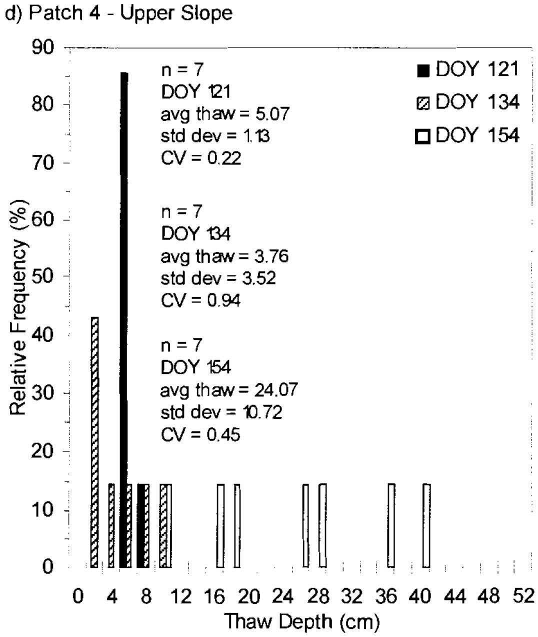

d) Patch 4 - Upper Slope

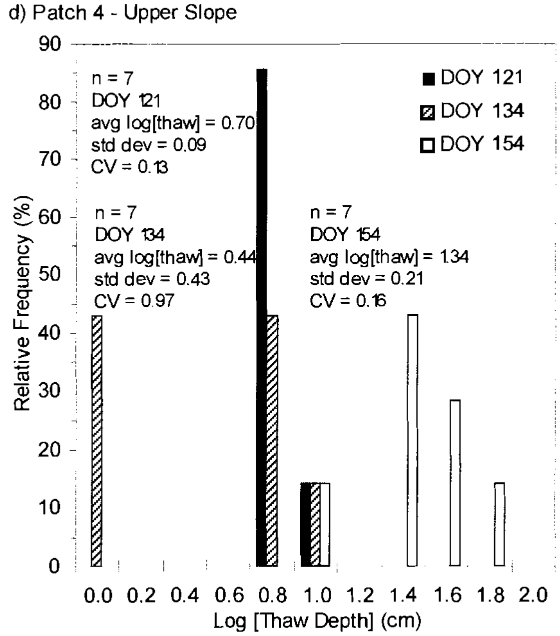

e) Patch 5 - Upper Slope

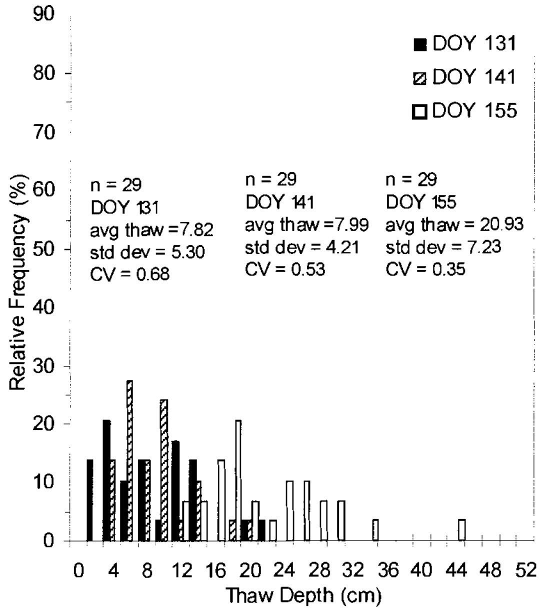

e) Patch 5 - Upper Slope

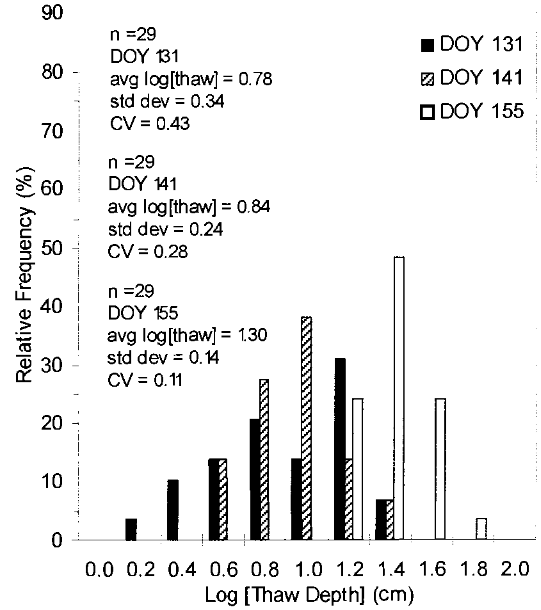

f) Patch 6 - Upper Slope

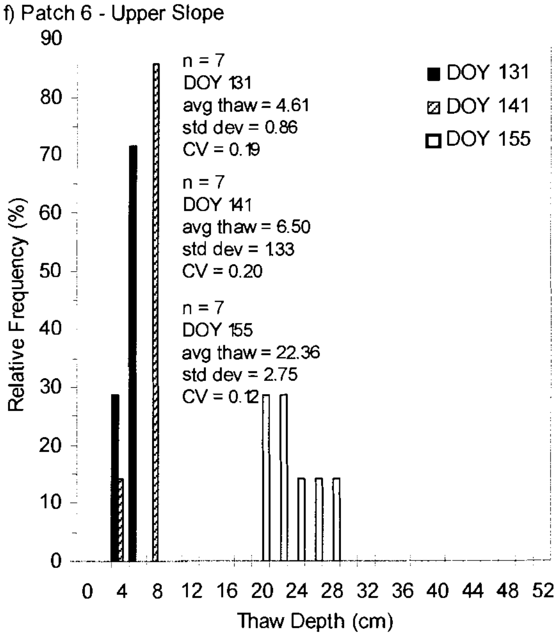

f) Patch 6 - Upper Slope

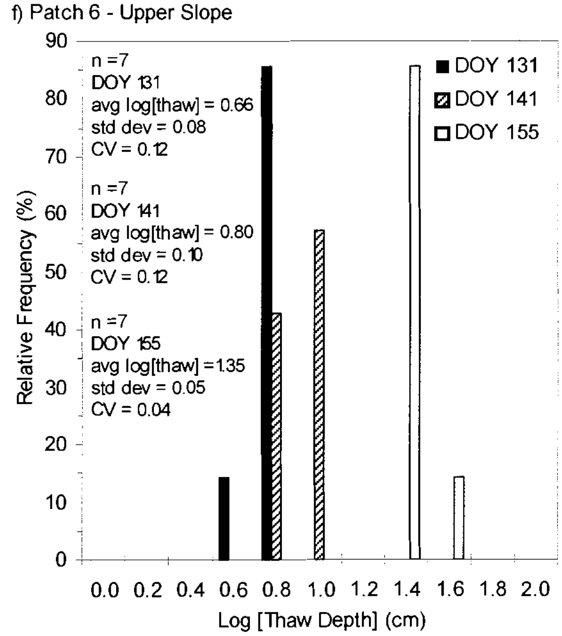

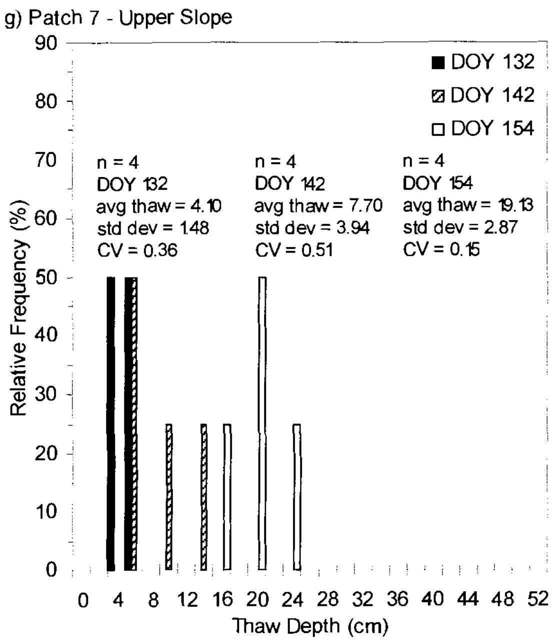
g) Patch 7 - Upper Slope
DOY 132
DOY 142
DOY 154
n = 4
DOY 132
avg thaw = 4.10
std dev = 1.48
CV = 0.36
n = 4
DOY 142
avg thaw = 7.70
std dev = 3.94
CV = 0.51
n = 4
DOY 154
avg thaw = 19.13
std dev = 2.87
CV = 0.15
Relative Frequency (%)
Thaw Depth (cm)

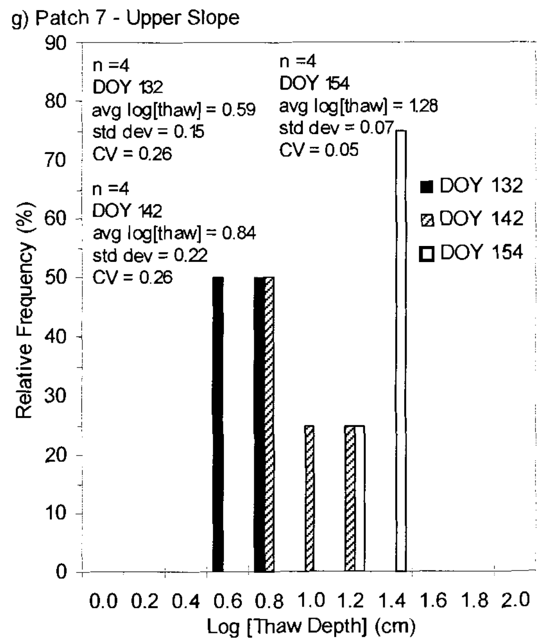
g) Patch 7 - Upper Slope
n =4
DOY 132
avg log[thaw] = 0.59
std dev = 0.15
CV = 0.26
n =4
DOY 154
avg log[thaw] = 1.28
std dev = 0.07
CV = 0.05
n =4
DOY 142
avg log[thaw] = 0.84
std dev = 0.22
CV = 0.26
DOY 132
DOY 142
DOY 154
Relative Frequency (%)
Log [Thaw Depth] (cm)

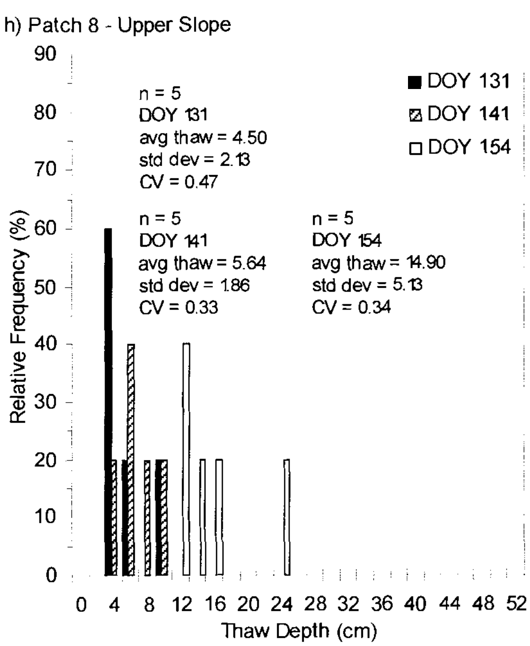
h) Patch 8 - Upper Slope
n = 5
DOY 131
avg thaw = 4.50
std dev = 2.13
CV = 0.47
DOY 131
DOY 141
DOY 154
n = 5
DOY 141
avg thaw = 5.64
std dev = 1.86
CV = 0.33
n = 5
DOY 154
avg thaw = 14.90
std dev = 5.13
CV = 0.34
Relative Frequency (%)
Thaw Depth (cm)

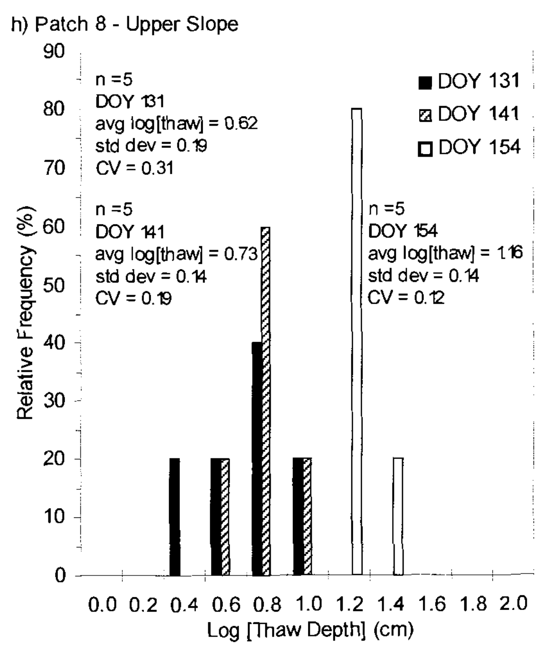
h) Patch 8 - Upper Slope
n =5
DOY 131
avg log[thaw] = 0.62
std dev = 0.19
CV = 0.31
DOY 131
DOY 141
DOY 154
n =5
DOY 141
avg log[thaw] = 0.73
std dev = 0.14
CV = 0.19
n =5
DOY 154
avg log[thaw] = 1.16
std dev = 0.14
CV = 0.12
Relative Frequency (%)
Log [Thaw Depth] (cm)

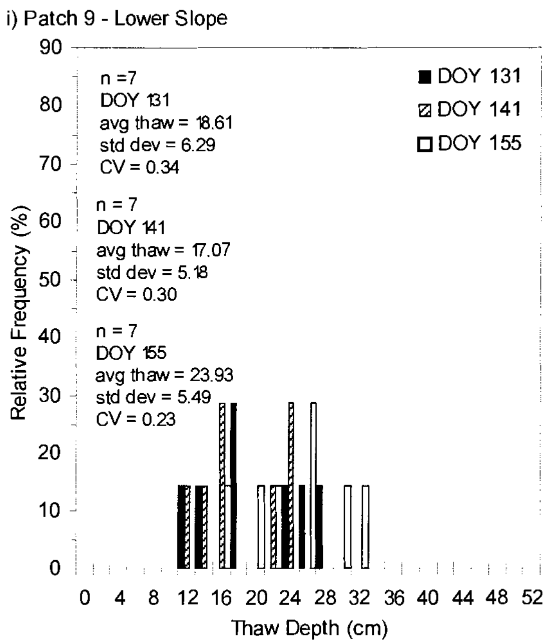
i) Patch 9 - Lower Slope
n =7
DOY 131
avg thaw = 18.61
std dev = 6.29
CV = 0.34
n = 7
DOY 141
avg thaw = 17.07
std dev = 5.18
CV = 0.30
n = 7
DOY 155
avg thaw = 23.93
std dev = 5.49
CV = 0.23
DOY 131
DOY 141
DOY 155
Relative Frequency (%)
Thaw Depth (cm)
0 4 8 12 16 20 24 28 32 36 40 44 48 52
0 10 20 30 40 50 60 70 80 90

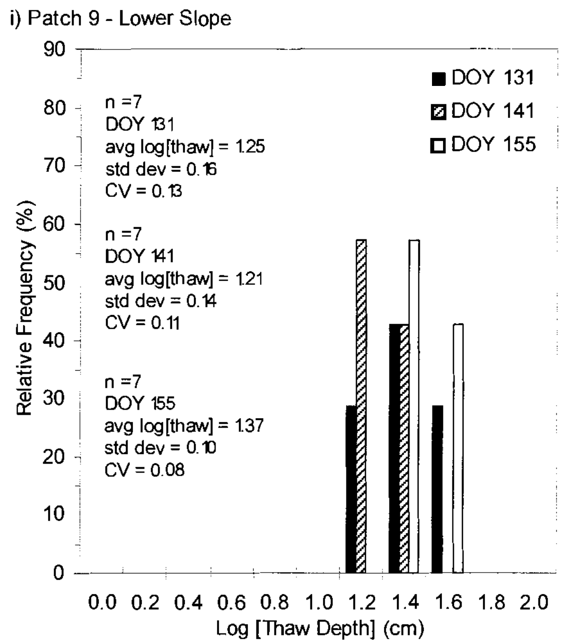
i) Patch 9 - Lower Slope
n =7
DOY 131
avg log[thaw] = 1.25
std dev = 0.16
CV = 0.13
n =7
DOY 141
avg log[thaw] = 1.21
std dev = 0.14
CV = 0.11
n =7
DOY 155
avg log[thaw] = 1.37
std dev = 0.10
CV = 0.08
DOY 131
DOY 141
DOY 155
Relative Frequency (%)
Log [Thaw Depth] (cm)
0.0 0.2 0.4 0.6 0.8 1.0 1.2 1.4 1.6 1.8 2.0
0 10 20 30 40 50 60 70 80 90

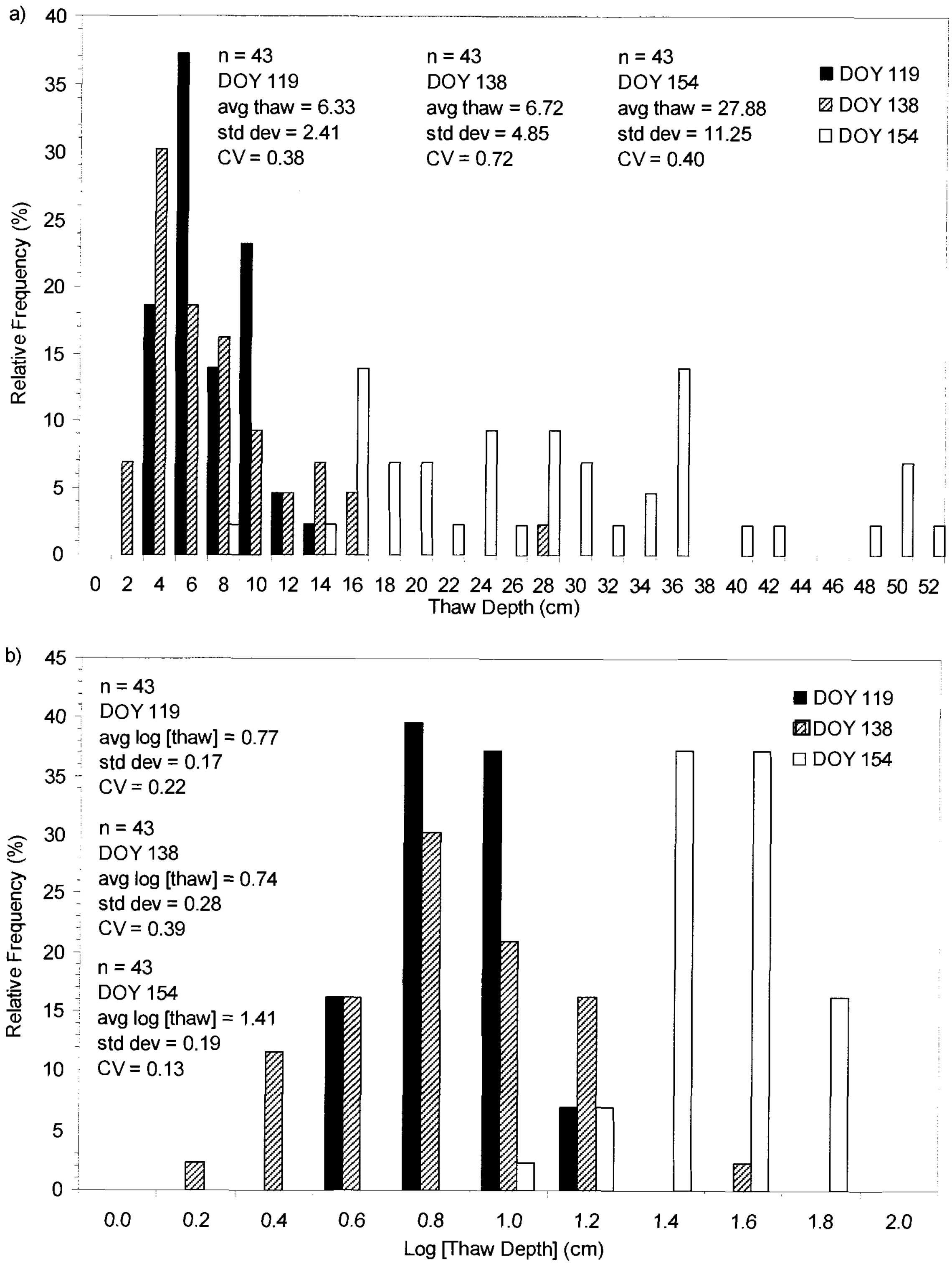

Figure 6-3: a) Histogram of all thaw depth points on the slope that were measured starting on DOY 119 and b) Histogram of the log of thaw depth of the same points.

6.3 Temporal Variability of Soil Thaw Within A Patch

Figure 6-4 is a schematic of the north-facing slope; it shows the relative location of the patches, the meteorological tower, the soil pit and the snow survey transects for reference and comparison. Figure 6-5 illustrates the changes in thaw depth with time for a single point in each transect. Time is measured from the day the first thaw depth measurement (i.e., depth to the frost table) was made in the patch (i.e., when it became snow-free or when it first began to be monitored). Each line represents a time series of thaw depth for one point in the transect. Because there were a number of points along a transect (on any given day), the point with the smallest amount of "initial" thaw depth was chosen for plotting. Thus, each colour series begins at a progressively later day. The variation in start dates for each graph and for each point reflects the wide variability of date of snow-free conditions (and hence, commencement of thaw), across the slope. The thaw depth, interpolated from the position of the 0°C isotherm at the soil pit (Goeller, 2005), is also shown for comparison.

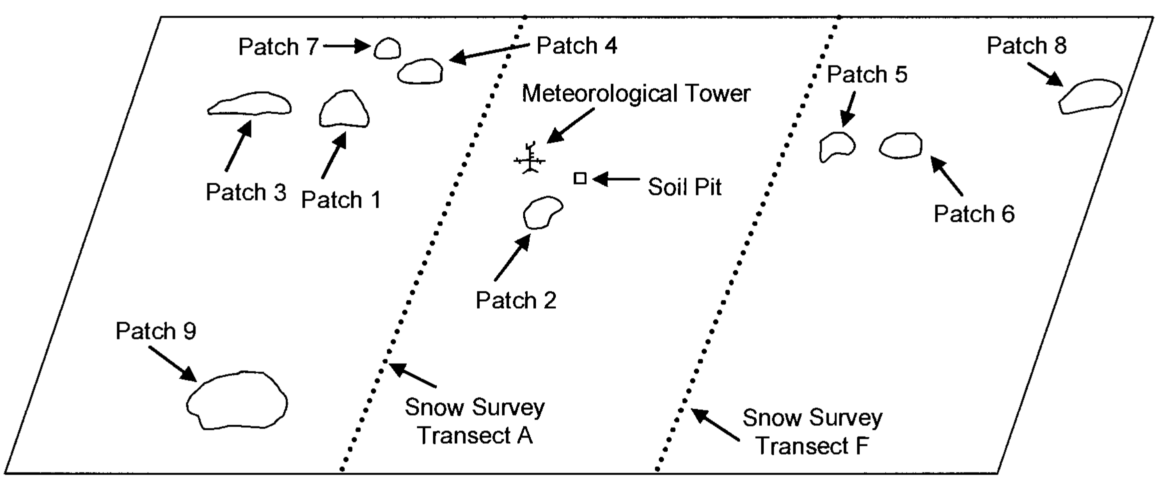

Figure 6-4: **Schematic of the north-facing slope and relative location of patches, meteorological tower, soil pit and snow survey transects for reference and comparison. Transects were set-up in approximately the centre of each patch. Two transects were set up in Patch 3 (T1 and T3) and Patch 5 (T1 and T2). Note that schematic is not to scale.**

In all of the patches, thaw progressed relatively slowly at the beginning of the melt period as evidenced by the flat appearance of most lines on the graphs (up to about day 20-25 from the time the first thaw depth measurements were made). The relatively cold periods, during which average daily air temperatures (Figure 5-5) remained at or dropped below 0°C (approximately from DOY 121-128 and DOY 133-137), are also reflected in the graphs: the thaw depths during that time are at or remain near zero. This was typically followed by rapid descent of the frost table once most of the snowcover had been removed and daily air and surface temperatures began to increase and generally remained above freezing (i.e., after DOY 137).

In general, the thaw depths calculated from the position of the 0°C isotherm (see Section 3.2.5) at the soil pit seem to correspond reasonably with thaw depths in the patches (i.e., falling within the same range of thaw depths over the relatively same period of time). However, one notable difference is that the thaw depths calculated from the position of the 0°C isotherm at the soil pit suggest that the frost table depth declined rapidly and then slackened. In particular, after DOY 151, the slope of the soil pit's thaw depth with time changes quite abruptly, as thaw slows down considerably compared to changes in thaw depth at other points over the hillslope. The reason for this is unclear; however, the discrepancy between the soil pit and patch measurements could be explained by two main factors. Although the 0°C isotherm (i.e., cryofront) has been shown to reasonably approximate the frost table (Hinkel et al., 2001; Carey and Woo, 1998), Goeller (2005) linearly interpolated the actual rate of frost table decline between the temperature sensors in the soil pit. This is because the exact location of the frost table at any point between the spacing of the temperature sensors (at most 0.1 m) is unknown (Goeller, 2005). Also, during the phase change from ice to water, the soil temperature should remain at 0°C and, therefore, the cyrofront may not necessarily correspond to the thaw depth (i.e., depth to the frost table/frozen saturated layer) during this time. However, Goeller (2005) does indicate that the soil temperature rose above 0°C the day following the passing of the cyrofront, thus indicating a maximum potential temporal error of one day in predicting the position of the cyrofront. Second, the soil profile at the soil pit, and its associated properties (see Table 1-1), may be quite different from many of the patches. Unfortunately, because soil profiles at the individual thaw depth measurement locations were not described, average values of organic soil thickness and mineral soil thickness were assigned to each patch based on visual observations of a few points within each patch. Also, the soil pit was located in an area adjacent to a local area of water accumulation (microdepression). Therefore, it could be that at that one particular area where the soil pit was located, thaw depth did increase rapidly at the beginning of the snowmelt period, and then decrease. Thus, the timing and magnitude of soil thaw observed at this particular soil pit may not be representative of the other portions of the hillslope.

Figure 6-5: **Thaw depth over time for a single point located along the transect in each patch. Time is measured from the day the first soil thaw measurement was made in the patch. Each line represents how a single point thaws with time based on when it first became snow-free (or first began to be monitored), relative to the first thaw depth measurement in the patch. The blue line shows the change in thaw depth with time, interpolated from the 0°C isotherm (Goeller, 2005) at the soil pit, for comparison.**

See following pages.

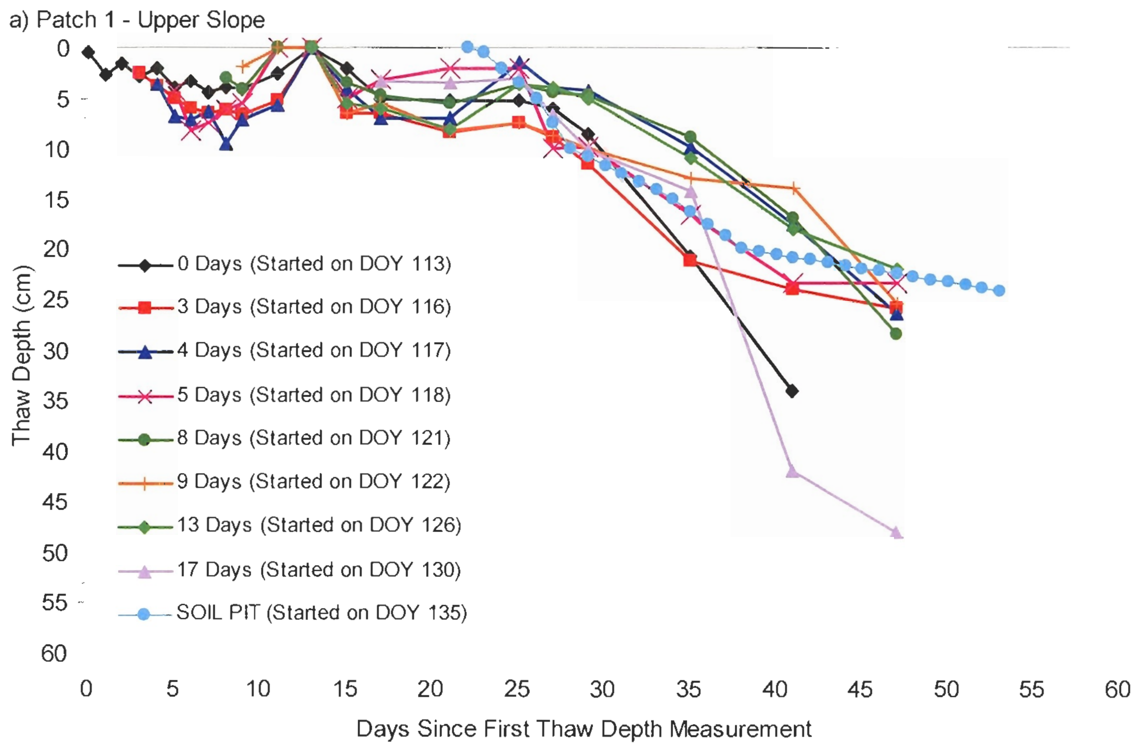
a) Patch 1 - Upper Slope
Thaw Depth (cm)
Days Since First Thaw Depth Measurement
0 Days (Started on DOY 113)
3 Days (Started on DOY 116)
4 Days (Started on DOY 117)
5 Days (Started on DOY 118)
8 Days (Started on DOY 121)
9 Days (Started on DOY 122)
13 Days (Started on DOY 126)
17 Days (Started on DOY 130)
SOIL PIT (Started on DOY 135)

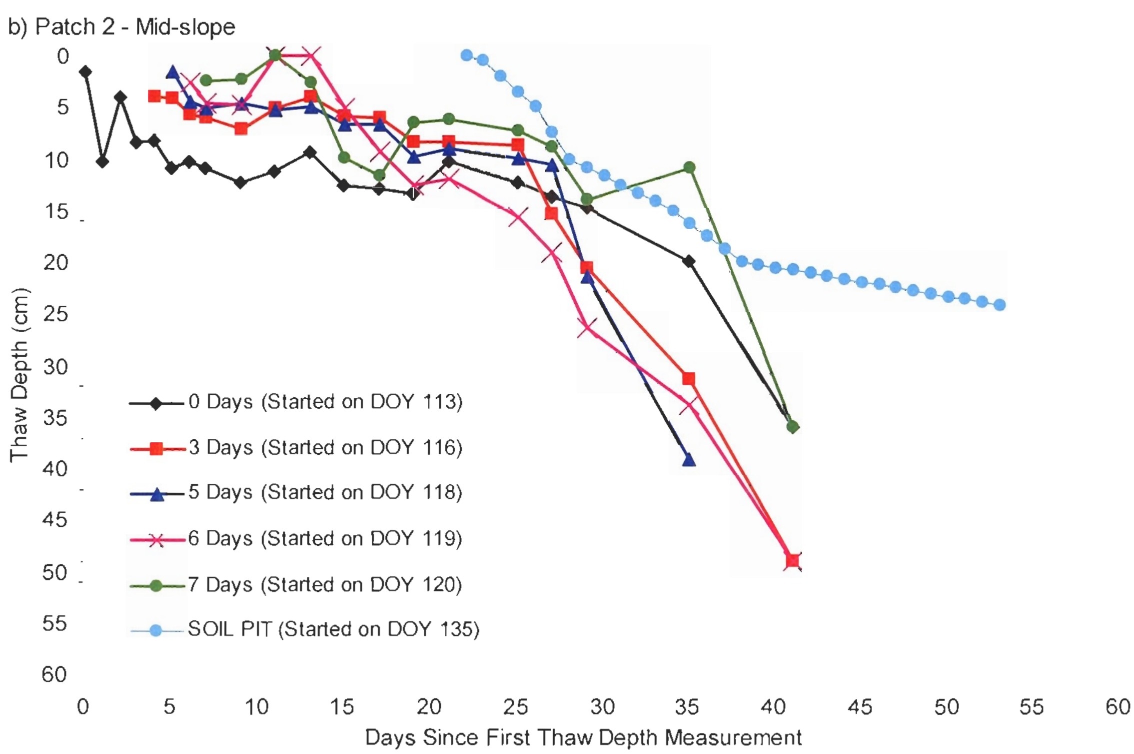
b) Patch 2 - Mid-slope
Thaw Depth (cm)
Days Since First Thaw Depth Measurement
0 Days (Started on DOY 113)
3 Days (Started on DOY 116)
5 Days (Started on DOY 118)
6 Days (Started on DOY 119)
7 Days (Started on DOY 120)
SOIL PIT (Started on DOY 135)

c) Patch 3 (T1) - Upper Slope

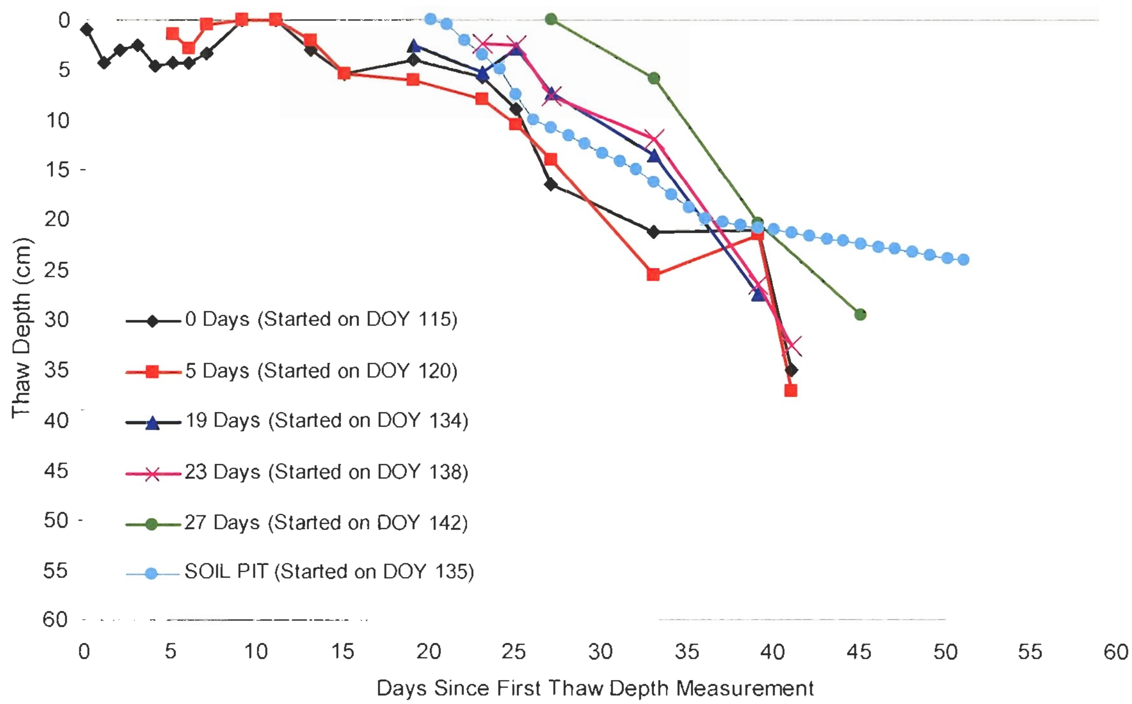

d) Patch 3 (T3) - Upper Slope

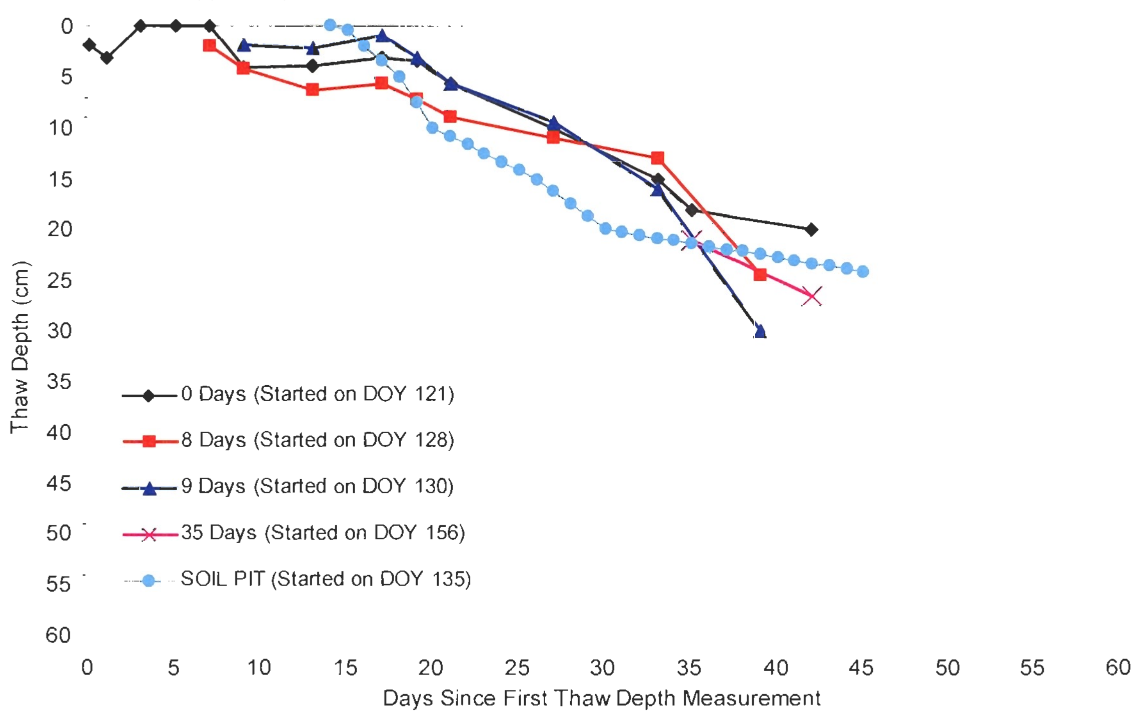

e) Patch 4 - Upper Slope

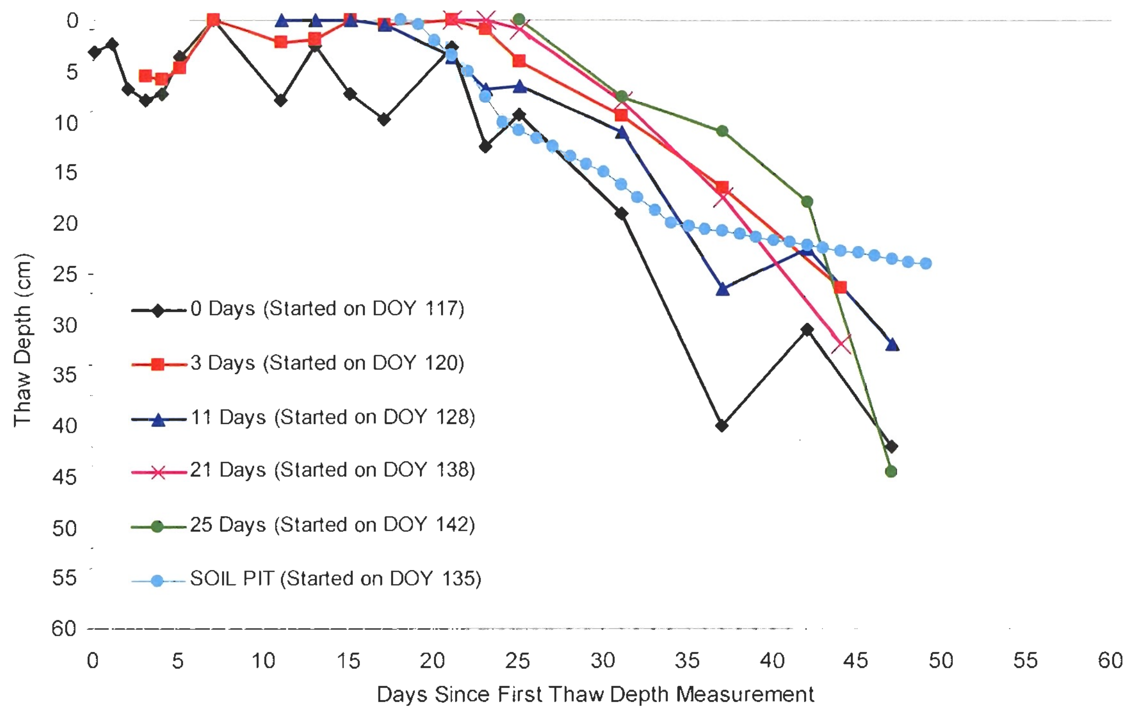

f) Patch 5 (T1) - Upper Slope

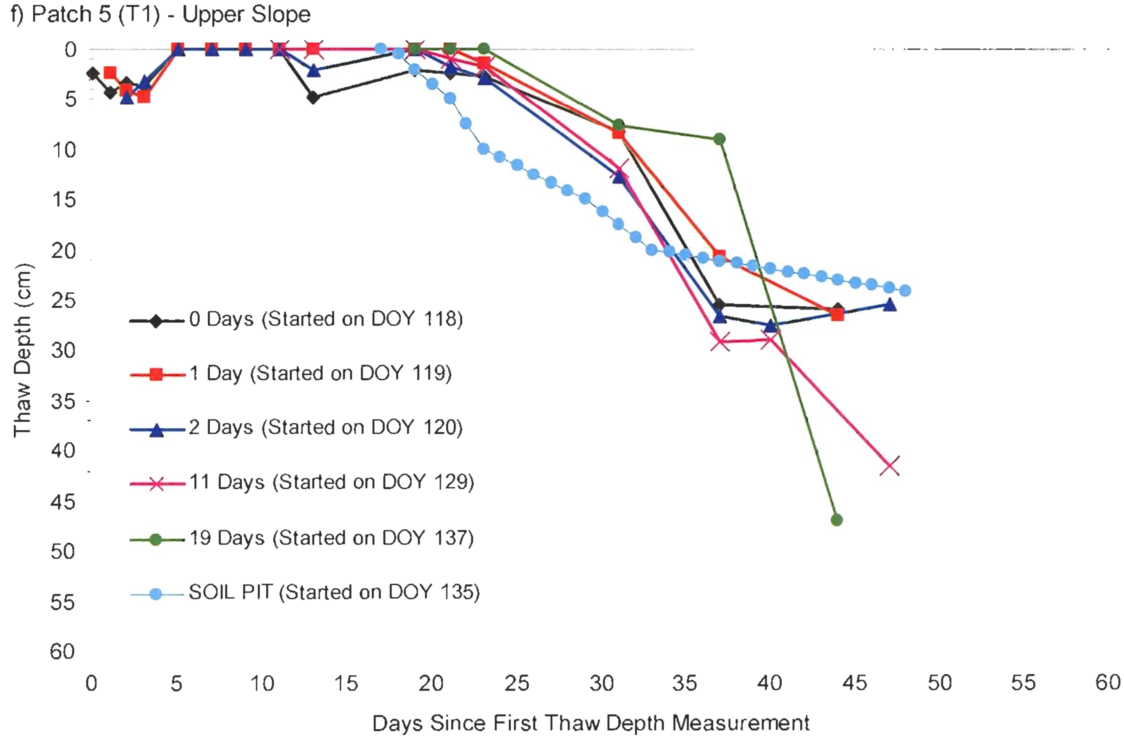

g) Patch 5 (T2) - Mid Slope

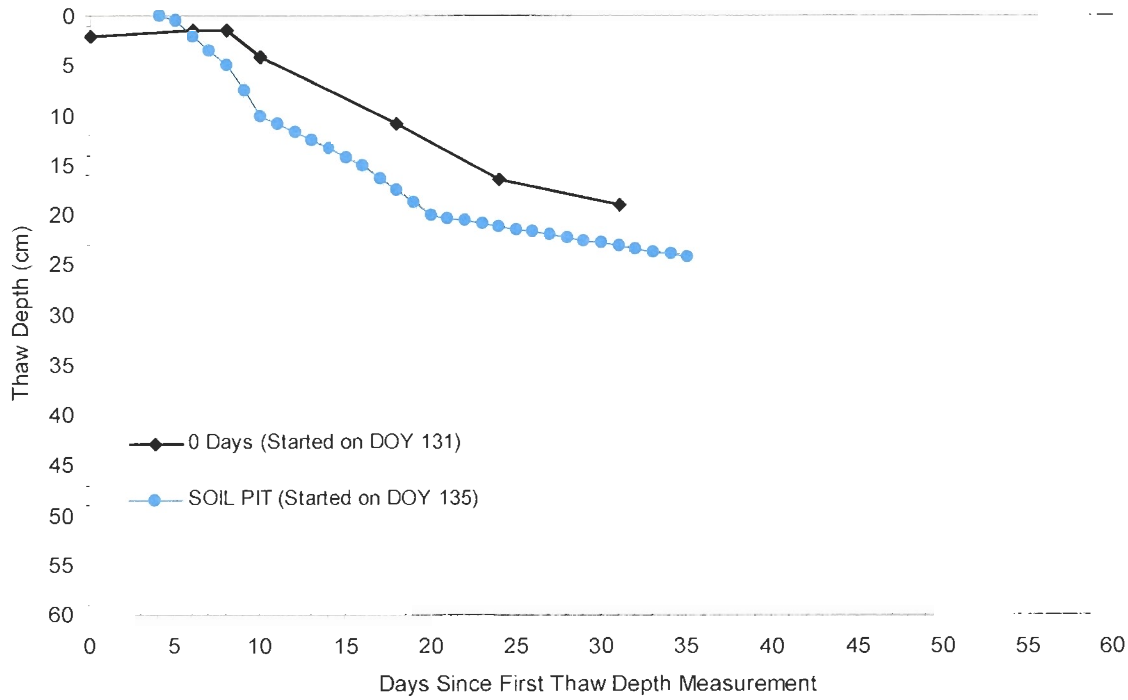

h) Patch 6 - Upper Slope

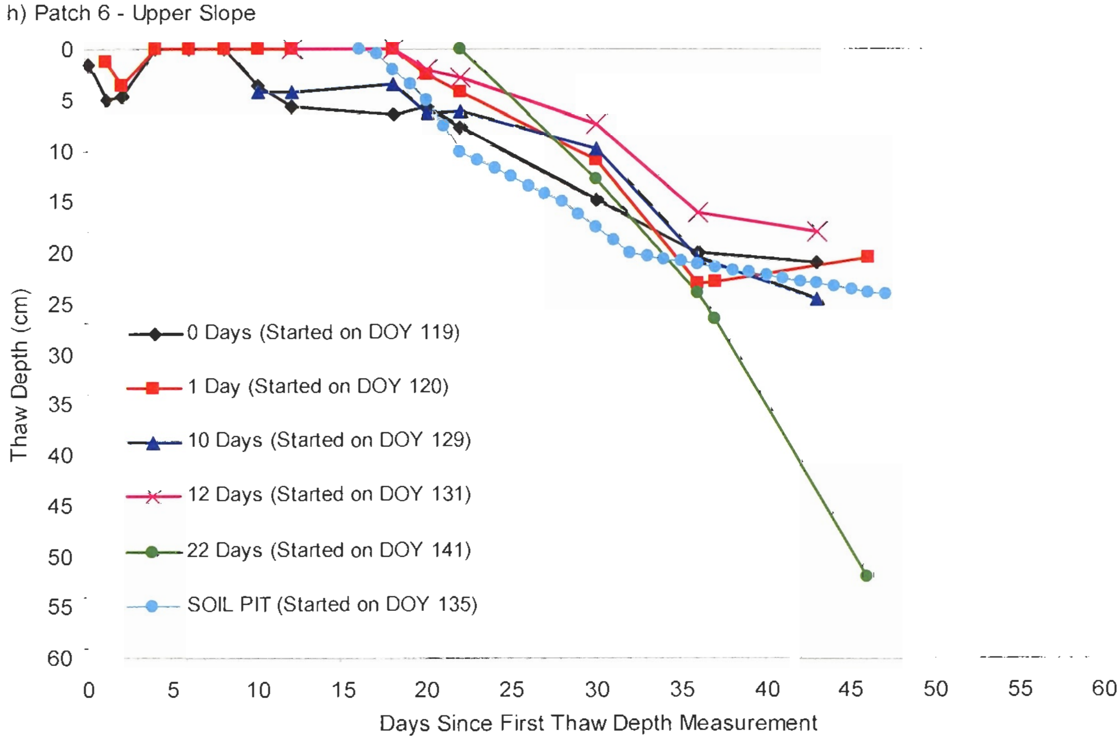

i) Patch 7 - Upper Slope

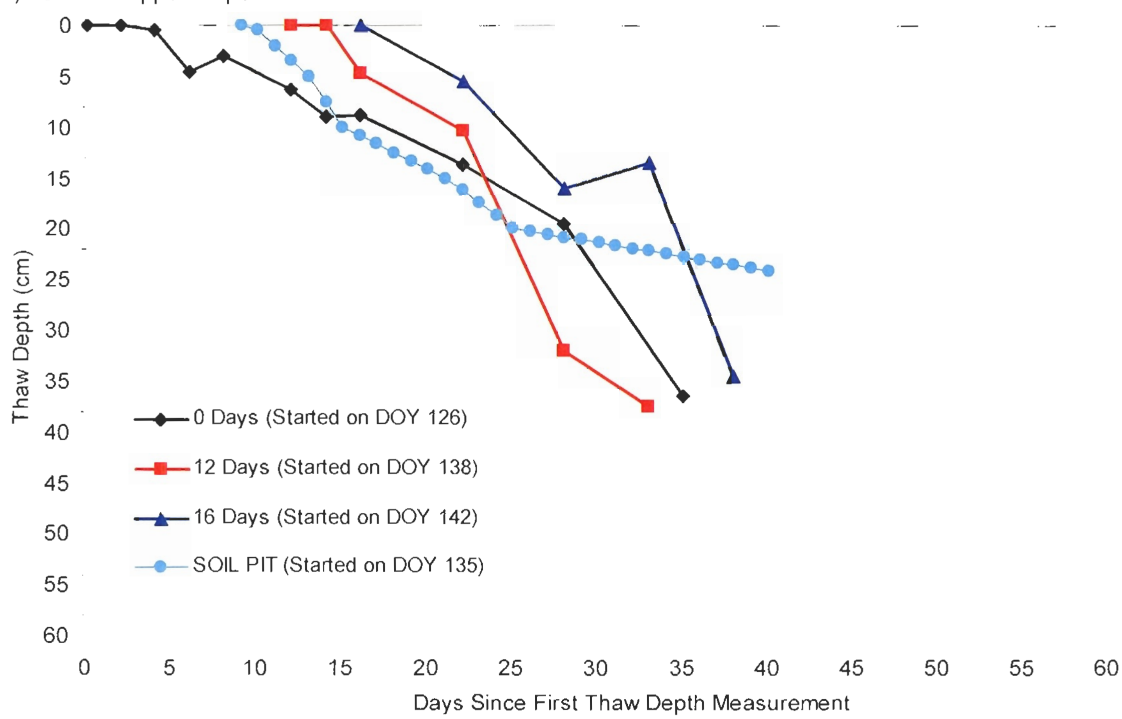

j) Patch 8 - Upper Slope

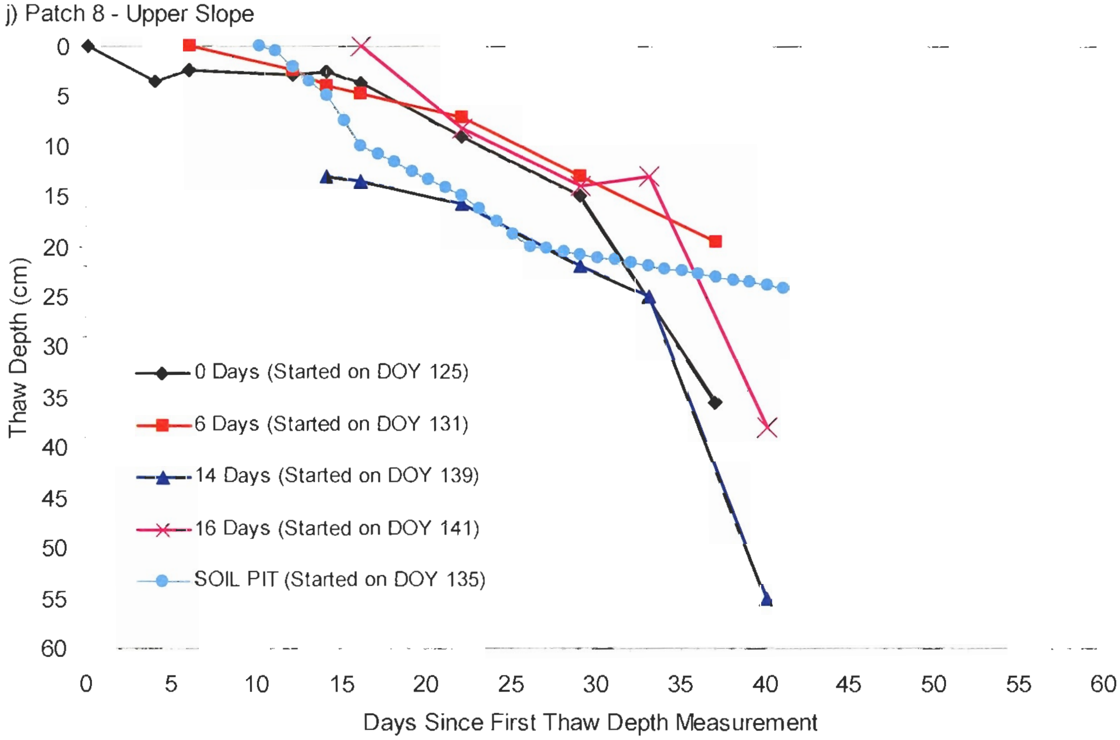

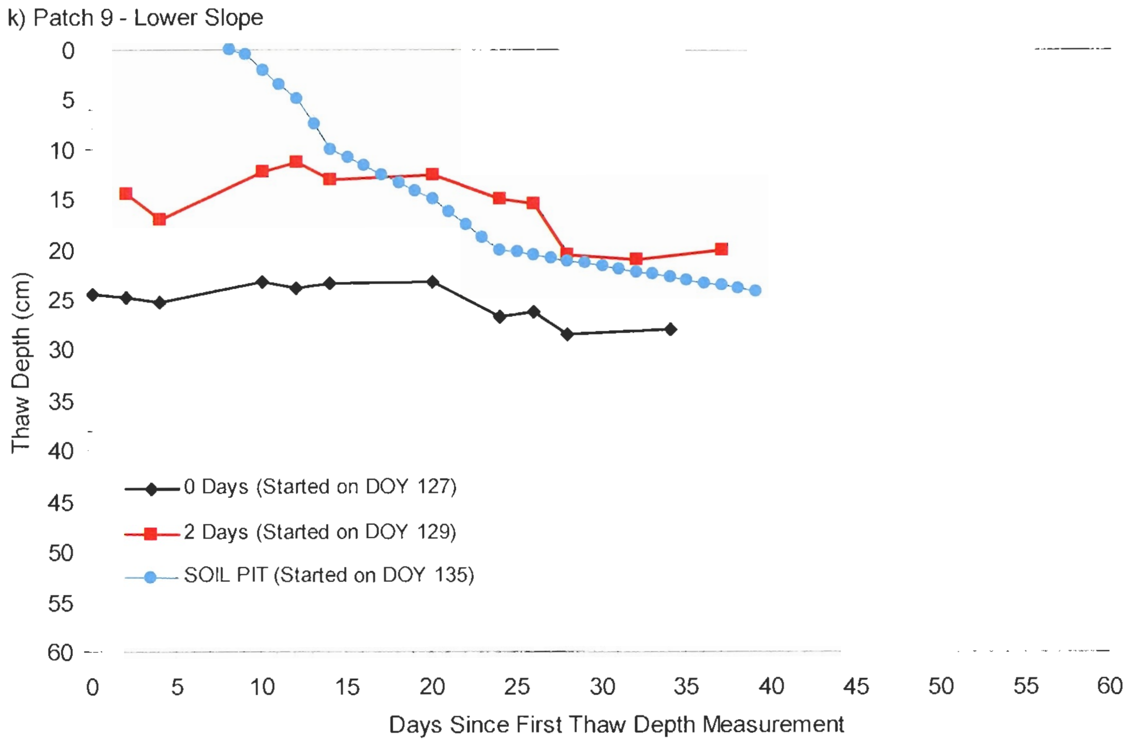
k) Patch 9 - Lower Slope
Thaw Depth (cm)
0
5
10
15
20
25
30
35
40
45
50
55
60
0 Days (Started on DOY 127)
2 Days (Started on DOY 129)
SOIL PIT (Started on DOY 135)
0
5
10
15
20
25
30
35
40
45
50
55
60
Days Since First Thaw Depth Measurement

Most of the individual point thaw measurements in the patches had thaw depths that varied between 0-15 cm over the first 15 days of thaw depth monitoring (with the exception of Patch 9, located on the lower slope). After this time, most points showed a greater increase in thaw depth. One would expect that points that became snow-free early on in the melt period (and hence began to thaw early on as well), would have larger thaw depths later on in the melt period, compared to points that had more recently become snow-free (i.e., the older points would have had a 'head start' on thaw). However, this did not always appear to be the case. In some patches, although the monitoring of many points started at different times (either because more points became snow-free or additional points were added later); the final range of thaw depths within a patch did not differ substantially.

For example, in Patch 1, a point that was monitored starting on DOY 116 had an initial thaw depth of 2.5 cm, which increased to 26.0 cm on DOY 160. A point that was monitored as of DOY 122 (8 days later) within the same patch had an initial thaw depth of 1.9 cm, which increased to 25.5 cm on DOY 160. Thus, although the first point effectively had an 8-day 'head start' on thaw, the thaw depths for both those two points on DOY 160 were approximately the same. In Patch 6, a point that was monitored from DOY 129 onwards (May 9 – or 10 days after the first thaw depth measurements in that patch were made) had a thaw depth (24.5 cm), which was similar to a point that had been monitored since DOY 119 (21.0 cm). Conversely, other patches did show a marked difference in thaw depths (for example, see Patches 7 and 8). In Patch 7, a point that was monitored as of DOY 126 had an initial thaw depth of 0.0 cm, and increased to 19.5 cm on DOY 154 (28 days later). However, a point that was monitored starting on DOY 138 (12 days after the previous point), had an initial thaw depth of 0.0 cm, and a thaw depth of 32.0 cm on DOY 154. It should be noted, however, that Figure

6-5 represents thaw at selected single points in each patch. Other points in the same patch (i.e., along the same transect) may or may not exhibit the same behaviour. If there was more than one point on any given day, the single point with the smallest initial thaw depth, out of a possible number of points that had become snow-free on any given day, was plotted.

Patch 9 was the only patch that was monitored on the lower part of the hillslope where the organic layer and overlying vegetation was the thickest (see Table 3-1 and Table 3-2). The first thaw depth measurements made in this patch were on DOY 127 (May 7). Based on the daily digital slope photos, this area became snow-free on approximately DOY 120 (April 30). As a result, thaw depths in Patch 9 were already ~25 cm on the first day of monitoring. Although the frost table continued to descend as snowmelt progressed, the presence of the thicker organic layer likely insulated the soil and prevented it from thawing as quickly as the upper patches on the slope. The insulative effect of the overlying organic layer was particularly noticeable later in the study period (June), once most of the snowcover ablated. Walker et al. (2003) also found that the summer insulative effect of the vegetation mat resulted in a decreased thaw depth compared to other zonal sites along a bioclimatic gradient. The insulating properties of peat and organic soil (due largely to their low thermal conductivity) are well known, and have been reported in many studies (e.g., Walker et al., 2003; Hinzman et al., 1991; Grzes, 1988; Slaughter and Kane, 1979). It also appears that the insulating effects of the organic material counteract the increase in thermal conductivity resulting from increases in soil moisture (discussed in the following section).

Given that there are several factors that influence the change in thaw depth, measuring thaw depth at set time increments alone may not adequately characterize ongoing processes during the soil thaw period. Measuring thaw rate, which is strongly dependant on the soil moisture content, may provide a better indication of how soil thaw changes over time. In addition, examining thaw rates allows for a better comparison of thaw depth across all the patches as it is the rate of change that is being compared and not the absolute depth of soil thaw. Therefore, the following discussion attempts to compare the variability in thaw depths across all the patches by examining thaw rates and soil moisture.

6.4 Soil Thaw Rate and Soil Moisture

Thaw rate (in $cm \cdot d^{-1}$) was calculated for every point on a transect, and a mean thaw rate (which includes both negative and positive changes in thaw depth) for the entire transect was determined for each time interval. Therefore, each point in Figure 6-6 represents a mean thaw rate for the entire transect on a given day and thus, this figure represents the change in the spatial mean thaw rate for each transect with time. Mean soil thaw rate showed little change with time; however, it should be noted that the number of monitoring points within each patch increased with time as snowmelt progressed, thus effectively "diluting" or minimizing the thaw rate (i.e., each point on the graphs represents an average of an increasing number of measurement points with time, some of which include small thaw and/or negative thaw rates).

The mean thaw rate for each transect, calculated for the entire monitoring period demonstrated that Patch 9 did indeed have one of the lowest mean thaw rates (0.43 cm/day), whereas the mean thaw rate of the other patches (with the exception of Patch 6) ranged from 0.57 - 1.03 $cm \cdot d^{-1}$ (Table 6-1). However, it must be noted that these mean thaw rates include both negative and positive thaw rates and also have different start and end dates (since patches were monitored as they became snow-free). Nonetheless, the low thaw rate for Patch 9 does suggest that this area had probably 'thawed out' before monitoring began. Ideally, a lower slope patch would have been available for monitoring earlier in the study period and, therefore, the effects of the thicker organic layer and/or drainage from upslope on thaw rate could have been better examined.

Soil moisture measurements were recorded concurrently, and at the same points where soil thaw depth was measured. Mean soil moisture was determined by calculating the average soil moisture of all points along the transect. However, soil moisture in this study was only measured at the near surface (0-5 cm), and thus beyond this depth it is difficult to separate the contrasting effects of the insulative properties of the organic soil and soil moisture on thaw depth. Figure 6-6 shows the mean near surface (0-5 cm) liquid soil moisture plotted along with mean thaw rate for transects across each patch.

Although individual soil moisture readings were highly spatially variable (as demonstrated by the large standard deviations), mean near surface (0-5 cm) soil moisture exhibited little variability within each patch (Figure 6-6), usually ranging between 20-30% VWC. McCartney et al. (2006) and Quinton and Gray (2003) found low variability in mean near surface soil moisture at Granger Basin as well. Quinton and Gray (2003) observed that the transition time from a "wet" (during snowmelt) to "dry" (after draining and thawing) regime was less than 5 days. In this study, peak values of near surface soil moisture occurred in late May/early June, after much of the snowcover had already been depleted. Only two patches (Patch 5 (T1) and Patch 6) show an increase in soil moisture with time at approximately the same time; Patch 5 and 6 were located beside each other on the upper portions of the north-facing slope. On DOY 141, mean soil moisture at Patch 5 (T1) is 0.25, and increases to 0.45 on DOY 149. Similarly, in Patch 6, mean soil moisture on DOY 141 is 0.29, and increases to 0.44 on DOY 149. (Figure 6-6). None of the other patches show such a marked increase in soil moisture during this time. It is not clear why these two particular patches showed an increase in soil moisture, although one might speculate that the hydrology/drainage of the site play a role. The potential role of drainage is discussed in the following section.

Figure 6-6: Mean thaw rate and mean near surface (0-5 cm) liquid soil moisture for each transect over time. Error bars represent the standard deviation.

See following pages.

a) Patch 1 - Upper Slope

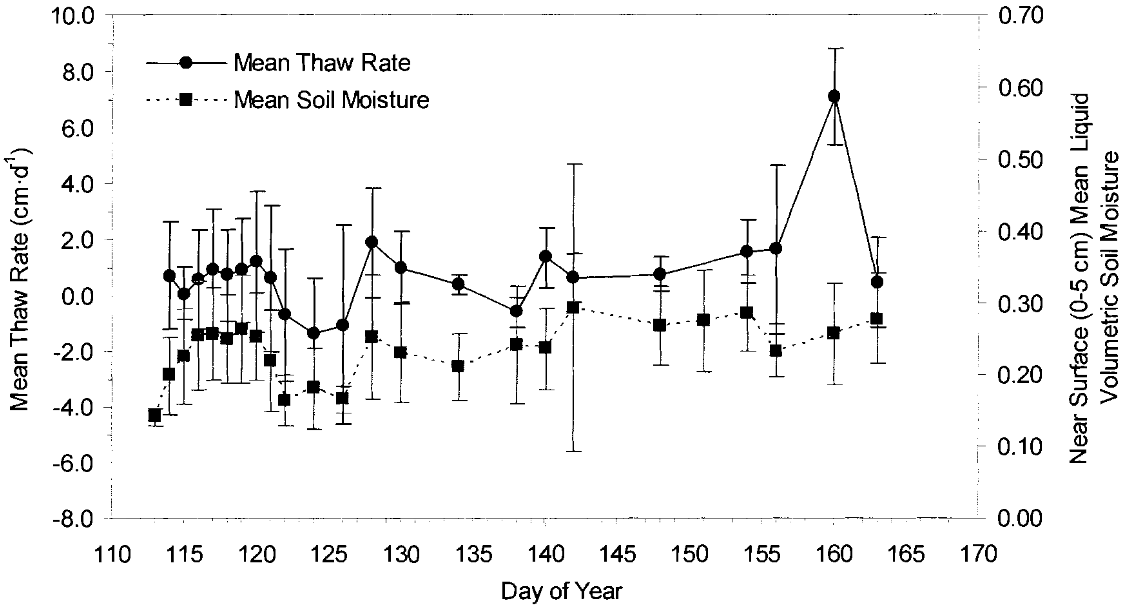

b) Patch 2 - Mid-Slope

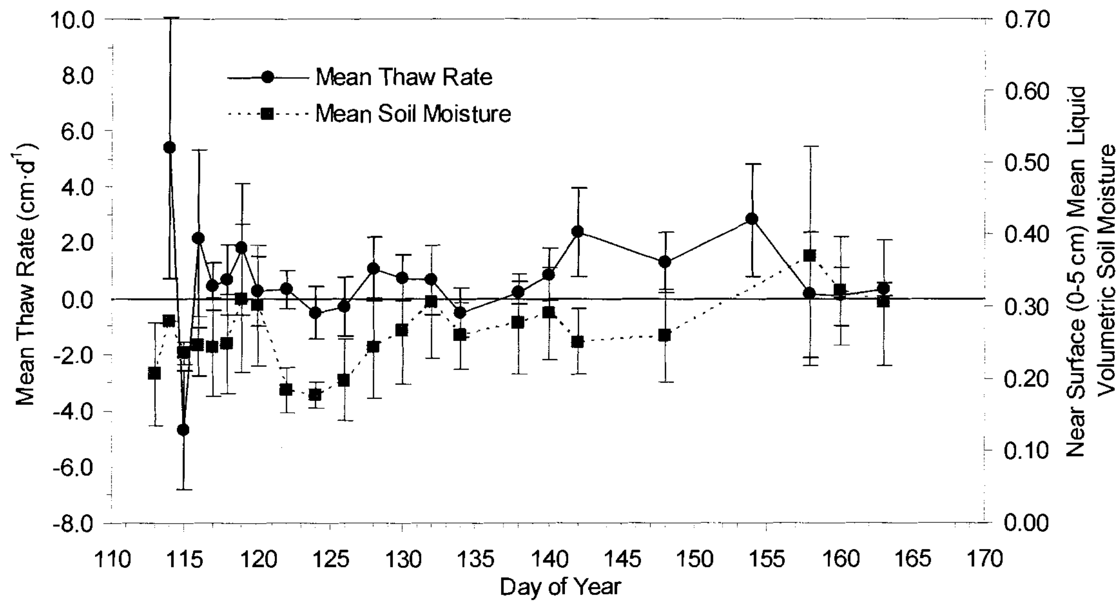

c) Patch 3 (T1) - Upper Slope

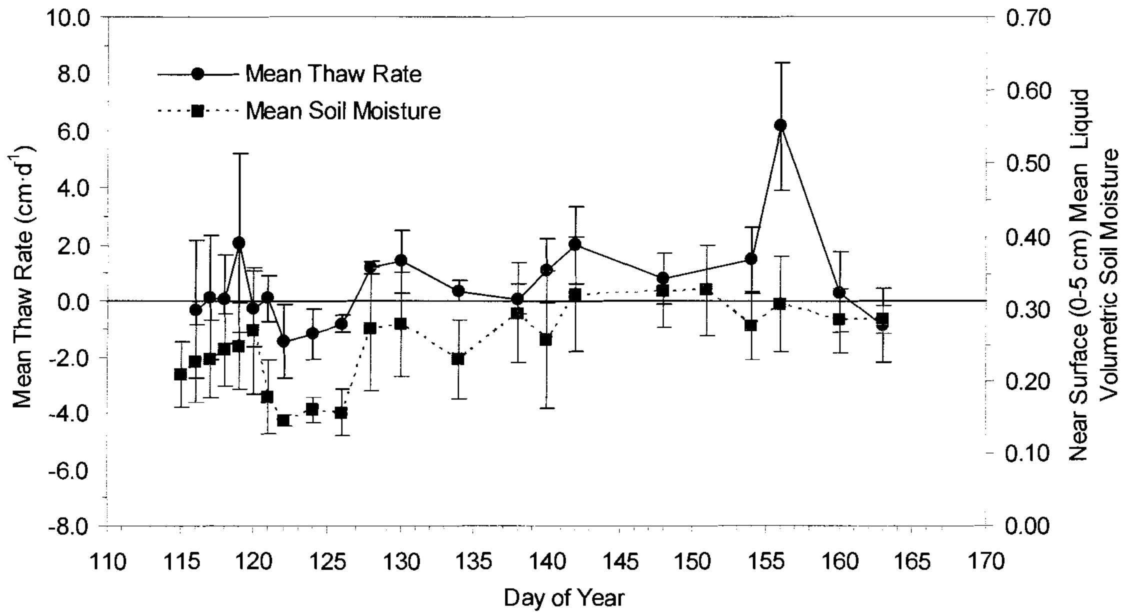

d) Patch 3 (T3) - Upper Slope

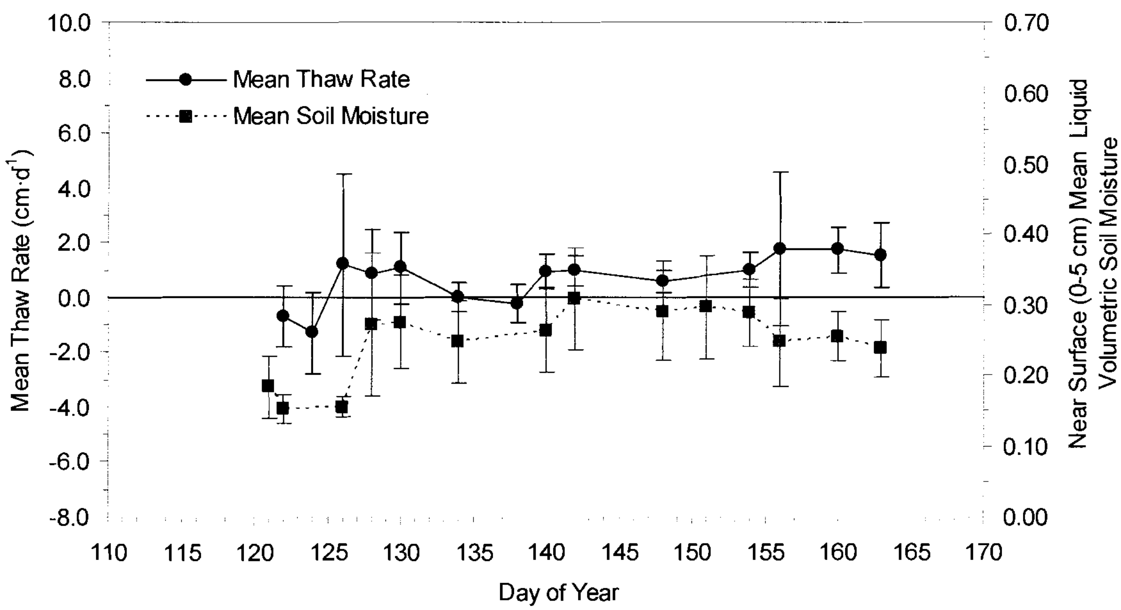

e) Patch 4 - Upper Slope

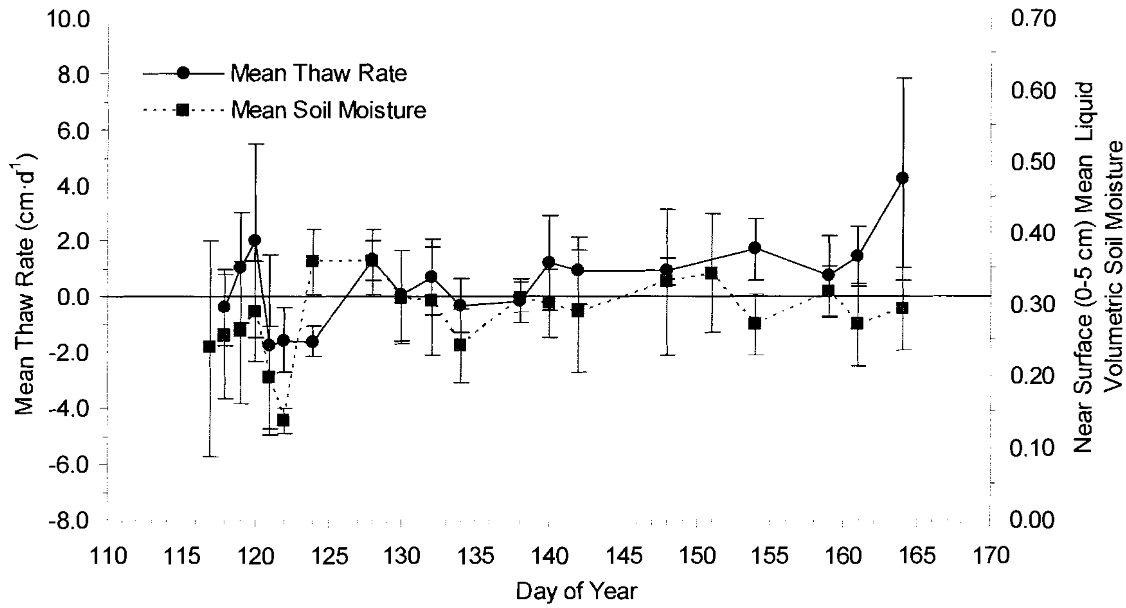

f) Patch 5 (T1) - Upper Slope

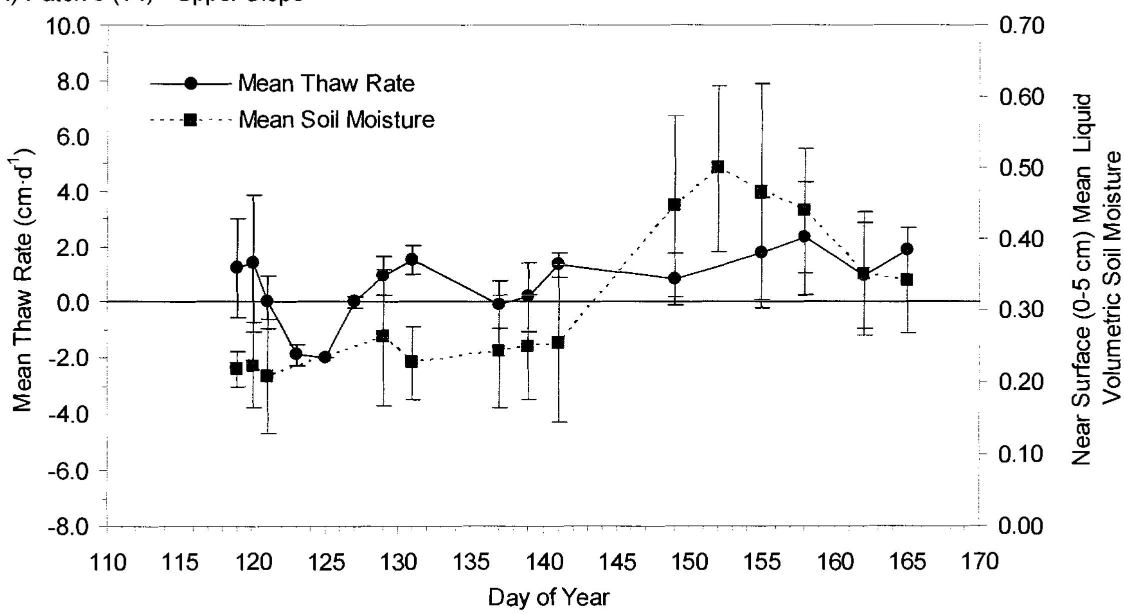

g) Patch 5 (T2) - Mid-Slope

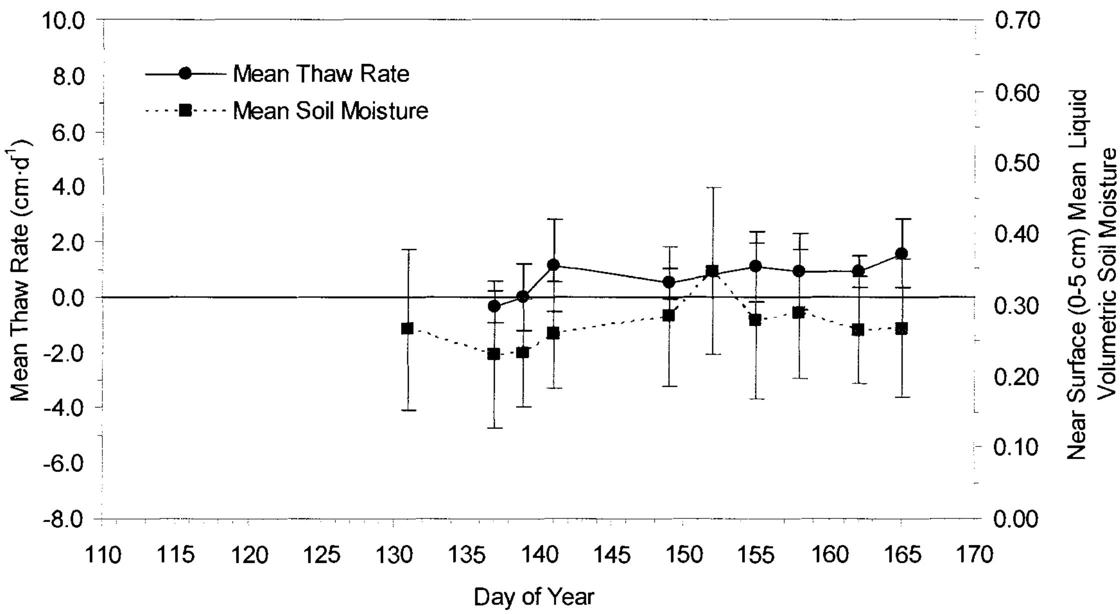

h) Patch 6 - Upper Slope

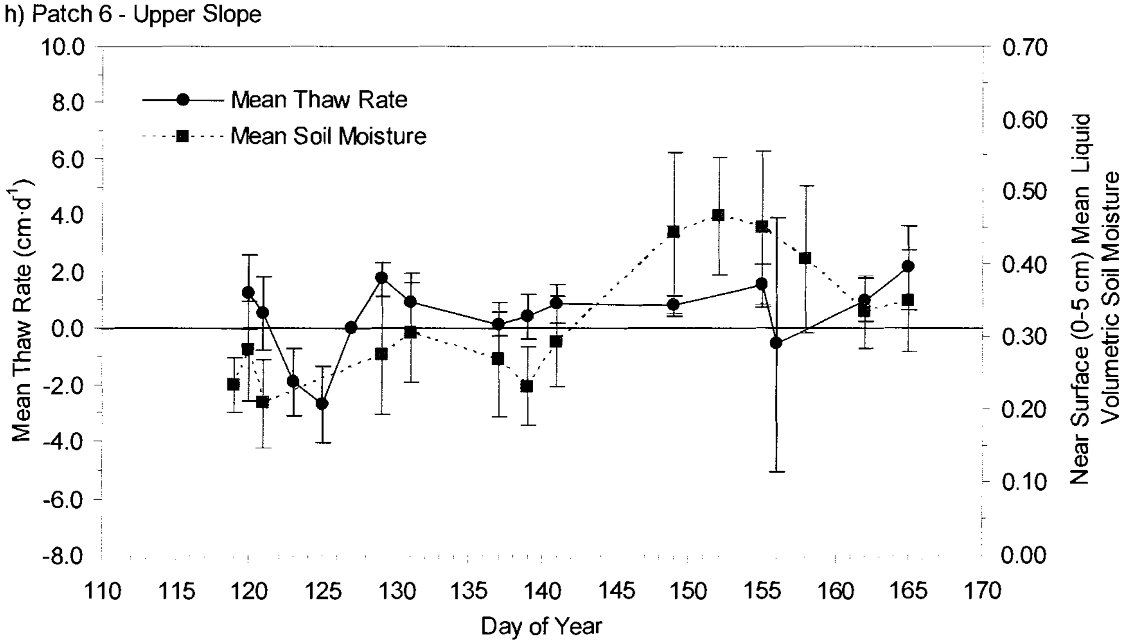

i) Patch 7 - Upper Slope

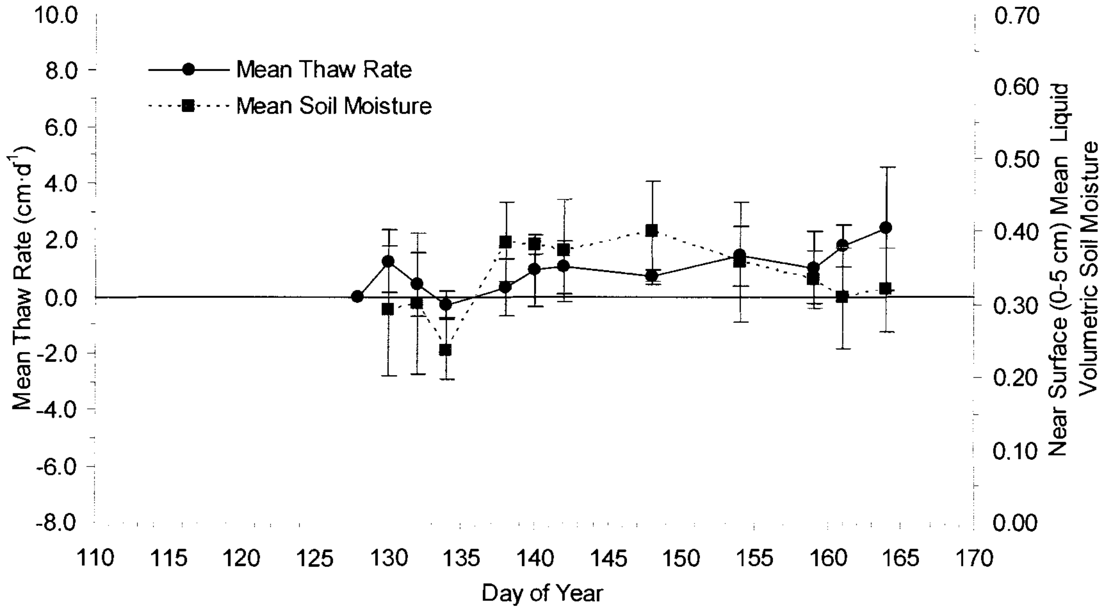

j) Patch 8 - Upper Slope

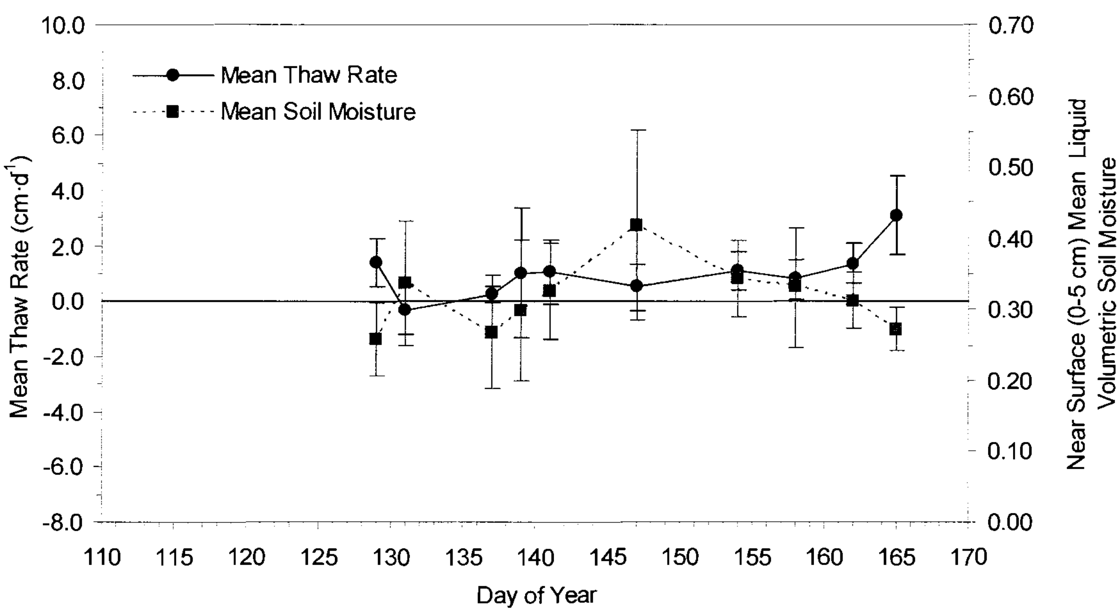

k) Patch 9 - Lower Slope

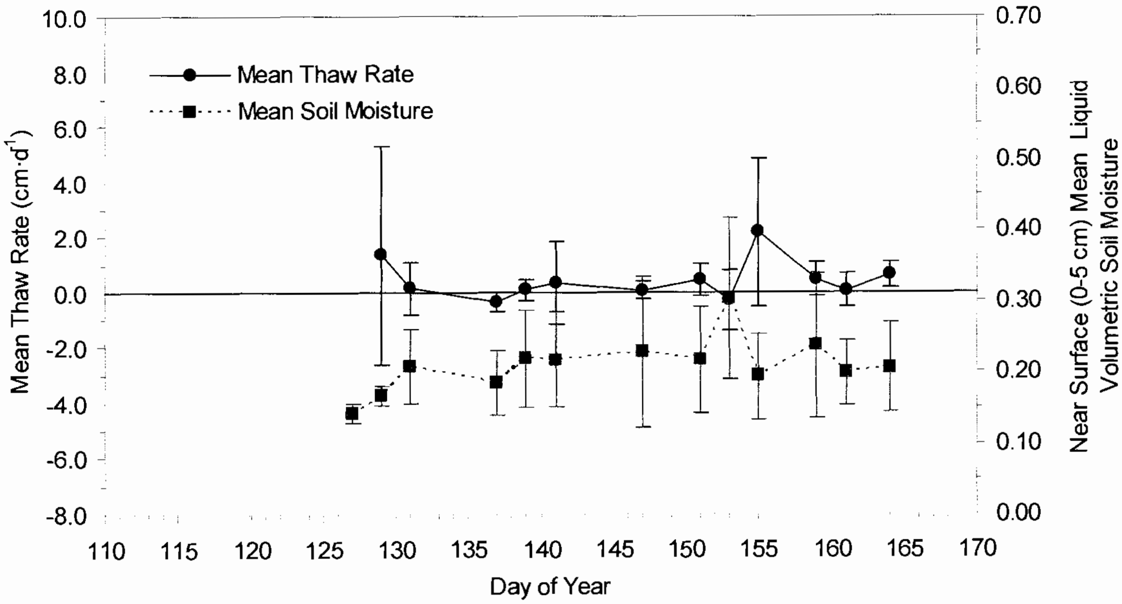

Table 6-1: Mean thaw rate for all transects and the soil pit over the entire monitoring period.

	Start DOY	End DOY	Monitoring Time (Days)	*Mean Thaw Rate ($cm \cdot d^{-1}$)	Standard Error
Patch 1	114	163	50	0.85	0.35
Patch 2	114	164	51	0.70	0.38
Patch 3 (T1)	116	163	48	0.62	0.37
Patch 3 (T3)	122	163	42	0.66	0.24
Patch 4	118	164	47	0.57	0.34
Patch 5 (T1)	119	165	47	0.65	0.31
Patch 5 (T2)	137	165	29	0.72	0.22
Patch 6	120	165	46	0.41	0.34
Patch 7	130	164	35	1.00	0.22
Patch 8	129	165	37	1.03	0.28
Patch 9	129	164	36	0.43	0.21
**Soil Pit	135	166	32	0.78	**0.64

*Mean thaw rate for the patches is the mean of all daily mean thaw rates, including both positive and negative daily mean thaw rates.
**Mean thaw rate for the soil pit is the mean of the daily thaw rate, interpolated from the zero degree isotherm. Therefore, the standard deviation is shown (instead of standard error).

6.4.1 Relationship Between Soil Moisture Content, Drainage and Rate of Soil Thaw

Soil thaw has been closely linked to, but is not entirely dependent on, trends in soil moisture (Carey and Woo, 2000; Hinzman et al., 1991). As soil thaw progresses, water replaces the ice and, consequently, there is a reduction in the thermal conductivity of the soil – thus, leading to a lower rate of thaw. To examine the relation between thaw rate and soil moisture at this site, a series of graphs were constructed.

First, plots of soil thaw rate and soil moisture at a single point within each patch were constructed (Figure 6-7). The points used were the same individual points that were used to construct Figure 6-5. The only patch that displayed a negative correlation between soil moisture and thaw rate was Patch 9 (lower slope). The soil pit also showed a negative relationship. However, it should be noted that soil moisture for the soil pit is the daily average soil moisture from all 6 sensors in the soil pit and thaw rate is interpolated from the zero-degree isotherm. All the other patches displayed a weak positive relation. These results suggest, at least for a single point within each patch, that a high rate of soil thaw corresponds to a high moisture content, which might be anticipated based on the fact that as soil thaw occurs, there is an increase in the amount of moisture present.

Given the somewhat unexpected results for a single point within a patch, a similar exercise was performed for the entire patch by plotting the mean thaw rate against the mean moisture content for each patch (Figure 6-8). While the R^2 values are altogether quite low, the trends suggest both positive and negative relations. Patch 9 has the strongest negative correlation ($R^2 = 0.36$). Since this patch was located at the bottom of the slope, moisture draining from upslope probably kept this area wetter than some other patches. This suggests that the decrease in thaw rate may have been caused by an increase in soil moisture. However, this patch also had the thickest organic layer, which could have also caused a decrease in thaw rate due to the insulative effect of the organic soil, thereby making it difficult to make a conclusive statement about the relationship between soil moisture and thaw rate.

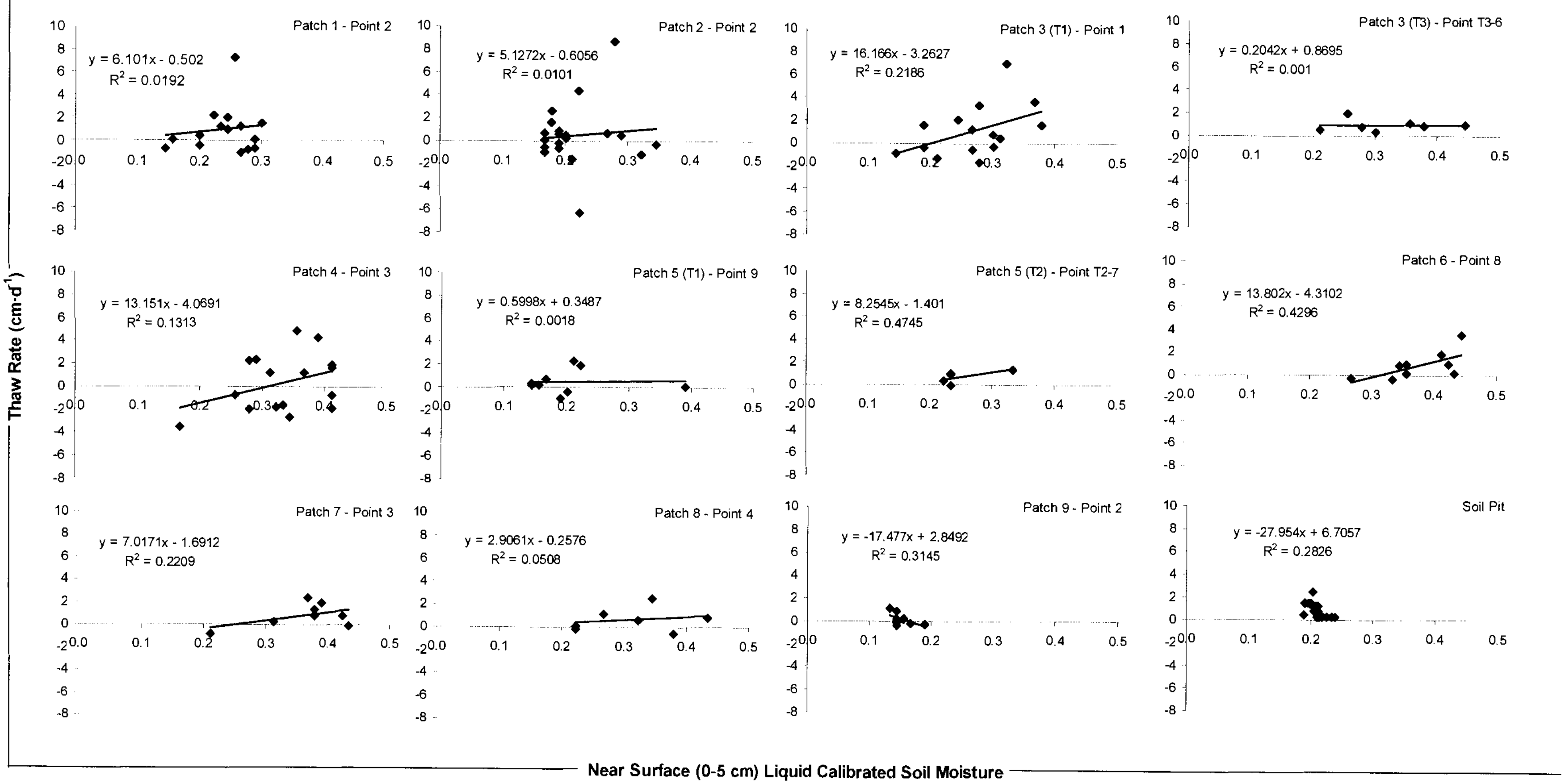

Figure 6-7: Relation between soil moisture and thaw rate for a single point within each transect and for the soil pit. Note that thaw rate for the soil pit was interpolated from the zero-degree isotherm and soil moisture for the soil pit was the average soil moisture from all sensors located in the soil pit .

Regardless of the possible explanation for Patch 9, there appears to be no clear explanation for the negative correlation observed at other patches. One possible explanation is the biased sampling of soil moisture. Moisture content measurements were made only in the upper 5 cm, and may not be representative of moisture content at greater depth. For example, once the snow has ablated, the surface starts to desiccate, leading to low soil moisture conditions at the upper soil surface. However, the deeper layers may be considerably wetter, either due to melting of the ice (as the frost table descends) or from lateral drainage upslope. Thus, the moisture measurements may indicate dry conditions, but in reality, there is considerable water present near the frost table, thus leading to a positive relation. To explore whether this latter effect might account for the lack of correlation between mean thaw rate and liquid soil moisture, only those points that had a mean thaw depth between 0-5 cm were plotted (Figure 6-9); however, no correlation is observed. Perhaps a more vertically integrated measure of soil moisture, such as mean soil moisture throughout the profile, could provide an improved quantification of the relationship between soil moisture and thaw depth or rate of thaw.

Another possible explanation is the dynamic hydrologic conditions, and how these relate to changes in the thermal parameters of the soil. As thaw progresses, water replaces the ice. Because $K_{water} < K_{ice}$, heat will not be conducted away as easily as when the soil was frozen, therefore, the heat builds up and results in a greater depth of thaw. Thus, leading to conclusion that soil thaw rate increases as soil moisture increases (a positive relation). However, if the soil is well drained, then moisture content is not observed to increase despite the fact that the frost table is descending. As well, advective heating from water flowing downslope may be sufficient to cause warming and thaw even though overlying soils may remain frozen with low unfrozen water content.

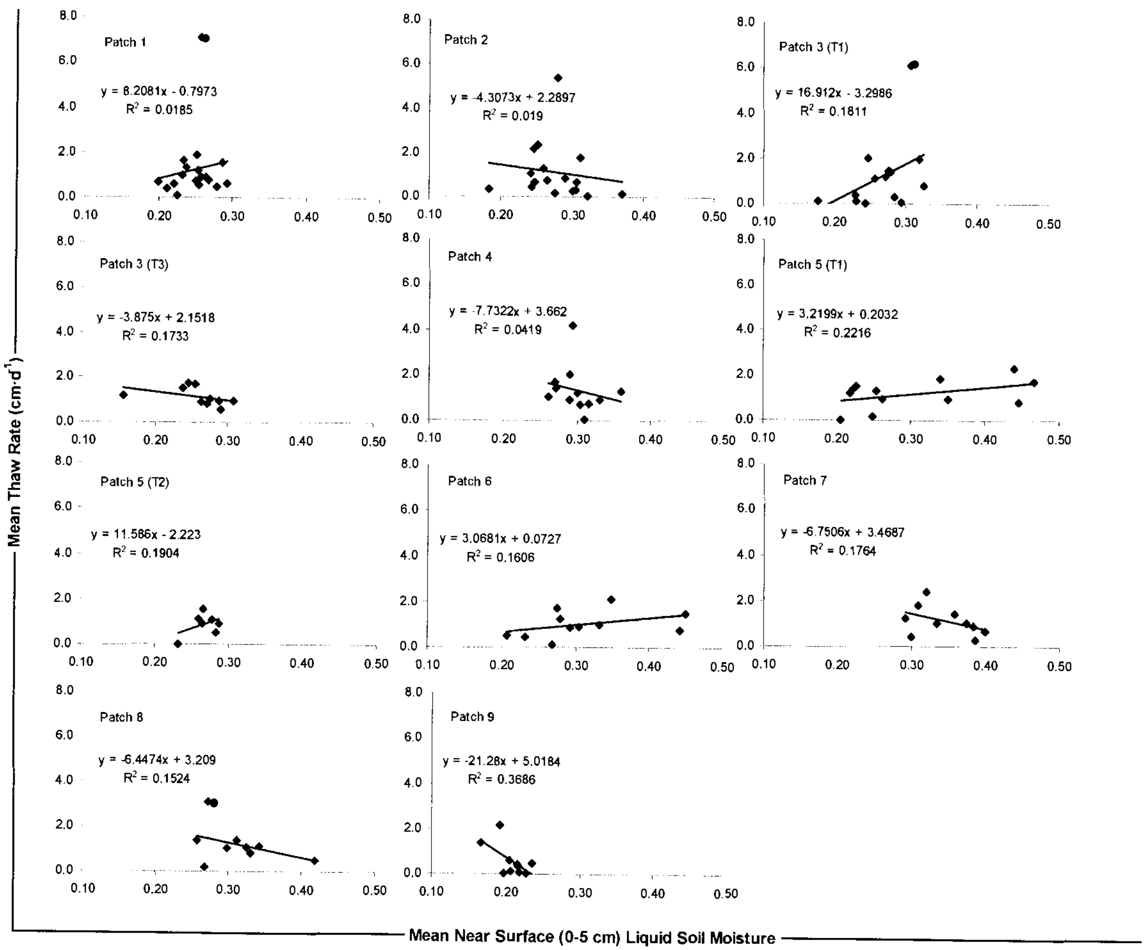

Figure 6-8: Mean thaw rate and mean soil moisture for each patch

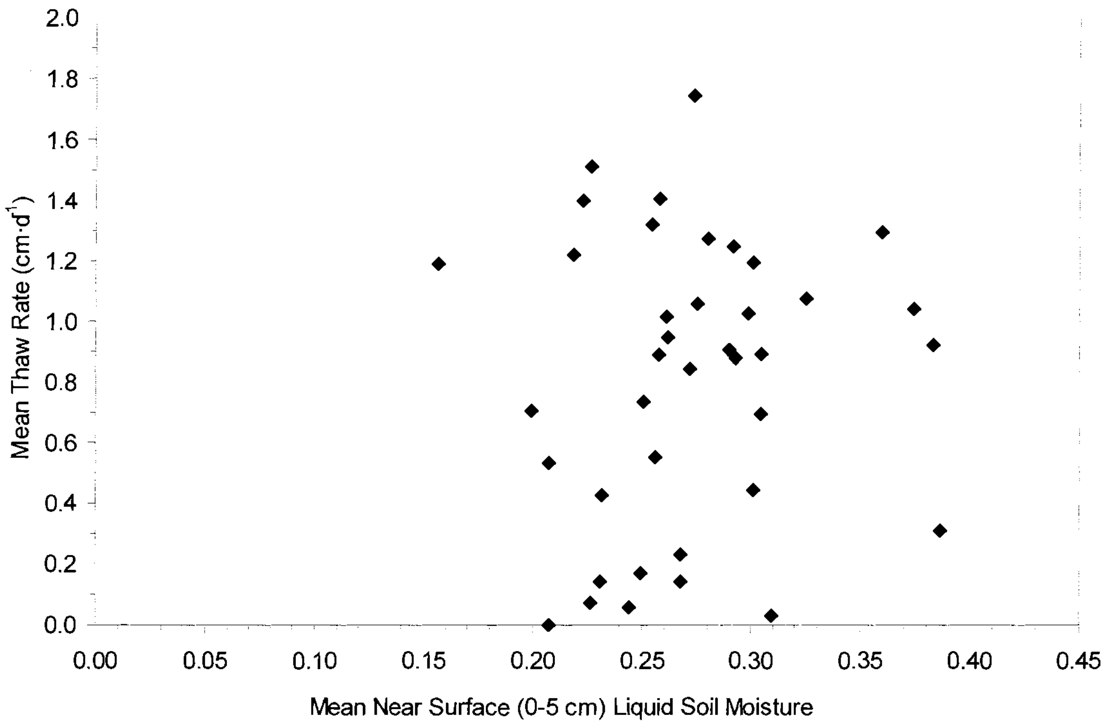

Figure 6-9: **Relationship between mean liquid soil moisture measurements and mean positive soil thaw rates for those points where the mean thaw depth was between 0-5 cm (n = 39).**

Unfortunately, the relation between drainage and moisture content could not be teased out of the data.

The results of the soil thaw study suggest that drainage, including both moisture draining from an area and draining into an area, is perhaps confounding the relationship between thaw rate and moisture content. Pomeroy (personal communication, September 28, 2005) suggested that the convective transport of heat from meltwater passing through a patch would have an effect on thaw energy. Indeed, lateral subsurface flow is a common occurrence in permafrost regions (Quinton and Gray, 2001; Quinton et al., 2000; Quinton and March, 1999). The presence of a continuous and relatively thick saturated layer in the lower slope area (Patch 9) supports the notion that this saturated area may have been supplied by subsurface drainage from upslope (Carey and Woo, 1999).

6.5 Soil Thaw Energy

As the soil begins to thaw, almost all of Q_g goes toward melting the ice and lowering the frost table. As the frost table descends with time, the depth over which energy is transferred to the frozen soil increases. As a result, the thermal gradient (dT/dz) decreases, and Q_i becomes smaller with time. Thus, as thaw continues, the contribution of Q_i decreases, and the other fluxes (Q_p and Q_s) provide a greater contribution to Q_g.

Data obtained from the soil pit provide a measure of the soil heat flux and its subsurface partitioning of energy. However, these fluxes would vary over the hillslope, since snowcover duration, soil moisture (water and ice) content, and other factors that influence their magnitude can vary widely over permafrost hillslopes (Quinton et al., 2005; Carey and Woo, 2000). In this section, the relation between Q_i and Q^* are discussed with reference to both the soil pit study by Goeller (2005) and the current hillslope study.

6.5.1 Partitioning of Q_g at the Soil Pit

Temperature and moisture measurements made at the soil pit at the study site in 2003 were used by Goeller (2005) to calculate soil heat flux using the thermo-calorimetric method as outlined by Woo and Xia (1996) and Farouki (1981). In his study, Goeller (2005) analyzed soil pit data from 2003, and found that from DOY 137-165, the cumulative soil heat flux (ΣQ_g) was 57 $MJ \cdot m^{-2}$ and the cumulative energy flux required to lower the frost table (ΣQ_i) was 48 $MJ \cdot m^{-2}$. Therefore, over this time period (DOY 137-165), Q_i = 84%, Q_p = 15% and Q_s = 1% of Q_g, suggesting that Q_i is the dominant component of Q_g during the melt period. Cumulative Q_g calculated thermo-calorimetrically at the soil pit and was found to be 17% of cumulative Q*. This value corresponds well with that of Halliwell and Rouse (1987) who found that on a cumulative basis in permafrost terrain, Q_g is approximately 16-18% of net-all wave radiation. Goeller (2005) concluded that a linear index model for Q_g could provide a reasonable approximation of thaw depth, although rapid thaw occurring early in the melt period was underrepresented.

In the current study, the depth of soil thaw is defined as the depth from the ground surface to the frozen saturated layer (i.e., frost table). Quinton et al. (2005) also found that thaw depth measurements made with a graduated steel rod essentially produced the same results as thaw rate calculated from the change in the position of the zero degree isotherm using soil temperature data. This suggests that although the thermo-calorimetric method of calculating Q_i is much more rigorous and data intensive, the graduated steel rod method provides a reasonable estimate of the flux, and that the graduated steel rod measurements taken across the hillslope are representative of spatially and temporally variable soil thaw.

It is worth noting that while earlier work such as Goeller (2005) and Quinton et al. (2005) used a cumulative method to extract the relation among Q_g, Q_i and Q*, this approach was not used in this study due to the fact that accumulated values have a strong tendency to be dominated by time, thus potentially resulting in a false positive relationship (i.e. time correlates very well to time and may overshadow a poor relation between the values being accumulated) (Pomeroy, personal communication, May 9, 2006).

6.5.2 Soil Thaw and Net Radiation

Net radiation observations obtained from the hillslope meteorological tower during snow-free conditions are considered to represent the snow-free portions of the slope, because slope angle varies within 5° of a mean of 20°, sky view is fairly uniform, and "albedo is remarkably uniform across the valley" (Pomeroy et al., 2003). Carey and Woo (2000) measured net radiation at two different points on a single study slope (upslope and downslope) in Wolf Creek and similarly found that net radiation differed by less than 2% over their study period. The small-scale variation of net radiation to the surface over the entire melt period on the slope is largely controlled by the timing of snowcover ablation (Quinton et al., 2005). Therefore, net radiation measurements obtained from the hillslope meteorological tower were assumed to be representative of net radiation at the snow-free patches. A regression equation between slope-corrected incoming shortwave radiation and measured net radiation at the hillslope meteorological tower (R^2 = 0.88) was used to estimate net radiation prior to DOY 128 (Figure 4-5). Figure 6-10 is a plot of daily mean net radiation and daily mean soil thaw energy. Unfortunately, no relation was observed. A possible explanation for the lack of correlation is that there is likely a time lag for the soil heat flux to actually penetrate into the ground and thaw the soil (Pomeroy, personal communication, July 21, 2006), and that this time lag is probably more than one day. A fact supporting this idea is that there was also a time lag observed in the 'freezing' of the soil. The time periods when air temperatures dropped below 0°C and when this was actually reflected in the 'lack of soil thaw' and/or the actual refreezing of some areas did no correspond exactly but was actually lagged by a few days – see Chapter 7). Thus, perhaps a correlation between daily Q^* and daily Q_i may not realistically be expected.

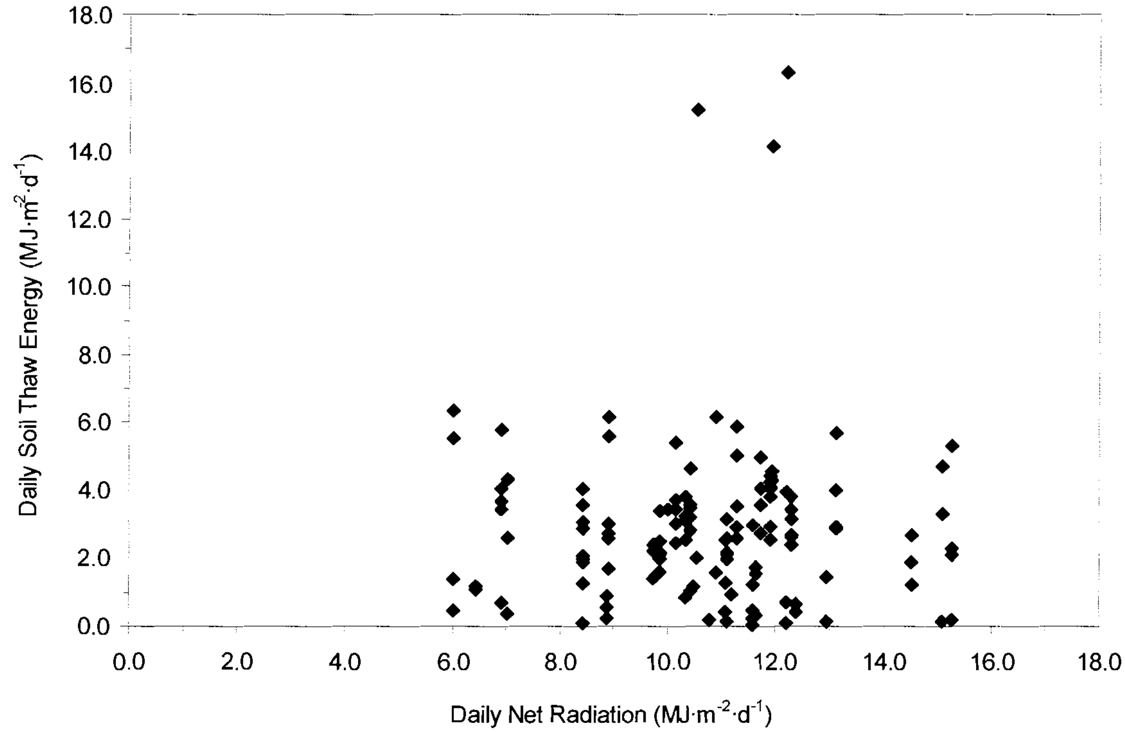

Figure 6-10: Daily net radiation and positive daily soil thaw energy for all eleven transects (located within the nine patches, n = 130) over the study period, DOY 114-165.

In order to arrive at a relation between Q_i and Q*, mean values for each were calculated for each patch (Figure 6-11 and Table 6-2). During the study period, there were periods of 'refreezing' or 'negative' soil thaw, which resulted in negative values of Q_i. Generally, there were 2-3 periods of continuously positive Q_i, interrupted by a few negative Q_i values. Any daily mean negative Q_i values were not included in determining an overall patch mean Q_i, as a negative Q_i would indicate freezing rather than thawing conditions. Table 6-2 summarizes the mean daily Q_i and Q* that were computed for each patch and for the soil pit. The overall slope mean Q_i for all eleven transects located within the nine patches was 2.83 ± 0.55 $MJ \cdot m^{-2} \cdot d^{-1}$ or 26% of Q*. At the soil pit, mean Q_i was 1.66 ± 1.43 $MJ \cdot m^{-2} \cdot d^{-1}$ or 15% of Q*.

The mean Q_i value, and its percentage of Q^*, derived from thaw depth measurements at the patches was higher than that obtained from the soil pit. This value (Q_i/Q^* = 26%) is also much higher than what is generally found in the literature (Quinton and Gray, 2001; Carey and Woo, 1998; Woo and Xia, 1996) for other permafrost terrain although it is important to note that there is generally a large degree of variability in the partitioning of Q_i as it depends on a variety of factors such as differences in terrain, slope, organic layer thickness, soil moisture, etc. The reason for this discrepancy is uncertain, but possible explanations are that after DOY 151, the slope of the soil pit's thaw depth with time changed quite abruptly and thaw slowed down considerably compared to changes in thaw depth at other points over the hillslope. This would result in a lower average rate of thaw for the soil pit compared to the slope, and a correspondingly lower value for Q_g. The other discrepancy between the two methods is that Goeller (2005) used a cumulative approach to estimate the percentage of Q^* contributing to Q_g, while this study considered an average approach and represented Q_i as a percentage of Q^*.

One of the early assumptions of this research was that soil thaw is solely the result of conductive heat transfer. But as mentioned previously (in Chapter 1), Zhao et al. (1997) suggest that convective heat transfer into frozen soils is an important heat transfer process and cannot be neglected. Thus, the percentage of Q^* contributing to Q_i, as discussed above, neglects other potentially important contributions to soil thaw. In the following section, the contribution of energy from the infiltration and refreezing of snowmelt water is discussed.

Table 6-2: **Mean soil thaw energy and net radiation for all 11 transects (located within the 9 patches) and the soil pit over the monitoring period. The slope mean is the overall mean value for the entire slope, taken as the mean of all patches. Q_i and Q^* are in $MJ \cdot m^{-2} \cdot d^{-1}$.**

	Patch 1		**Patch 2**		**Patch 3 (T1)**		**Patch 3 (T3)**		**Patch 4**		**Patch 5 (T1)**		**Patch 5 (T2)**		**Patch 6**		**Patch 7**		**Patch 8**		**Patch 9**		**Soil Pit**	
	Q_i	Q^*	Q_i	Q^*	Q_i	Q^*	Q_i	Q^*	Q_i	Q^*	Q_i	Q^*	Q_i	Q^*	Q_i	Q^*	Q_i	Q^*	Q_i	Q^*	Q_i	Q^*	Q_i	Q^*
Mean	3.28	10.37	3.10	10.29	3.22	10.43	3.04	10.60	3.25	10.31	3.14	10.77	2.22	11.65	2.63	10.54	3.03	10.42	2.78	11.96	1.49	11.28	1.66	11.31
Standard Error	0.82	0.40	0.85	0.51	1.00	0.47	0.27	0.44	0.49	0.81	0.38	0.73	0.46	0.73	0.39	0.61	0.47	0.93	0.41	0.50	0.56	0.94	0.26	0.43
n	18		18		14		10		12		11		7		11		10		9		10		29	
Q_i as a % of Q^*	31.68		30.09		30.88		28.62		31.53		29.12		19.07		24.95		29.10		23.27		13.21		14.70	
Start-End DOY	114	163	114	164	117	160	126	163	119	164	119	165	139	165	120	165	130	164	129	165	129	164	137	165
***Slope Mean**	**2.83**	**10.78**																						
Standard Deviation	**0.55**	**0.58**																						
n	**11**	**11**																						

*Slope mean is the mean Qi of all the patches (not including the soil pit).

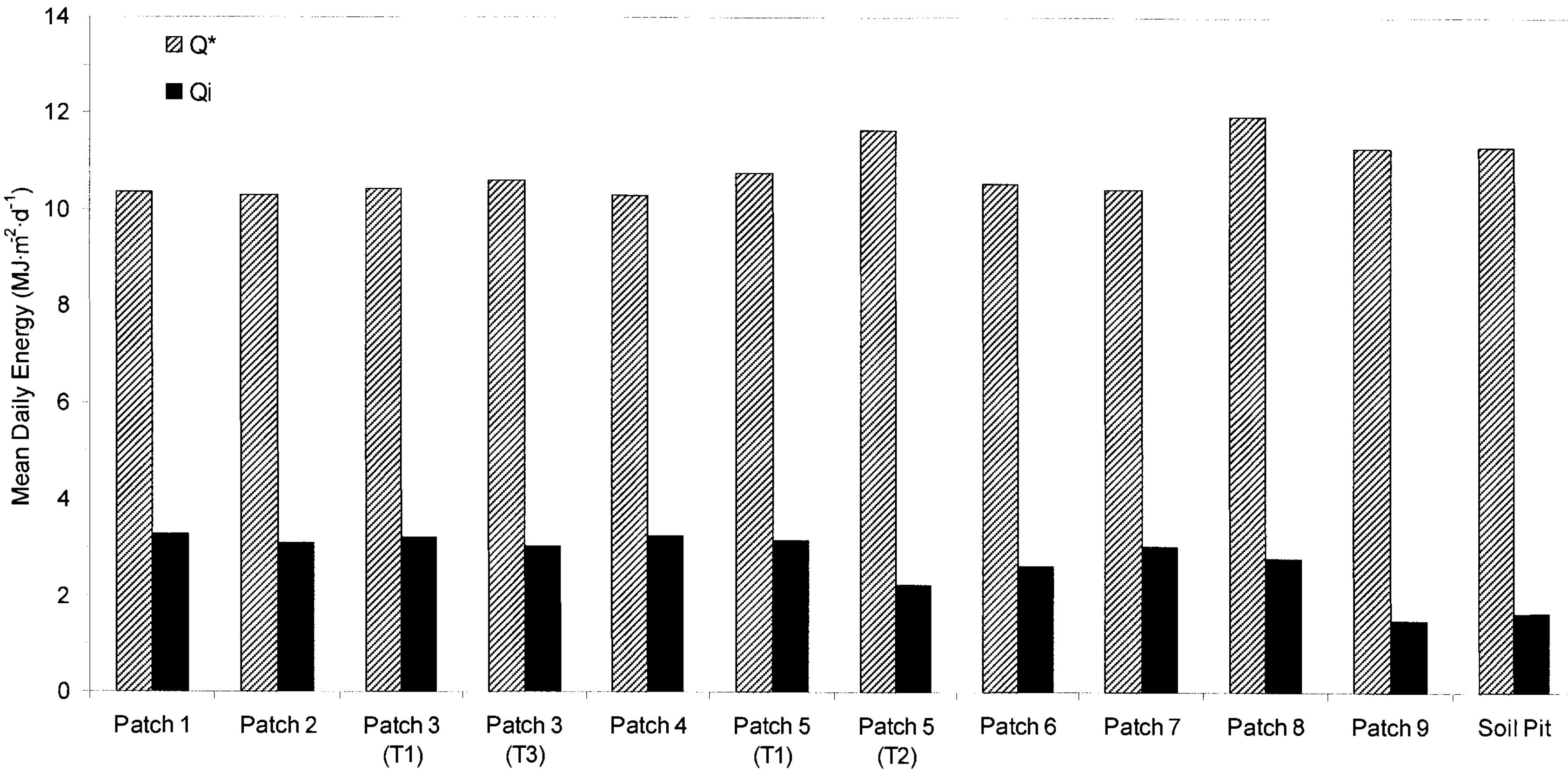

Figure 6-11: **Mean soil thaw energy and net radiation for all 11 transects (located within the 9 patches) and the soil pit over the monitoring period.**

6.5.3 Incorporating Energy from Infiltrating and Freezing Meltwater

McCartney et al. (2006) estimated infiltration into frozen soils at Granger Basin using 2003 data by subdividing the basin into nine HRU's (Hydrologic Response Units) based on their vegetation, soils, physiographic and hydrographic characteristics. One of these HRU's was the north-facing slope, the same north-facing slope upon which this research was conducted. McCartney et al. (2006) used the parametric equation of Zhao and Gray (1999) for cumulative infiltration:

$$INF = CS_0^{2.92}(1 - S_I)^{1.64}[(273.15 - T_I)/273.15]^{-0.45} t_0^{0.44} \tag{6-1}$$

where, INF is the frozen soil infiltration over the melt period (in mm), C is a coefficient, S_0 is the surface saturation moisture content at the soil surface (in $mm^3 \cdot mm^{-3}$), S_I is the average soil saturation (water and ice) of the top 0.4 m soil layer at the start of infiltration (in $mm^3 \cdot mm^{-3}$), T_I is the average soil temperature for the 0.4 m soil layer at the start of infiltration (in Kelvin), and t_0 is the infiltration opportunity time (in hours). Using Equation 6-1 and the parameter values obtained from McCartney et al. (2006), it was determined that approximately 216 mm of cumulative infiltration would occur during the melt period of 2003 on the north-facing slope.

To determine how much energy would be carried by this infiltrating meltwater into the soil, Equation 1-9 was employed. Recall that Equation 1-9 calculates the convection of heat by infiltrating water, Q_{INF}. The equation consists of three terms where C_w is the volumetric heat capacity of water (4.19×10^6 $J \cdot K^{-1} \cdot m^{-3}$), ΔT is the difference in temperature between rainwater or snowmelt water and the soil (Kelvin), and dF/dt is the rate of infiltrating water ($m \cdot s^{-1}$). McCartney et al. (2006) determined the average soil temperature for the 0.4 m soil layer at the start of infiltration to be -0.4°C. The temperature of the infiltrating snowmelt water was assumed to be approximately 0°C.

Thus, ΔT = 0.4. The rate of infiltrating water was determined by dividing the cumulative infiltration (216 mm) by the infiltration opportunity time, t_0 (which McCartney et al., 2006 calculated to be 953 hours). Thus, dF/dt = 6.3 x 10^{-8} m·s^{-1}, giving a Q_{INF} of 0.11 W·m^{-2} (or 0.01 MJ m^{-2}·d^{-1}). In comparison to the values for Q_i (calculated in the previous section), the contribution from infiltrating water appears to be minimal. Thus, the assumption of a purely conductive regime appears to be supported.

However, if all of this water were to freeze in the soil, the latent energy released (per unit area per time) can be determined using:

$$Q_{freeze} = \frac{h_f \cdot v_{water} \cdot \rho_{water}}{t_0} \tag{6-2}$$

where Q_{freeze} is the latent heat energy released (in W·m^{-2}), h_f is the latent heat of fusion of ice (333500 J·kg^{-1}), v_{water} is the volume of water per unit area (0.216 m^3·m^{-2}), ρ_{water} is the density of water (1000 kg·m^{-3}), and t_0 is the infiltration opportunity time (3430800 s) from Equation 6-1 (converted from hours into seconds). Thus, Q_{freeze} = 21.00 W·m^{-2} or 1.81 MJ·m^{-2}·d^{-1} is released when this infiltrating meltwater freezes. The significance of this amount of energy (from both the infiltration and freezing meltwater) in modifying the magnitude of soil thaw energy is discussed below.

The amount of energy advected from the infiltration and subsequent release of latent heat due to the freezing of this meltwater was calculated to be 0.01 MJ m^{-2}·d^{-1} and 1.81 MJ m^{-2} day^{-2}, respectively. If this amount of energy contributed to warming the soil prior to actual thaw, then the amount of energy contributing to soil thaw from radiation would be correspondingly less. In the previous section, it was determined that Q_i = 2.83 MJ·m^{-2}·d^{-1}. However, Q_{INF} + Q_{freeze} = 1.82 MJ·m^{-2}·d^{-1}. Thus, only (2.83 – 1.82) = 1.01 MJ·m^{-2}·d^{-1} would actually be contributed from Q*. This results in a 9.4% contribution from Q* to Q_i, as opposed to 26% estimated by not accounting for the energy from infiltrating and refreezing meltwater. In the following chapter, Q_i, Q_{INF} and Q_{freeze} are used to estimate soil thaw depth over the hillslope.

CHAPTER 7: ESTIMATING SOIL THAW ENERGY OVER THE HILLSLOPE

7.1 Introduction

According to Quinton et al. (2004), current methods of modelling active layer thaw appear to provide reasonable results for thaw at a point, but are unable to capture the relatively large variability of thaw over the slope. For example, in their study, the ground below the meteorological tower became snow-free relatively late and, therefore, soil thaw in their model simulation began later than was observed at many points. In this study, the opposite situation occurred, where the ground below the meteorological tower became snow-free relatively earlier than the rest of the slope. Clearly, the placement of the meteorological tower is critical to obtaining representative values of Q^* for snow-covered and snow-free surfaces at the hillslope scale. Consequently, there are significant uncertainties in distributing Q^* for different surfaces over the hillslope.

Nevertheless, this chapter attempts to spatially distribute the energy that is used to thaw the soil (and hence lower the frost table) over the hillslope, in order to develop a more accurate picture of how the hillslope thaws. In Chapters 5 and 6, the mean contribution of net radiation to snowmelt and to soil thaw was defined. Therefore, the relationship between net radiation and soil thaw energy along with the snowcover depletion curve (Figure 5-6) are used to derive an areal distribution of soil thaw over the north-facing slope at four representative days during the melt season using the theoretical framework described in the following section. The four DOY's were chosen in order to obtain a 'snapshot' of the hillslope at various stages of soil thaw in order to understand how the distribution of soil thaw depths changes with time. Also, since this method is dependent on estimating soil thaw depths immediately after snowcover removal, and continuing to estimate them after, the choice of DOY's was limited to when actual measurements of soil thaw were obtained immediately after a point on a transect had become snow-free. The contribution of infiltrating and freezing meltwater to soil pre-warming is also represented.

7.2 Hillslope Conceptual Flowchart

Figure 7-1 is a conceptual flowchart of the analogous energy flux processes that occur over a typical permafrost hillslope. The way in which incoming energy at the surface is used is dependent on the nature of that surface. If the surface is snow-covered, then most of the available incoming energy will be used to melt the snow. If the surface is snow-free, then a certain portion of the available incoming energy will be used to melt the ice in the active layer and, therefore, thaw the soil (i.e., lower the frost table). A cross-sectional view (Figure 7-2) illustrates how an idealized snow-free patch grows in the lateral direction (along the slope) and thaws in the vertical direction (down through the soil profile). However, in the previous chapter, it was demonstrated that infiltrating and freezing meltwater may contribute to warming of the soil prior to thaw even though no actual thaw was observed when the snowcover was removed. Goeller (2005) found that when the ground became snow-free above the soil pit at Granger Basin, subsurface soil temperatures were at or near 0°C. He suggested that the percolation of and subsequent freezing of meltwater into the soil prior to ground exposure could have explained this. This also suggests that prior to thawing, frozen soil layers were not initially saturated, but that the percolation and freezing of the meltwater may have filled and sealed some or all available pores (Goeller, 2005; Woo, 1986; Woo and Steer, 1983).

Field observations made on the north-facing slope during this study never actually found a 'thaw depth' on ground that had immediately become snow-free. The presence of a thaw depth was also tested underneath the snowcover by inserting the graduated steel rod into the ground while there was snowcover above it, and no thaw depth was measured (i.e., the ground was frozen and saturated underneath the snowcover). However, the potential for a 'thaw depth' to exist before the removal of the snowcover was a possibility due to potential downslope advection from a snow-free patch to the snow-covered soil and also from lateral drainage of meltwater. Nevertheless, given that no thaw depth was observed in this study, yet the potential for infiltrating water existed, it seems reasonable to conclude that the infiltration and freezing of meltwater may have simply warmed the soil, but not resulted in thaw. Therefore, once the snow cover had been removed, it would not take much more energy to result in rapid thaw.

The role of infiltrating and freezing meltwater is represented in the conceptual flowchart (Figure 7-1) and slope profiles (Figure 7-2) as soil "pre-warming". In this study, the term "soil pre-warming" refers to the freezing of infiltrated meltwater and the subsequent release of latent energy that raises the temperature of the soil close to 0 °C (Goeller, 2005; Quinton et al., 2005; Rist and Phillips, 2005, Zhao et al., 1997). It is important to note that this soil pre-warming does not result in 'thaw' (i.e. lowering of the frost table by the melting of ice in the soil) but instead raises the temperature of the frozen ground, thus requiring less energy to melt the ice and lower the frost table once the ground becomes snow-free. Because the estimate of infiltration was only available as a cumulative value at the end of the melt period (McCartney et al., 2006), incorporating Q_{INF} into the temporal calculations of soil thaw at the hillslope scale was difficult. As this energy acts to pre-warm the soil prior to thaw, it was added to the energy from Q* only for the initial period following exposure.

Figure 7-3 shows an idealized diagram of snowmelt and soil thaw on a hillslope, which was developed by combining processes that occur in both Figure 7-1 and Figure 7-2. In Figure 7-3 (i), the slope is 100% snow covered, there are no snow-free areas and, therefore, the thaw depth on the slope is zero. In the second diagram (Figure 7-3 (ii)), some of the snowcover has ablated, creating bare patches. These bare patches have a thaw depth equal to the thaw depth measured (and/or estimated) on that given day (in this example, DOY 114). This total thaw depth includes both the energy contribution from Q* and from pre-warming of the soil (due to the infiltration and freezing of meltwater).

In Figure 7-3 (iii), snow continues to melt and new areas of the slope are exposed. In addition, areas that were exposed on DOY 114 continue to thaw. Therefore, in Figure 7-3 (iii) the red contours have a thaw depth equal to the thaw depth measured (and/or estimated) on DOY 120. Thus, areas first exposed on DOY 114 will now have a thaw depth = 'DOY 114' + 'DOY 120'. This process continues such that in Figure 7-3 (iv), newly snow-free areas will have a thaw depth equal to the thaw depth measured (and/or estimated) on DOY 131. In this Figure, areas exposed on DOY 120 will have a thaw depth = 'DOY 120' + 'DOY 131'. Snow-free areas exposed on DOY 114 will have a thaw depth = 'DOY 114' + 'DOY 120' + 'DOY 131', etc.

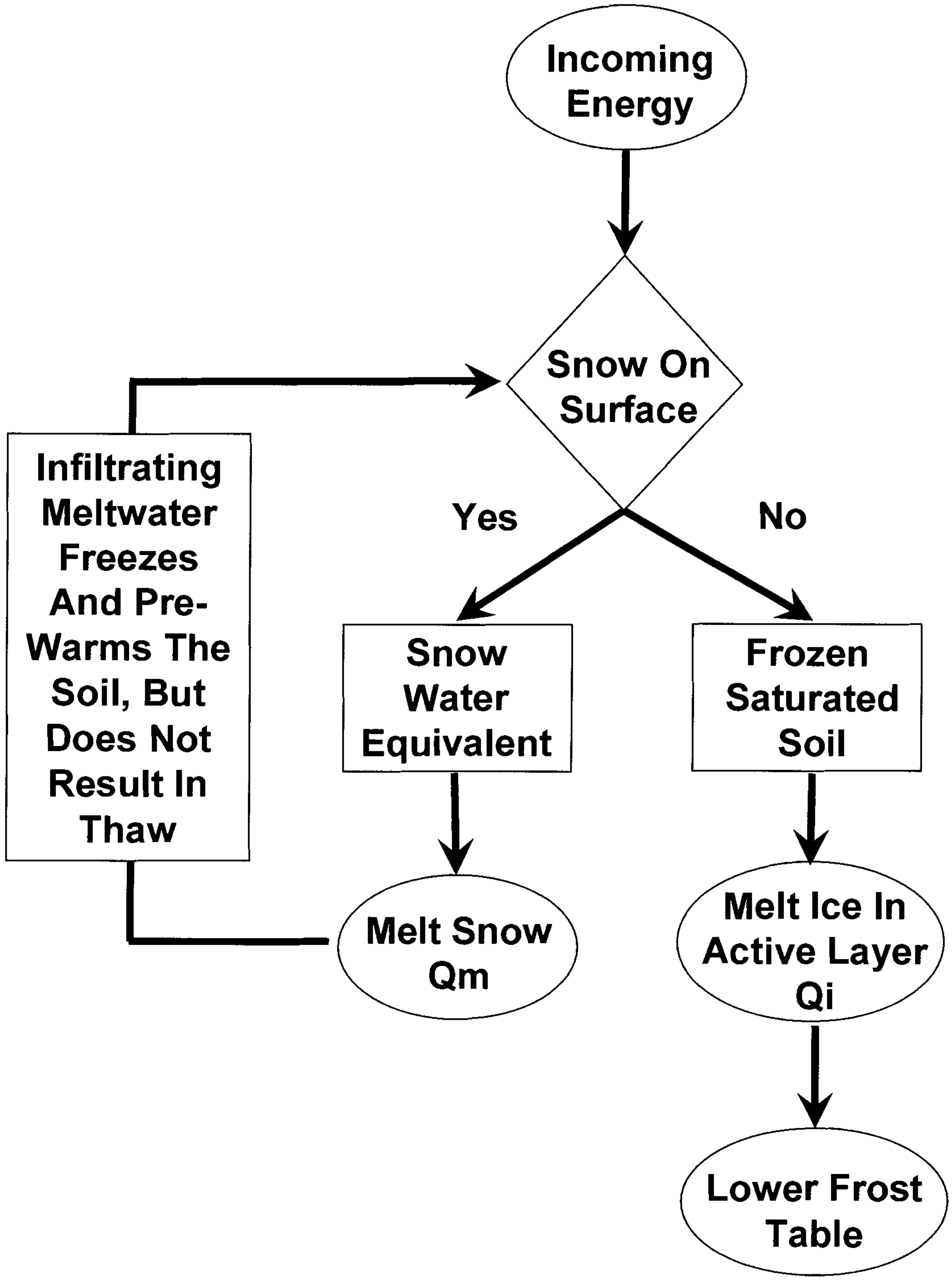

Figure 7-1: Conceptual flowchart of active layer development. Incoming energy is used to melt the snowcover. Once the snowcover has been removed, part of the available incoming energy can be used to melt the ice in the active layer and lower the frost table (i.e., thaw the soil).

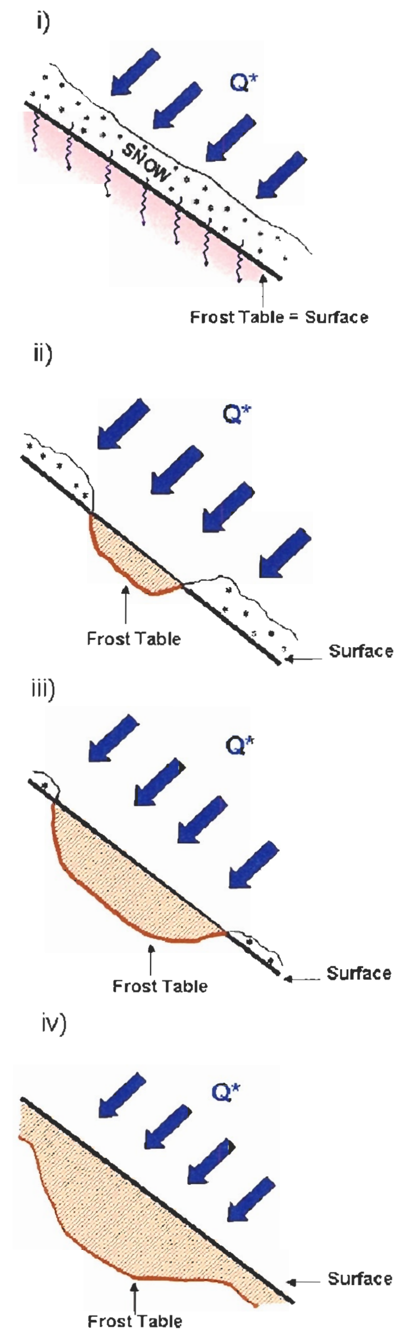

Figure 7-2: Cross-sectional view of the idealized growth of a snow-free patch and the subsequent spatial variations in thaw depth that occur. Energy from infiltrating and freezing meltwater does not result directly in soil thaw, but rather pre-warms the soil such that immediately following ground exposure, initial soil thaw is rapid. The potential for soil thaw before snowcover removal does exist due to the possibility of downslope advection from the snow-free patch to the snow-covered soil and/or from lateral drainage of meltwater from upslope. However, these processes were not observed in this study.

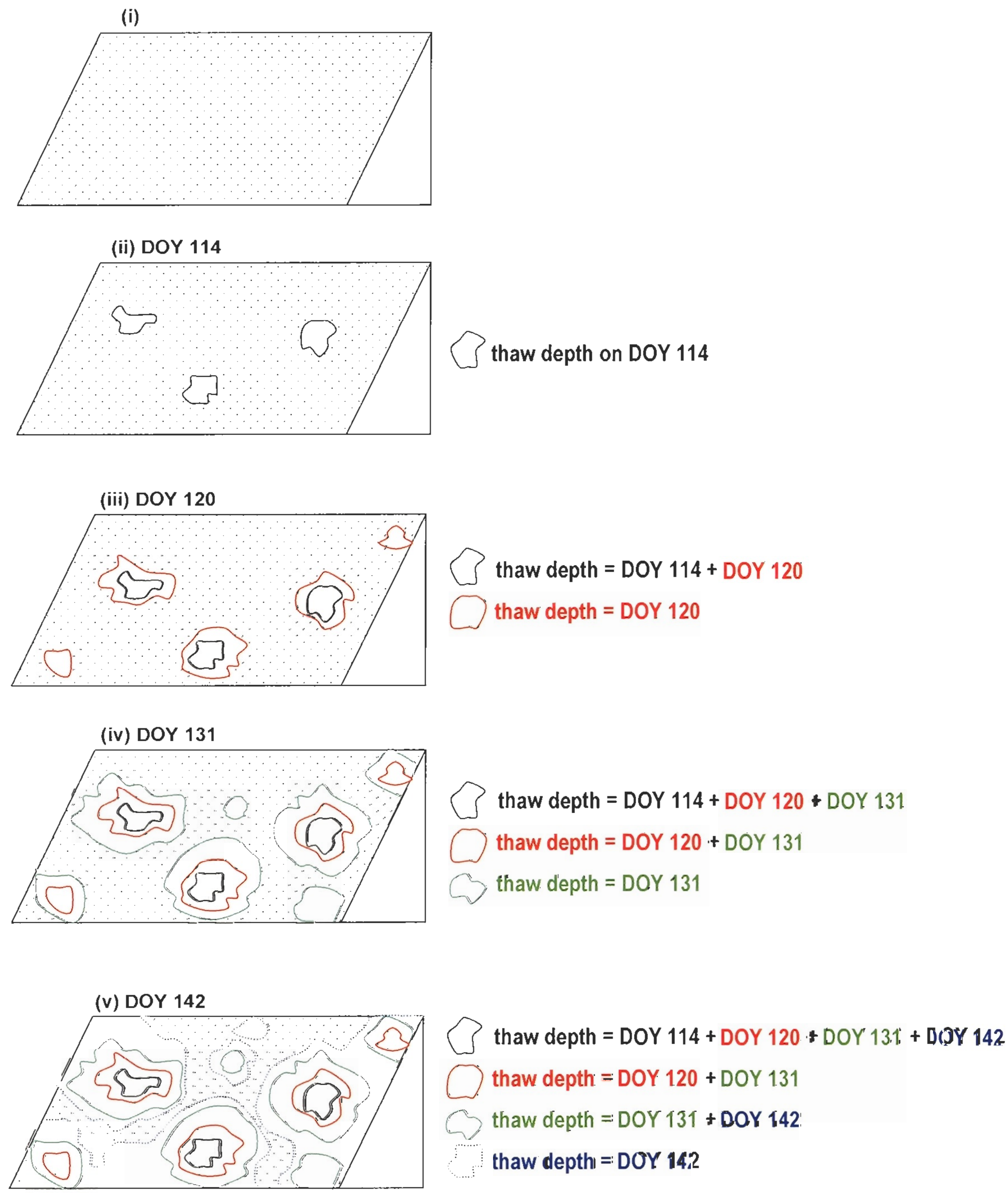

Figure 7-3: Oblique view of the sequential process by which snow-free patch growth occurs. Each new area that is exposed will have a thaw depth based on the amount of incoming energy plus the energy from pre-warming. Older snow-free areas will have a thaw depth equal to this plus their old thaw depth (no pre-warming contribution).

7.3 Estimating Soil Thaw Over The North-Facing Slope

The spatial distribution of soil thaw was determined for four days during the snowmelt period, corresponding to snow-covered areas of 89% (April 24/DOY 114), 51% (April 30/DOY 120), 28% (May 11/DOY 131) and 13% (May 22/DOY 142) as shown in Figure 7-4. For each time period, the methodology consisted of, first, estimating the amount of thaw that would have resulted from the release of stored energy from both the infiltration and freezing of meltwater (prior to actual soil thaw) – thus contributing to soil pre-warming. In these calculations, this energy (1.82 $MJ \cdot m^{-2} \cdot d^{-1}$) is applied only to the first snow-free period. In the subsequent intervals, thaw is calculated from the contribution of Q* (i.e., 9.4%). The rate of thaw over each time interval is calculated using Equation 1-10. The percentage of Q* that contributes to Q_i is considered an average value for the entire soil thaw period. A mean thaw depth for the slope was then estimated by multiplying the thaw rate by the number of days to the next estimation day, and adding this value to the previously estimated thaw depth. This number was then compared to the measured mean thaw depth on the slope (i.e., the mean of all points on the slope that were measured on this date).

In undertaking this analysis, a number of assumptions were necessary. First, since the study period began on DOY 112 (April 22) when the slope was 96% snow-covered (Figure 5-6), there was no way to actually verify what date the slope was 100% snow-covered. A best-fit line through the percent snow covered area depletion curve (Figure 5-6) suggests that the slope was 100% snow covered on DOY 111 (April 21). Thus, it was assumed that the slope started to become snow-free on April 21. Second, since the hillslope meteorological tower became snow-free on DOY 128 (May 8), there were no measured Q* values for snow-free surfaces prior to this date, even though there were snow-free areas on the slope. For these situations, Q* was modelled using the method described in Section 4.2.2, as modelled net radiation over the snow-free surface after DOY 128 (May 8) reasonably approximated measured values. Third, it is assumed that although the stored energy (from the infiltration and freezing of the meltwater) accumulating beneath the snow cover prior to melt did not result in observable thaw; the amount of stored energy is applied equally over the first interval following melt. This is likely an approximation to the actual conditions, but effectively allows this energy to be incorporated.

a) DOY 114 (April 24) – 89% snow-covered

b) DOY 120 (April 30) – 51% snow-covered

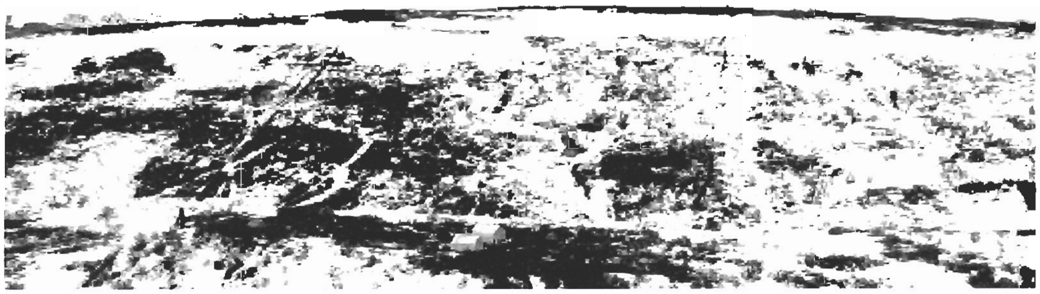

c) DOY 131 (May 11) – 28% snow-covered

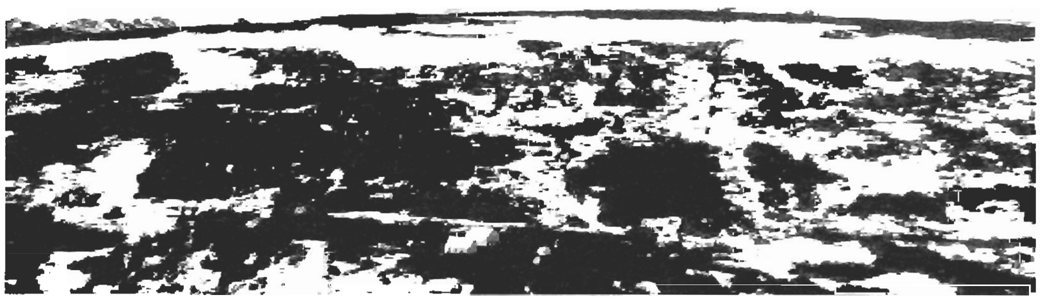

d) DOY 142 (May 22) – 13% snow-covered

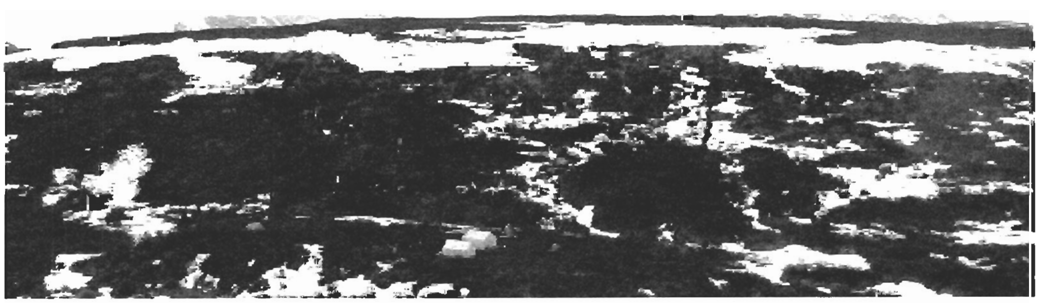

Figure 7-4: Photos of the north-facing slope taken from a point half-way up the opposing slope across the valley. Photos were taken from the same point and from roughly the same time each day. Photos in this figure represent snow-covered areas of 89%, 51%, 28% and 13% respectively.

Table 7-1 summarizes the mean measured and mean calculated cumulative thaw depths for the slope. In this table, the estimated total thaw depth for each given DOY is shown in bold type. These values are then added to the estimated thaw depths for the previous intervals (resulting in a cumulative estimated thaw depth). For example, Q* on DOY 114 was 10.53 $MJ\cdot m^{-2}$. Of this, 9.4% is partitioned into Q_i (or 0.99 $MJ\cdot m^{-2}$), yielding a thaw rate of $dh/dt = 0.37\ cm\cdot d^{-1}$. But if the energy from the infiltration and freezing of meltwater is also converted into a thaw rate (1.82 $MJ\cdot m^{-2}\cdot d^{-1}$= 0.68 $cm\cdot d^{-1}$) and added to the thaw rate from net radiation, then the thaw depth on DOY 114 is estimated to be (0.68 $cm\cdot d^{-1}$)*(4 days) + 0.37 cm = 3.1 cm, assuming the first interval for this day is DOY 111-DOY 114 (i.e., 4 days). This represents a mean thaw depth of 3.1 cm in the snow-free areas on the north-facing slope on DOY 114. The mean measured thaw depth on DOY 114 was a comparable 4.5 cm. For the following time intervals, the thaw rate is calculated solely as a percentage of net radiation (i.e., 9.4% of daily Q* is used to estimate the daily thaw rate, and thaw depths are accumulated for each subsequent estimation interval).

In the next column, Q* on DOY 120 was 6.90 $MJ\cdot m^{-2}$, of which Q_i is estimated as 0.65 $MJ\cdot m^{-2}$. Again, if the energy from the infiltration and freezing of meltwater is also converted into a thaw rate and added to the thaw rate obtained from radiation, then the total estimated thaw depth on DOY 120 = 4.3 cm. The mean measured thaw depth on DOY 120 was 5.1 cm.

Following this same procedure (i.e., adding the estimated thaw depth for the current day to that of the previous days), the measured and estimated thaw depths correspond reasonably well although thaw is slightly underestimated for the first two intervals, and slightly overestimated in the second two intervals. Note that there was also a period of refreezing around DOY 131 (shaded grey column in Table 7-1). Figure

7-5 is a plot of measured and estimated thaw depths for points that became snow-free on DOY 114. Although there are only 4 points available for comparison, the linear relationship is reasonable (R^2 = 0.75).

The two most likely explanations for the early time discrepancy in thaw depth is, first, the assumption of 100% snowcover on DOY 111, which could result in an inaccurate initial condition for the calculations. If the ground had begun to thaw earlier than DOY 111, the initial estimate of thaw depth would be underestimated (as observed). Second, an underestimate of the amount of stored energy from infiltrating and freezing meltwater. Recall that a uniform amount of energy (1.82 $MJ \cdot m^{-2} \cdot d^{-1}$) was applied daily in the interval prior to snowcover removal.

Another explanation is the possible role of slope drainage. Kane et al. (2001) stated that on slopes underlain by permafrost, the movement of water along 'water tracks' (areas of enhanced soil moisture) resulted in deeper thaw depths (convective heat transfer). As discussed previously, no relation between drainage and moisture content could be determined for this study, due to the fact that moisture measurements were made in only the upper 5 cm of soil and because of the complex microtopography on the slope that would have resulted in complex drainage patterns.

Another source of error inherent to applying this method at this site include; an overestimation of ice content, which would result in an underestimate of thaw since there is actually less ice in the ground to thaw, than what is expected (since the calculation of Q_i is dependent on the assumption that ice content equals porosity). Finally, while the method appears to provide reasonable estimates of rate of change, it is limited in that it does not account for times when the slope is 'refreezing'. For example, refreezing around DOY 131 is not accounted for in the thaw accumulation calculation.

The increased spatial variability of soil thaw observed over time is the result of the accumulation of energy (Q_i) in the areas that have became snow-free early on, compared to those areas that have just recently become snow-free. Since the ground does not begin to thaw until the snowcover is removed, areas that have just become snow-free have a frost table that is at or near the surface, whereas areas that became snow-free earlier on and have already begun to thaw will continue to thaw with the added energy. For example, the 11% of the slope that was snow-free on DOY 114 will receive the same amount of energy that the most recently snow-free areas will, but will have an overall greater thaw depth than those areas that have just recently become snow-free. Thus, observations of the spatial variability in soil thaw suggest that this method of estimating thaw depth is potentially useful and can result in a more accurate representation of active layer development at a hillslope scale, compared to what is provided by current methods that rely on point measurement of active layer thaw, which can result in an over or underestimation of subsurface flow rates.

Table 7-1: **Summary of mean estimated and mean measured thaw depths on the north-facing slope at four different dates. Only the first interval has the effect of Q_{INF} and Q_{freeze} incorporated into the estimates of thaw depth. After that interval, thaw energy is calculated solely from the contribution of Q* (i.e., once the snowcover has been removed). Estimated thaw depths were calculated by adding the estimated thaw rate between each DOY interval to the previously estimated thaw depth. All thaw depths are in cm. Shaded column indicates a freezing period.**

	DATE	DOY 114	DOY 120	DOY 131	DOY 142
	% Snow-Free	11	49	72	87
	Daily $Q_{INF} + Q_{freeze}$ ($MJ \cdot m^{-2} \cdot d^{-1}$)	1.82	1.82	1.82	1.82
	Daily Q* ($MJ \cdot m^{-2} \cdot d^{-1}$)	10.53	6.90	7.03	8.90
	Mean Q_i ($MJ \cdot m^{-2} \cdot d^{-1}$)	0.99	0.65	0.66	0.83
Date Snow-Free	**DOY 114 (APRIL 24)**				
	Estimated Thaw Depth from $Q_{INF} + Q_{freeze}$	2.71			
	Estimated Thaw Depth from Q for that DOY	0.37			
	**Estimated Cumulative Thaw Depth	**3.1**	5.2	8.8	12.4
	Mean Measured Thaw Depth	4.5	6.5	6.5	9.7
	DOY 120 (APRIL 30)				
	Estimated Thaw Depth from $Q_{INF} + Q_{freeze}$		4.1		
	Estimated Thaw Depth from Q for that DOY		0.24		
	**Estimated Cumulative Thaw Depth		**4.3**	7.9	11.4
	Mean Measured Thaw Depth		5.1	5.0	9.1
	DOY 131 (MAY 11)				
	Estimated Thaw Depth from $Q_{INF} + Q_{freeze}$			7.5	
	Estimated Thaw Depth from Q for that DOY			0.25	
	**Estimated Cumulative Thaw Depth			**7.7**	11.2
	Mean Measured Thaw Depth			6.8	8.6
	DOY 142 (MAY 22)				
	Estimated Thaw Depth from $Q_{INF} + Q_{freeze}$				7.45
	Estimated Thaw Depth from Q for that DOY				0.31
	**Estimated Cumulative Thaw Depth				**7.8**
	Mean Measured Thaw Depth				3.3

* "Estimated thaw depth from Q* for that DOY" is calculated only from Q_i as a % of Q*
** "Estimated cumulative thaw depth" is calculated by adding the pre-warming energy to the energy from Q* for the first interval, and adding only the energy from Q* for each interval thereafter.

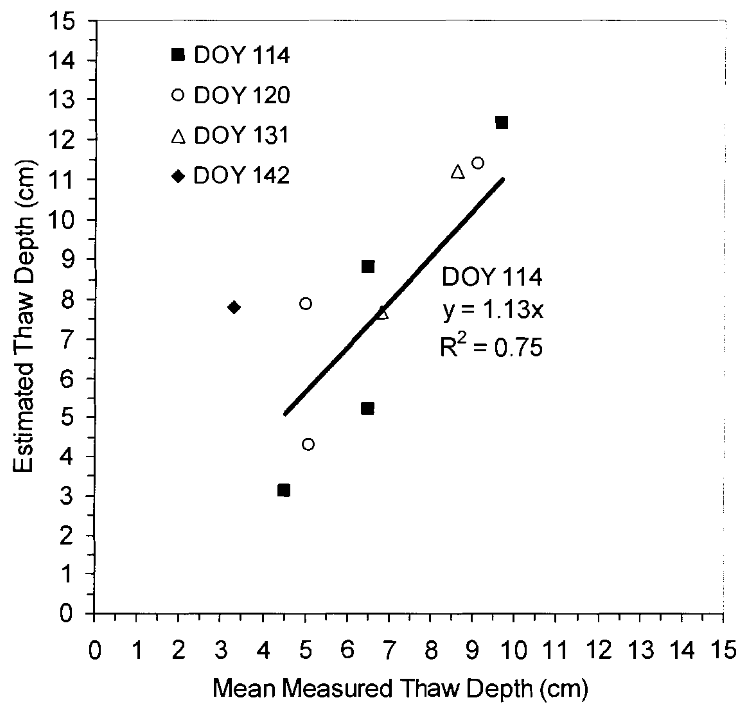

Figure 7-5: Calculated (estimated) versus mean measured thaw depths as reported in Table 7-1 for points that became snow-free on DOY 114, DOY 120, DOY 131 and DOY 142. The trendline is for the DOY 114 times series (square markers).

CHAPTER 8: CONCLUSIONS AND RECOMMENDATIONS

Improving the understanding and representation of ground thaw at the hillslope scale is an important step in gaining a greater overall understanding of the processes that control drainage and soil moisture on tundra hillslopes. The overall purpose of this study was to determine the relation between net radiation and the energy used to melt snow and thaw the snow-free ground during the snowmelt season, and use these relations to predict soil thaw at the hillslope scale.

A major limitation of the snowmelt energy component of the study was the limited period for which Q* data were available for the hillslope. Over the relatively short time period (six days), for which net radiation and melt energy could be compared, Q* contributes, on average, approximately 91% and 94% to melt the drift and non-drift snow, respectively. The mean Q_m for both the non-drift and drift was approximately 4 $MJ \cdot m^{-2} \cdot d^{-1}$, although the non-drift Q_m would be expected to be higher due to the presence of shrubs enhancing the melt rate. Future work could explore the relation between the turbulent fluxes of sensible and latent heat, and ground heat flux, which may perhaps lead to a more 'robust' empirical method to calculate snowmelt.

Soil thaw is highly spatially and temporally variable over small scales (i.e., 0.5 m). Soil thaw rate was shown to be related to liquid soil moisture measured in the near surface; however, both positive and negative correlations were observed, with no clear pattern among the transects. The drainage of soil moisture away from the transect is thought to be the primary factor controlling the rate of soil thaw, but this effect could not be quantified because soil moisture was measured only within the upper 5 cm.

This research has also shown that the partitioning of energy at the surface is reasonably consistent (9.4% of Q* is used to thaw the soil) at the hillslope scale, when the effects of infiltration and freezing of meltwater into the soil are taken into account. It must be noted that values can range widely depending on a wide variety of site-specific factors, such as quantity and state of soil moisture, organic soil thickness, topography, vegetation, snowcover duration, slope and aspect. Also, whether the relations are consistent from year to year at the same site is an important factor in determining the transferability of these relationships for future modelling purposes. Unfortunately, this study only analyzed a single year of data, and it is suggested that possible future research could compare inter-annual partitioning.

One of the other major drawbacks of this study was that there was only one measurement of net radiation on the slope. Ideally, radiation measurements would be available continuously for a snow surface and a snow-free surface so that partitioning relations and comparisons with melt and thaw energy would be more reliable and representative; however, even if this were to be achieved, the patchiness that occurs during melt would still complicate the 'view' of the sensor and hence the data. Also, the timing and date of the first snow-free patches would aid in determining the initial start time of thaw.

A preliminary assumption in this thesis was that thaw was due only to conduction from the surface. However, if there are additional sources of energy contributing to soil thaw, then the actual measured thaw depths will be greater than what they would be based solely on conduction from a radiatively-warmed surface, thus leading to elevated estimates of Q_i. Consequently, an attempt was made to quantify the energy released from the infiltration and freezing of meltwater, and to account for it when estimating soil thaw over the hillslope. Although much work remains to be done with regards to adequately characterizing and quantifying the contribution of radiation to soil thaw energy, the method presented in this thesis does represent a promising approach for the estimation of soil thaw based on a direct link between surface fluxes and the subsurface energy regime.

REFERENCES

Affleck, R. T., and S. A. Shoop. 2001. Spatial Analysis of Thaw Depth. Technical Report ERDC/CRREL TR-01-1, US Army Corps of Engineers Cold Regions Research and Engineering Laboratory.

Anderton, S. P., S. M. White, and B. Alvera. 2002. Micro-Scale Spatial Variability and the Timing of Snow Melt Runoff in a High Mountain Catchment. Journal of Hydrology **268**:158-176.

Bailey, W. G., E. J. Weick, and J. D. Bowers. 1989. The Radiation Balance of Alpine Tundra, Plateau Mountain, Alberta, Canada. Arctic and Alpine Research **21**:126-134.

Bewley, D., J. W. Pomeroy, and R. Essery. submitted. Processes of Solar Radiation Transfer Through a Sub-Arctic Shrub Canopy.1-28.

Bliss, L. C., and N. V. Matveyeva. 1992. Circumpolar Arctic Vegetation. Pages 59-89 *in* F. S. Chapin, R. L. Jefferies, J. F. Reynolds, G. R. Shaver, and J. Svoboda, editors. Arctic Ecosystems in a Changing Climate: An Ecological Perspective. Academic Press, San Diego.

Boelter, D. H. 1965. Hydraulic Conductivity of Peats. Soil Science **100**:227-231.

Boike, J., K. Roth, and O. Ippisch. 2003. Seasonal Snow Cover on Frozen Ground: Energy Balance Calculations of a Permafrost Site Near Ny-Alesund, Spitsbergen. Journal of Geophysical Research **108**.

Brown, J., and N. A. Grave. 1979. Physical and Thermal Disturbance and Protection of Permafrost. Special Report 79-5 US Army CRREL.

Campbell, S. I. 2001. HydroSense Instruction Manual. Instruction Manual Campbell Scientific Canada Corporation, Edmonton.

Carey, S. K., and W. L. Quinton. 2005. Evaluating Runoff Generation During Summer Using Hydrometric, Stable Isotope and Hydrochemical Methods in a Discontinuous Permafrost Alpine Catchment. Hydrological Processes **19**:95-114.

Carey, S. K., and M.-k. Woo. 2000. Within-Slope Variability of Ground Heat Flux, Subarctic Yukon. Physical Geography **21**:407-417.

Carey, S. K., and M.-k. Woo. 1999. Hydrology of Two Slopes in Subarctic Yukon, Canada. Hydrological Processes **13**:2549-2562.

Carey, S. K., and M.-k. Woo. 1998. A Case Study of Active Layer Thaw and its Controlling Factors. Pages 127-131 *in* 7th International Conference on Permafrost. Centre d'etudes nordiques, Quebec.

Church, M. 1974. Hydrology and Permafrost with Reference to Northern North America. Pages 7-20 *in* Permafrost Hydrology; Proceedings of Workshop Seminar. Canadian National Committee, International Hydrological Decade, Ottawa.

Dean, T. J., J. P. Bell, and A. J. B. Baty. 1987. Soil Moisture Measurement by An Improved Capacitance Technique, Part 1: Sensor Design and Performance. Journal of Hydrology **93**:67-78.

Dingman, S. L. 2002. Physical Hydrology, Second edition. Prentice-Hall Inc., New Jersey.

Dingman, S. L. 1973. Effects of Permafrost on Stream Flow Characteristics in the Discontinuous Permafrost Zone of Central Alaska. Pages 447-453 *in* Permafrost: the North American Contribution to the Second International Conference (North American Contribution). Washington National Academy of Sciences, Washington.

Dirmhirn, I., and F. D. Eaton. 1975. Some characteristics of the albedo of snow. Journal of Applied Meteorology **14**:375-379.

Dunne, T., and L. B. Leopold. 1978. Water in Environmental Planning. W.H. Freeman and Company, New York.

Evett, S. R., and J. L. Steiner. 1995. Precision of Neutron Scattering and Capacitance Type Soil Water Content Gauges From Field Calibration. Journal of the Soil Science Society of America **59**:961-968.

Farouki, O. T. 1981. The Thermal Properties of Soils in Cold Regions. Cold Region Science and Technology **5**:67-75.

Foster, J. L. 1989. The Significance of the Date of Snow Disappearance on the Arctic Tundra as a Possible Indicator of Climate Change. Arctic and Alpine Research **21**:60-70.

French, H. M. 1996. The Periglacial Environment. Longman Group Limited, Singapore.

Garnier, B. J., and A. Ohmura. 1970. The Evaluation of Surface Variations in Solar Radiation Income. Solar Energy **13**:21-34.

Goeller, N. T. 2005. Measurement of Selected Thermal and Physical Properties of Organic Soil By Direct and Indirect Methods. M.Sc. Simon Fraser University, Burnaby.

Gomersall, C. E., and K. M. Hinkel. 2001. Estimating the Variability of Active Layer Thaw Depth in Two Physiographic Regions of Northern Alaska. Geographical Analysis **33**:141-155.

Granger, R. J., J. W. Pomeroy, and J. Parviainen. 2002. Boundary Layer Integration Approach to Advection of Sensible Heat to a Patchy Snow Cover. Hydrological Processes **16**:3559-3569.

Gray, D. M., D. E. L. Erickson, and F. Abbey. 1974. Energy Studies in an Arctic Environment. Technical Report 74-18, University of Saskatchewan, Saskatoon.

Grzes, M. 1988. Summer Thawing of Different Grounds - An Empirical Model for Western Spitsbergen. Pages 361-363 *in* K. Senneset, editor. 5th International Conference on Permafrost. Tapir Publishers, Trondheim, Norway.

Halliwell, D. H., and W. R. Rouse. 1987. Soil Heat Flux in Permafrost: Characteristics and Accuracy of Measurement. Journal of Climatology **7**:571-584.

Harding, R. J., and J. W. Pomeroy. 1996. The energy balance of the winter boreal landscape. Journal of Climate **9**:2778-2787.

Hillel, D. 1998. Environmental Soil Physics. Academic Press, San Diego.

Hillel, D. 1982. Introduction to Soil Physics. Academic Press, New York.

Hinkel, K. M., F. Paetzold, F. E. Nelson, and J. G. Bockheim. 2001. Patterns of Soil Temperature and Moisture in the Active Layer and Upper Permafrost at Barrow, Alaska: 1993-1999. Global and Planetary Change **29**:293-309.

Hinzman, L. D., D. L. Kane, R. E. Gieck, and K. R. Everett. 1991. Hydrologic and Thermal Properties of the Active Layer in the Alaskan Arctic. Cold Region Science and Technology **19**:95-110.

Hubley, R. C. 1955. Measurements of diurnal variations in snow albedo on Lemon Creek Glacier, Alaska. Journal of Glaciology **2**:560-563.

Huo, Z. 1991. Measurement and Modelling of the Radiation Budget of Alpine Tundra, Plateau Mountain, Alberta, Canada. M.Sc. Simon Fraser University, Vancouver.

James, W., and A. R. Vieira-Ribeiro. 1975. Effect of Spatially Disaggregated Snowmelt on Seasonal Degree-Day-Factor Variations in the High Arctic. Pages 289-295 *in* Proceedings, Canadian Hydrology Symposium.

Janowicz, J. R., N. R. Hedstrom, J. W. Pomeroy, R. J. Granger, and S. K. Carey. 2004. Wolf Creek Research Basin Water Balance Studies. Pages 195-204 *in* Northern Research Basins Water Balance. International Association of Hydrological Sciences, Victoria, Canada.

Janowicz, J. R. 1999. Wolf Creek Research Basin - Overview. Pages 121-130 *in* J. W. Pomeroy and R. J. Granger, editors. Wolf Creek Research Basin: Hydrology, Ecology and Environment. National Water Research Institute, Saskatoon.

Kaminsky, K. Z., and R. Dubayah. 1997. Estimation of Surface Net Radiation in the Boreal Forest and Northern Prairie from Shortwave Flux Measurements. Journal of Geophysical Research **102**:29707-29716.

Kane, D. L., K. M. Hinkel, D. J. Goering, L. D. Hinzman, and S. L. Outcalt. 2001. Non-Conductive Heat Transfer Associated With Frozen Soils. Global and Planetary Change **29**:275-292.

Kane, D. L., L. D. Hinzman, C. S. Benson, and G. E. Liston. 1991. Snow Hydrology of a Headwater Arctic Basin. Water Resources Research **27**:1099-1109.

Killingtveit, X., and K. Sand. 1991. On Areal Distribution of Snowcover in a Mountainous Area. *in* T. D. Prowse and C. S. L. Ommanney, editors. Northern Hydrology, Selected Perspectives. National Hydrology Research Institute, Saskatoon.

Kirnbauer, R., G. Bloschl, P. Waldhausl, and F. Hochstoger. 1991. An Analysis of Snow Cover Patterns as Derived From Oblique Aerial Photographs. *in* Snow, Hydrology and Forests in High Alpine Areas. IAHS, Vienna.

Lee, Y.-H., and L. Mahrt. 2004. An Evaluation of Snowmelt and Sublimation Over Short Vegetation in Land Surface Modelling. Hydrological Processes **18**:3543-3557.

Leverington, D. 1995. A Field Survey of Late-Summer Depths to Frozen Ground at Two Study Areas Near Mayo, Yukon Territory, Canada. Permafrost and Periglacial Processes **6**:373-379.

Ling, F., and T. Zhang. 2003. Impact of the Timing and Duration of Seasonal Snow Cover on the Active Layer and Permafrost in the Alaskan Arctic. Permafrost and Periglacial Processes **14**:141-150.

Liston, G. E., and M. Sturm. 1998. A Snow-Transport Model for Complex Terrain. Journal of Glaciology **44**:498-516.

Lundberg, A., and J. Beringer. 2005. Albedo and Snowmelt Rates Across a Tundra-to-Forest Transition. Pages 1-10 *in* 15th International Northern Research Basins Symposium and Workshop, Lulea to Kvikkjokk, Sweden.

Male, D. H., and R. J. Granger. 1981. Snow Surface Energy Exchange. Water Resources Research **17**:609-627.

Male, D. H., and D. M. Gray. 1981. Snowcover Ablation and Runoff. Pages 776 *in* D. H. Male and D. M. Gray, editors. Handbook of Snow: Principles, Processes, Management and Use. Pergamon Press, Willowdale.

Marsh, P. 1999. Snowcover Formation and Melt: Recent Advances and Future Prospects. Hydrological Processes **13**:2117-2134.

Maykut, G. A., and P. E. Church. 1973. Radiation Climate of Barrow, Alaska. Journal of Applied Meteorology **12**:620-628.

McCartney, S. E. 2006. Spatial Variability of Snowmelt Water Balances in a Sub-Arctic Catchment, Wolf Creek, Yukon. M.Sc. University of Saskatchewan, Saskatoon.

McCartney, S. E., S. K. Carey, and J. W. Pomeroy. 2006. Intra-basin Variability of Snowmelt Water Balance Calculations in a Subarctic Catchment. Hydrological Processes **20**:1001-1016.

McFadden, J. P., M. Sturm, R. A. Pielke, and F. S. Chapin III. 2001. Interactions of Shrubs and Snow in Arctic Tundra: Measurements and Models. Pages 317-325 *in* Soil-Vegetation-Atmosphere Transfer Schemes and Large-Scale Hydrological Models. International Association of Hydrological Sciences, Maastricht, The Netherlands.

McGuffie, K., and A. Henderson-Sellers. 1985. The Diurnal Hysteresis of Snow Albedo. Journal of Glaciology **31**:188-189.

McKay, D. C., and G. W. Thurtell. 1978. Measurements of the Energy Fluxes Involved in the Energy Budget of a Snow Cover. American Meteorological Society **17**:339-349.

Meteorological Service of Canada (MSC), 2005. Canadian Climate Normals 1971-2000, http://www.climate.weatheroffice.ec.gc.ca/climate_normals/index_e.html

Muller, S. W. 1947. Permafrost or Permanently Frozen Ground and Related Engineering Problems. Edwards, Ann Arbor.

Nakai, Y., T. Sakamoto, T. Terajima, K. Kitamura, and T. Shirai. 1999. The Effect of Canopy-Snow on the Energy Balance Above a Coniferous Forest. Hydrological Processes **13**:2371-2382.

Neumann, N., and P. Marsh. 1998. Local Advection of Sensible Heat in the Snowmelt Landscape of Arctic Tundra. Hydrological Processes **12**:1547-1560.

Nixon, J. F. 1975. The Role of Convective Heat Transport in the Thawing of Frozen Soils. Canadian Geotechnical Journal **12**:425-429.

Nixon, J. F., and E. C. McRoberts. 1973. A Study of Some Factors Affecting the Thawing of Frozen Soils. Canadian Geotechnical Journal **10**:439-425.

Oke, T. R. 1987. Boundary Layer Climates. Routledge, London.

Oliphant, A. J., R. A. Spronken-Smith, A. P. Sturman, and I. F. Owens. 2003. Spatial Variability of Surface Radiation Fluxes in Mountainous Terrain. Journal of Applied Meteorology **42**:113-128.

Oliver, H. R. 1992. Studies of Surface Energy Balance on Sloping Terrain. International Journal of Climatology **12**:55-68.

Outcalt, S. L., C. Goodwin, G. Weller, and J. Brown. 1975. Computer Simulation of the Snowmelt and Soil Thermal Regime at Barrow, Alaska. Water Resources Research **11**:709-715.

Paltineanu, I. C., and J. L. Starr. 1997. Real-Time Soil Water Dynamics Using Multisensor Capacitance Probes: Laboratory Calibration. Journal of the Soil Science Society of America **61**:1576-1585.

Pomeroy, J. W., D. Bewley, R. Essery, N. R. Hedstrom, T. Link, R. J. Granger, J. E. Sicart, C. R. Ellis, and J. R. Janowicz. 2006. Shrub Tundra Snowmelt. Hydrological Processes **20**:923-941.

Pomeroy, J. W., B. Toth, R. J. Granger, N. R. Hedstrom, and R. L. H. Essery. 2003. Variation in Surface Energetics During Snowmelt in a Subarctic Mountain Catchment. Journal of Hydrometerology **4**:702-719.

Pomeroy, J. W., N. R. Hedstrom, and J. Parviainen. 1999. The Snow Mass Balance of Wolf Creek, Yukon: Effects of Snow Sublimation and Redistribution. Pages 15-30 *in* J. W. Pomeroy and R. J. Granger, editors. Wolf Creek Research Basin: Hydrology, Ecology and Environment. National Water Research Institute, Saskatoon.

Pomeroy, J. W., and D. M. Gray. 1995. Snowcover: Accumulation, Relocation and Management. Minister of Supply and Services Canada, Saskatoon.

Price, A. G., and T. Dunne. 1976. Energy Balance Computation of Snowmelt in a Subarctic Area. Water Resources Research **12**:686-694.

Price, J. S. 1983. The Effect of Hydrology on Ground Freezing in a Watershed With Organic Terrain. Pages 1009-1014 *in* 4th International Conference on Permafrost.

Putkonen, J. 1998. Soil Thermal Properties and Heat Transfer Near Ny-Alesund, Northwestern Spitsbergen, Svalbard. Polar Research **17**:165-179.

Quinton, W. L., T. Shirazi, S. K. Carey, and J. W. Pomeroy. 2005. Soil Water Storage and Active-Layer Development in a Sub-Alpine Tundra Hillslope, Southern Yukon Territory, Canada. Permafrost and Periglacial Processes **16**:369-382.

Quinton, W. L., S. K. Carey, and N. T. Goeller. 2004. Snowmelt Runoff From Northern Alpine Tundra Hillslopes: Major Processes and Methods of Simulation. Hydrology and Earth Systems Science **8**:877-890.

Quinton, W. L., and D. M. Gray. 2003. Subsurface Drainage from Organic Soils in Permafrost Terrain: The Major Factors to be Represented in a Runoff Model. Pages 1-6 *in* International Conference on Permafrost, Davos, Switzerland.

Quinton, W. L., and D. M. Gray. 2001. Estimating Subsurface Drainage from Organic-Covered Hillslopes Underlain by Permafrost: Toward a Combined Heat and Mass Flux Model. Pages 333-341 *in* Sixth IAHS Scientific Assembly. IAHS, Maastricht, The Netherlands.

Quinton, W. L., D. M. Gray, and P. Marsh. 2000. Subsurface Drainage From Hummock-Covered Hillslopes in the Arctic Tundra. Journal of Hydrology **237**:113-125.

Quinton, W. L., and P. Marsh. 1999. A Conceptual Framework for Runoff Generation in a Permafrost Environment. Hydrological Processes **13**:2563-2581.

Rist, A., and M. Phillips. 2005. First Results of Investigations on Hydrothermal Processes Within The Active Layer Above Alpine Permafrost In Steep Terrain. Norwegian Journal of Geography **59**:177-183.

Romanovsky, V. E., and T. E. Osterkamp. 2000. Effects of Unfrozen Water on Heat and Mass Transport Processes in the Active Layer and Permafrost. Permafrost and Periglacial Processes **11**:219-239.

Romanovsky, V. E., and T. E. Osterkamp. 1995. Interannual Variations of the Thermal Regime of the Active Layer and Near-Surface Permafrost in Northern Alaska. Permafrost & Periglacial Processes **6**:313-335.

Roth, K., and J. Boike. 2001. Quantifying the Thermal Dynamics of a Permafrost Site Near Ny-Alesund Svalbard. Water Resources Research **37**:2901-2914.

Roulet, N. T., and M.-k. Woo. 1986. Wetland and Lake Evaporation in the Low Arctic. Arctic and Alpine Research **18**:195-200.

Rouse, W. R. 1984. Microclimate of Arctic Tree Line 2. Soil Microclimate of Tundra and Forest. Water Resources Research **20**:67-73.

Rouse, W. R. 1982. Microclimate of Low Arctic Tundra and Forest at Churchill, Manitoba. Pages 68-80 *in* H. M. French, editor. Proceedings of Fourth Canadian Permafrost Conference. National Research Council of Canada, Ottawa.

Sauer, T. J. 2002. Heat Flux Density. Pages 1233-1248 *in* J. H. Dane and G. C. Topp, editors. Methods of Soil Analysis - Part 4 Physical Methods. Soil Science Society of America, Wisconsin.

Saunders, I. R. 1990. Radiation and Energy Budgets of Alpine Tundra, Scout Mountain, Southern British Columbia, Canada. PhD. Simon Fraser University, Vancouver.

Seyfried, M. S., and M. D. Murdock. 2001. Response of a New Soil Water Sensor to Variable Soil, Water Content, and Temperature. Soil Science Society of America Journal **65**:28-34.

Seyfried, M. S., and B. P. Wilcox. 1995. Scale and the Nature of Spatial Variability: Field Examples Having Implications for Hydrologic Modeling. Water Resources Research **31**:173-184.

Shook, K. 1995. Simulation of the Ablation of Prairie Snowcovers. Ph.D. University of Saskatchewan, Saskatoon.

Shook, K. 1993. Fractal Geometry of Snowpacks During Ablation. M.Sc. University of Saskatchewan, Saskatoon.

Shook, K., and D. M. Gray. 1997. Snowmelt Resulting From Advection. Hydrological Processes **11**:1725-1736.

Sicart, J. E., J. W. Pomeroy, R. Essery, and D. Bewley. submitted. Incoming Long-Wave Radiation to Melting Snow: Observations, Sensitivity and Estimation in Northern Environments. Pages 1-22

Sicart, J. E., J. W. Pomeroy, E. R.L.H, H. J., L. T., and M. D. 2004. A Sensitivity Study of Daytime Net Radiation During Snowmelt to Forest Canopy and Atmospheric Conditions. Journal of Hydrometeorology **5**:774-784.

Slaughter, C. W., and D. L. Kane. 1979. Hydrologic Role of Shallow Organic Soils in Cold Climates. Pages 380-389 *in* Canadian Hydrology Symposium 79 - Cold Climate Hydrology. Canadian National Research Council, Vancouver.

Turcotte, D. S. 2002. Radiation Budget, Ground Thermal Regime and Hydrological Balance of a Low Arctic Basin, Coppermine River, NWT. M.Sc. Wilfred Laurier University, Waterloo.

U.S. Army Corps of Engineers, North Pacific Division. 1956. Snow Hydrology: Summary Report of the Snow Investigations. U.S. Army Corps of Engineers, Portland, Oregon.

Walker, D. A., G. J. Jia, H. E. Epstein, M. K. Raynolds, F. S. Chapin III, C. Copass, L. D. Hinzman, J. A. Knudson, H. A. Maier, G. J. Michaelson, F. E. Nelson, C. L. Ping, V. E. Romanovsky, and N. I. Shikomanov. 2003. Vegetation-Soil-Thaw-Depth Relationships Along a Low-Arctic Bioclimate Gradient, Alaska: Synthesis of Information from the ATLAS Studies. Permafrost and Periglacial Processes **14**:103-123.

Weller, G., and B. Holmgren. 1974. The Microclimates of the Arctic Tundra. Journal of Applied Meteorology **13**:854-862.

Willis, I. C., N. S. Arnold, and B. W. Brock. 2002. Effect of Snowpack Removal on Energy Balance, Melt and Runoff in a Small Supraglacial Catchment. Hydrological Processes **16**:2721-2749.

Winther, J. G., F. Godtliebsen, S. Gerland, and P. E. Isachsen. 2002. Surface Albedo in Ny-Ålesund, Svalbard: Variability and Trends During 1981-1997. Global Planetary Change **32**:127-139.

Woo, M.-k., P. Marsh, and J. W. Pomeroy. 2000. Snow, Frozen Soils and Permafrost Hydrology in Canada 1995-1998. Hydrological Processes **14**:1591-1611.

Woo, M.-k. 1998. Arctic Snow Cover Information for Hydrological Investigations at Various Scales. Nordic Hydrology **29**:245-266.

Woo, M.-k., and Z. Xia. 1996. Effects of Hydrology on the Thermal Conditions of the Active Layer. Nordic Hydrology **27**:129-142.

Woo, M.-k. 1986. Permafrost Hydrology in North America. Atmosphere-Ocean **24**:201-234.

Woo, M.-k., R. Heron, P. Marsh, and P. Steer. 1983. Comparison of Weather Station Snowfall With Winter Snow Accumulation in High Arctic Basins. Atmosphere-Ocean **21**:312-325.

Woo, M.-k., R. Heron, and P. Steer. 1981. Catchment Hydrology of a High Arctic Lake. Cold Region Science and Technology **5**:29-41.

Woo, M.-k. 1976. Hydrology of a Small Canadian High Arctic Basin During the Snowmelt Period. Catena **3**:155-168.

Yamazaki, T., and J. Kondo. 1992. The Snowmelt and Heat Balance in Snow-Covered Forested Area. Journal of Applied Meteorology **31**:1322-1327.

Zhao, L., D. M. Gray, and D. H. Male. 1997. Numerical Analysis of Simultaneous Heat and Mass Transfer During Infiltration into Frozen Ground. Journal of Hydrology 200:345-363.

Zhao, L., and D. M. Gray. 1999. Estimating Snowmelt Infiltration Into Frozen Soils. Hydrological Processes **13**:1827-1842.

APPENDICES

Appendix A – Day of Year Conversion Chart

Day	Month March	April	May	June	July
	Day Of Year				
1	60	91	121	152	182
2	61	92	122	153	183
3	62	93	123	154	184
4	63	94	124	155	185
5	64	95	125	156	186
6	65	96	126	157	187
7	66	97	127	158	188
8	67	98	128	159	189
9	68	99	129	160	190
10	69	100	130	161	191
11	70	101	131	162	192
12	71	102	132	163	193
13	72	103	133	164	194
14	73	104	134	165	195
15	74	105	135	166	196
16	75	106	136	167	197
17	76	107	137	168	198
18	77	108	138	169	199
19	78	109	139	170	200
20	79	110	140	171	201
21	80	111	141	172	202
22	81	112	142	173	203
23	82	113	143	174	204
24	83	114	144	175	205
25	84	115	145	176	206
26	85	116	146	177	207
27	86	117	147	178	208
28	87	118	148	179	209
29	88	119	149	180	210
30	89	120	150	181	211
31	90		151		212

Appendix B – Soil Moisture Calibrations

Soil Tin Dimensions: Radius = 2.5 cm, Height = 3.5 cm, Volume = 68.7 cm^3

Sample	Date	Time	HydroSense VWC (%)	Period	Tare (g)	Wet Weight (tare + soil) (g)	m_{wet} (g)	Dry Weight (tare + soil) (g)	m_{dry} (g)	GWC	Sample VWC (%)
Test Patch	21-Apr-03	5:00 PM	37	1.15	16	88	72	54.6	38.6	0.87	49
Patch 2 - 4	26-Apr-03	5:45 PM	9	0.89	16	40	24	18.5	2.5	8.60	31
Patch 1 - 1	26-Apr-03	1:31 PM	28	1.07	16	66	50	37.0	21.0	1.38	42
Patch 3 - 7	28-Apr-03	4:09 PM	19	0.99	15	66	51	48.9	33.9	0.50	25
Patch 4 - 3	28-Apr-03	4:58 PM	28	1.07	15	45	30	23.3	8.3	2.61	32
Patch 4 - 3	30-Apr-03	7:47 PM	23	1.03	16	44	28	25.6	9.6	1.92	27
Patch 4 - b/t 4 + 5	2-May-03	1:38 PM	5	0.84	16	45	29	31.0	15.0	0.93	20
Patch 1 - D2	2-May-03	2:33 PM	3	0.82	15	30	15	18.9	3.9	2.85	16
Patch 3 - T3-15	4-May-03	11:49 AM	5	0.85	17	32	15	18.6	1.6	8.37	19
Patch 2 - 1	4-May-03	1:19 PM	7	0.87	15	38	23	20.3	5.3	3.34	26
Patch 6 - 4	10-May-03	2:51 PM	29	1.08	16	50	34	27.4	11.4	1.98	33
Patch 8 - 9	11-May-03	6:30 PM	33	1.12	16	76	60	40.6	24.6	1.44	52
Patch 1 - U5	18-May-03	3:00 PM	39	1.17	16	77	61	33.3	17.3	2.53	64
Patch 9 - D2	27-May-03	4:26 PM	12	0.92	15	47	32	21.5	6.5	3.92	37
Patch 8 - U8	27-May-03	7:24 PM	42	1.19	16	58	42	24.4	8.4	4.00	49
Patch 3 - U6	28-May-03	12:19 PM	21	1.01	15	86	71	61.4	46.4	0.53	36
Patch 1 - U8	28-May-03	4:58 PM	15	0.95	16	70	54	36.0	20.0	1.70	49
Patch 4 - near 7	28-May-03	7:31 PM	20	1.00	15	72	57	22.4	7.4	6.70	72
Patch 6 - near U7	29-May-03	11:03 AM	24	1.04	15	50	35	23.4	8.4	3.17	39
Patch 5 - U3	29-May-03	7:12 PM	39	1.17	15	73	58	33.2	18.2	2.19	58
Patch 7 - 1	3-Jun-03	12:30 PM	12	0.92	15	44	29	29.8	14.8	0.96	21
Patch 9 - near WT-4	10-Jun-03	12:31 PM	7	0.87	16	28	12	18.6	2.6	3.62	14
Patch 3 - U4	15-Jun-03	2:43 PM	17	0.97	16	74	58	45.6	29.6	0.96	41
Patch 1 - U6	15-Jun-03	3:34 PM	18	0.98	16	56	40	43.1	27.1	0.48	19
Patch 3 - WT-T3-26	15-Jun-03	5:03 PM	11	0.91	16	61	45	48.9	32.9	0.37	18
Patch 4 - 5	16-Jun-03	12:36 PM	11	0.91	16	55	39	40.0	24.0	0.63	22
Patch 8 - WT-3 May 21	16-Jun-03	1:16 PM	20	1.00	16	70	54	43.8	27.8	0.94	38
Patch 5 - T2-13	16-Jun-03	1:27 PM	11	0.91	16	33	17	24.4	8.4	1.02	13
Patch 2 - WT-D3	16-Jun-03	1:33 PM	7	0.86	16	27	11	20.9	4.9	1.24	9

Appendix C – Linearly Interpolated Albedo and Resulting Net Radiation Values

DOY	Albedo	Calculated Q* (W/m^2)	GB4 Measured Q* (W/m^2)
112.02	0.800	-48.443	-34.877
112.04	0.800	-45.075	-34.879
112.06	0.800	-43.487	-31.458
112.08	0.800	-43.580	-29.716
112.10	0.800	-43.032	-30.462
112.13	0.800	-40.724	-28.880
112.15	0.800	-37.386	-31.561
112.17	0.800	-34.756	-30.689
112.19	0.800	-30.974	-30.754
112.21	0.800	-26.928	-31.142
112.23	0.800	-25.554	-32.951
112.25	0.800	-28.332	-23.066
112.27	0.800	-31.154	-15.021
112.29	0.800	-30.639	-12.696
112.31	0.800	-22.768	2.736
112.33	0.800	-11.048	3.665
112.35	0.800	12.260	13.277
112.38	0.800	12.645	8.398
112.40	0.800	4.802	9.855
112.42	0.800	40.964	22.834
112.44	0.800	44.886	7.238
112.46	0.800	10.799	-2.261
112.48	0.800	-0.967	14.007
112.50	0.800	3.675	16.629
112.52	0.800	2.155	23.353
112.54	0.800	5.706	23.855
112.56	0.800	1.817	21.847
112.58	0.800	16.930	24.832
112.60	0.800	29.198	32.950
112.63	0.800	8.654	34.789
112.65	0.800	-11.779	32.581
112.67	0.800	-17.370	30.767
112.69	0.800	-32.087	20.418
112.71	0.800	-31.685	22.175
112.73	0.800	-37.801	13.695
112.75	0.800	-41.784	12.217
112.77	0.800	-41.272	13.947
112.79	0.800	-46.728	11.380
112.81	0.800	-44.880	-6.333
112.83	0.800	-46.563	-30.083
112.85	0.800	-47.182	-28.116
112.88	0.800	-45.860	-31.055
112.90	0.800	-47.544	-15.851
112.92	0.800	-51.148	-8.910
112.94	0.800	-44.601	-25.310
112.96	0.800	-42.816	-28.088
112.98	0.800	-42.084	-19.179
113.00	0.800	-44.416	-19.245

DOY	Albedo	Calculated Q* (W/m^2)	GB4 Measured Q* (W/m^2)
113.02	0.800	-52.974	-22.088
113.04	0.800	-54.840	-18.666
113.06	0.800	-55.794	-15.048
113.08	0.800	-54.662	-21.185
113.10	0.800	-52.458	-31.940
113.13	0.800	-52.429	-31.683
113.15	0.800	-58.656	-10.714
113.17	0.800	-61.418	-18.991
113.19	0.800	-61.793	-21.704
113.21	0.800	-61.334	-30.425
113.23	0.800	-60.386	-32.170
113.25	0.800	-59.940	-31.105
113.27	0.800	-59.289	-30.523
113.29	0.800	-55.709	-20.478
113.31	0.800	-43.521	4.792
113.33	0.800	-24.604	5.687
113.35	0.800	-30.005	-3.452
113.38	0.800	-29.265	-0.955
113.40	0.800	-4.337	16.048
113.42	0.800	8.567	14.036
113.44	0.800	13.788	8.761
113.46	0.800	21.163	6.778
113.48	0.800	24.748	6.808
113.50	0.800	24.937	-1.035
113.52	0.800	25.352	-1.451
113.54	0.800	23.883	3.024
113.56	0.800	18.691	-0.574
113.58	0.800	15.217	-6.869
113.60	0.800	9.864	-8.482
113.63	0.800	4.835	-11.545
113.65	0.800	-0.704	-11.286
113.67	0.800	-9.069	-8.222
113.69	0.800	-16.831	-4.804
113.71	0.800	-24.618	-3.514
113.73	0.800	-32.331	0.258
113.75	0.800	-39.916	-6.384
113.77	0.800	-39.968	-11.608
113.79	0.800	-38.375	-21.023
113.81	0.800	-43.516	-28.374
113.83	0.800	-46.223	-28.601
113.85	0.800	-48.660	-21.444
113.88	0.800	-53.403	-4.349
113.90	0.800	-54.099	-6.505
113.92	0.800	-52.282	-29.513
113.94	0.800	-49.105	-41.581
113.96	0.800	-46.534	-42.327
113.98	0.800	-44.673	-41.427
114.00	0.800	-42.365	-38.880
114.02	0.800	-40.886	-38.754
114.04	0.800	-41.345	-40.919
114.06	0.800	-38.250	-37.857

DOY	Albedo	Calculated Q* (W/m^2)	GB4 Measured Q* (W/m^2)
114.08	0.800	-38.897	-38.374
114.10	0.800	-37.770	-38.118
114.13	0.800	-35.583	-38.186
114.15	0.800	-34.684	-38.318
114.17	0.800	-36.856	-37.738
114.19	0.800	-36.297	-36.125
114.21	0.800	-34.218	-34.930
114.23	0.800	-33.242	-34.865
114.25	0.800	-33.023	-34.867
114.27	0.800	-31.367	-34.160
114.29	0.800	-27.747	-17.726
114.31	0.800	-16.207	5.821
114.33	0.800	4.330	17.525
114.35	0.800	8.980	17.243
114.38	0.800	18.113	15.120
114.40	0.800	29.666	-6.167
114.42	0.800	36.153	-17.487
114.44	0.800	42.543	-4.617
114.46	0.800	49.247	9.450
114.48	0.800	52.544	14.716
114.50	0.800	56.127	18.837
114.52	0.800	55.950	16.188
114.54	0.800	55.296	20.615
114.56	0.800	51.358	20.113
114.58	0.800	46.485	17.075
114.60	0.800	41.128	12.533
114.63	0.800	34.736	11.502
114.65	0.800	27.873	11.584
114.67	0.800	20.295	11.390
114.69	0.800	8.052	11.584
114.71	0.800	-1.345	10.026
114.73	0.800	-9.199	9.108
114.75	0.800	-18.860	6.268
114.77	0.800	-27.047	-7.612
114.79	0.800	-34.873	-22.530
114.81	0.800	-42.414	-27.879
114.83	0.800	-46.224	-32.587
114.85	0.800	-50.221	-35.138
114.88	0.800	-54.173	-38.497
114.90	0.800	-55.839	-38.697
114.92	0.800	-55.969	-40.281
114.94	0.800	-55.154	-42.191
114.96	0.800	-54.281	-41.358
114.98	0.800	-55.205	-41.393
115.00	0.800	-55.575	-41.976
115.02	0.800	-54.178	-41.172
115.04	0.800	-53.648	-42.367
115.06	0.800	-51.346	-41.015
115.08	0.800	-49.441	-38.758
115.10	0.800	-50.079	-42.343
115.13	0.800	-49.237	-42.603

DOY	Albedo	Calculated Q* (W/m^2)	GB4 Measured Q* (W/m^2)
115.15	0.800	-48.701	-42.603
115.17	0.800	-48.693	-42.380
115.19	0.800	-48.566	-42.284
115.21	0.800	-47.849	-39.638
115.23	0.800	-47.413	-38.735
115.25	0.800	-46.406	-38.543
115.27	0.800	-46.951	-36.026
115.29	0.800	-45.492	-6.606
115.31	0.800	-32.796	24.518
115.33	0.800	-3.736	40.453
115.35	0.800	5.538	43.236
115.38	0.800	15.781	32.295
115.40	0.800	25.947	19.937
115.42	0.800	33.416	13.159
115.44	0.800	39.849	13.130
115.46	0.800	44.466	15.052
115.48	0.800	46.492	20.429
115.50	0.800	48.792	31.937
115.52	0.800	49.149	38.900
115.54	0.800	46.979	45.723
115.56	0.800	43.997	46.779
115.58	0.800	39.265	44.601
115.60	0.800	32.450	39.193
115.63	0.800	24.365	33.730
115.65	0.800	15.708	32.222
115.67	0.800	4.248	30.606
115.69	0.800	-3.900	29.631
115.71	0.800	-10.782	24.006
115.73	0.800	-17.134	23.394
115.75	0.800	-26.632	18.186
115.77	0.800	-33.285	6.966
115.79	0.800	-38.315	-10.344
115.81	0.800	-43.137	8.755
115.83	0.800	-58.306	-21.300
115.85	0.800	-66.710	-34.613
115.88	0.800	-66.386	-34.780
115.90	0.800	-67.781	-38.076
115.92	0.800	-70.562	-39.631
115.94	0.800	-71.222	-38.701
115.96	0.800	-71.139	-41.610
115.98	0.800	-70.270	-47.969
116.00	0.800	-65.927	-50.327
116.02	0.799	-69.506	-49.393
116.04	0.798	-69.350	-43.621
116.06	0.797	-70.906	-46.463
116.08	0.795	-72.447	-47.142
116.10	0.794	-73.801	-48.661
116.13	0.793	-74.479	-50.339
116.15	0.792	-78.513	-50.340
116.17	0.791	-78.386	-50.342
116.19	0.790	-81.499	-50.345

DOY	Albedo	Calculated Q* (W/m^2)	GB4 Measured Q* (W/m^2)
116.21	0.789	-80.369	-50.348
116.23	0.788	-78.025	-50.349
116.25	0.786	-74.751	-50.316
116.27	0.785	-73.879	-45.413
116.29	0.784	-67.528	-10.510
116.31	0.783	-52.189	20.816
116.33	0.782	-26.109	46.283
116.35	0.781	-19.047	59.192
116.38	0.780	4.901	72.401
116.40	0.779	13.219	75.902
116.42	0.777	14.837	79.931
116.44	0.776	19.331	80.666
116.46	0.775	25.717	80.063
116.48	0.774	28.846	77.228
116.50	0.773	30.057	72.170
116.52	0.772	36.814	68.089
116.54	0.771	37.224	67.385
116.56	0.770	36.657	68.550
116.58	0.768	24.882	62.311
116.60	0.767	11.777	57.800
116.63	0.766	9.727	54.014
116.65	0.765	4.009	53.847
116.67	0.764	-6.505	48.419
116.69	0.763	-14.918	43.770
116.71	0.762	-22.589	39.678
116.73	0.761	-30.523	36.227
116.75	0.759	-42.618	31.300
116.77	0.758	-53.447	13.980
116.79	0.757	-62.240	-10.237
116.81	0.756	-71.178	-16.627
116.83	0.755	-73.501	-27.100
116.85	0.754	-78.352	-27.138
116.88	0.753	-88.423	-28.560
116.90	0.751	-82.563	-34.398
116.92	0.750	-88.105	-38.370
116.94	0.749	-87.850	-38.698
116.96	0.748	-82.936	-38.701
116.98	0.747	-79.642	-38.802
117.00	0.746	-77.357	-40.031
117.02	0.745	-69.567	-39.939
117.04	0.744	-67.869	-40.552
117.06	0.742	-66.760	-42.102
117.08	0.741	-63.222	-42.588
117.10	0.740	-63.527	-42.622
117.13	0.739	-63.507	-42.688
117.15	0.738	-61.591	-42.591
117.17	0.737	-62.306	-42.851
117.19	0.736	-62.558	-48.209
117.21	0.735	-59.123	-47.243
117.23	0.733	-57.459	-42.985
117.25	0.732	-54.602	-42.601

DOY	Albedo	Calculated Q* (W/m^2)	GB4 Measured Q* (W/m^2)
117.27	0.731	-51.230	-38.988
117.29	0.730	-48.561	4.746
117.31	0.729	-27.662	41.786
117.33	0.728	8.275	68.789
117.35	0.727	26.170	87.999
117.38	0.726	41.975	95.739
117.40	0.724	54.206	96.401
117.42	0.723	63.661	94.190
117.44	0.722	73.839	94.935
117.46	0.721	78.203	99.581
117.48	0.720	81.152	106.652
117.50	0.719	80.633	111.520
117.52	0.718	78.679	113.719
117.54	0.716	76.936	113.613
117.56	0.715	72.144	110.255
117.58	0.714	66.870	100.722
117.60	0.713	62.514	94.194
117.63	0.712	56.773	87.252
117.65	0.711	40.116	80.505
117.67	0.710	22.097	71.194
117.69	0.709	14.744	66.459
117.71	0.707	3.665	59.800
117.73	0.706	-8.395	51.777
117.75	0.705	-18.450	38.457
117.77	0.704	-28.966	18.922
117.79	0.703	-40.309	-7.599
117.81	0.702	-51.353	-19.250
117.83	0.701	-58.763	-28.215
117.85	0.700	-64.449	-35.086
117.88	0.698	-72.427	-38.473
117.90	0.697	-73.548	-40.864
117.92	0.696	-70.659	-44.932
117.94	0.695	-72.844	-49.970
117.96	0.694	-70.406	-47.619
117.98	0.693	-70.157	-46.235
118.00	0.692	-68.741	-43.334
118.02	0.691	-67.441	-42.595
118.04	0.689	-65.736	-42.599
118.06	0.688	-65.493	-42.602
118.08	0.687	-66.140	-42.638
118.10	0.686	-65.597	-42.608
118.13	0.685	-66.675	-42.611
118.15	0.684	-67.790	-42.613
118.17	0.683	-67.496	-42.613
118.19	0.682	-65.371	-42.613
118.21	0.680	-66.188	-41.807
118.23	0.679	-64.283	-40.259
118.25	0.678	-65.647	-39.937
118.27	0.677	-62.351	-33.611
118.29	0.676	-54.827	23.295
118.31	0.675	-26.844	60.638

DOY	Albedo	Calculated Q* (W/m^2)	GB4 Measured Q* (W/m^2)
118.33	0.674	16.695	94.868
118.35	0.672	32.607	115.388
118.38	0.671	48.498	129.947
118.40	0.670	66.141	139.596
118.42	0.669	80.077	143.900
118.44	0.668	92.816	148.406
118.46	0.667	100.542	150.967
118.48	0.666	106.642	155.590
118.50	0.665	110.538	160.871
118.52	0.663	112.403	158.672
118.54	0.662	110.961	153.751
118.56	0.661	107.470	147.301
118.58	0.660	102.846	140.213
118.60	0.659	94.470	130.085
118.63	0.658	84.094	118.842
118.65	0.657	75.207	112.232
118.67	0.656	63.495	102.123
118.69	0.654	50.704	93.548
118.71	0.653	37.181	83.634
118.73	0.652	20.459	68.933
118.75	0.651	4.922	53.061
118.77	0.650	-9.235	29.969
118.79	0.649	-20.935	2.067
118.81	0.648	-34.167	-13.986
118.83	0.647	-45.528	-16.984
118.85	0.645	-49.410	-26.913
118.88	0.644	-54.491	-33.879
118.90	0.643	-60.374	-38.691
118.92	0.642	-62.841	-42.503
118.94	0.641	-62.759	-46.411
118.96	0.640	-62.447	-46.775
118.98	0.639	-64.049	-43.778
119.00	0.638	-64.084	-42.589
119.02	0.636	-65.490	-42.591
119.04	0.635	-63.636	-42.594
119.06	0.634	-64.612	-42.597
119.08	0.633	-66.269	-42.601
119.10	0.632	-67.348	-42.603
119.13	0.631	-66.430	-42.604
119.15	0.630	-64.843	-40.767
119.17	0.628	-62.385	-40.252
119.19	0.627	-63.118	-42.416
119.21	0.626	-63.119	-41.255
119.23	0.625	-62.447	-42.578
119.25	0.624	-63.332	-42.193
119.27	0.623	-60.486	-35.382
119.29	0.622	-54.056	39.412
119.31	0.621	-13.764	81.136
119.33	0.619	32.277	123.868
119.35	0.618	60.216	151.998
119.38	0.617	81.139	175.972

DOY	Albedo	Calculated Q* (W/m^2)	GB4 Measured Q* (W/m^2)
119.40	0.616	99.164	192.816
119.42	0.615	113.524	204.665
119.44	0.614	128.806	215.218
119.46	0.613	140.680	221.785
119.48	0.612	154.242	233.401
119.50	0.610	153.335	224.676
119.52	0.609	149.088	219.235
119.54	0.608	145.731	213.603
119.56	0.607	142.102	218.852
119.58	0.606	131.532	212.072
119.60	0.605	128.692	200.553
119.63	0.604	110.876	177.333
119.65	0.603	86.274	162.380
119.67	0.601	72.908	139.756
119.69	0.600	66.606	133.518
119.71	0.599	50.246	113.199
119.73	0.598	35.861	93.785
119.75	0.597	21.868	74.511
119.77	0.596	3.102	45.680
119.79	0.595	-7.603	17.994
119.81	0.593	-22.035	-5.199
119.83	0.592	-32.528	-13.085
119.85	0.591	-41.080	-21.724
119.88	0.590	-51.131	-28.336
119.90	0.589	-53.062	-36.208
119.92	0.588	-51.790	-39.471
119.94	0.587	-48.888	-43.764
119.96	0.586	-49.038	-46.641
119.98	0.584	-47.008	-46.646
120.00	0.583	-47.973	-47.554
120.02	0.582	-29.764	-50.298
120.04	0.581	-29.934	-50.335
120.06	0.580	-29.800	-50.337
120.08	0.579	-30.599	-50.339
120.10	0.578	-31.994	-50.344
120.13	0.577	-32.005	-50.348
120.15	0.575	-32.258	-50.317
120.17	0.574	-30.536	-50.351
120.19	0.573	-25.012	-50.354
120.21	0.572	-24.929	-50.355
120.23	0.571	-26.335	-47.194
120.25	0.570	-29.662	-32.185
120.27	0.569	-26.128	-22.953
120.29	0.568	-10.479	-6.632
120.31	0.566	15.931	40.066
120.33	0.565	8.735	24.189
120.35	0.564	20.099	33.953
120.38	0.563	53.911	77.672
120.40	0.562	99.406	124.176
120.42	0.561	61.447	92.146
120.44	0.560	78.858	123.135

DOY	Albedo	Calculated Q* (W/m^2)	GB4 Measured Q* (W/m^2)
120.46	0.559	146.221	219.702
120.48	0.557	159.618	214.697
120.50	0.556	121.010	196.695
120.52	0.555	191.051	278.225
120.54	0.554	119.543	233.868
120.56	0.553	45.014	144.591
120.58	0.552	65.488	197.906
120.60	0.551	59.650	193.103
120.63	0.549	43.937	174.368
120.65	0.548	51.983	198.172
120.67	0.547	37.256	182.922
120.69	0.546	13.773	127.290
120.71	0.545	23.475	145.749
120.73	0.544	34.074	82.676
120.75	0.543	29.111	116.387
120.77	0.542	-20.204	55.180
120.79	0.540	-36.705	43.386
120.81	0.539	-31.844	9.229
120.83	0.538	-51.317	4.013
120.85	0.537	-62.148	10.845
120.88	0.536	-68.135	-4.086
120.90	0.535	-77.684	-9.551
120.92	0.534	-75.345	-16.263
120.94	0.533	-80.323	-25.461
120.96	0.531	-78.401	-36.501
120.98	0.530	-76.194	-40.667
121.00	0.529	-80.040	-41.994
121.02	0.528	-99.315	-51.941
121.04	0.527	-103.317	-56.882
121.06	0.526	-101.593	-62.080
121.08	0.525	-99.619	-65.861
121.10	0.524	-98.975	-65.866
121.13	0.522	-99.641	-65.875
121.15	0.521	-98.908	-65.879
121.17	0.520	-96.968	-65.882
121.19	0.519	-96.830	-65.885
121.21	0.518	-96.088	-65.887
121.23	0.517	-95.240	-65.889
121.25	0.516	-93.787	-65.147
121.27	0.514	-89.131	-44.566
121.29	0.513	-75.753	49.581
121.31	0.512	-15.179	101.338
121.33	0.511	43.712	161.711
121.35	0.510	73.822	197.439
121.38	0.509	102.575	234.357
121.40	0.508	120.791	254.814
121.42	0.507	136.067	273.581
121.44	0.505	151.505	289.235
121.46	0.504	160.614	296.174
121.48	0.503	164.689	295.356
121.50	0.502	167.035	292.094

DOY	Albedo	Calculated Q* (W/m^2)	GB4 Measured Q* (W/m^2)
121.52	0.501	170.152	286.939
121.54	0.500	165.631	276.546
121.56	0.499	159.006	265.962
121.58	0.498	148.932	249.086
121.60	0.496	136.151	231.158
121.63	0.495	120.933	212.030
121.65	0.494	102.028	189.543
121.67	0.493	81.626	164.506
121.69	0.492	62.792	145.207
121.71	0.491	43.029	123.007
121.73	0.490	22.989	97.882
121.75	0.489	14.093	91.887
121.77	0.487	-2.208	60.835
121.79	0.486	-68.735	-5.833
121.81	0.485	-44.466	-6.426
121.83	0.484	-61.527	-18.520
121.85	0.483	-74.688	-31.364
121.88	0.482	-90.749	-26.170
121.90	0.481	-93.983	-36.662
121.92	0.480	-97.368	-45.573
121.94	0.478	-99.946	-50.356
121.96	0.477	-97.520	-48.746
121.98	0.476	-99.795	-45.650
122.00	0.475	-94.933	-53.242
122.02	0.474	-88.949	-57.802
122.04	0.473	-89.685	-56.063
122.06	0.472	-89.084	-55.324
122.08	0.470	-87.815	-56.489
122.10	0.469	-88.821	-53.423
122.13	0.468	-87.444	-55.362
122.15	0.467	-86.947	-53.587
122.17	0.466	-87.003	-54.009
122.19	0.465	-87.522	-48.359
122.21	0.464	-87.767	-48.586
122.23	0.463	-87.614	-49.427
122.25	0.461	-86.176	-50.395
122.27	0.460	-78.937	-30.773
122.29	0.459	-67.271	50.926
122.31	0.458	-1.688	102.326
122.33	0.457	60.724	164.028
122.35	0.456	96.546	202.848
122.38	0.455	125.387	235.441
122.40	0.454	149.221	265.165
122.42	0.452	169.901	287.885
122.44	0.451	186.843	306.036
122.46	0.450	204.384	324.389
122.48	0.449	214.937	327.981
122.50	0.448	223.919	331.530
122.52	0.447	212.225	316.472
122.54	0.446	203.824	305.367
122.56	0.445	204.525	299.192

DOY	Albedo	Calculated Q* (W/m^2)	GB4 Measured Q* (W/m^2)
122.58	0.443	129.237	228.108
122.60	0.442	81.659	197.269
122.63	0.441	121.971	238.215
122.65	0.440	107.667	211.913
122.67	0.439	125.747	230.988
122.69	0.438	48.553	147.726
122.71	0.437	8.727	122.402
122.73	0.436	-25.654	104.478
122.75	0.434	24.432	147.938
122.77	0.433	16.271	109.171
122.79	0.432	-31.283	66.717
122.81	0.431	-22.139	78.237
122.83	0.430	-65.962	-9.430
122.85	0.429	-81.026	-15.653
122.88	0.428	-91.959	-16.429
122.90	0.426	-89.395	-35.765
122.92	0.425	-89.369	-41.321
122.94	0.424	-87.878	-48.650
122.96	0.423	-87.869	-34.578
122.98	0.422	-84.427	-35.779
123.00	0.421	-82.122	-22.412
123.02	0.420	-68.812	-16.923
123.04	0.419	-71.296	-27.485
123.06	0.417	-68.359	-41.600
123.08	0.416	-69.293	-30.717
123.10	0.415	-68.125	-23.901
123.13	0.414	-63.512	-25.712
123.15	0.413	-63.282	-9.367
123.17	0.412	-55.138	-11.725
123.19	0.411	-47.490	-10.369
123.21	0.410	-41.289	-22.160
123.23	0.408	-42.166	-25.876
123.25	0.407	-40.750	-17.703
123.27	0.406	-36.993	-1.569
123.29	0.405	-2.047	6.422
123.31	0.404	18.074	12.285
123.33	0.403	10.247	19.990
123.35	0.402	43.719	46.905
123.38	0.401	27.743	43.220
123.40	0.399	35.708	51.900
123.42	0.398	83.494	135.367
123.44	0.397	48.070	95.806
123.46	0.396	49.783	105.599
123.48	0.395	45.344	102.330
123.50	0.394	17.977	74.833
123.52	0.393	100.656	225.696
123.54	0.391	110.950	266.993
123.56	0.390	6.011	75.040
123.58	0.389	15.605	119.532
123.60	0.388	78.580	189.182
123.63	0.387	95.479	180.499

DOY	Albedo	Calculated Q* (W/m^2)	GB4 Measured Q* (W/m^2)
123.65	0.386	139.474	226.249
123.67	0.385	84.999	165.972
123.69	0.384	21.806	119.681
123.71	0.382	46.201	137.014
123.73	0.381	9.718	76.749
123.75	0.380	-15.689	69.416
123.77	0.379	21.508	108.427
123.79	0.378	-42.021	8.370
123.81	0.377	-28.192	25.223
123.83	0.376	-28.917	19.253
123.85	0.375	-28.003	-7.300
123.88	0.373	-34.572	-34.294
123.90	0.372	-41.630	-39.916
123.92	0.371	-46.502	-22.995
123.94	0.370	-48.184	-12.080
123.96	0.369	-35.814	-14.793
123.98	0.368	-33.696	-7.752
124.00	0.367	-35.295	-7.914
124.02	0.366	-44.262	-14.634
124.04	0.364	-48.976	-16.734
124.06	0.363	-51.821	-19.706
124.08	0.362	-51.726	-26.361
124.10	0.361	-52.413	-30.399
124.13	0.360	-48.076	-30.560
124.15	0.359	-45.653	-23.552
124.17	0.358	-47.476	-15.508
124.19	0.357	-50.848	-15.509
124.21	0.355	-55.489	-15.510
124.23	0.354	-58.391	-15.510
124.25	0.353	-63.048	-15.251
124.27	0.352	-60.346	-7.335
124.29	0.351	-38.686	6.510
124.31	0.350	-26.350	8.378
124.33	0.349	4.496	55.065
124.35	0.347	40.280	118.661
124.38	0.346	31.056	116.706
124.40	0.345	62.232	177.396
124.42	0.344	92.066	251.860
124.44	0.343	87.032	257.503
124.46	0.342	109.867	242.550
124.48	0.341	182.903	235.367
124.50	0.340	257.695	269.426
124.52	0.338	153.234	207.450
124.54	0.337	206.465	256.408
124.56	0.336	104.402	176.132
124.58	0.335	203.397	226.196
124.60	0.334	251.271	328.512
124.63	0.333	145.832	241.562
124.65	0.332	103.574	173.773
124.67	0.331	92.487	140.043
124.69	0.329	41.202	118.225

DOY	Albedo	Calculated Q* (W/m^2)	GB4 Measured Q* (W/m^2)
124.71	0.328	-2.218	113.209
124.73	0.327	-0.182	118.045
124.75	0.326	44.369	138.353
124.77	0.325	-15.720	81.143
124.79	0.324	-33.667	45.468
124.81	0.323	-46.328	39.694
124.83	0.322	-53.794	10.935
124.85	0.320	-52.762	20.979
124.88	0.319	-29.263	16.990
124.90	0.318	-39.852	-25.955
124.92	0.317	-51.674	-19.596
124.94	0.316	-57.083	-24.150
124.96	0.315	-56.981	-32.648
124.98	0.314	-54.640	-39.723
125.00	0.313	-51.281	-49.964
125.02	0.311	-58.579	-50.386
125.04	0.310	-59.564	-50.001
125.06	0.309	-59.453	-49.650
125.08	0.308	-60.355	-48.909
125.10	0.307	-60.543	-49.588
125.13	0.306	-59.483	-46.616
125.15	0.305	-59.282	-46.131
125.17	0.303	-57.258	-46.295
125.19	0.302	-58.174	-46.298
125.21	0.301	-60.023	-48.886
125.23	0.300	-58.880	-47.402
125.25	0.299	-61.325	-45.302
125.27	0.298	-50.352	-20.930
125.29	0.297	-29.035	7.618
125.31	0.296	111.854	122.391
125.33	0.294	153.186	153.592
125.35	0.293	214.367	215.292
125.38	0.292	213.569	227.088
125.40	0.291	209.496	217.779
125.42	0.290	304.900	324.102
125.44	0.289	329.288	345.080
125.46	0.288	210.453	232.837
125.48	0.287	283.811	300.999
125.50	0.285	260.181	290.680
125.52	0.284	279.084	292.497
125.54	0.283	264.310	280.053
125.56	0.282	247.475	260.925
125.58	0.281	238.100	277.396
125.60	0.280	178.951	246.727
125.63	0.279	196.704	212.561
125.65	0.278	192.131	245.441
125.67	0.276	234.494	232.306
125.69	0.275	174.405	168.905
125.71	0.274	159.388	154.857
125.73	0.273	127.569	125.037
125.75	0.272	54.243	70.982

DOY	Albedo	Calculated Q* (W/m^2)	GB4 Measured Q* (W/m^2)
125.77	0.271	49.939	57.964
125.79	0.270	43.009	35.577
125.81	0.268	11.255	5.981
125.83	0.267	-13.707	-11.711
125.85	0.266	-32.355	-17.778
125.88	0.265	-53.566	-31.653
125.90	0.264	-67.595	-40.399
125.92	0.263	-70.450	-48.797
125.94	0.262	-72.644	-57.261
125.96	0.261	-73.084	-58.106
125.98	0.259	-75.045	-58.110
126.00	0.258	-75.435	-54.274
126.02	0.257	-72.275	-52.471
126.04	0.256	-72.730	-56.384
126.06	0.255	-74.237	-53.641
126.08	0.254	-72.284	-54.158
126.10	0.253	-69.307	-51.093
126.13	0.252	-68.395	-50.383
126.15	0.250	-66.046	-49.320
126.17	0.249	-67.029	-48.998
126.19	0.248	-67.563	-48.384
126.21	0.247	-71.206	-50.355
126.23	0.246	-69.965	-49.226
126.25	0.245	-64.810	-38.827
126.27	0.244	-46.550	-15.275
126.29	0.243	-12.691	51.064
126.31	0.241	96.859	118.172
126.33	0.240	95.252	111.605
126.35	0.239	131.247	135.802
126.38	0.238	94.676	109.458
126.40	0.237	172.158	180.074
126.42	0.236	147.815	152.434
126.44	0.235	302.147	307.407
126.46	0.234	332.357	333.964
126.48	0.232	358.818	358.959
126.50	0.231	244.493	288.342
126.52	0.230	283.872	319.607
126.54	0.229	284.969	327.906
126.56	0.228	266.384	300.988
126.58	0.227	282.384	330.383
126.60	0.226	190.063	254.368
126.63	0.224	224.688	309.299
126.65	0.223	104.887	229.458
126.67	0.222	139.412	228.820
126.69	0.221	120.658	218.682
126.71	0.220	210.827	300.786
126.73	0.219	205.805	268.108
126.75	0.218	30.454	74.989
126.77	0.217	-14.517	36.825
126.79	0.215	-31.385	70.394
126.81	0.214	-26.523	75.614

DOY	Albedo	Calculated Q* (W/m^2)	GB4 Measured Q* (W/m^2)
126.83	0.213	-26.051	68.675
126.85	0.212	-25.959	21.555
126.88	0.211	-31.060	27.104
126.90	0.210	-41.749	11.461
126.92	0.209	-50.725	-5.913
126.94	0.208	-63.597	-28.046
126.96	0.206	-63.524	-39.635
126.98	0.205	-59.706	-50.355
127.00	0.204	-56.048	-50.359
127.02	0.203	-53.261	-48.521
127.04	0.202	-52.409	-37.774
127.06	0.201	-49.756	-50.371
127.08	0.200	-52.839	-50.376
127.10	0.199	-51.391	-50.378
127.13	0.197	-51.713	-50.348
127.15	0.196	-51.247	-48.057
127.17	0.195	-54.430	-32.071
127.19	0.194	-53.796	-34.137
127.21	0.193	-55.687	-26.839
127.23	0.192	-58.372	-14.050
127.25	0.191	-58.536	-14.179
127.27	0.189	-36.181	-11.465
127.29	0.188	-7.487	-3.301
127.31	0.187	2.490	-1.975
127.33	0.186	35.559	29.448
127.35	0.185	54.500	49.377
127.38	0.184	285.739	294.495
127.40	0.183	236.044	278.151
127.42	0.182	122.256	166.259
127.44	0.180	180.192	187.450
127.46	0.179	153.624	191.690
127.48	0.178	236.155	283.252
127.50	0.177	91.186	142.763
127.52	0.176	74.905	135.452
127.54	0.175	246.620	288.225
127.56	0.174	454.223	447.875
127.58	0.173	384.123	434.453
127.60	0.171	112.865	188.151
127.63	0.170	20.317	84.339
127.65	0.169	8.353	87.713
127.67	0.168	180.094	217.343
127.69	0.167	247.798	271.126
127.71	0.166	251.330	300.372
127.73	0.165	216.570	283.932
127.75	0.164	70.099	160.999
127.77	0.162	168.322	213.390
127.79	0.161	81.649	142.582
127.81	0.160	0.510	86.714
127.83	0.159	-20.363	48.879
127.85	0.158	-26.303	17.762
127.88	0.157	-17.989	2.815

DOY	Albedo	Calculated Q* (W/m^2)	GB4 Measured Q* (W/m^2)
127.90	0.156	-23.199	-10.035
127.92	0.155	-29.751	-25.234
127.94	0.153	-29.297	-44.534
127.96	0.152	-31.140	-50.348
127.98	0.151	-35.152	-50.354
128.00	0.150	-44.070	-50.358

* Shaded entry indicates DOY when SR50 Snow Depth Sensor recorded snow-free conditions at the hillslope meteorological tower (GB4).

Appendix D – Measured and Modelled Incoming Longwave Radiation Using The Parameterisation of Sicart et al. (submitted)

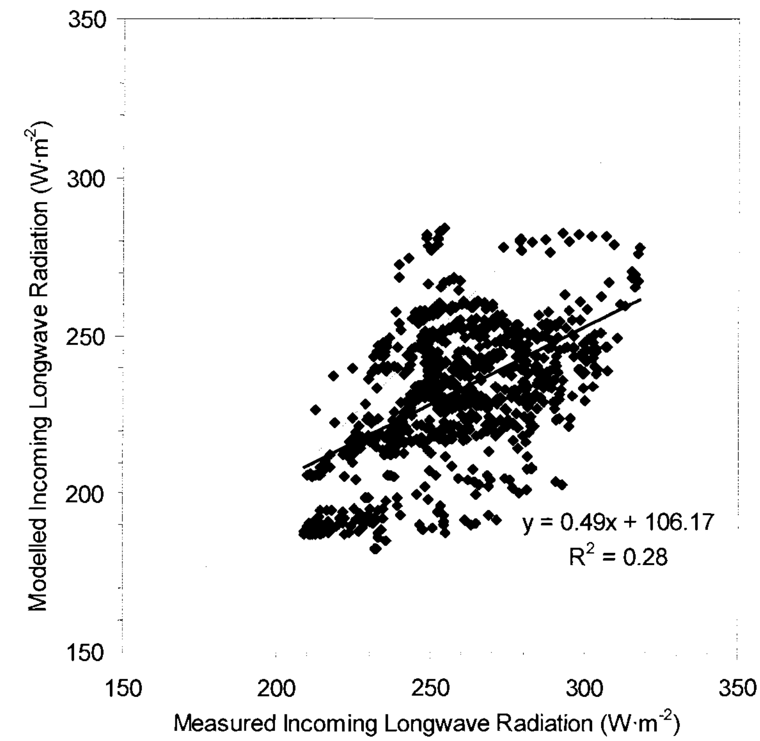

A plot showing a comparison of the modelled (using the parameterisation of Sicart et al., and 'measured incoming longwave radiation'.

An upward-looking pyrgeometer recorded incoming longwave near the valley bottom meteorological tower for approximately 2 weeks in May of 2003 (D. Bewley, personal communication, May 27, 2005). There was also a continuous set of measurements available from a meteorological tower located on a plateau site above the hillslope. A regression between these two data sets was made to allow an extrapolation of the incoming longwave data near the valley bottom back in time through to April (D. Bewley, personal communication, May 27, 2005). When the data co-exist, they are fairly similar, as incoming longwave radiation is relatively spatially consistent over a scale of a few kilometres in all but very mountainous terrain. Thus, the 'measured incoming longwave radiation' data are the extrapolated values calculated from the regression of measured incoming longwave radiation at the plateau site and available incoming longwave radiation at the valley bottom.

Appendix E – Measured and Modelled Snow Q* from DOY 60-112

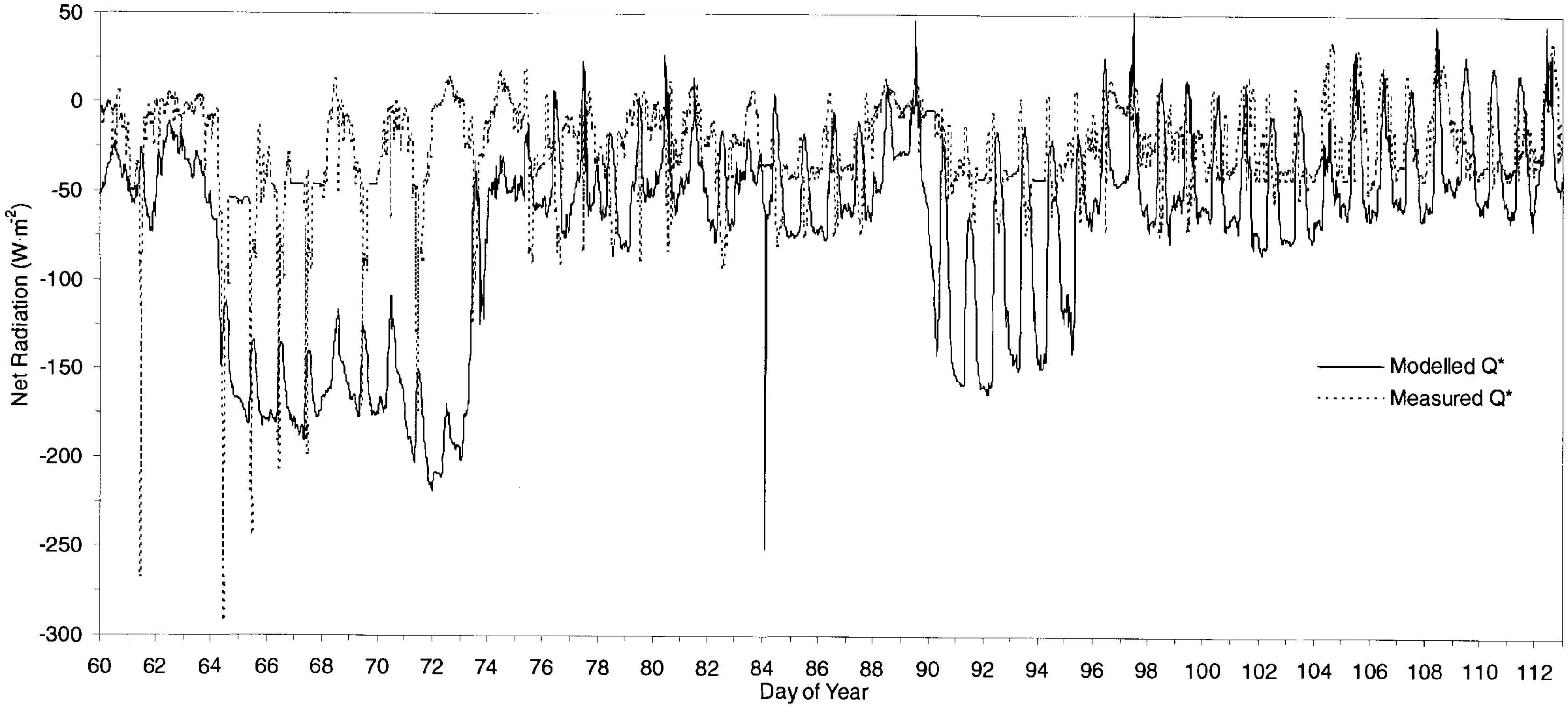

Measured and modelled snow Q* using an albedo value of 0.8 from DOY 60 (March 1) to DOY 112 (April 22) to determine if it is possible to model Q* over a relatively uniform snow-free surface (without the effects of shrub exposure